Impact of Climate Change on Precipitation Extremes and Pluvial Flooding in Europe

Parisa HOSSEINZADEHTALAEI

Supervisor:
Prof. Patrick Willems

Members of Examination Committee:
Prof. Herman Neuckermans, chairman
Prof. Jaak Monbaliu
Prof. Wim Thiery
Prof. Piet Termonia
(Ghent University & Royal Meteorological Institute of Belgium)
Prof. Hamid Moradkhani
(University of Alabama)

Dissertation presented in partial fulfilment of the requirements for the degree of Doctor of Engineering Science (PhD): Civil Engineering

September 2020

© 2020 KU Leuven, Science, Engineering & Technology
Uitgegeven in eigen beheer, Parisa Hosseinzadehtalaei, Kasteelpark Arenberg 40 – bus 2448, B-3001 Heverlee (Belgium)

Alle rechten voorbehouden. Niets uit deze uitgave mag worden vermenigvuldigd en/of openbaar gemaakt worden door middel van druk, fotokopie, microfilm, elektronisch of op welke andere wijze ook zonder voorafgaandelijke schriftelijke toestemming van de uitgever.

All rights reserved. No part of the publication may be reproduced in any form by print, photoprint, microfilm, electronic or any other means without written permission from the publisher.

Acknowledgements

My deep gratitude goes to my supervisor Prof. Patrick Willems. Patrick, I look up to you as a dedicated professor and respected researcher. I really appreciate our useful discussions and brainstorming sessions. I have been remained amazed that despite your busy schedule, you were able to go through the final draft of my papers and thesis and meet me in less than a week with comments and suggestions. You gave me all the freedom to pursue my research, while ensuring that I stay on track and do not deviate from the core of my research. Before starting my PhD under your supervision, I was PhD student in my country which I quit. Now, I do not regret and I think I could not have made a better choice.

I am appreciative to Prof. Jaak Monbaliu, Prof. Hamid Moradkhani, Prof. Wim Thiery and Prof. Piet Termonia for their feedback and the approval of my work. I highly value your efforts to attend the ceremony, and the time taken to assess my dissertation. I look forward to future opportunities for collaboration. I would also like to acknowledge Prof. Herman Neuckermans for his willingness to be the chairman of my thesis committee.

I have been lucky that my office was the biggest in our lab and hence had a chance to interact with nice people from different continents. I am also grateful to the following university staff: Anita, Rita, Danny and Freddy for their assistance whenever I approached them. I am also thankful to all my Iranian friends in Belgium who made me feel supported.

My beloved, Hossein for constant unconditional support and encouragement, and love. You are the biggest source of my strength and no matter what, you are always on my side. We have always been sharing our knowledge and have had fruitful scientific collaborations. Aside being a great spouse, you are the best friend to me.

My adorable and darling son, Arnik words cannot describe my feeling to you. Last year of my PhD was amazing because of you. You little one, brought lots of joy and happiness to our life. My little man, your beautiful smile took tiredness and sadness from me in difficult moments. Noting to me is sweeter

than your smile; through your eyes, I see the world anew. Thank you for making me a mom and being your mom is the greatest honor of my life.

And last but not least, I would like to express my deeper and huge thanks to my parents and my two older brothers who, despite the distance, have always been on my side. Their support is beyond words, distance and time.

Parisa Hosseinzadehtalaei
September 2020

Abstract

Extreme precipitation and flood are among the major climate-related disasters which cause thousands of fatalities and billions of euros in damages each year. The risk of these events is expected to increase remarkably under changing climatic and socioeconomic conditions, increasing pressure on vulnerable societies and ecosystems. Yet, the impact of the changing conditions on sub-daily extreme precipitation and pluvial flooding and their related risk has not been well studied due primarily to the scarcity of sub-daily precipitation observations and model simulations, a limited availability of detailed and consistent data on future vulnerability components and the computationally expensive continental flood modeling. This PhD dissertation therefore explores the impact of future climatic and socioeconomic changes on sub-daily extreme precipitation, intensity-duration-frequency (IDF) curves and pluvial flooding over Europe.

First, the impact of future anthropogenic climate change on 3-hourly extreme precipitation with return periods ranging between 5 and 50 years over Europe is investigated using the simulations from regional climate models (RCMs) with 0.11° resolution from the Coordinate Downscaling Experiment over Europe (EURO-CORDEX) ensemble. The robustness of the signals is examined based on a regionalized signal-to-noise (S2N) technique by taking into account a spatial dependence incorporated spatial pooling (regionalization) to decrease the noise due to internal variability and to achieve improved statistics. The effectiveness of the spatial pooling is evaluated by a sensitivity analysis to precipitation times scale, precipitation intensity, season, climate model resolution and greenhouse gas concentration. The results indicate an intensification of 3-hourly extreme precipitation over Europe at the end of the 21st century for all seasons except summer for which a bipolar pattern (increase in the north and decrease in the south) is discerned. For the non-mitigation scenario of Representative Concentration Pathway (RCP) 8.5, the regionalized winter 3-hourly extreme precipitation changes over 9×9 model grid cells are statistically significant in roughly 72%, 65%, 59% and 48% of the European

area for 5-, 15-, 25- and 50-year return periods respectively, whereas 16-21% of the area will experience significant changes in summer. The S2N values for 3-hourly extreme precipitation changes rise after the spatial pooling by about a factor of 1.4-1.7 for all seasons except summer when they decline by about a factor of 0.78. The results of sensitivity analysis reveal that the regionalization influence is sensitive - in order of decreasing importance - to season, precipitation time scale, precipitation intensity, future greenhouse gas concentration scenario and climate model spatial resolution. Whenever and wherever short-duration convective precipitation is dominant, the precipitation time scale is found to be more important, which is the case seasonally for summer and regionally for south Europe.

Subsequently, the impact of future anthropogenic climate change on precipitation IDF relationships is examined. As a pilot study, future IDF curves are firstly developed for Belgium by using large ensembles of global climate models (GCMs) and RCMs. Building upon the findings from the case study in Belgium, the methodology is extended for Europe and the future IDF curves are developed considering duration ranging from 30 minutes to 24 hours and return periods ranging between 1 and 100 years. The future continental-scale IDF curves are developed in the framework of the quantile perturbation downscaling by applying climate change signals from the EURO-CORDEX RCMs on current IDF curves obtained from high spatial and temporal resolution remote sensing based precipitation products. The results reveal that under climate change, future IDF curves will be uplifted (16-27%, depending on duration and return period) and steepened (17-25%, depending on return period), with a larger degree under RCP8.5 compared to RCP4.5. The upward shift in IDF curves is caused by the intensification of rainstorms under climate change, while a larger increase for shorter duration rainstorms leads to a steepening of the curves. In addition to the intensity of rainstorms, their frequency is also projected to increase such that the frequency of 50-year and 100-year events will be doubled under RCP4.5 and tripled under RCP8.5.

Furthermore, this PhD dissertation analyzes the impact of future climatic and socioeconomic changes on pluvial flooding over Europe. To this end, pluvial

flooding is quantified using a satellite-based data driven approach for 20-, 30-, 50- and 100-year return periods. To elucidate the impact of changes in both climatic and socioeconomic conditions on floods at the continental, regional and national levels, the Shared Socioeconomic Pathways (SSPs) are merged with RCPs, integrating hazard and several social, economic and agricultural exposure-vulnerability proxy indicators. The results reveal that future flood hazard increases for different return periods and scenarios by the end of this century. A ubiquitous drastic increase up to 87% is also projected for future flood risks of different return periods over Europe, with eastern and southern regions experiencing the highest risk increase. A fossil-fuel based development (SSP5 combined with RCP8.5) in the future would lead to 14-15% higher flood risk compared to a sustainable development (SSP1 combined with RCP4.5), which goes up to 23% in north Europe. The amplified future flood risk is predominantly driven by climate change, although with a large uncertainty, rather than socioeconomic drivers. In almost all the European countries, the changes in flood hazard are far larger than the exposure-vulnerability changes.

As the knowledge on the uncertainty of future projections is indispensable for future planning in the face of climatic and socioeconomic changes, special attention is paid to this matter throughout this dissertation. The uncertainty is quantified in the future projections of different variables including extreme precipitation, IDF curves and flood risk. The uncertainty analysis shows GCM uncertainty as the dominant source in extreme precipitation projections for Belgium for all return periods and durations compared to GCM initial conditions and RCPs. By taking an ensemble of the EURO-CORDEX RCMs, the uncertainty associated with the choice of RCMs is found to be larger than the other uncertainty components in the projection of more extreme precipitation. Similar to the Belgian case study, the uncertainty in the projections of extreme precipitation and IDF curves at the European scale is larger for longer return periods. The uncertainty is, with a lesser extent, dependent on duration, being larger for shorter durations. The uncertainty assessment in the projections of European pluvial flood risk indicates a spatially and temporally varying

magnitude of total and fractional uncertainties over the continent, with climate model uncertainty as the dominant source.

The overall results of this dissertation call attention to the vulnerability of the existing water infrastructure systems. The expected changes in precipitation characteristics namely intensity, duration and frequency must be incorporated for the future design of urban water systems as well as in adaptation planning. In order to diminish future flood risk over Europe, priority should be given to the limitation of the radiative forcing to reduce the increasing flood hazard, which demands a global effort, along with the reduction of social and agricultural vulnerabilities.

This PhD dissertation highlights some challenges and research directions that need further investigation in the future. For instance, it suggests the use of multi-model multi-member convection-permitting model experiments to assess the effectiveness of the spatial pooling for local convective precipitation storms. It also proposes that snow processes need to be involved in the development of IDF curves in the snow-dominated regions in Europe, where an extreme precipitation event can be mainly snowfall, which is not immediately available for rainfall-runoff processes, or where snowmelt or rain-on-snow rates exceed extreme rainfall. The dissertation also recommends the flood quantification by using an advanced hydrological model including drainage system components to validate the results of the data-driven approach, and the inclusion of more proxy indicators revenant to flooding and at smaller spatial scales for flood risk assessments.

Nederlandse samenvatting

Extreme neerslag en overstromingen behoren tot de grote klimaatgerelateerde rampen die wereldwijd jaarlijks duizenden dodelijke slachtoffers en miljarden euro's aan schade veroorzaken. Het risico van deze gebeurtenissen zal naar verwachting de komende decennia nog sterk toenemen als gevolg van het veranderend klimaat en socio-economische evoluties. Dit zal vooral grote gevolgen hebben voor onze kwetsbare samenlevingen en ecosystemen. Terwijl de risico's van overstromingsrisico's langs de kust en langs grote rivieren reeds uitgebreid bestudeerd werden is dit minder het geval voor pluviale overstromingen als gevolg van extreme neerslag van korte-duur. De redenen waarom deze laatste risico's nog niet uitgebreid bestudeerd werden, zijn velerlei. De voornaamste is dat er wereldwijd niet zo veel kwaliteitsvolle lange-termijn meetreeksen van korte-duur extreme neerslag beschikbaar zijn. Een andere reden is de zeer beperkte kennis over de kwetsbaarheid van de maatschappij en de ecosystemen voor dergelijke uitzonderlijke lokale meteorologische gebeurtenissen. Verder hebben continentale pluviale overstromingsmodellen nog een zeer lange rekentijd wat hun gebruik sterk bemoeilijkt. Met die nood in het achterhoofd, onderzoekt dit proefschrift de impact van toekomstige klimatologische en socio-economische veranderingen op extreme neerslag en dit voor tijdschalen kleiner dan een dag. Dit gebeurde voor de continentale schaal van Europa. Impactresultaten werden afgeleid zowel onder de vorm van veranderingen in de neerslagintensiteit-duur-frequentie (IDF) verbanden als veranderingen in de pluviale overstromingskansen en –risico's.

Eerst werd de impact bestudeerd van de toekomstige antropogene klimaatverandering op de 3-uur extreme neerslag en dit voor terugkeerperiodes tussen de 5 en 50 jaar. Dit gebeurde met behulp van de simulatieresultaten van regionale Europese klimaatmodellen (RCM's) met een resolutie van 0,11° afkomstig van het EURO-CORDEX project. De robuustheid van het klimaatveranderingssignaal werd onderzocht door geregionaliseerd de signaal-ruis-verhouding (S2N) te bestuderen en dit rekening houdend met de ruimtelijke correlatie. Hierbij werd een ruimtelijke pooling (regionalisatie) doorgevoerd om de ruis als gevolg van interne variabiliteit te verminderen en om verbeterde statistieken te bekomen. De effectiviteit van de ruimtelijke pooling werd

geëvalueerd door een gevoeligheidsanalyse en dit in functie van de tijdschaal, de intensiteit van de neerslag, het seizoen, de resolutie van het beschouwde klimaatmodel en het beschouwde scenario voor de toekomstige broeikasgasconcentraties. De resultaten wijzen op een verhoging van de 3-uur extreme neerslag boven Europa tegen het einde van de 21e eeuw en dit voor alle seizoenen behalve de zomer waarvoor een bipolair patroon (toename in het noorden en afname in het zuiden) wordt waargenomen. Voor het broeikasgasscenario RCP8.5 tonen de geregionaliseerde impactresultaten voor de 3-uur extreme neerslag in de winter statistisch significante neerslagveranderingen voor ongeveer 72%, 65%, 59% en 48% van de oppervlakte van Europa bij respectievelijk terugkeerperiodes van 5, 15, 25 en 50 jaar. Voor de zomer ligt dat percentage tussen de 16% en de 21%. De S2N-waarden voor de 3-uur extreme neerslagveranderingen stijgen na de ruimtelijke pooling met ongeveer een factor 1,4 - 1,7 voor alle seizoenen behalve in de zomer waar ze dalen met ongeveer een factor 0,78. De resultaten van de gevoeligheidsanalyse laten zien dat de regionalisatie-invloed - in afnemende mate - gevoelig is voor het seizoen, de tijdschaal, de neerslagintensiteit, het broeikasgasscenario en de ruimtelijke resolutie van het klimaatmodel. In gebieden waar kortstondige convectieve neerslag dominant is, blijkt de tijdschaal voor neerslag belangrijker te zijn. Dit laatste is vooral het geval in de zomermaanden in Zuid-Europa.

Vervolgens werd de impact bestudeerd van de toekomstige antropogene klimaatverandering op de IDF-verbanden voor extreme neerslag. Hierbij werden eerst toekomstige IDF-verbanden afgeleid voor België door gebruik te maken van een ruime set van mondiale klimaatmodellen (GCM's) en RCM's. Voortbouwend op de bevindingen van die analyse werd de methodologie daarna op gans Europa toegepast. De toekomstige IDF-curven werden afgeleid voor tijdsduren tussen de 30 minuten en 24 uur en voor terugkeerperiodes tussen 1 en 100 jaar. Om de toekomstige IDF-verbanden af te leiden, werd gebruik gemaakt van de kwantielperturbatiemethode. Hierbij werden de klimaatveranderingssignalen voor extreme neerslag, zoals afgeleid van de simulatieresultaten van de EURO-CORDEX RCM's, toegepast op de IDF-verbanden voor het huidig klimaat. Deze laatste werden afgeleid door gebruik te maken van neerslagdata met hoge ruimtelijke en temporele resolutie verkregen via teledetectie. De resultaten tonen dat de toekomstige klimaatverandering de neerslagintensiteiten in de IDF-verbanden zal verhogen

(16-27%, afhankelijk van de tijdsduur en de terugkeerperiode) en de IDF-curven steiler zal doen lopen (17-25%, afhankelijk van terugkeerperiode), dus de kortere-duur neerslagintensiteiten meer zal verhogen dan de langere-duur neerslagintensiteiten. De toename is logischerwijs groter voor de broeikasgasscenario's die gepaard gaan met een sterkere toename in de uitstoot en concentratie aan broeikasgassen (sterkere toename voor het RCP8.5-scenario t.o.v. het RCP4.5-scenario). Door een intensivering van de regenbuien onder klimaatverandering verschuiven de IDF-curven naar boven, terwijl de sterkere toename voor de kortere-duur regenbuien leidt tot steilere curven. Naast de intensiteit van de regenbuien, zal ook hun frequentie naar verwachting toenemen. De kort-duur (sub-dagelijkse) neerslagintensiteiten van een regenbui met een terugkeerperiode van 50 à 100 jaar kunnen in grootteorde verdubbelen bij het RCP4.5-scenario en verdrievoudigen bij het RCP8.5-scenario.

Aangezien de onzekerheid van de toekomstprojecties nog groot is, is het belangrijk om die onzekerheid in rekening te brengen, ook in planningsprojecten die gebruik maken van de toekomstprognoses. Daarom werd in dit proefschrift deze onzekerheid ook bestudeerd. De onzekerheidsanalyse toont aan dat de GCM-onzekerheid (de onzekerheid van de mondiale klimaatmodelresultaten) de belangrijkste onzekerheidsbron is. Ze is belangrijker dan de onzekerheid van de initiële condities die bij de GCM-simulaties gebruikt worden. Ze is ook belangrijker dan de onzekerheid in de toekomstige concentraties aan broeikasgassen (de verschillen tussen de RCP-scenario's). De onzekerheid is logischerwijs groter voor de grotere terugkeerperiodes. De onzekerheid verschilt ook met de tijdsduur waarover de neerslagintensiteiten bestudeerd worden, met een grotere onzekerheid voor de kortere tijdsduren. Ook zijn er sterke ruimtelijke variaties binnen Europa.

De algemene resultaten bij dit proefschrift tonen de hoge kwetsbaarheid aan van de bestaande infrastructuur (rioleringen en andere stedelijke afwateringsstelsels). Bij het toekomstig ontwerp en beheer van deze infrastructuur houdt met best rekening met de toekomstevoluties inzake extreme korte-duur neerslag zoals in dit proefschrift afgeleid. Hierbij houdt men best rekening met de relevante tijdschalen in functie van het responsgedrag van het stedelijk afwateringssysteem en de ontwerpterugkeerperiodes. Ook bestaande stelsels kunnen via diezelfde informatie aangepast worden (klimaatadaptatie).

Het proefschrift belicht ook enkele uitdagingen voor de toekomst en suggesties voor bijkomend onderzoek. Zo wordt bijvoorbeeld geadviseerd om

via een set aan hoge-resolutie klimaatmodellen die ook convectie expliciet modelleren, de effectiviteit van de ruimtelijke pooling voor extreme lokale regenbuien verder te onderzoeken. Ook wordt voorgesteld om sneeuw bijkomend te betrekken bij het afleiden van de IDF-curven. Dat laatste is vooral van belang voor de door sneeuw gedomineerde regio's in Europa, waar extreme regenval vaak in de vorm van sneeuw kan voorkomen. Sneeuw zorgt niet meteen voor neerslagafstroming, maar wanneer de sneeuw smelt kan het wel voor extreem grote afstroming zorgen. Verder wordt aanbevolen om voor het analyseren van de impact op pluviale overstromingen bijkomend gebruik te maken van geavanceerde hydrologische modellen die rekening houden met het stedelijk afwateringssysteem. Dergelijke modellen bestaan al voor individuele steden en gemeenten, maar de toepassing ervan op de schaal van Europa wordt nog een hele uitdaging, vooral inzake rekentijd. Ook is er nood aan meer gegevens om de modellen te valideren. Het inschakelen van burgerwetenschap biedt hier zeer interessante mogelijkheden.

List of Abbreviations

ADR: Age Dependency Ratio 151
BIC: Bayesian Information Criterion 109
C-C: Clausius Clapeyron 2
CF: Change factor 73
CMIP5: Coupled Model Intercomparison Project Phase 5 14
CMORPH: Climate Prediction Center Morphing method 14
CV: Coefficient of Variation 117
DEM: Digital Elevation Model 12
DE-MC: Differential Evolution Markov Chain 105
DJF: December-January-February 23
DRR: Deliberate Disaster Risk Reduction 143
ESDAC: European Soil Data Centre 147
ESGF: Earth System Grid Federation server 21
ESS: Effective Sample Size 24
EURO-CORDEX: Coordinated Downscaling Experiment over Europe 14
EVI: Exposure-Vulnerability Index 150
FFD: Fossil-Fuel based Development 164
GCM: General Circulation Model 5
GDP: Gross Domestic Product 150
IDF: Intensity-Duration-Frequency 3
IIASA: International Institute for Applied Systems Analysis 146
IPCC: Intergovernmental Panel on Climate Change 2
IS: Impervious Surface 147
JJA: June-July-August 23
LES: Linear Equation System 95
MAM: March-April-May 23
MCMC: Markov Chain Monte Carlo 111
MSLP: Mean Sea Level Pressure 27
NCAR: National Center for Atmospheric Research 146
NOAA: National Oceanic and Atmospheric Administration 104
PCA: Principal Component Analysis 64
PMW: Passive Satellite Microwave 106

POT: Peak Over Threshold 61
RCM: Regional Climate Model 14
RCP: Representative Concentration Pathway 15
REA: Reliability Ensemble Average 99
S2N: Signal to Noise 18
SDS: Spatial Downscaling Signal 25
SON: September-October-November 23
SP: Spatial Pooling 40
SRES: Special Report on Emissions Scenarios 32
SSP: Shared Socioeconomic Pathways 15
TDS: Temporal Downscaling Signal 26
USDA: United States Department of Agriculture 12

Table of Contents

Abstract v

Nederlandse samenvatting ix

List of Abbreviations xiii

CHAPTER 1 INTRODUCTION 1

1.1 Overview of hydrological impact of climate change 2

1.2 Uncertainty in climate change impact studies 4

1.3 Pluvial flood risk assessment, mitigation and adaptation strategies 6

1.4 Research objectives and questions 10

1.5 Methodological framework 12

1.6 Dissertation structure 14

CHAPTER 2 CLIMATE CHANGE IMPACT ON EXTREME PRECIPITATION IN EUROPE 17

Summary 18

2.1 Introduction 18

2.2 Materials and methods 21
- 2.2.1 Climate model simulations 21
- 2.2.2 Analyses of signal and signal-to-noise for extreme precipitation 23
- 2.2.3 Regionalization of extreme precipitation changes and its sensitivity analysis 23
- 2.2.4 Scale dependency of extreme precipitation changes 25

2.3 Results and discussion 26

2.4 Conclusions 50

CHAPTER 3 CLIMATE CHANGE IMPACT ON IDF CURVES IN BELGIUM 53

Summary 54

3.1 Introduction 55

3.2 Materials and methods 57
3.2.1 Model data 57
3.2.2 Observed data 60
3.2.3 Development of IDF curves for the current and future climate 61
3.2.4 Uncertainty analysis 63

3.3 Results and discussion 67
3.3.1 Current climate IDF curves 67
3.3.1.1 GCM-based current IDF curves 67
3.3.1.2 RCM-based current IDF curves 68
3.3.2 Future climate IDF curves 70
3.3.2.1. GCM-based future IDF curves 70
3.3.2.2. RCM based future IDF curves 73
3.3.3 Uncertainty analysis of projected changes in IDF statistics 77
3.3.3.1. GCM-based uncertainty analysis 77
3.3.3.2. RCM-based uncertainty analysis 90

3.4 Conclusions 98

CHAPTER 4 CLIMATE CHANGE IMPACT ON IDF CURVES IN EUROPE 101

Summary 102

4.1 Introduction 102

4.2 Materials and Methods 105
4.2.1 Data 106
4.2.1.1 Observation datasets 106
4.2.1.2 Climate model simulations 107
4.2.2 Extreme value analysis 108

4.2.3 Development of IDF curves 111
4.2.4 High quantile estimation bias from short records 114

4.3 Results and discussion 115
4.3.1 Changes in the probability distribution of short-duration extreme precipitation 115
4.3.2 Changes in the intensity and frequency of short-duration extreme precipitation 120
4.3.3 Towards building future climate-proof infrastructure 127

4.4 Conclusions 138

CHAPTER 5 EUROPEAN PLUVIAL FLOOD RISK 141

Summary 142

5.1 Introduction 142

5.2 Materials and methods 145
5.2.1 Data 145
5.2.1.1 Precipitation observations 145
5.2.1.2 Climate model simulations 146
5.2.1.3 Exposure and vulnerability data 146
5.2.1.4 Spatial data for flood estimation 147
5.2.2 Quantification of flood hazard 147
5.2.3 Quantification of exposure and vulnerability 150
5.2.4. Quantification of flood risk 154

5.3 Results and discussion 156

5.4 Conclusions 168

CHAPTER 6 SYNTHESIS AND OUTLOOK 171

6.1 Introduction 172

6.2 Key research findings 172

6.3 Caveats and future works 177

BIBLIOGRAPHY..... 183

CURRICULUM VITAE 213

PHD-RELATED AWARD, PUBLICATIONS AND ACTIVITIES 215

List of Figures

Figure 1.1: Classification of uncertainties in climate change projections..... 6

Figure 1.2: Methodological framework of PhD dissertation. 13

Figure 1.3: PhD dissertation structure. 16

Figure 2.1: Signal (S; first and third columns) and signal-to-noise (S2N; second and fourth columns) for European 3-hourly extreme precipitation of 5-year return period after spatial pooling over 9×9 grid cells based on the 5-member ensemble of the RCA4 model with 12 km resolution for different seasons (winter: first row; spring: second row; summer: third row; autumn: fourth row) under RCP4.5 (first and second columns) and RCP8.5 (third and fourth columns). In signal-to-noise maps, regions of insignificant changes are masked by grey color, while S2N larger than 1.35 and 1.76 denotes significant changes at the 90% and 95% confidence levels, respectively. 28

Figure 2.2: Signal (S; first and third columns) and signal-to-noise (S2N; second and fourth columns) for European 3-hourly extreme precipitation of 15-year return period after spatial pooling over 9×9 grid cells based on the 5-member ensemble of the RCA4 model with 12 km resolution for different seasons (winter: first row; spring: second row; summer: third row; autumn: fourth row) under RCP4.5 (first and second columns) and RCP8.5 (third and fourth columns). In signal-to-noise maps, regions of insignificant changes are masked by grey color, while S2N larger than 1.35 and 1.76 denotes significant changes at the 90% and 95% confidence levels, respectively. 29

Figure 2.3: Signal (S; first and third columns) and signal-to-noise (S2N; second and fourth columns) for European 3-hourly extreme precipitation of 25-year return period after spatial pooling over 9×9 grid cells based on the 5-member ensemble of the RCA4 model with 12 km resolution for different seasons (winter: first row; spring: second row; summer: third row; autumn: fourth row) under RCP4.5 (first and second columns) and RCP8.5 (third and fourth columns). In signal-to-noise maps, regions of insignificant changes are masked by grey color, while S2N larger than 1.35 and 1.76 denotes significant changes at the 90% and 95% confidence levels, respectively. 30

Figure 2.4: Signal (S; first and third columns) and signal-to-noise (S2N; second and fourth columns) for European 3-hourly extreme precipitation of 50-year return period after spatial pooling over 9×9 grid cells based on the 5-member ensemble of the RCA4 model with 12 km resolution for different seasons (winter: first row; spring: second row; summer: third row; autumn: fourth row) under RCP4.5 (first

and second columns) and RCP8.5 (third and fourth columns). In signal-to-noise maps, regions of insignificant changes are masked by grey color, while S2N larger than 1.35 and 1.76 denotes significant changes at the 90% and 95% confidence levels, respectively. 31

Figure 2.5: (a-d) Continental signals and (e-h) the European area (%) with the significant S2N at the 95% confidence level for (a, b, e, f) 3-hourly and (c, d, g, h) daily extreme precipitation under (a, c, e, g) RCP4.5 and (b, d, f, h) RCP8.5. The results are based on a spatial pooling over 9×9 grid cells using the 5-member ensemble of the RCA4 model with 12 km resolution. 33

Figure 2.6: Noise for European 3-hourly (first and third columns) and daily (second and fourth columns) extreme precipitation of 50-year return period after spatial pooling over 9×9 grid cells based on the 5-member ensemble of the RCA4 model with 12 km resolution for different seasons (winter: first row; spring: second row; summer: third row; autumn: fourth row) under RCP4.5 (first and second columns) and RCP8.5 (third and fourth columns). 34

Figure 2.7: Same as for Figure 2.1, but for daily precipitation. 36

Figure 2.8: Same as for Figure 2.2, but for daily precipitation. 37

Figure 2.9: Same as for Figure 2.3, but for daily precipitation. 38

Figure 2.10: Same as for Figure 2.4, but for daily precipitation. 39

Figure 2.11: Comparison between the European area (%) with the significant S2N at the 95% confidence level before (-SP) and after (+SP) spatial pooling over 9×9 grid cells, for (a, c) 3-hourly and (b, d) daily extreme precipitation of (a, b) 5- and (c, d) 15-year return periods based on the 5-member ensemble of the RCA4 model with 12 km resolution. 40

Figure 2.12: Comparison of European daily 50-year extreme precipitation signals after spatial pooling over 9×9 grid cells between different EURO-CORDEX RCMs (RCA4 RCM nested in MPI-ESM-LR GCM: first column; CCLM RCM nested in MPI-ESM-LR GCM: second column; REMO RCM nested in MPI-ESM-LR GCM: third column; RCA4 RCM nested in IPSL-CM5A-MR GCM: fourth column; WRF RCM nested in IPSL-CM5A-MR GCM: fifth column) with 12 km resolution for different seasons (winter: first row; spring: second row; summer: third row; autumn: fourth row) under RCP4.5. 41

Figure 2.13: Comparison of European daily 50-year extreme precipitation signals after spatial pooling over 9×9 grid cells between different EURO-CORDEX RCMs (RCA4 RCM nested in MPI-ESM-LR GCM: first column; CCLM RCM nested in MPI-ESM-LR GCM: second column; REMO RCM nested in MPI-ESM-LR

GCM: third column; RCA4 RCM nested in IPSL-CM5A-MR GCM: fourth column; WRF RCM nested in IPSL-CM5A-MR GCM: fifth column) with 12 km resolution for different seasons (winter: first row; spring: second row; summer: third row; autumn: fourth row) under RCP8.5. 42

Figure 2.14: Regionalization factors for the signal, noise and S2N of European extreme precipitation of (a, c, e, g) 5- and (b, d, f, h) 15-year return periods based on the 5-member ensemble of the RCA4 model with 12 km resolution for different seasons (winter: a, b; spring: c, d; summer: e, f; autumn: g, h) under RCP8.5. 44

Figure 2.15: Regionalization factors for the signal, noise and S2N of European extreme precipitation of (a, c, e, g) 5- and (b, d, f, h) 15-year return periods for different seasons (winter: a, b; spring: c, d; summer: e, f; autumn: g, h) under RCP4.5 based on the 5-member ensemble of the RCA4 model with 12 km resolution. 45

Figure 2.16: Sensitivity analysis of regionalization to (a) precipitation time scale, (b) model spatial resolution, (c) RCP, (d) return period and (e) season. The results are based on the 5-member ensemble of the RCA4 model. Note that S2N values are smoothed because of averaging. The median of regionalization factors over all model grid cells across Europe is shown by black cross in panels a-d and by black horizontal line in panel e. 47

Figure 2.17: (a) Sensitivity analysis of regionalization to model spatial resolution based on the 8-member ensemble of all EURO-CORDEX RCMs (RCA4, CCLM, REMO, WRF) and (b-e) spatial downscaling signal (SDS) of extreme precipitation changes based on the 8-member ensemble of all EURO-CORDEX RCMs (RCA4, CCLM, REMO, WRF) over different European sub-regions for (b, d) 5- and (c, e) 15-year return periods and under (b, c) RCP4.5 and (d, e) RCP8.5. In panel a, the median of regionalization factors over all model grid cells across Europe is shown by black cross. In panels b-e, the scatters for each season from left to right are for north EU (-11-40° longitudes & 54.5-71° latitudes), west EU (-11-12° longitudes & 44-54.5° latitudes), east EU (12-40° longitudes & 44-54.5° latitudes) and south EU (-11-40° longitudes & 36-44° latitudes), respectively. 48

Figure 2.18: Comparison between the spatial downscaling signal (SDS) and the temporal downscaling signal (TDS) of extreme precipitation changes based on the 5-member ensemble of the RCA4 model over different European sub-regions for (a, c) 5- and (b, d) 15-year return periods and under (a, b) RCP4.5 and (c, d) RCP8.5 (North EU: -11-40° longitudes & 54.5-71° latitudes; West EU: -11-12° longitudes & 44-54.5° latitudes; East EU: 12-40° longitudes & 44-54.5° latitudes; South EU: -11-40° longitudes & 36-44° latitudes). 50

Figure 3.1: Comparison of precipitation simulations over a matrix of 3×3 EURO-CORDEX model gridcells in which the central grid is the closest to Uccle station, a: 0.11° simulations of RCA4 RCM nested in MPI-ESM-LR GCM, b: 0.44° simulations of REMO2009 RCM nested in MPI-ESM-LR GCM. 59

Figure 3.2: Validation of precipitation IDF curves derived from CMIP5 runs based on Uccle observations for the historical period (1961-1990) (observation lines for the 1- and 10-year return periods are shown in blue and black colors, respectively). 67

Figure 3.3: Validation of the current climate IDF curves for the 0.11° (a) and 0.44° (b) RCMs based on the Uccle station and E-OBS observations for 10-year, 1-year and 1-month return periods and (c) comparison between the 0.11° and 0.44° simulations with identical combination of GCMs and RCMs (both the vertical and horizontal axes are scaled logarithmically). 69

Figure 3.4: Change factors (from 1961-1990 to 2071-2100) for precipitation IDF statistics of different return periods and aggregation levels, and for different RCPs (top and bottom of the box show the 75th and 25th percentiles of change factors, respectively; top and bottom of the whiskers show the 5th and 95th percentiles, respectively; blue and red dots represent the median and outliers, respectively). 72

Figure 3.5: Future IDF curves (2071-2100) after quantile perturbation based on the CMIP5 GCMs for different RCPs versus the existing IDF curves (1961–1990) at Uccle station (observation lines for the 1- and 10-year return periods are shown in blue and black colors, respectively). 73

Figure 3.6: Change factors of the EURO-CORDEX RCMs for extreme precipitation for 10-year (a, b), 1-year (c, d) and 1-month (e, f) return periods and under RCP4.5 (a, c, e) and RCP8.5 (b, d, f) scenarios (Box defines interquartile range with its top and bottom corresponding to the 25th and 75th percentiles, respectively; horizontal red line inside the box represents the median (50th percentile); whiskers represent the 5th and 95th percentiles, respectively; outliers are depicted as red crosses). 75

Figure 3.7: Comparison between change factors of the EURO-CORDEX simulations of 0.11° and 0.44° resolutions with identical combination of GCMs and RCMs for extreme precipitation under RCP4.5 (a) and RCP8.5 (b) scenarios, combining all durations (Box defines interquartile range with its top and bottom corresponding to the 25th and 75th percentiles, respectively; horizontal red line inside the box represents the median (50th percentile); whiskers represent the 5th and 95th percentiles, respectively; outliers are depicted as red crosses)..... 76

Figure 3.8: Projected IDF curves for all 0.11° (a) and 0.44° RCM (b) runs for 10-year, 1-year and 1-month return periods and (c, d) comparison between the 0.11° and

0.44° simulations with identical combination of GCMs and RCMs for RCP4.5 (c) and RCP8.5 (d) (both the vertical and horizontal axes are scaled logarithmically; current climate IDF curves based on the Uccle station observations are shown in black color in the sub-plots a and b). 77

Figure 3.9: Changes (from 1961-1990 to 2071-2100) in daily design precipitation for different GCMs, RCPs and GCM initial conditions. In each of the subplots, one uncertainty source is varied and the changes for the other two uncertainty sources are averaged. 79

Figure 3.10: Percentage of total variation in change factors for design precipitation amounts explained by GCMs, RCP scenarios and GCM initial conditions uncertainties (uncertainty is defined as the scenario range of change factors).... 81

Figure 3.11: Comparison of median (left column) and range (right column) in the ensembles with different sample sizes (population consists of 200 randomly produced numbers with similar value range to precipitation change factors; smaller sample sizes are randomly selected from the population and this is repeated a large number of times; top and bottom of the box show the 75th and 25th percentiles of randomly generated values, respectively; top and bottom of the whiskers show the 5th and 95th percentiles, respectively; horizontal black line in the middle of the box represents the median). 82

Figure 3.12: GCM and GCM initial condition uncertainties using the same sample size (4 members) as RCPs for design precipitation changes (4 GCMs or CSIRO-Mk3.6.0 runs are randomly selected from the 15 GCMs or the 10 CSIRO-Mk3.6.0 runs and this is repeated a large number of times; GCM and GCM initial condition uncertainties are shown in cyan and yellow boxes, respectively; RCP uncertainty is shown with blue dashed line; top and bottom of the box show the 75th and 25th percentiles of uncertainty range, respectively; top and bottom of the whiskers show the 5th and 95th percentiles, respectively; horizontal red line in the middle of the box and red cross represent the median and outliers, respectively). 83

Figure 3.13: Comparison of median (left column) and range (right column) of change factors for different GCM ensemble sizes (smaller sample sizes are randomly selected from the 15 GCMs and this is repeated a large number of times; uncertainty range is computed as the difference between the high and low climate scenarios defined based on the 95% confidence intervals; top and bottom of the box show the 75th and 25th percentiles of change factors, respectively; top and bottom of the whiskers show the 5th and 95th percentiles, respectively; horizontal black line in the middle of the box and hollow black dot represent the median and outliers, respectively). 85

Figure 3.14: Comparison of median (left column) and range (right column) of change factors for GCM initial conditions with different number of runs (smaller sample sizes are randomly selected from the 10 GCM initial conditions and this is repeated a large number of times; Uncertainty range is computed as the difference between the high and low climate scenarios defined based on the 95% confidence intervals; top and bottom of the box show the 75th and 25th percentiles of change factors, respectively; top and bottom of the whiskers show the 5th and 95th percentiles, respectively; horizontal black line in the middle of the box and hollow black dot represent the median and outliers, respectively). 86

Figure 3.15: Comparison of uncertainty ranges considering four and two RCPs (uncertainty range is computed as the difference between the high and low climate scenarios defined based on the 95% confidence intervals). 88

Figure 3.16: Comparison of uncertainty ranges for GCM initial conditions for different GCMs with the same number of runs (uncertainty range is computed as the difference between the high and low climate scenarios defined based on the 95% confidence intervals). 90

Figure 3.17: Variance decomposition results for the total uncertainty in the change factors computed using the EURO-CORDEX 0.11° RCMs for extreme precipitation after missing data construction in RCM×GCM combinations: percentage of total variance explained by GCMs, RCMs, RCPs and cross-terms components. 92

Figure 3.18: Variance decomposition results for the total uncertainty in the change factors computed using the EURO-CORDEX 0.44° RCMs for extreme precipitation after missing data construction in RCM×GCM combinations: percentage of total variance explained by GCMs, RCMs, RCPs and cross-terms components. 93

Figure 3.19: Comparison of total variance contributions between two cases with high and two cases with low amount of cross term (HCU: high amount of cross uncertainty; LCU: low amount of cross uncertainty). 95

Figure 3.20: Variance decomposition results for the total uncertainty in the change factors computed using the EURO-CORDEX 0.11° RCMs for extreme precipitation without missing data construction in the RCM×GCM combinations: percentage of total variance explained by GCMs, RCMs, RCPs and cross-terms components. 96

Figure 3.21: Variance decomposition results for the total uncertainty in the change factors computed using the EURO-CORDEX 0.44° RCMs for extreme precipitation without missing data construction in RCM×GCM combinations:

percentage of total variance explained by GCMs, RCMs, RCPs and cross-terms components. 97

Figure 4.1: Methodological framework of the study (DE-MC: Differential Evolution Markov Chain; T: Return period). 105

Figure 4.2: (a) Percentage of the POT series of different datasets with GPD as the best fitting distribution and (b) the spatial distribution of Bayesian information criterion (BIC) of the best fitted model. In panel a, clustered bar plots represent the results for five RCM runs. In panel b, the BIC values are normalized over the location parameters of the corresponding grid cells and Q1, Q2, Q3, Q4 and Q5 denote the first, second, third, fourth and fifth quintiles of the BIC values, respectively. . 109

Figure 4.3: Violin plots comparing the median, the spread, and the density of (a, c, e) the GPD parameters around corresponding durations derived from the CMORPH and MSWEP datasets and (b, d, f) the changes in the GPD parameters for 3-hourly extreme precipitation between RCP4.5 and RCP8.5 for different durations using the median of the EURO-CORDEX RCM simulations (a, b: location; c, d: scale; e, f: shape). The median is shown by the thick horizontal line on the violin plots and the maximum and minimum values are represented as the top and bottom of the plots, respectively. Note that the wider the violin plot, the higher the density. The scale parameters for the current climate are normalized over the corresponding location parameters. Note that the absolute changes are calculated for the shape parameter owing to the existence of negative shape parameter values. 116

Figure 4.4: Spatial distribution of the GPD parameters (location: a, b, c; scale: d, e, f; shape: g, h, i) for (a, d, g) historical (1998-2017) and (b, c, e, f, h, i) future (2071-2100) extreme precipitation events of 30-min duration under (b, e, h) RCP4.5 and (c, f, i) RCP8.5 over Europe derived from the CMORPH dataset. The future parameter values are obtained by applying climate change signals on historical parameter values in the framework of the quantile perturbation downscaling method. The climate change signals are computed for the period 2071–2100 with respect to the reference 1971-2000. 117

Figure 4.5: Spatial distribution of the GPD parameters (location: a, b, c; scale: d, e, f; shape: g, h, i) for (a, d, g) historical (1979-2016) and (b, c, e, f, h, i) future (2071-2100) extreme precipitation events of 3-hr duration under (b, e, h) RCP4.5 and (c, f, i) RCP8.5 over Europe derived from the MSWEP dataset. The future parameter values are obtained by applying climate change signals on historical parameter values in the framework of the quantile perturbation downscaling method. The climate change signals are computed for the period 2071–2100 with respect to the reference 1971-2000. 118

Figure 4.6: (a, b) Spatial median of the extreme precipitation changes derived from the median of the EURO-CORDEX RCM simulations as a function of storm durations and return periods for (a) RCP4.5 and (b) RCP8.5, and (c, d) violin plots showing the median, the spread, and the density of return periods under future climatic conditions of extreme daily and 3-hourly precipitation events historically associated with return periods of (c) 50 and (d) 100 years for individual grid cells. The median is shown by the thick horizontal line on the violin plots and the maximum and minimum values are represented as the top and bottom of the plots, respectively. Note that the wider the violin plot, the higher the density. The changes are computed for the period 2071–2100 with respect to the reference 1971-2000. 121

Figure 4.7: Spatial distribution of the changes in extreme precipitation of (a, b, c, d) 3-, (e, f, g, h) 6-, (i, j, k, l) 12- and (m, n, o, p) 24-hr durations and (a, e, i, m) 2-, (b, f, j, n) 10-, (c, g, k, o) 50- and (d, h, l, p) 100-year return periods derived from the ensemble median of the EURO-CORDEX RCM runs under RCP4.5. The climate change signals are computed based on GPD with its parameters estimated by the DE-MC method for the period 2071–2100 with respect to the reference 1971-2000. 123

Figure 4.8: As Figure 4.7 but for RCP8.5. 124

Figure 4.9: Comparison of the spatial median of the extreme precipitation changes between medium (2050s) and far (2080s) future periods as a function of return periods for (a, b) 3-, (c, d) 6-, (e, f) 12- and (g, h) 24-hr storm durations under (a, c, e, g) RCP4.5 and (b, d, f, h) RCP8.5. Lines and uncertainty bands represent ensemble median and ± 2 EURO-CORDEX RCM ensemble standard deviation, respectively. The climate change signals are computed based on GPD with its parameters estimated by the maximum likelihood method for the period 2041–2070 or 2071–2100 with respect to the reference 1971-2000. 125

Figure 4.10: Comparison of the spatial median of the GPD and GEV derived extreme precipitation changes as a function of return periods for (a, b) 3-, (c, d) 6-, (e, f) 12- and (g, h) 24-hr storm durations under (a, c, e, g) RCP4.5 and (b, d, f, h) RCP8.5. Lines and uncertainty bands represent ensemble median and ± 2 EURO-CORDEX RCM ensemble standard deviation, respectively. The climate change signals are computed for the period 2071–2100 with respect to the reference 1971-2000. The parameters are estimated by the maximum likelihood method. 126

Figure 4.11: Precipitation quantiles of the EURO-CORDEX RCM runs (a, c, e, g) before and (b, d, f, h) after bias correction using the quantile perturbation method based on hourly precipitation observations at (a, b) De Bilt, (c, d) Eelde, (e, f) Flushing and (g, h) Volkel stations in The Netherlands. The quantiles are computed

based on GPD with its parameters estimated by the maximum likelihood method. 128

Figure 4.12: Spatial distribution of (a-d) historical (1998-2017) and (e-l) future (2071-2100) extreme precipitation events of 30-min duration for the return periods of (a, e, i) 2, (b, f, j) 10, (c, g, k) 50 and (d, h, l) 100 years under (e, f, g, h) RCP4.5 and (i, j, k, l) RCP8.5 over Europe based on the CMORPH dataset. The future extreme precipitation values are obtained by applying climate change signals on historical extreme precipitation in the framework of the quantile perturbation downscaling method. The climate change signals are computed based on GPD with its parameters estimated by the DE-MC method for the period 2071–2100 with respect to the reference 1971-2000. 129

Figure 4.13: Spatial distribution of (a-d) historical (1979-2016) and (e-l) future (2071-2100) extreme precipitation events of 3-hr duration for the return periods of (a, e, i) 2, (b, f, j) 10, (c, g, k) 50 and (d, h, l) 100 years under (e, f, g, h) RCP4.5 and (i, j, k, l) RCP8.5 over Europe based on the MSWEP dataset. The future extreme precipitation values are obtained by applying climate change signals on historical extreme precipitation in the framework of the quantile perturbation downscaling method. The climate change signals are computed based on GPD with its parameters estimated by the DE-MC method for the period 2071–2100 with respect to the reference 1971-2000. 130

Figure 4.14: Comparison between current CMORPH and future climate scenario IDF curves at some European locations for RCP8.5, along with the model uncertainty bound, indicating different projections of the EURO-CORDEX ensemble members, and distribution parameter uncertainty bound, indicating different estimations of the DE-MC method (a: Brussels (BL), b: De Kooy (NL), c: Eelde (NL), d: Kiev (UA), e: Prague (CZ), f: Barcelona (ES)). The uncertainty bounds are based on the 90% confidence intervals. 132

Figure 4.15: Probability distribution function (PDF) of the top four theoretical distributions among the 16 considered distributions and of the empirical distribution based on the CMORPH dataset at some European locations (a: Brussels (BL), b: De Kooy (NL), c: Eelde (NL), d: Kiev (UA), e: Prague (CZ), f: Barcelona (ES))..... 133

Figure 4.16: Probability distribution function (PDF) of the top four theoretical distributions among the 16 considered distributions and of the empirical distribution based on 10-min precipitation observations at (a) Uccle station for a 100-year period (1901-2000) and hourly precipitation observations at (b) De Kooy and (c) Eelde stations for a 70-year period (1951-2020)..... 134

Figure 4.17: Spatial median of the changes in the form of IDF curves (slope and ordinate) derived from the ensemble median of the EURO-CORDEX RCMs. Changes in the ordinate of IDF curves are shown for different precipitation durations. The relative changes are computed based on GPD with its parameters estimated by the DE-MC method for the period 2071-2100 with respect to the reference 1971-2000. 135

Figure 4.18: Bias in GPD-based quantile estimations using short records. (a) Ratio of the quantiles derived from short records to those from long records versus extrapolation ratio; (b) Comparison of the shape parameter estimated by the DE-MC method from 3-hourly MSWEP precipitation data of 20 (1997-2016) and 38 (1979-2016) year lengths at all European grid cells. In panel a, for the gridded observations, the continental median of the ratios over all European grid cells is shown and century-long 10-min raingauge data (1901-2000) are from Uccle station in central Belgium. 136

Figure 4.19: Fraction of the total uncertainty in the projected extreme precipitation changes for (a) 3-, (b) 6-, (c) 12-, and (d) 24-hr durations as a function of return periods explained by the uncertainties of climate models (Model), emission scenarios (Scenario), extreme value distributions (Distribution) and distribution parameter estimation methods (Parameter). The relative changes are computed for the period 2071–2100 with respect to the reference 1971-2000. 138

Figure 5.1: (a) Potential infiltration over Europe calculated based on (b) slope along with the soil type classes presented in Table 5.1..... 149

Figure 5.2: a) Comparison of changes in Europe's floods of 20-, 30-, 50- and 100-year return periods between RCP4.5 and RCP8.5 at the grid level and b) changes in Europe's floods of 20- and 100-year return periods under RCP8.5 at the continental, regional and national scales. The changes are computed for the period 2071–2100 with respect to the reference 1971-2000 and the results for the median of the EURO-CORDEX RCM simulations are shown. Note that the wider the violin plot, the higher the density. Horizontal lines in violin plots show 25th, 50th and 75th percentiles of the changes in all grid cells over Europe. See Table 5.3 for countries considered in each European region. 157

Figure 5.3: Flood hazard of 20-, 30-, 50- and 100-year return periods in Europe for current climate conditions (1971-2000) and for the 2071-2100 period under RCP4.5, and RCP8.5. The index was normalized over all countries, return periods, scenarios and time periods (i.e., normalization over all the 12 cases) and then classified into five classes from very low to very high, each of which corresponding to a quintile of the 0.05-0.95 range. 158

Figure 5.4: Decomposition of projected changes in 20-, 30-, 50- and 100-year flood risks at the regional and continental levels into exposure-vulnerability and hazard components under Sustainability and Fossil-fuel based development (FFD) scenarios. N EU: North Europe; S EU: South Europe; W EU: West Europe; E EU: East Europe; EU: Europe. See Table 5.3 for countries considered for each region. The EVI and risk results are based on an equal weight (EW) scheme. 159

Figure 5.5: a) Comparison of combined exposure-vulnerability index (EVI) with equal weights (EW), proportional weights (PW) and random weights (RW) schemes for baseline socioeconomic conditions and for the year 2085 under Sustainability (Sus.) and Fossil-fuel based development (FFD) scenarios and b) country level projected changes in social, agricultural and economic vulnerabilities under Sus. and FFD scenarios. Note that the wider the violin plot, the higher the density. Horizontal line in violin plots show 50th percentile of EVI over European countries. In panel b, the changes are computed for the year 2085 with respect to the baseline year 2010. 160

Figure 5.6: Combined exposure-vulnerability index (EVI) with equal weights (EW), proportional weights (PW) and random weights (RW) schemes in Europe for baseline socioeconomic conditions (2010) and for the year 2085 under Sustainability and Fossil-fuel based development (FFD) scenarios. The index was normalized spatially (over all countries) and temporally (over all scenarios and time periods) for each weighting scheme separately (i.e., normalization over the three cases in each row) and then classified into five classes from very low to very high, each of which corresponding to a quintile of the 0.05-0.95 range. 162

Figure 5.7: Risk of floods with return periods of 20, 30, 50 and 100 years in Europe for current climate conditions and for the 2071-2100 period under Sustainability and Fossil-fuel based development (FFD) scenarios. The index was normalized over all countries, return periods, scenarios and time periods (i.e., normalization over all the 12 cases) and then classified into five classes from very low to very high, each of which corresponding to a quintile of the 0.05-0.95 range. 164

Figure 5.8: Decomposition of country-level projected changes in (a, c) 20- and (b, d) 100-year flood risks into exposure-vulnerability and hazard components under (a, b) Sustainability and (c, d) Fossil-fuel based development scenarios. In each case, countries are sorted in a descending order of flood risk changes. See Table 5.3 for countries code. See Figure 5.9 for 30- and 50-year flood risks. 165

Figure 5.9: Decomposition of country-level projected changes in (a, c) 30- and (b, d) 50-year flood risks into exposure-vulnerability and hazard components under (a, b) Sustainability and (c, d) Fossil-fuel based development scenarios. In each case,

countries are sorted in descending order of flood risk changes. See Table 5.3 for countries code. 166

Figure 5.10: Fraction of the total variance of projected risk changes of floods with return periods of (a) 20, (b) 30, (c) 50 and (d) 100 years at the continental and regional scales explained by the uncertainties of climate models, combined future scenarios and weighting schemes of EVI. N EU: North Europe; S EU: South Europe; W EU: West Europe; E EU: East Europe; EU: Europe. See Table 5.3 for countries considered in each region. 167

Figure 5.11: Exposure-vulnerability hotspots for European countries under (a) Sustainability and (b) Fossil-fuel based development scenarios. These hotspots should be taken into account for a disaster risk reduction (DRR) for future flood risks in Europe. 169

List of Tables

Table 1.1: Advantages and disadvantages of different adaptation actions. 9

Table 1.2: Summary of data used in this study. 14

Table 2.1: Characteristics of the EURO-CORDEX RCMs and the driving CMIP5 GCMs used in the present study. 22

Table 3.1: Summary of 15 climate models from CMIP5 used in this study. 58

Table 3.2: The EURO-CORDEX 0.11° RCM × driving CMIP5 GCM matrix; labels Y and X indicate the availability of the corresponding RCM × GCM pair for the scenarios RCP 4.5 and 8.5, respectively. 66

Table 3.3: The EURO-CORDEX 0.44° RCM × driving CMIP5 GCM matrix; labels Y and X indicate the availability of the corresponding RCM × GCM pair for the scenarios RCP 4.5 and 8.5, respectively. 66

Table 3.4: Precipitation intensity difference (%) between the median of EURO-CORDEX 0.44° and 0.11° simulations (0.44°-0.11°) for different return periods and durations 70

Table 4.1: Spatial coefficient of variation (CV) of the GPD parameters over Europe for observed extreme precipitation events of different durations derived from the CMORPH and MSWEP datasets. 117

Table 5.1: Modified USDA (USDA, 2016) potential soil infiltration rates (mm/hr) based on soil texture and slope. 150

Table 5.2: Determinants of combined exposure-vulnerability index and their relevance to flood risk. 151

Table 5.3: European regions and corresponding countries considered in this study. 152

CHAPTER 1

Introduction

1.1 Overview of hydrological impact of climate change

Global warming and the ongoing changes in all components of the climate system under the emission of greenhouse gases lead to an increase in the frequency and intensity of extreme weather and climate events. It will, in turn, enhance the risk posed to people and ecosystems. To limit the pervasive and irreversible climate change risk, reduction of greenhouse gases emission together with implementation of adaptation strategies is essential (IPCC, 2014).

Changes in frequency and intensity of extreme precipitation are among the possible consequence of climate change though with a larger uncertainty compared with mean values (IPCC, 2012). The extreme precipitation increase is due primarily to the increase in atmospheric moisture content in a warmer atmosphere following the Clausius-Clapeyron (C-C) relation, at an approximate rate of 7% $°C^{-1}$ (Trenberth et al., 2003). For very extreme sub-daily precipitation for which there is no limitations in moisture availability and supply (Molnar et al., 2015), the scaling rate may exceed the C-C relation and follow a super C-C relationship (e.g., Lenderink et al., 2011; Loriaux et al., 2013). The highest changes in sub-daily extreme precipitation in Europe are expected for northern Europe (Scandinavia) and the lowest ones in southern Europe (Spain) (Larsen et al., 2009). A similar change gradient from south Europe towards the north was reported for the frequency of extreme precipitation (Kundzewicz et al., 2005).

The increase in sub-daily extreme precipitation will affect urban runoff and sewer overflows, and consequently flooding incidences in urban areas. The present sewer systems in various regions of the globe are eventually insufficient to deal with the more severe extreme precipitation events in the future. The vulnerability of the urban sewer systems will change with the return period, duration and intensity of storms (Alam and Elshorbagy, 2015). The efficiency of storm water facilities (e.g., sewers, storm water management ponds, street curbs, swales) will be affected; most likely leading to a decrease of their level of services (Desramaut, 2008) and to more frequent urban flooding as a result of extreme precipitation events. Such type of flooding is hereafter called pluvial flooding, as opposed to river flooding or coastal flooding. Due to the many

recent pluvial flooding episodes, the study of extreme precipitation changes and its impact on urban drainage systems has received considerable attention in recent years (Willems et al., 2012a, 2012b; Arnbjerg-Nielsen et al., 2013).

The impact of climate change on sewer systems will be a great challenge in the forthcoming decades, because of the subsequent adverse impact on environment, society, health and economy. Inasmuch as the alterations due to climate change will not always happen gradually and linearly, hereupon cities should be prepared for unexpected changes (Loftus et al., 2011). It can also be inferred that the range of changes in flood water level, frequency and volume is higher than that in sub-daily precipitation extremes. The magnifying effect of climate change for urban flooding was also pointed out by Coulthard et al. (2012) and Dale et al. (2015). It is attributed to the non-linear urban water system response to rainfall due to a complex interaction between different climatic, hydrological and geomorphic factors involved.

Municipal water management infrastructure such as sewers, storm water management ponds or detection basins and street curbs are generally designed based on the properties of extreme rainfall in the form of Intensity-Duration-Frequency (IDF) curves. These curves are widely used in hydrological design and as decision support information in flood risk and water management (Watt and Marsalek, 2013). Existing urban water systems have been designed based on certain design criteria derived from historical data. These systems (currently very old in many cities) designed on the basis of the past climate situation are probably not suitable for the current or future climate and will face with an overload problem due to intensified precipitation (Berggren et al., 2008). The importance of revising the design criteria for incorporating the climate change impact has been addressed in a number of studies (Mailhot et al., 2007; Mailhot and Duchesne 2010; Peck et al., 2012; Willems, 2013; De Paola et al., 2014; Madsen et al., 2014; Ahmed and Tsanis, 2016; Shrestha et al., 2017; Courty et al., 2019). One indeed has to prevent urban infrastructure from performing below the design criteria (Mirhosseini et al., 2013). Such revision of the criteria may need to be complemented by other types of adaptation strategies in order to be sufficiently prepared to cope with extreme precipitation changes (Peck et al., 2012).

Despite the importance and urgency mentioned above, the number of climate change impact studies on urban hydrology is, however, still limited. This may be, among other reasons, due to the unavailability of sub-daily data in many regions of the world. Urban hydrology indeed involves short response times to rainfall, typically at sub-daily time scales (Westra et al., 2014; Blenkinsop et al., 2017; Thorndahl et al., 2017).

With the goal to obtain an overall picture of urban hydrological challenges linked to climate change, this PhD dissertation comprehensively evaluates the future climate change impact on sub-daily extreme precipitation and pluvial flooding and related uncertainties in Europe.

1.2 Uncertainty in climate change impact studies

Possible changes in the future precipitation are provided by climate models, but the model projections are uncertain (Tabari et al., 2019; Lehner et al., 2020). Notwithstanding a significant improvement in the last generations of these models, their projections are subject to large uncertainties. The uncertainties in climate change projections are broadly classified into epistemic and ontological uncertainties (Figure 1.1). The ontological uncertainty, also called random, stochastic, aleatory or variability uncertainty, is considered unknowable. It refers to the variability of the natural system (Lee et al., 2006) which is not reducible. The epistemic uncertainties arises by our limited knowledge. Among others are our incomplete theoretical understanding of the climate system (Knutti et al., 2008; Knutti and Sedláček, 2013) such as climate feedbacks (Knutti and Hegerl, 2008; Collins et al., 2011), carbon cycle processes (Friedlingstein et al., 2006; Booth et al., 2012) and gravity-wave drag and its susceptible interplay with large-scale dynamics (Shepherd, 2014) along with unknown future climate changes and possible future trajectories of socio-economic changes such as population change, technology and economic development and energy usage (Nakicenovic et al., 2000). The epistemic uncertainty is reducible by improving knowledge through research, data collection and modelling (Refsgaard et al., 2013; de Moel et al., 2015; Döll and Romero-Lankao, 2017).

The amount of uncertainty is different in the future projections of different variables. The uncertainties are generally larger for extreme precipitation compared with the mean values, because of the mismatch between the spatial and temporal scales of the climate models and the actual size of meteorological systems generating the extreme events (Berggren et al., 2008; Mailhot and Duchesne, 2010; Hosseinzadehtalaei et al., 2017, 2018). The resolution of the current generation of general circulation models (GCMs) is still coarse and unable to capture sub-grid scale processes (Wilby and Wigley, 2000; Frei et al., 2006; Hassanzadeh et al., 2014; Lee and Park, 2017). The processes that cannot be resolved in horizontal grid spacing of GCMs are parameterized, which is a source of large bias and uncertainty in the simulations (Prein et al., 2013; Kendon et al., 2014; Olsson et al., 2015; Mendoza et al., 2016).

Apart from the need for high spatial resolution data, sub-daily precipitation data are needed to simulate pluvial flooding. However, climate models rarely provide such high temporal resolution data. To meet this need, precipitation data from climate models are temporally downscaled or disaggregated to the scale required for flood simulations. However, temporal downscaling adds another source of uncertainty, leading to a higher uncertainty of short duration extreme precipitation in comparison to the longer durations (Semadeni-Davies et al., 2008; Ryo et al., 2014; Chandra et al., 2015). The uncertainty associated with temporal downscaling methods is not usually considered in climate change studies, and entails in an unknown uncertainty contribution (Arnbjerg-Nielsen, 2012). In the case of sub-daily precipitation data simulations from high resolution climate models, they are less accurate due to the difficulty in the modeling of the atmospheric processes that control rare short duration extremes such as convection.

These extreme precipitation uncertainties are directly transferred to future flood simulations. These uncertainties include the choice among GCMs for climate system simulations under a certain emission scenario, the choice among emission scenarios representing possible pathways of future climate forcing, the choice among GCM initial conditions representing multiple realizations of internal variability and the choice among downscaling methods representing different ways to transfer the coarse scale precipitation extremes from climate

models to the small scale precipitation extremes for urban watersheds. Sub-daily extreme precipitation changes also contain a large internal climate variability (Kianfar et al., 2016).

The uncertainty of flood projections is further expanded by the complexity of regional changes in meteorology and hydrology (IPCC, 2012; Thieken et al., 2016). For instance, a source of uncertainty for urban flooding projections can be the interaction between the local urban climate and the global climate change (Jung et al., 2011) as the urban micro climate is also influenced by urbanization through the urban canopy layer and the heat island as well as varying aerosol composition (Ntelekos et al., 2010). The existence of the large uncertainties in the impact assessment makes it challenging to define appropriate adaptation actions for urban flooding. Nevertheless, the uncertainty analysis of extreme precipitation and flooding projections provides precious information for a better interpretation of climate change impact and to mitigate the associated flood risk. For assessing uncertainties in flooding, an ensemble approach, at which different setups to describe the climate and hydrology systems are considered, is needed (Olsson et al., 2009).

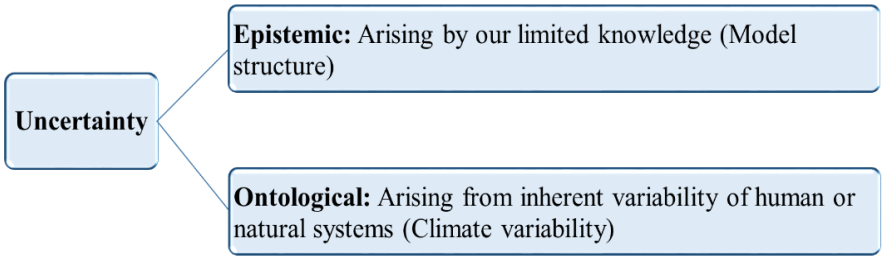


Figure 1.1: Classification of uncertainties in climate change projections.

1.3 Pluvial flood risk assessment, mitigation and adaptation strategies

Risk is defined as the interaction of hazard, exposure and vulnerability (Ahmadalipour et al., 2019). In a more general definition, risk is a combination

of likelihood and consequence (Morlot, 2003). It is characterized as the likelihood of hazards multiplied by the magnitude of the consequences in the case of the hazard occurrence (IPCC, 2014). Hazard is the possible occurrence of natural events or trends. Exposure is the presence of people, property, systems, resources and all elements that are located in hazard prone zone and are subject to potential losses. The exposed elements that can be adversely affected by hazards are considered as vulnerability (Agard et al., 2014; Alfieri et al., 2015). Vulnerability is related to the capacity of a society to anticipate, cope with, endure, and recover from the negative consequences of physical events (Wisner et al., 2004).

All components of risk are dynamic, varying over time and space. Changes in hazards reflect the impact of anthropogenic climate change next to natural climate variability, while changes in exposure and vulnerability are driven by both climatic and non-climatic factors. The dynamic of all risk components have to be considered for future risk analyses under different storylines of changing hazard, exposure and vulnerability (Cardona et al., 2012).

One of the most common and destructive natural hazards is pluvial flooding. Pluvial flood risk is increasing due to the influence of global warming, causing to an increase in the flood hazard including intensity and frequency of extreme precipitation which is the key element of flood risk assessment, as well as socio-economic development such as population growth with its improper spatial distribution, economic growth with an increasing concentration of assets in hazard prone areas and urbanization. Owing to the adverse consequences of the increased flood risk on environment, society, health and economy, cities should be prepared for such changes by undertaking appropriate adaptation strategies.

Adaptation strategies for any types of hazard, including pluvial flooding are generally classified in four groups: grey actions consisting of technical and civil engineering solutions, green actions consisting of the approaches based on the ecosystem and use of nature, soft actions including changing human behavior and government's style, and combined actions (EEA, 2013). The advantages and disadvantages of different adaptation actions are summarized in Table 1.1 to identify the most efficient adaptation measures for pluvial flood risks. Although each of the adaptation actions has its own pros and cons, combining

all these types of adaptation actions will be most effective for a robust decision-making in the future. In this context, to deal with large uncertainties involved in future climate change as well as socio-economic developments and manage flood risk, a flexible and iterative adaptation approach is needed. Adaptation pathways and so-called 'adaptive management' can be used to achieve a flexible adaptation policy, which provides a framework for decision making under uncertainty.

The design and planning of such adaptation solutions, however, needs information about the changes in extreme precipitation and this for the relevant return periods (e.g. design criteria) and time scales (responses times of the system to extreme rainfall), together with the uncertainties. They also need assessments on the corresponding changes in the pluvial flood hazard and risks. This PhD dissertation aims to meet these needs.

Table 1.1: Advantages and disadvantages of different adaptation actions.

Adaptation action	Example	Working mechanism	Advantages	Disadvantages	References
Grey	- Enlargement or renovation of sewer pipes - Repair of breakdowns for sewer systems - Installation of pumps and reservoirs	Increasing the drainage capacity and/or storage capacity of the catchment	- Easily applicable - High priority for policy makers	- High costs and investment risk - Short life of service - Structural inflexibility - Single-purpose	EEA (2012) EEA (2013) Voskamp and Van de Ven (2015)
Green	- Parks - Gardens -Bioswales - Trees - Green roofs - Topographical adjustment	Reducing rainwater-runoff by affecting water infiltration and storage in the soil	- Low risk option in view of the multitude of uncertainties associated with climate change - Cost-effective in terms of overall conception and management costs and end of life - Environmental and ecological benefits - Promoting quality of life by creating a more comfortable urban environments through improved air quality and restricted urban heat island effects	- Maintenance needs - Risk of tree root penetration into built infrastructure - Vegetation and green cover drying out during drought conditions - Acceptability: people's willingness to accept it in their neighborhood	Fletcher et al. (2015) Boteler et al. (2015) Daigneault et al. (2016) EEA (2016) Barra (2016) Chini et al. (2017) Derkzen et al. (2017)
Soft	- Setup and improvement of real-time flood forecasting and warning systems - Land-use planning	Raising awareness, gathering and sharing information on new methods and technologies, developing proper policies and strategies and changing standards and internal organizational systems	- Low-cost solutions - Easily integrable in long-term adaptation plans and strategies	- Not always applicable - Complex because of dealing with different stakeholders, decision-makers and local communities for providing robust, low-regret solutions for a long-term planning	Hallegatte and Dumas (2008) Martin et al. (2010) EEA (2013) Boteler et al. (2015)

1.4 Research objectives and questions

Considering the importance of climate change impact on extreme events and the needs specified in the previous section, the main objective of this study is quantifying climate change impact on extreme precipitation and urban flood frequency over Europe to support water management decisions at local and regional scales. Climate change impact studies on flood risk and particularly for pluvial flooding are typically implemented at basin or local scales, national or continental scale assessments are limited. Accordingly, European pluvial flood risk under climate change is also quantified in this research.

Based on this overall objective of this PhD dissertation, the following primary research questions (RQ), each with several secondary questions, were formulated:

RQ1) How will climate change affect extreme precipitation?

1.1 Is it possible to achieve more robust extreme precipitation changes by reducing the internal variability of the extremes through spatial pooling?
1.2 Does climate change footprint on extreme precipitation have any spatial pattern over Europe?
1.3 How does the climate change impact on sub-daily extreme precipitation differ from that on daily extreme precipitation?
1.4 How does the climate change impact vary with precipitation extremity?
1.5 Is there any seasonality in the future changes of extreme precipitation?
1.6 What is the role of climate model spatial resolutions on extreme precipitation changes?
1.7 How sensitive are future extreme precipitation changes with the level of greenhouse gas concentrations?

RQ2) How will climate change affect IDF curves?

2.1 Is it feasible to develop continental-scale IDF curves based on high spatial and temporal resolution remote sensing based precipitation products?

2.2 How does the climate change impact vary with the duration of design rainstorms and how would it affect the form of the IDF curves?

2.3 How can the possible changes in the form of IDF curves be explained in terms of the projected changes in statistical distribution parameters?

2.4 Will the form of IDF curves change homogenously over Europe?

2.5 How does climate change influence the frequency of design rainstorms?

RQ3) How will climate and socio-economic changes affect pluvial flooding?

3.1 Is it possible to quantify pluvial flooding using a satellite-based data driven approach as an alternative to the computationally expensive continental flood simulations?

3.2 How does flood risk vary with future climatic and socioeconomic storylines? And to what extent the projected flood risk can be avoided by shifting future climatic and socioeconomic developments from a fossil-fuel based development to a sustainable one?

3.3 To what extent the projected changes in flood risk can be attributed to the changes in hazard and exposure-vulnerability components?

3.4 How do the spatial and temporal dynamics of hazard and exposure-vulnerability affect the flood risk over Europe? And what are the most vulnerable European countries to pluvial flooding?

3.5 What are the exposure-vulnerability hotspots of European countries considering different social, economic and agricultural proxy indicators?

RQ4) How large is the uncertainty in extreme precipitation and flood projections and what are the main uncertainty contributors?

4.1 What is the major source of uncertainty in extreme precipitation and flood projections in order to give priority to reduce them?

4.2 How do uncertainties vary with the intensity, duration and frequency of extreme precipitation and flooding?

4.3 What is the effect of different sample sizes of uncertainty sources on their magnitudes? And how a variance decomposition method can be developed to limit the influence of larger sample size and make a fair comparison between different uncertainty components?

1.5 Methodological framework

The general methodological framework of this research is presented in Figure 1.2. It comprises three major parts. Part A illustrates the description of IDF curves development in which extreme value analysis is applied on precipitation data from observations, model historical and scenario simulations. To calculate climate change signals, the extreme precipitation of different intensities and durations for the historical period is compared with the corresponding extreme precipitation for the scenario periods. Consequently, future IDF curves are developed by perturbing the IDF relationships of the current climate by applying the climate change signals in the framework of the quantile perturbation downscaling method.

In part B, potential infiltration needs to be quantified as an essential element to quantify flood hazard. To estimate potential infiltration rate following the United States Department of Agriculture (USDA) procedure, soil texture from satellite data and the average slope derived from Digital Elevation Model (DEM) are used. Consequently, flood hazard is quantified by taking into account potential infiltration rate (Part B) and the design precipitation for sewer systems over which runoff happens (Part A).

In part C, remote sensing based flood hazard (Parts A and B) is combined with exposure-vulnerability indexes including social, economic and agricultural indicators to assess future European flood risk.

To proceed with the methodology and achieve the mentioned objectives of the PhD dissertation, different temporal and spatial resolution precipitation data from global, regional climate models as well as different types of observations are used. The datasets are briefed in Table 1.2.

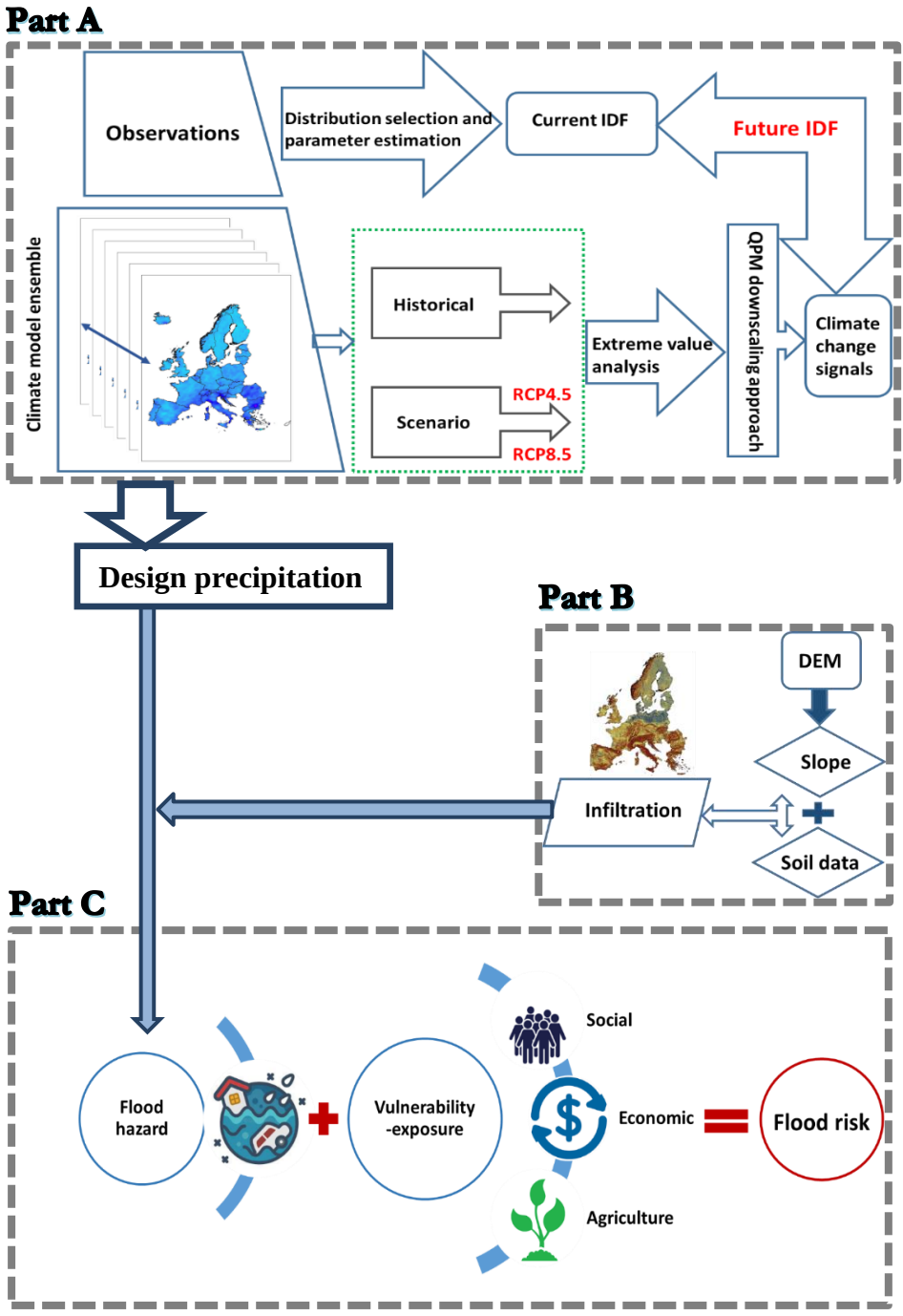


Figure 1.2: Methodological framework of PhD dissertation.

Table 1.2: Summary of data used in this study.

Name of dataset	Type of dataset	Domain	Spatial resolution	Temporal resolution
CMIP5	GCM	Global	100-500 km	Daily
EURO-CODEX	RCM	Europe	12 & 50 km	Daily & 3-hourly
E-OBS	Gridded observations	Europe	55 & 27 km	Daily
MSWEP	Gridded observations	Global	12 km	3-hourly
CMORPH	Gridded observations	Quasi global	8 km	30 min
Raingauge	Point observations	Belgium & The Netherlands	-	10 min & hourly

CMIP5: Coupled Model Intercomparison Project Phase 5; EURO-CORDEX: Coordinated Downscaling Experiment over Europe; GCM: Global Climate Model; RCM: Regional Climate Model; MSWEP: Multi-Source Weighted-Ensemble Precipitation; CMORPH: Climate Prediction Center Morphing method.

1.6 Dissertation structure

The dissertation is structured in six chapters as illustrated in Figure 1.3. Chapters 2-5 address research questions, which are published in international journal articles.

In the first chapter, introduction, research objectives, methodological framework and structure of the PhD dissertation are presented.

The second chapter is allocated to investigate future extreme precipitation over Europe, addressing research question 1. In this chapter, the climate change signals and their robustness for sub-daily extreme precipitation of different return periods varying from 5 to 50 years over Europe are examined. In addition, by applying a spatial pooling technique, its effectiveness on robustness of signals is assessed. Then, sensitivity of regionalization to season, precipitation time scale, precipitation intensity, emission scenario and model spatial resolution is evaluated.

The third chapter addresses the impact of climate change on precipitation intensity-duration-frequency (IDF) relationships for central Belgium. To do so,

climate change scenario provided by the CMIP5 GCMs and the EURO-CORDEX RCMs for different return periods and durations are applied on current IDF curves to obtain future design precipitation. Furthermore, the magnitude of uncertainty in future extreme precipitation related to the choice of GCM, RCM, RCP and initial conditions are also assessed to cover research question 2 and 4.

The fourth chapter is a continental extension of the third chapter. In this chapter, the methodology applied in the third chapter to build future IDF curves in Belgium as a pilot case is refined to develop IDF curves over Europe. To develop European sub-daily IDF curves for different return periods and durations, high temporal and spatial resolution remote sensing based products and an ensemble of sub-daily EURO-CORDEX RCMs are used.

Building upon findings from chapter 4 in developing future European IDF relations, as the IDF curves being the design criteria of sewer systems, chapter 5 focuses on pluvial flood risk assessment in Europe at continental, regional and national scales by taking into account both climate change and socioeconomic developments in which two RCP-SSP combined scenarios, namely sustainability (SSP1 & RCP4.5) and Fossil- Fuel based development (SSP5 & RCP8.5) are evaluated. To this end, the changes in pluvial flood intensity are derived from sub-daily EURO-CORDEX regional climate model data from the historical period to the future period under the two combined emission and socio-economic scenarios. Observed sub-daily extreme precipitation data from high resolution satellite are then perturbed to obtain future flood intensities in Europe for different return periods. The pluvial flooding magnitude regarding each return period or exceedance probability is determined based on an extreme value analysis. For projecting future changes in flood magnitude, the threshold above which flooding occurs should be defined. To find this threshold, the design standard for sewer systems is used. This threshold is applied to calculate flood magnitude for the current and future climates, and finally obtain the changes in the flood magnitude.

Owing to the importance of uncertainty analyses in climate change projections, it is addressed and quantified in different chapters of this PhD dissertation.

The sixth chapter consists of key findings of the five scientific publications from the core of this dissertation. The answers to the research questions, the limitations of the study and the recommendations for future research are also provided in this chapter.

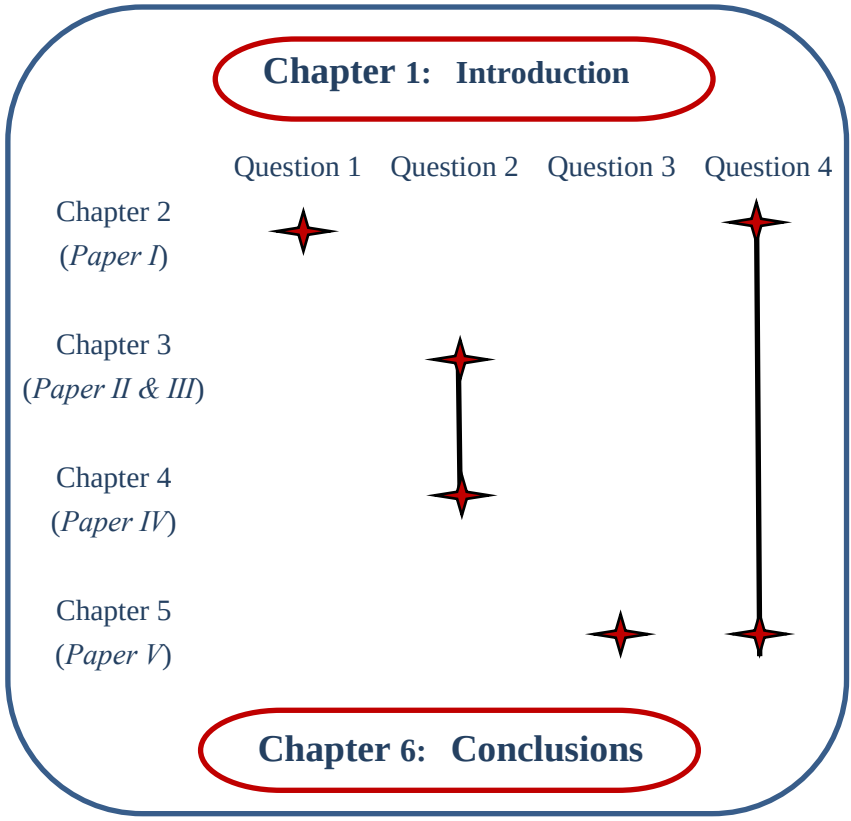


Figure 1.3: PhD dissertation structure.

CHAPTER 2

Climate Change Impact on Extreme Precipitation in Europe

This chapter was published as:

Hosseinzadehtalaei, P., Tabari, H., Willems, P. (2019) Regionalization of anthropogenically forced changes in 3 hourly extreme precipitation over Europe. *Environmental Research Letters*, 14(12), 124031

Summary

Future extreme precipitation events are expected to be influenced by climate change; however, the robustness of this anthropogenically forced response in respect to projection uncertainty especially for sub-daily extremes is not fully understood. We analyze the impact of anthropogenic climate change on 3-hourly extreme precipitation with return periods ranging between 5 and 50 years over Europe using the RCA4 model ensemble simulations at 0.11° resolution. The robustness of the signals is examined based on a regionalized signal-to-noise (S2N) technique by taking the spatial pooling into account and the efficacy of the regionalization is tested by a sensitivity analysis. The results show an increasing signal in 3-hourly extreme precipitation over Europe for all seasons except summer for which a bipolar pattern (increase in the north and decrease in the south) is discerned. For the business-as-usual scenario RCP8.5, the regionalized winter 3-hourly extreme precipitation signals over 9×9 model grid cells are statistically significant in roughly 72%, 65%, 59% and 48% of the European area for 5-, 15-, 25- and 50-year return periods respectively, while 16-21% of the area will experience significant changes in summer. The S2N values for 3-hourly extreme precipitation changes rise after the spatial pooling by about a factor of 1.4-1.7 for all seasons except summer when they decline by about a factor of 0.78. The results of sensitivity analysis reveal that the regionalization influence is sensitive - in order of decreasing importance - to season, precipitation time scale, precipitation intensity, emission scenario and model spatial resolution. The precipitation time scale is particularly important seasonally in summer and regionally in south Europe when/where short-duration convective precipitation is dominant.

2.1 Introduction

An intensification of extreme precipitation is projected by climate models by the end of the 21st century (e.g., Willems et al., 2012; IPCC, 2013; Scoccimarro et al., 2013; Fischer et al., 2013; Pendergrass and Hartmann, 2104; Donat et al., 2016; Wang et al., 2017; Prein et al., 2017; Hosseinzadehtalaei et al., 2017;

Kendon et al., 2018). This intensification is due to several factors. The increase in atmospheric moisture content in a warming climate plays the most important role, which leads to an increase of precipitation intensities by about 7% per degree of surface warming based on the Clausius–Clapeyron (C-C) relationship (Westra et al., 2014; Ban et al., 2015; Lenderink and Fowler, 2017). Other influencing factors are the changes in the temperature lapse rate and anomaly and in vertical wind velocities (Pfahl et al., 2017).

The projected increases of extreme precipitation under anthropogenic climate change have crucial implications for future water management and urban planning, especially in terms of flood hazards (Kendon et al., 2017). Future water resources are more under stress as precipitation is less but more intense, which at the same time emphasizes the need for more precise projection of extreme precipitation changes (Pall et al., 2007; Kendon et al., 2010). The projections are usually performed by means of global climate models (GCMs). GCM simulations are, however, typically at course spatial (hundreds of kilometers) and temporal (daily) resolutions which poses some limitations to accurately capture more details such as land topography or orographic effects and mesoscale processes (Tabari et al., 2016). Therefore, dynamical downscaling has been implemented using regional climate models (RCMs), which provide an improved representation of the physical processes in the atmosphere and the topographic variability which cannot be captured by the coarse resolution of GCMs (Soares et al., 2018; Dosio and Fischer, 2018). Several RCM ensembles have been developed applying GCM results as boundary conditions covering Europe. For example, through the projects PRUDENCE (Christensen et al., 2007; Jacob et al., 2007) and ENSEMBLES (Van der Linden and Mitchell, 2009), RCM projections were obtained at the daily time scale and with a spatial resolution of 50 km for the former and 25 and 50 km for the latter. The EURO-CORDEX project (Coordinate Downscaling Experiment over Europe; Jacob et al., 2014) currently provides the new generation of RCM simulations (Feser et al., 2011; Casanueva et al., 2016; Prein et al., 2016; Giorgi et al., 2016). This ensemble provides the highest spatial and temporal resolution precipitation simulations over Europe at the grid size of 12

km and 3-hourly scale compared to the previous continental simulations, making this ensemble more relevant and suitable for local impact analysis.

The assessment of extreme precipitation signals over Europe by applying RCMs have been performed in several studies (Frei et al., 2006; Fowler et al., 2007; Kendon et al., 2008; Scossimarro et al., 2015; Rajczak et al., 2013; Jacob et al., 2014; Lehtonen et al., 2014; Rajczak and Schär, 2017; Nissen and Ulbrich, 2017). However, the robustness of these signals is less quantified which provides indispensable information for implementing proper adaptation strategies to cope with extreme events. Robust extreme precipitation signals are mainly influenced by projection uncertainty. The projection uncertainty in RCMs can be largely forced by the lateral boundaries, i.e. GCMs, caused by downscaling of large-scale meteorological fields and representation of more details such as topography (Giorgi et al., 2001). A larger projection uncertainty of precipitation changes compared to temperature changes has been pointed out in several studies (e.g., Murphy et al., 2004; Hawkins and Sutton, 2011), owing to the nonlinearity and local character of precipitation (Maraun, 2013; Sieck and Jacob, 2016; Aalbers et al., 2017; Madsen et al., 2017).

The large noise in extreme precipitation changes can be reduced by regionalization through spatial pooling over neighboring grid cells, boosting the robustness of extreme precipitation changes. In this way, longer time series with a homogenous statistical behavior are obtained (Kendon et al., 2008; Hanel et al., 2009; Kendon et al., 2010; Maraun et al., 2010; Sharkey and Winter, 2017). Such longer series also have the advantage that the changes in extreme events can be obtained with higher confidence. Kendon et al., (2008) demonstrated that robustness in winter and summer daily extreme precipitation noticeably increases by applying the spatial pooling. This method was also applied by Aalbers et al., (2017) to evaluate climate change signals in mean and extreme daily precipitation in Western Europe. Li et al., (2019) recently exploited the spatial pooling method to identify robust annual extreme precipitation-temperature scaling relationships across North America.

Although some efforts have been made to regionalize extreme precipitation changes using spatial pooling, the sensitivity of regionalization results to the duration of precipitation extremes and the spatial resolution of climate models

remains unquantified. Furthermore, the previous studies have mostly overlooked the spatial dependency among neighboring model grid cells, which is generated when the neighboring cells from time to time are affected by the same storm (Weiss et al., 2014). The regionalization is only effective when this spatial dependency is considered, especially for extreme precipitation compared to mean precipitation as the former is more influenced by natural variability at the local scale (Maraun et al., 2010; Martel et al., 2018). Ignoring the spatial dependence will result in an underestimation of the extremes (Hosking and Wallis, 1988; Bardet et al., 2011; Weiss et al., 2014; Goudenhoofdt et al., 2017). Other disputable issues for regionalization are the response of precipitation extremity to regionalization, seasonality of regionalization results and their sensitivity to greenhouse gas concentrations. In this chapter, we assess the robustness of the projected changes in 3-hourly and daily extreme precipitation over Europe using the RCA4 RCM ensemble through applying a signal-to-noise (S2N) analysis including a spatial pooling technique with a spatial dependency consideration to decrease the noise due to internal variability. The effectiveness of the regionalization (spatial pooling) is evaluated by a sensitivity analysis to precipitation times scale (3-hourly and daily), precipitation intensity (5- and 15-year return periods), season (four seasons), climate model resolution (12 and 50 km) and greenhouse gas concentration (RCP4.5 and RCP8.5).

2.2 Materials and methods

2.2.1 Climate model simulations

In the present study, high temporal and spatial EURO-CORDEX RCMs are utilized whose data are publicly available through the Earth System Grid Federation server (ESGF archive, http://esgf.org/). EURO-CORDX RCMs contain scenarios based on the latest phase of the Coupled Model Inter comparison project (CMIP5, Taylor et al., 2012). These high resolution simulations have horizontal grid resolutions of 0.44˚ (50 km) and 0.11˚ (12 km) over the European domain, both of which are used in this study. To obtain climate change signals, daily and 3-hourly simulations for the periods 1971-

2000 and 2071-2100 are considered as the historical and scenario (future) periods, respectively. Two Representative Concentration Pathway (RCP, Moss et al., 2010) scenarios of RCP4.5 and RCP8.5 respectively corresponding to mid and high concentration levels are used. Because of limited available simulations for the other two scenarios of RCP2.6 and RCP6.0, they were excluded. The used ensemble contains four RCMs of CCLM, RCA4, REMO, WRF nested in five CMIP5 GCMs (Table 2.1). The 3-hourly precipitation data are available only for the RCA4 model with 12 km resolution, while the remaining RCMs and the RCA4 model with 50 km resolution provide daily data. The precipitation simulations of the EURO-CORDEX RCMs have been validated in several studies (e.g., Prein and Gobiet, 2017).

Table 2.1: Characteristics of the EURO-CORDEX RCMs and the driving CMIP5 GCMs used in the present study.

RCMs	Institution	Driving GCMs (horizontal resolution in km: lat ×lon)	Historical/ Scenario	Horizontal resolution (km)	Temporal resolution
CCLM 4.8.17	CLM Community (CLMCOM)	MPI-ESM-LR (207×208)	His, RCP4.5 & RCP8.5	12 & 50	Daily
RCA4	Swedish Meteorological and Hydrological Institute (SMHI)	CNRM-CM5 (155×156), EC-EARTH (124×125), IPSL-CM5A-MR (141×278), HadGEM2-ES (139×208), MPI-ESM-LR (207×208)	His, RCP4.5 & RCP8.5	12 & 50	Daily & 3-hourly
REMO 2009	Climate Service Center (CSC)	MPI-ESM-LR (207×208)	His, RCP4.5 & RCP8.5	12 & 50	Daily
WRF311F	Institut Pierre Simon Laplace/Institut National de l'Environment Industriel et des Risques, France	IPSL-CM5A-MR (141×278)	His, RCP4.5 & RCP8.5	12 & 50	Daily

2.2.2 Analyses of signal and signal-to-noise for extreme precipitation

This study investigates the climate change impact on European extreme precipitation. Extreme precipitation is defined as precipitation with return periods of 5, 15, 25 and 50 years on the basis of the empirical distribution. The analyses are performed on a seasonal base in which defined seasons are winter [December-February (DJF)], spring [March-May (MAM)], summer [June-August (JJA)] and autumn [September-November (SON)]. Climate change signal is calculated for each model grid point over the domain as the ratio between the precipitation intensity for the scenario period and the corresponding intensity in the historical period for the same return period. For 3-hourly data, the changes in the maximum 3-hourly precipitation per day are considered to ensure that the extremes are taken from independent events. To assess the robustness in the 3-hourly and daily extreme precipitation changes, signal-to-noise (S2N) ratio is applied to determine the locations where anthropogenic forcing (i.e., signal S) is higher than projection uncertainty (i.e., noise N), which can be obtained from inter-simulations of an ensemble (Kay et al., 2015; Martel et al., 2018). S2N is calculated as below:

$$\mathrm{S2N}(\mathrm{d},\mathrm{T}) = \frac{\mathrm{CF}_{\mathrm{ensemble}\ (\mathrm{d},\mathrm{T})}}{\sigma_{\mathrm{ensemble}\ (\mathrm{d},\mathrm{T})}} \tag{2.1}$$

where $\mathrm{CF}_{\mathrm{ensemble}}\,(\mathrm{d},\mathrm{T})$ is the median of climate change signals over the 5-member ensemble of the RCA4 model for an intended return period (T) and precipitation duration (d) (i.e., signal), and $\sigma_{\mathrm{ensemble}\ (\mathrm{d},\mathrm{T})}$ is the standard deviation across the RCA4 model ensemble for the same return period and duration (i.e., noise).

2.2.3 Regionalization of extreme precipitation changes and its sensitivity analysis

To reduce grid-box noise for extreme precipitation arising from internal variability and to achieve improved statistics, we apply a spatial pooling method (Kendon et al., 2008) in which 3-hourly and daily precipitation data within

neighboring grid cells centered on the grid cell of interest are pooled to obtain a longer time series. Different degrees of spatial pooling are examined in this study: 3×3, 5×5, 7×7 and 9×9 arrays of neighboring grid cells corresponding to the spatial scales of 36 (150), 60 (250), 84 (350) and 108 (450) km for a 12 (50) km model, respectively. For instance, by pooling the data from nine grid cells in the case of 3×3 pooling, each of which with a 30-year record, the total sample size is expected to be equal to the sum of all the local sample sizes (i.e., 9 × 30 = 270 years). However, due to a spatial dependency among neighboring cells, the effective sample size (ESS) is smaller than that. The spatial dependency is created when the entire region is influenced by the same storm, causing a similar behavior of extremes in the neighboring cells. Based on the method developed by Weiss et al., (2014), the ESS for the time series in each model grid cell is given by

$$\mathrm{ESS} = \mathrm{n} \times \frac{\lambda_b}{\lambda_c} \tag{2.2}$$

where n is the length of data (30 years in our case), λ_b is the total number of extremes in the model grid box (3×3, 5×5, 7×7, 9×9) and λ_c is the number of extremes in the target model grid cell. $\frac{\lambda_b}{\lambda_c}$ varies between 1 and k, where k is the number of model grid cells (e.g., nine for 3×3 spatial pooling). It is close to one when the spatial dependency in the region is strong. Owing to a regionally and seasonally varying precipitation over Europe, a grid cell specific threshold (rather than an absolute value) is selected to define extremes, that is extreme precipitation with a 5-year return period for both daily and 3-hourly time scales.

The spatial pooling is performed for extreme precipitation of the historical and scenario periods separately, and the return periods (T) of extreme precipitation for each grid cell are estimated as T=ESS/i where ESS is the effective sample size calculated by Eq. 2.2 and i is the rank of precipitation quantiles. Later on, extreme precipitation changes at each grid cell over the domain are determined for each model run for different seasons and return periods. With the regionalization of the signals, we expect smaller noises and subsequently larger S2N values. To test this hypothesis, the S2N results after

and before the spatial pooling are compared. Finally, the significance of S2N is tested based on the ensemble size (m) using the t test (Kendon et al., 2008):

$$t = S2N\sqrt{\frac{m}{2}} \tag{2.3}$$

The effectiveness of the regionalization is examined by computing a ratio between signal, noise and S2N after and before regionalization (spatial pooling), which is called hereafter "regionalization factor". The regionalization sensitivity to precipitation time scale (3-hourly and daily), precipitation intensity (5-, 15-, 25- and 50-year return periods), season (four seasons), climate model resolution (12 and 50 km) and greenhouse gas concentration scenario (RCP4.5 and RCP8.5) is also analyzed. To this end, the sensitivity to precipitation time scale is determined by comparing S2N values between 3-hourly and daily precipitation, while the variations among all other factors are excluded by averaging. A similar procedure is adapted for the sensitivity analysis to the other factors. For the sensitivity analysis of the regionalization to model spatial scale, precipitation data of the 12 km RCMs are first regridded to a 50 km grid size using the bilinear interpolation method and then spatial pooling is performed.

2.2.4 Scale dependency of extreme precipitation changes

In addition to the sensitivity analysis of regionalization to spatial and temporal scales, the scale dependence of extreme precipitation signals without spatial pooling is further analyzed for different seasons and four considered return periods (5, 15, 25 and 50 years). In order to examine the effect of model spatial resolution on the projection of extreme precipitation, a spatial downscaling signal (SDS) statistic is defined. To calculate this statistic, climate change signals in percent obtained from the EURO-CORDEX RCMs with 12 km and 50 km spatial resolutions ($CF_{RCM_{12,50}(daily)}$) are compared with those from the driving CMIP5 GCMs ($CF_{GCM(daily)}$):

$$SDS = \frac{CF_{RCM_{12,50}(daily)}}{CF_{GCM(daily)}} \tag{2.4}$$

To compare the results of the models with different spatial resolutions by the SDS statistic, the native grid sizes of the GCMs and the 12 km RCMs are regridded to a 50 km grid size using the bilinear interpolation method.

Similar to the SDS statistic, a temporal downscaling signal (TDS) is defined to evaluate the influence of the temporal resolution of model simulations for extreme precipitation. For the calculation of this index, 3-hourly EURO-CORDEX extreme precipitation signals ($\mathrm{CF}_{\mathrm{RCM}_{12}(3\mathrm{hr})}$) in percent from the RCA4 model ensemble are compared with the daily signals from the same model ensemble ($\mathrm{CF}_{\mathrm{RCM}_{12}(\mathrm{daily})}$) for each model grid point in percent:

$$\mathrm{TDS} = \frac{\mathrm{CF}_{\mathrm{RCM}_{12}(3\mathrm{hr})}}{\mathrm{CF}_{\mathrm{RCM}_{12}(\mathrm{daily})}} \tag{2.5}$$

Negative SDS and TDS values denote opposite signal signs between GCMs and RCMs and between daily and sub-daily precipitation, respectively. The robustness of TDS and SDS is quantified based on the ensemble member agreement on the direction of the signal. TDS and SDS are robust when more than 80% of the ensemble members agree on the direction of the signal. Otherwise, they are interpreted as 'unreliable'.

2.3 Results and discussion

The projected seasonal changes in 3-hourly extreme precipitation of 5-, 15-, 25- and 50-year return periods along with their robustness in the form of S2N over the European domain are presented in Figures 2.1, 2.2, 2.3 and 2.4. The results indicate that 3-hourly extreme precipitation is projected to intensify in winter, spring and autumn for most of Europe for both RCP4.5 and RCP8.5 with more pronounced changes for RCP8.5. Following Kröner, (2016), the main controlling factor for these changes in European winter extreme precipitation is the thermodynamic effect rather than the lapse-rate and circulation effects. In summer, a decline in 3-hourly extreme precipitation is projected in the southern part of Europe over Spain, Italy, southern France, the northern part of the Mediterranean Sea and the southern and eastern parts of the Black Sea, which is in agreement with the study of Scoccimarro et al., (2015) for a less extreme

3-hourly precipitation (90th percentile) by employing the CMCC-CM model. This decrease can be as a consequence of the northward displacement of the subtropical high and the increase in mean sea level pressure (MSLP) change over Europe (Kjellström et al., 2017). Also, the changes in the lapse-rate are an important factor as the sensitivity of convective precipitation to change in atmospheric stability is higher (Kendon et al., 2010; Kröner et al., 2017). The warm air moves slowly from the Atlantic Ocean to land and gets warmer and dryer and causes a significant fraction of decrease in precipitation in the Southern part of Europe, especially the Mediterranean region. In contrast to southern Europe, extreme precipitation changes are projected to increase in all seasons in the northern and northeastern parts.

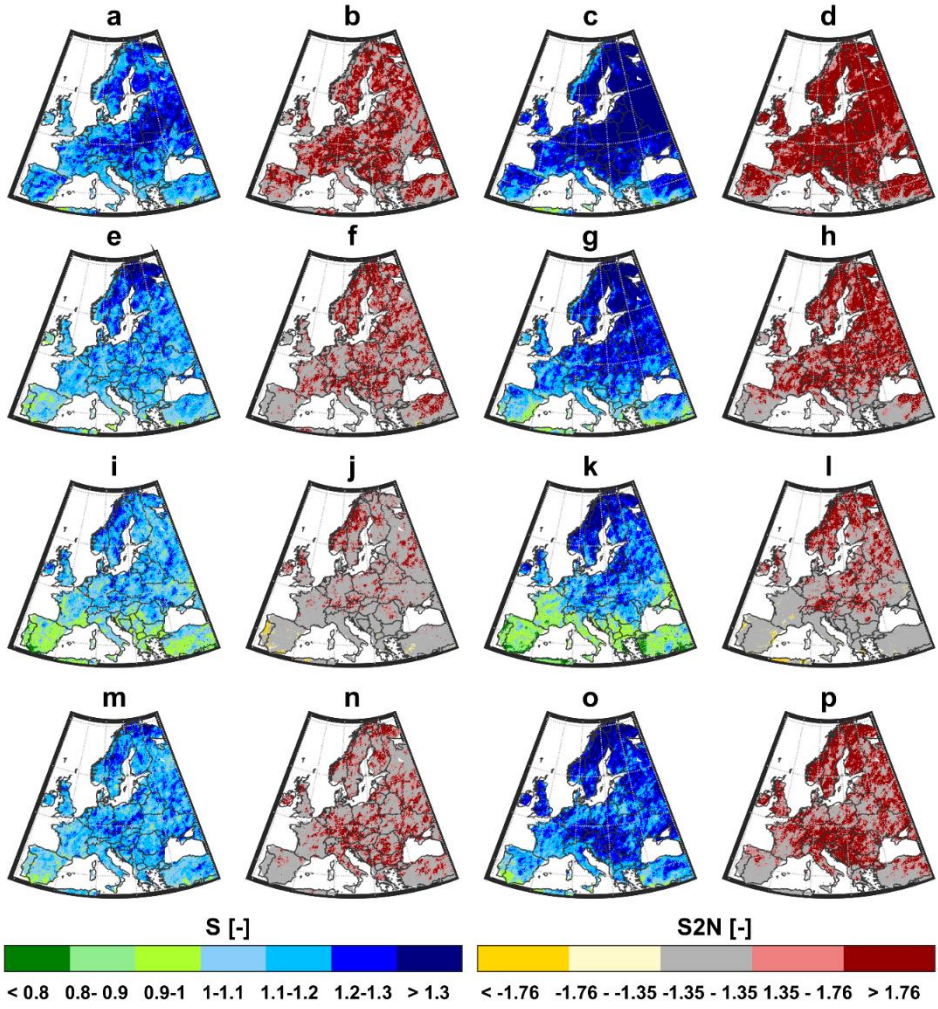


Figure 2.1: Signal (S; first and third columns) and signal-to-noise (S2N; second and fourth columns) for European 3-hourly extreme precipitation of 5-year return period after spatial pooling over 9×9 grid cells based on the 5-member ensemble of the RCA4 model with 12 km resolution for different seasons (winter: first row; spring: second row; summer: third row; autumn: fourth row) under RCP4.5 (first and second columns) and RCP8.5 (third and fourth columns). In signal-to-noise maps, regions of insignificant changes are masked by grey color, while S2N larger than 1.35 and 1.76 denotes significant changes at the 90% and 95% confidence levels, respectively.

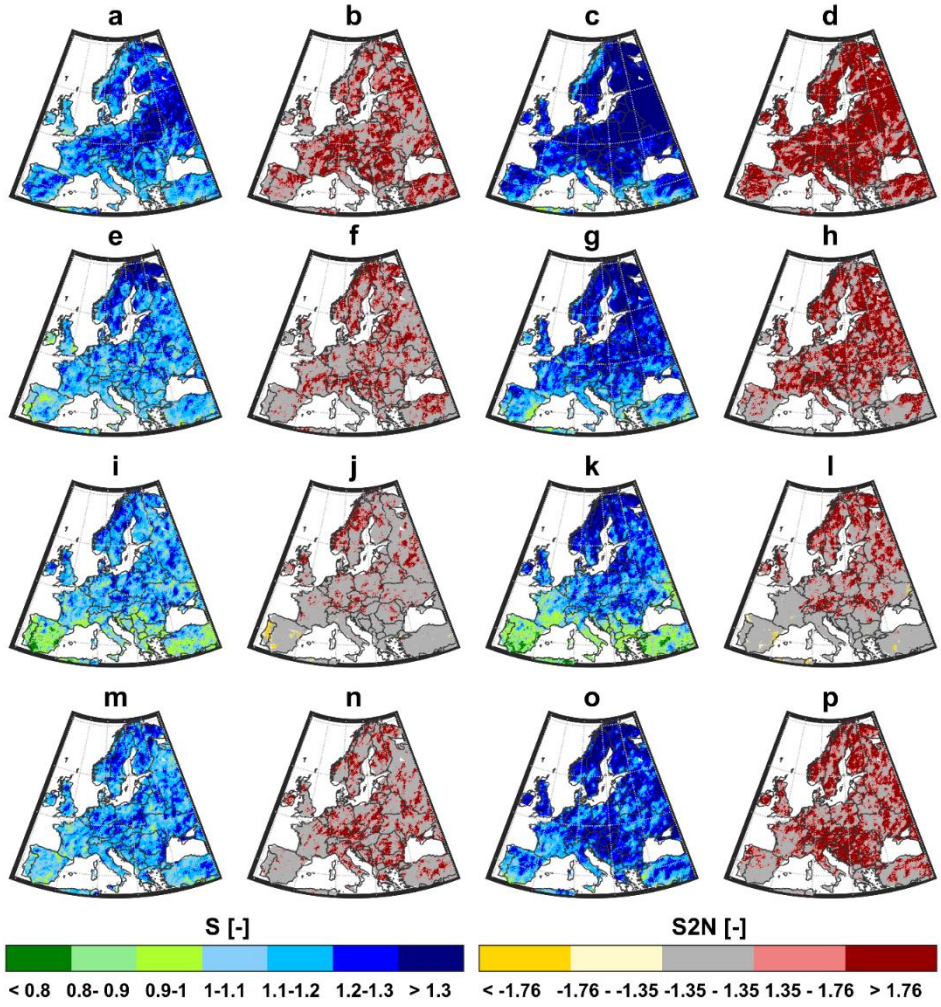


Figure 2.2: Signal (S; first and third columns) and signal-to-noise (S2N; second and fourth columns) for European 3-hourly extreme precipitation of 15-year return period after spatial pooling over 9×9 grid cells based on the 5-member ensemble of the RCA4 model with 12 km resolution for different seasons (winter: first row; spring: second row; summer: third row; autumn: fourth row) under RCP4.5 (first and second columns) and RCP8.5 (third and fourth columns). In signal-to-noise maps, regions of insignificant changes are masked by grey color, while S2N larger than 1.35 and 1.76 denotes significant changes at the 90% and 95% confidence levels, respectively.

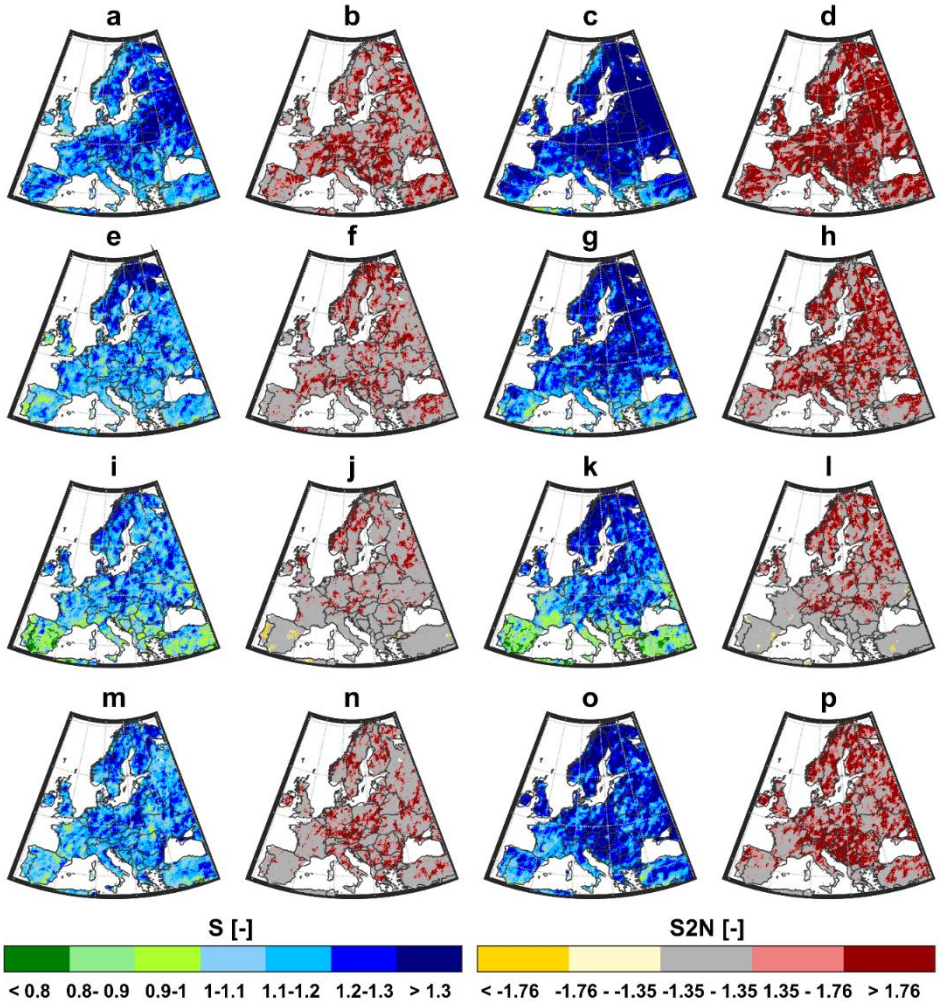


Figure 2.3: Signal (S; first and third columns) and signal-to-noise (S2N; second and fourth columns) for European 3-hourly extreme precipitation of 25-year return period after spatial pooling over 9×9 grid cells based on the 5-member ensemble of the RCA4 model with 12 km resolution for different seasons (winter: first row; spring: second row; summer: third row; autumn: fourth row) under RCP4.5 (first and second columns) and RCP8.5 (third and fourth columns). In signal-to-noise maps, regions of insignificant changes are masked by grey color, while S2N larger than 1.35 and 1.76 denotes significant changes at the 90% and 95% confidence levels, respectively.

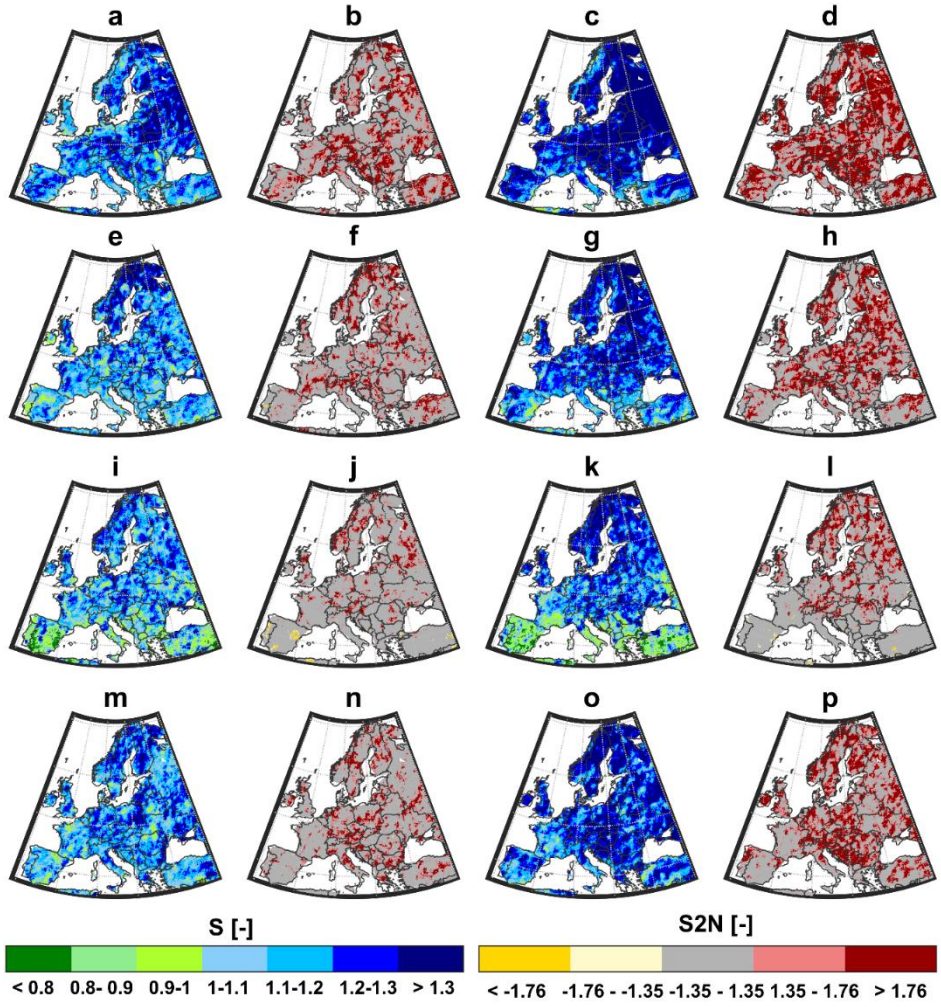


Figure 2.4: Signal (S; first and third columns) and signal-to-noise (S2N; second and fourth columns) for European 3-hourly extreme precipitation of 50-year return period after spatial pooling over 9×9 grid cells based on the 5-member ensemble of the RCA4 model with 12 km resolution for different seasons (winter: first row; spring: second row; summer: third row; autumn: fourth row) under RCP4.5 (first and second columns) and RCP8.5 (third and fourth columns). In signal-to-noise maps, regions of insignificant changes are masked by grey color, while S2N larger than 1.35 and 1.76 denotes significant changes at the 90% and 95% confidence levels, respectively.

Comparing the 3-hourly extreme precipitation changes among different seasons, the largest changes are expected in winter and the smallest in summer (Figure 2.5a, b). In contrast, noise in 3-hourly extreme precipitation projections is largest in summer and smallest in winter (Figure 2.6). In turn, changes in 3-hourly extreme precipitation are more robust in winter, and less robust in summer (Figure 2.5c-f). Although the signals get larger when precipitation gets more extreme from a return period of 5 years to 50 years, their robustness has an opposite pattern. A less significant change in more extreme precipitation is because of the larger internal variability of more extreme events (Räisänen and Joelsson, 2001; Hosseinzadehtalaei et al., 2018) or of high spatial heterogeneity in physical processes resulting in extreme precipitation intensification (Fischer et al., 2014; Vautard et al., 2014; Aalbers et al., 2017). The robustness is also more pronounced under RCP8.5. For RCP8.5 (RCP4.5), approximately 72% (42%), 65% (33%), 59% (29%) and 48% (24%) of the European area have significant changes (α=0.05) in winter 3-hourly extreme precipitation for 5-, 15-, 25- and 50-year return periods, respectively, while significant changes in summer extremes are seen in 21% (10%), 20% (10%), 19% (10%) and 16% (9%) of the area for the mentioned return periods. It shows the low climate signals compared to the high uncertainties in summer extreme precipitation as reported in the literature (Aalbers et al., 2017; Tabari and Willems, 2018). The decrease of the European area with significant changes from less extreme daily precipitation towards more extreme daily precipitation and from winter to summer was also reported using the HadRM3H RCM under the SRES A2 forcing scenario (Kendon et al., 2008).

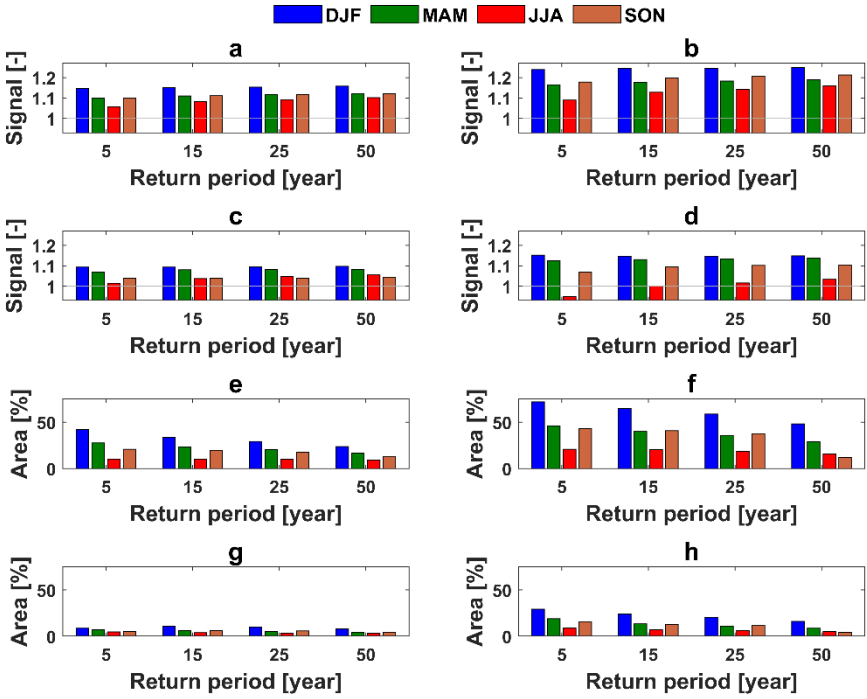


Figure 2.5: (a-d) Continental signals and (e-h) the European area (%) with the significant S2N at the 95% confidence level for (a, b, e, f) 3-hourly and (c, d, g, h) daily extreme precipitation under (a, c, e, g) RCP4.5 and (b, d, f, h) RCP8.5. The results are based on a spatial pooling over 9×9 grid cells using the 5-member ensemble of the RCA4 model with 12 km resolution.

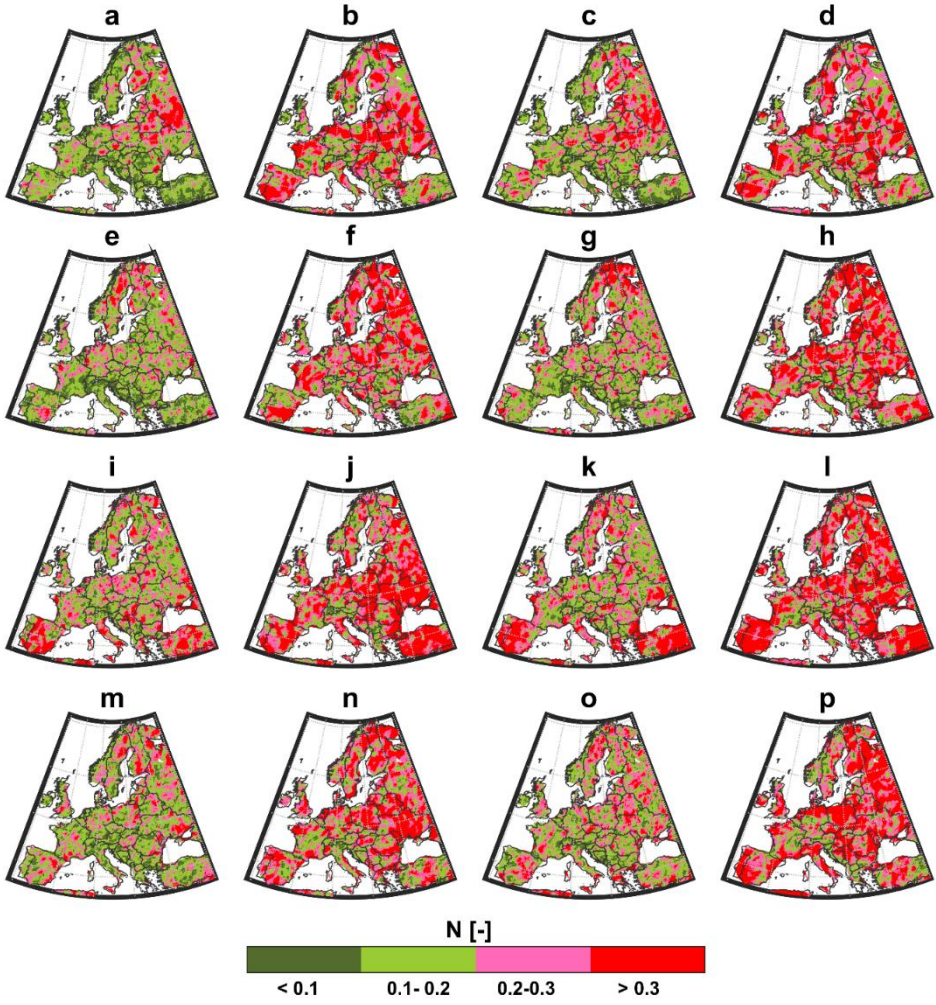


Figure 2.6: Noise for European 3-hourly (first and third columns) and daily (second and fourth columns) extreme precipitation of 50-year return period after spatial pooling over 9×9 grid cells based on the 5-member ensemble of the RCA4 model with 12 km resolution for different seasons (winter: first row; spring: second row; summer: third row; autumn: fourth row) under RCP4.5 (first and second columns) and RCP8.5 (third and fourth columns).

The significance and magnitude of the changes in daily extreme precipitation are also analyzed. After the spatial pooling, the significant changes in daily extreme precipitation over Europe are less widespread compared to 3-hourly extreme precipitation for all seasons and return periods (Figures 2.7-10). Significant changes in daily extreme precipitation are found in less than 16% of

the European area (Figure 2.11b, d). This highlights the importance of precipitation time scale in climate change impact assessment. The importance of precipitation time scale has been highlighted in many previous findings such that short-duration extreme precipitation increases with rising temperatures twice the rate expected from the C–C relation, the so-called “super C-C rate” (Lenderink and van Meijgaard, 2008; Haerter et al., 2010; Wang et al., 2017).

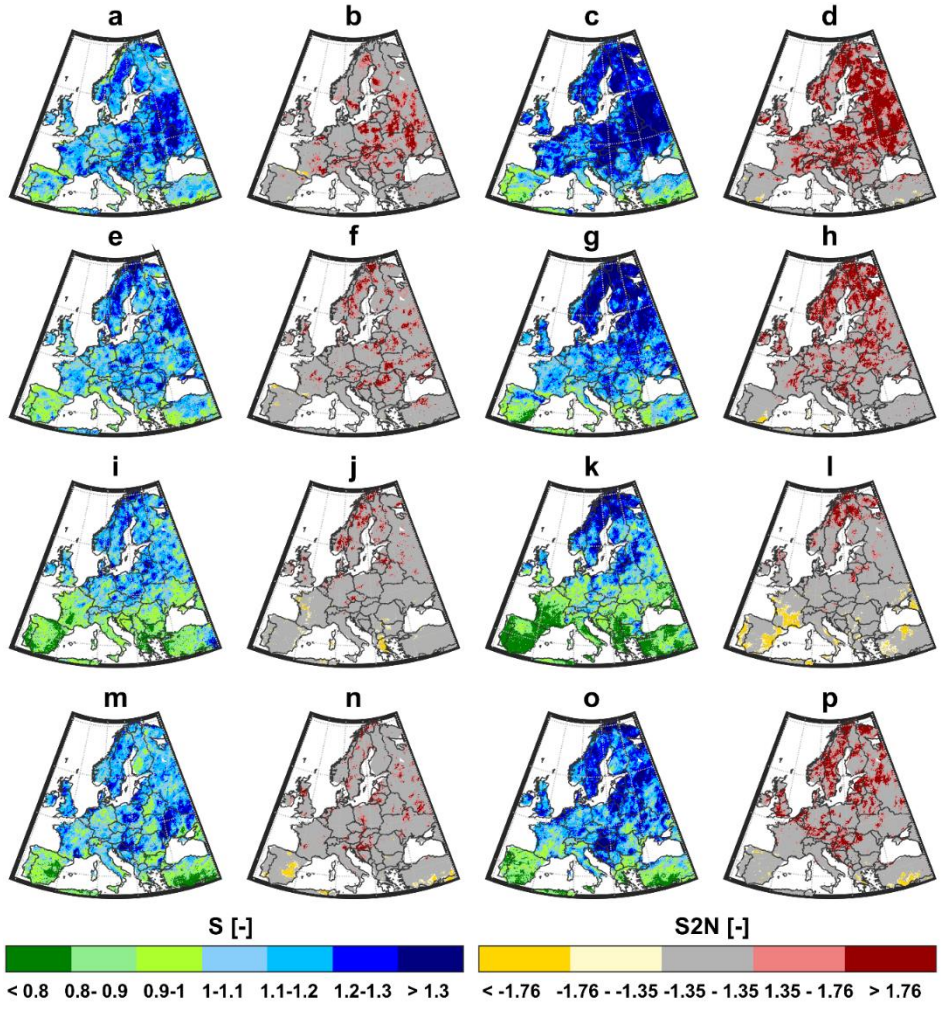


Figure 2.7: Same as for Figure 2.1, but for daily precipitation.

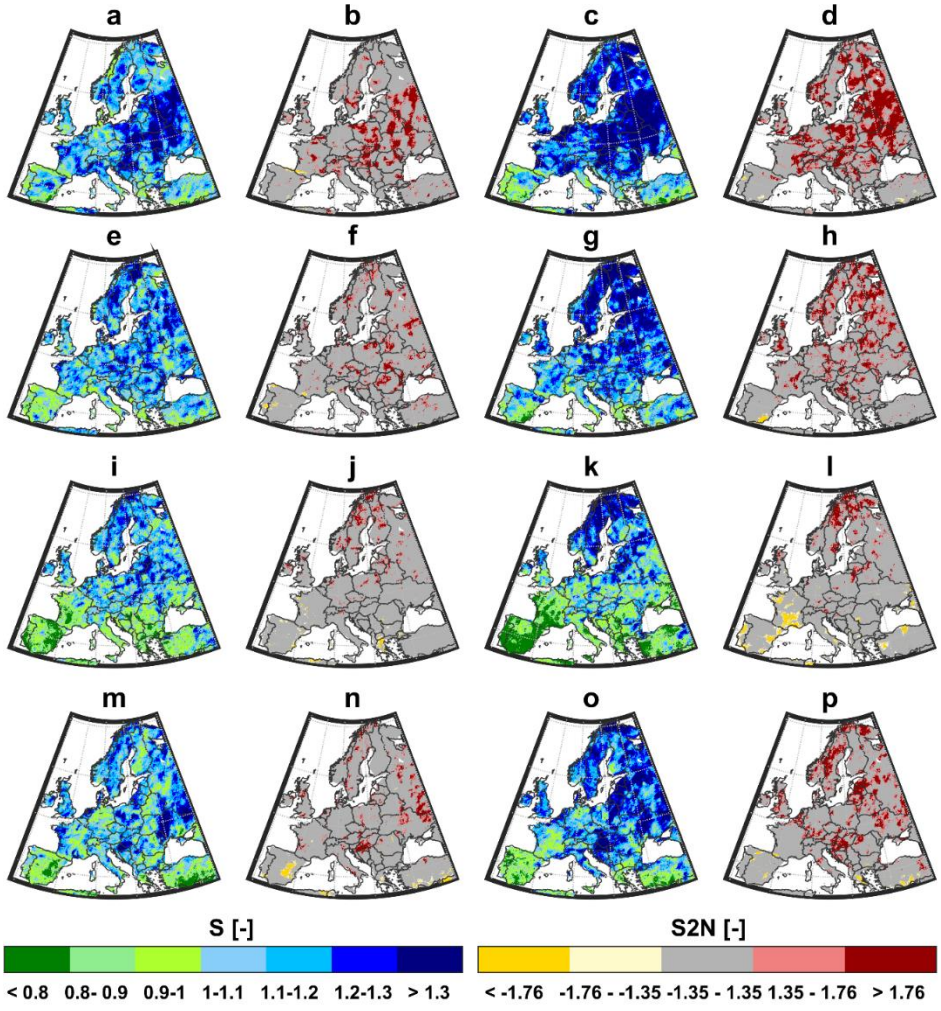


Figure 2.8: Same as for Figure 2.2, but for daily precipitation.

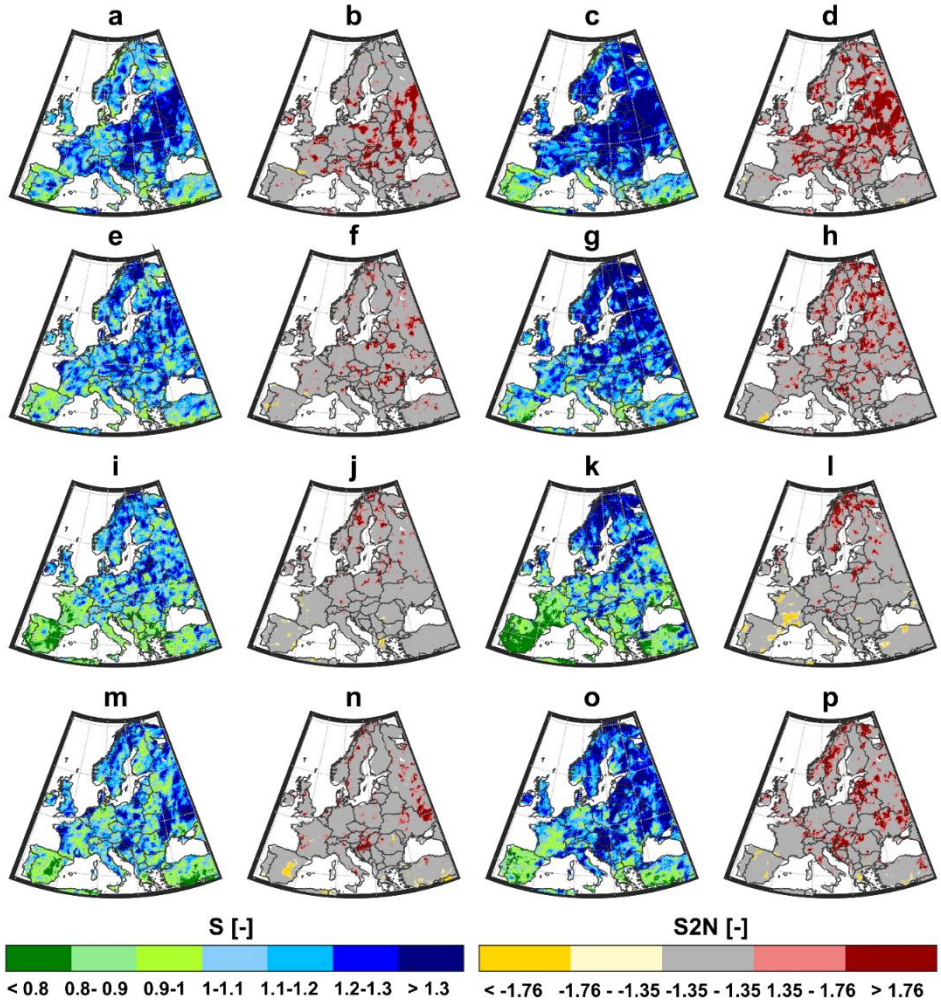


Figure 2.9: Same as for Figure 2.3, but for daily precipitation.

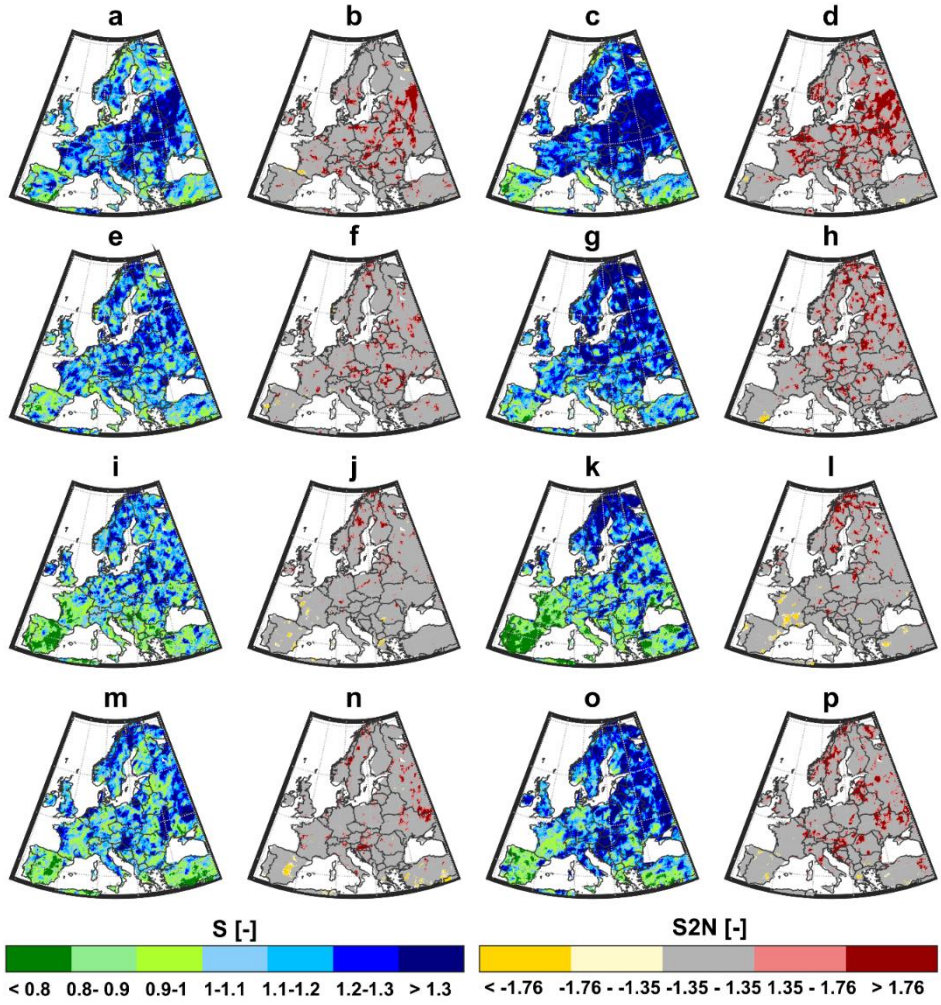


Figure 2.10: Same as for Figure 2.4, but for daily precipitation.

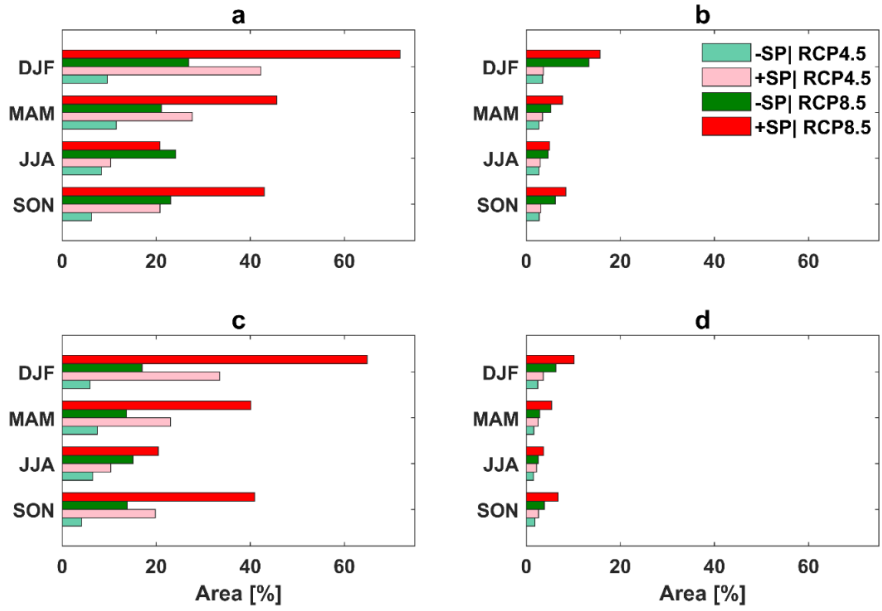


Figure 2.11: Comparison between the European area (%) with the significant S2N at the 95% confidence level before (-SP) and after (+SP) spatial pooling over 9×9 grid cells, for (a, c) 3-hourly and (b, d) daily extreme precipitation of (a, b) 5- and (c, d) 15-year return periods based on the 5-member ensemble of the RCA4 model with 12 km resolution.

A comparison of daily 50-year extreme precipitation signals after 9×9 spatial pooling between different EURO-CORDEX RCMs shows a high similarity in the spatial pattern and the magnitude of changes between the RCMs with the same parent GCM (Figures 2.12 and 2.13), confirming the results derived from the RCA4 model.

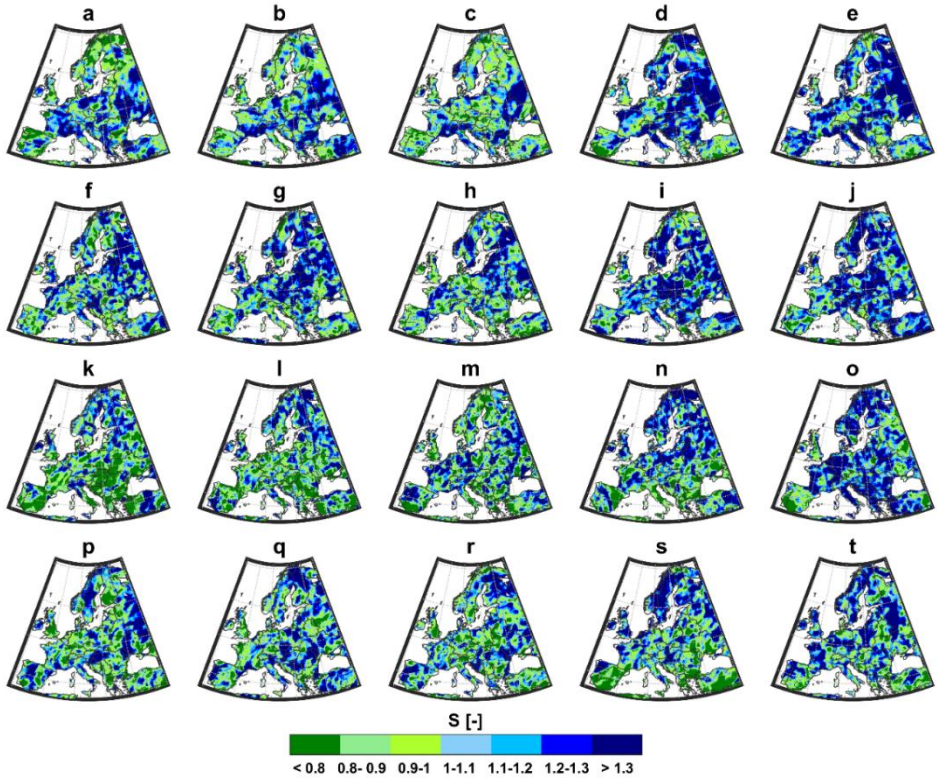


Figure 2.12: Comparison of European daily 50-year extreme precipitation signals after spatial pooling over 9×9 grid cells between different EURO-CORDEX RCMs (RCA4 RCM nested in MPI-ESM-LR GCM: first column; CCLM RCM nested in MPI-ESM-LR GCM: second column; REMO RCM nested in MPI-ESM-LR GCM: third column; RCA4 RCM nested in IPSL-CM5A-MR GCM: fourth column; WRF RCM nested in IPSL-CM5A-MR GCM: fifth column) with 12 km resolution for different seasons (winter: first row; spring: second row; summer: third row; autumn: fourth row) under RCP4.5.

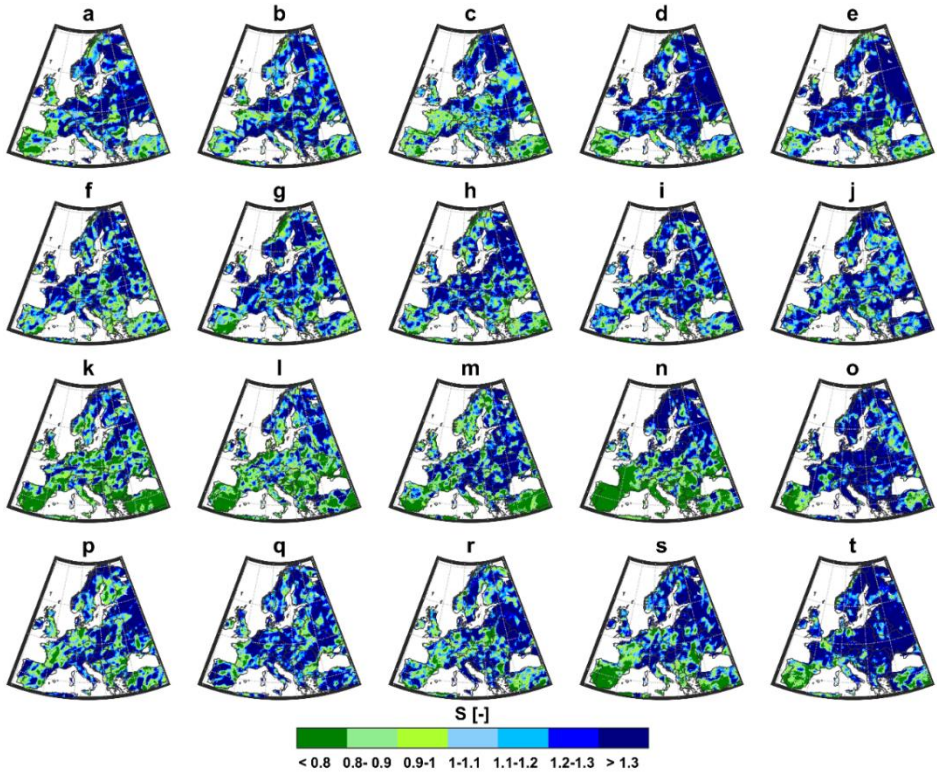


Figure 2.13: Comparison of European daily 50-year extreme precipitation signals after spatial pooling over 9×9 grid cells between different EURO-CORDEX RCMs (RCA4 RCM nested in MPI-ESM-LR GCM: first column; CCLM RCM nested in MPI-ESM-LR GCM: second column; REMO RCM nested in MPI-ESM-LR GCM: third column; RCA4 RCM nested in IPSL-CM5A-MR GCM: fourth column; WRF RCM nested in IPSL-CM5A-MR GCM: fifth column) with 12 km resolution for different seasons (winter: first row; spring: second row; summer: third row; autumn: fourth row) under RCP8.5.

To discern the regionalization influence on the robustness of the 3-hourly extreme precipitation signals, the percentage of the European area with significant S2N at the 95% confidence level and S2N values before and after the spatial pooling are compared in Figures 2.11 and 2.14, respectively. The results indicate that the 3-hourly extreme precipitation changes are more significant and robust on applying the spatial pooling across all seasons (except summer) and return periods for both RCPs compared to daily precipitation. The regionalization through the spatial pooling slightly decreases the signals of 3-hourly extreme precipitation and remarkably decreases the noises, ending up

with a S2N increase (Figures 2.14 and 2.15). The longer the return period is, the larger the influence of the spatial pooling will be. In fact, the spatial pooling reduces the higher noise in more extreme precipitation, leading to a noticeable increase in S2N. The S2N values increase by the spatial pooling levels from 3×3 to 9×9 grid cells. The S2N values for 3-hourly extreme precipitation of a 15-year (5-year) return period under RCP8.5 increase after the 9×9 spatial pooling by about a factor of 1.70 (1.61), 1.37 (1.24), 1.38 (1.15) for winter, spring and autumn, respectively and decreases by about a factor of 0.78 (0.64) for summer (Figure 2.14). The European area with significant S2N becomes about 4 and 6 times larger after the 9×9 spatial pooling for 5- and 15-year return periods, respectively (Figure 2.11). The regionalization factors are mostly larger for RCP4.5 than RCP8.5 (figures 2.14 and 2.15). This is due to a slightly larger decrease of extreme precipitation signals under RCP8.5 after the spatial pooling compared to RCP4.5, owing to its patchier spatial pattern which is more smoothed out.

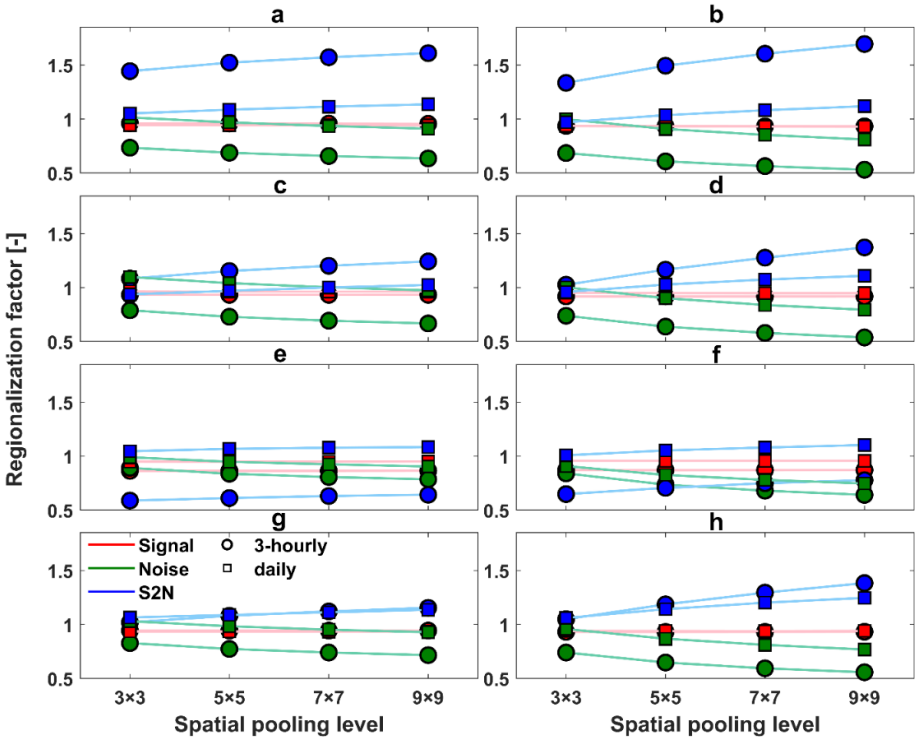


Figure 2.14: Regionalization factors for the signal, noise and S2N of European extreme precipitation of (a, c, e, g) 5- and (b, d, f, h) 15-year return periods based on the 5-member ensemble of the RCA4 model with 12 km resolution for different seasons (winter: a, b; spring: c, d; summer: e, f; autumn: g, h) under RCP8.5.

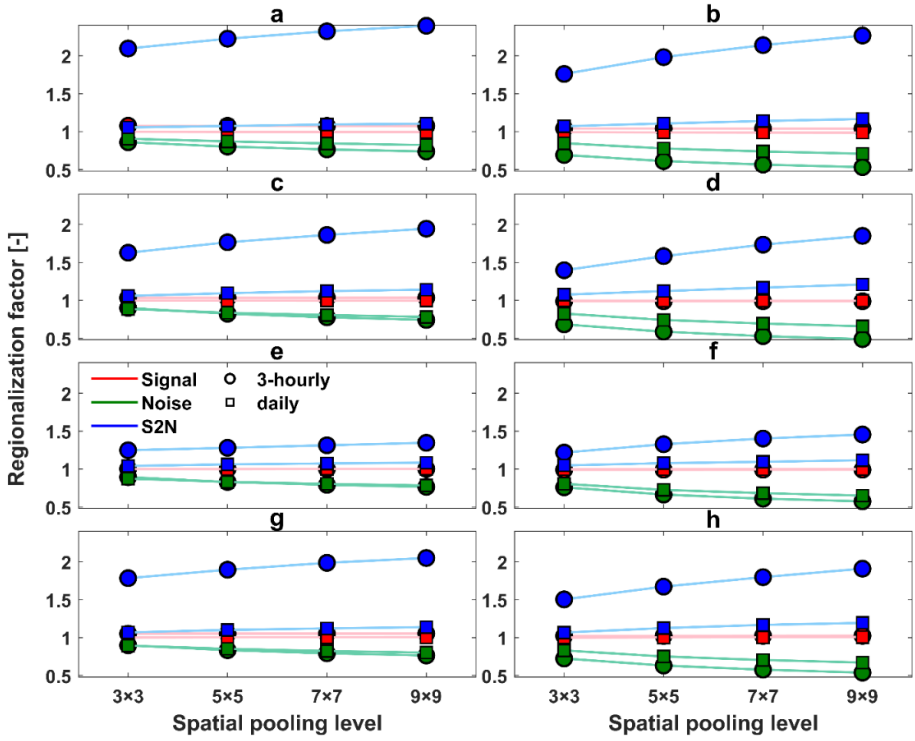


Figure 2.15: Regionalization factors for the signal, noise and S2N of European extreme precipitation of (a, c, e, g) 5- and (b, d, f, h) 15-year return periods for different seasons (winter: a, b; spring: c, d; summer: e, f; autumn: g, h) under RCP4.5 based on the 5-member ensemble of the RCA4 model with 12 km resolution.

To examine the effectiveness of the regionalization, a sensitivity analysis is implemented. The results indicate that the regionalization influence is sensitive - in order of decreasing importance - to season, precipitation time scale, precipitation intensity, emission scenario and model spatial resolution (Figure 2.16). The highest sensitivity to the seasons can be attributed to different types of precipitation in different seasons: mainly convective in summer and large-scale in winter. The regionalization factors in winter is 29%, 31%, 31% and 32% higher than the ones in summer for 3×3, 5×5, 7×7 and 9×9 spatial pooling levels, respectively (Figure 2.16e). Precipitation time scale is the second most influential factor on regionalization, with a higher regionalization factor for 3-hourly extreme precipitation compared to daily extremes. The sensitivity to time scale rises with the spatial pooling level from 12% regionalization factor

difference in 3×3 level to 23% in 9×9 level (Figure 2.16a). While precipitation intensity is not important for a regionalization over small areas (5% regionalization factor difference for 3×3 spatial pooling), its importance substantially rises for the regionalization over larger areas, so that regionalization factors of 15-year extremes are up to 18% higher than those for 5-year extremes for 9×9 spatial pooling (Figure 2.16d). In contrast, the sensitivity to RCP is independent of the spatial pooling level and regionalization factors for RCP4.5 are about 10% larger in comparison to RCP8.5 for all levels (Figure 2.16c). The model spatial resolution is the least important factor for the regionalization of extreme precipitation changes. The regionalization factors of the RCA4 runs with a 12 km spatial scale are 8-12% larger than the ones for the 50-km RCA4 runs (Figure 2.16b), while considering all EURO-CORDEX RCM runs the difference is between 6% and 9% (Figure 2.17a). Kendon et al., (2008) found a regionalization factor of 1.2 for daily extreme precipitation in winter and summer for 3×3 spatial pooling, while a factor in the order of 1.1 is found in this study for 5-year extreme precipitation under RCP4.5 from the 50 km RCM. The smaller regionalization factor for daily extremes obtained here is mainly attributed to considering the spatial dependency among neighboring grid cells for the spatial pooling in our case. Other possible reasons for the difference can be the use of a different climate model (HadRM3H in Kendon et al., (2008)), different extreme precipitation indicators (mean daily precipitation exceeding the 95th percentile of wet days in Kendon et al., (2008)) and a different emission scenario (SRES A2 scenario in Kendon et al., (2008)).

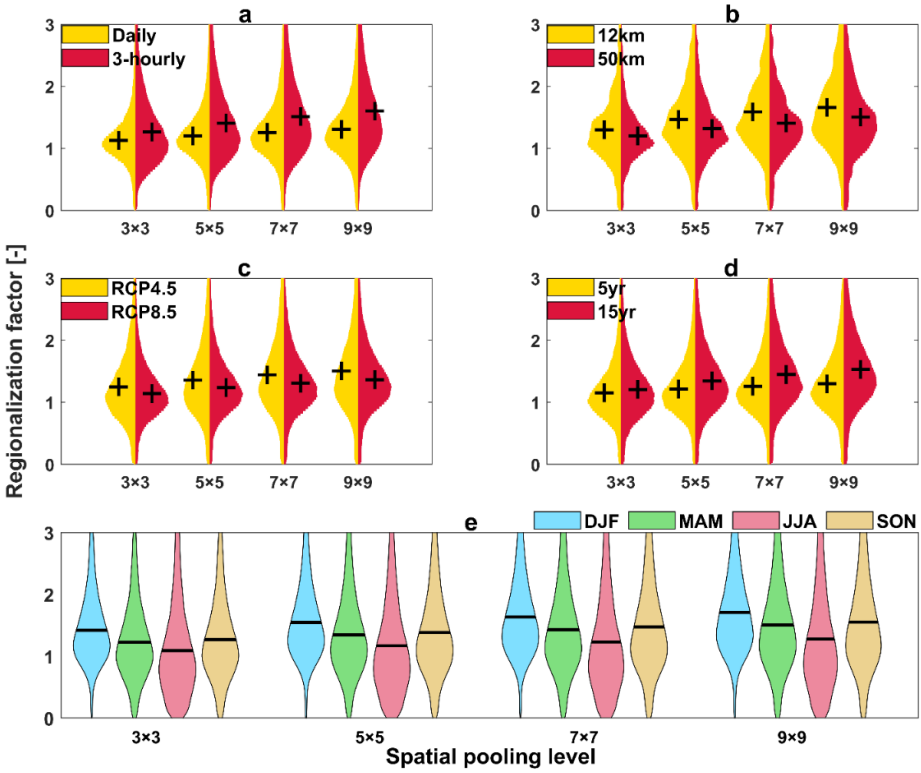


Figure 2.16: Sensitivity analysis of regionalization to (a) precipitation time scale, (b) model spatial resolution, (c) RCP, (d) return period and (e) season. The results are based on the 5-member ensemble of the RCA4 model. Note that S2N values are smoothed because of averaging. The median of regionalization factors over all model grid cells across Europe is shown by black cross in panels a-d and by black horizontal line in panel e.

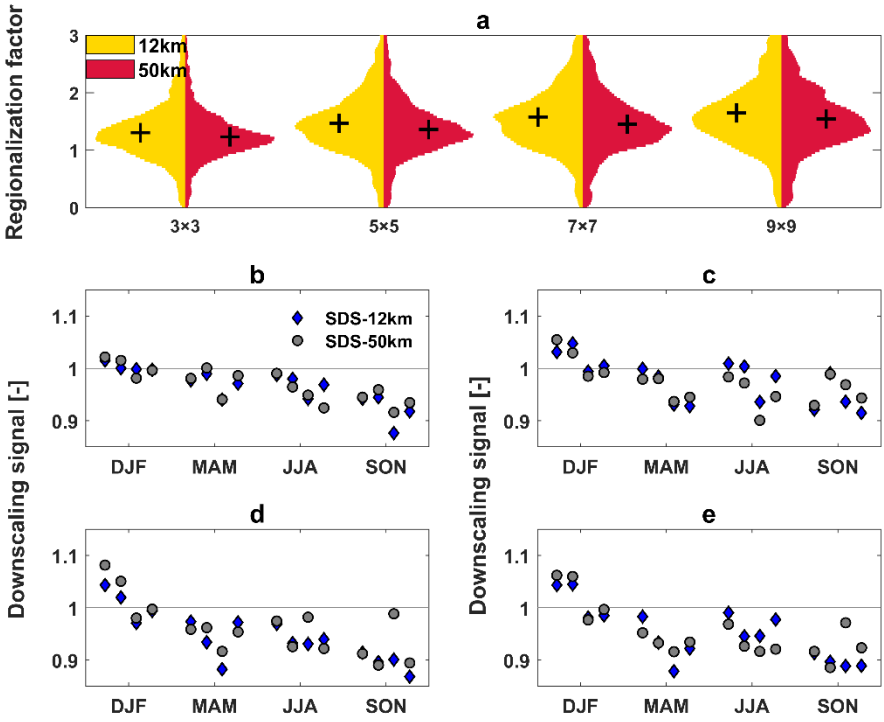


Figure 2.17: (a) Sensitivity analysis of regionalization to model spatial resolution based on the 8-member ensemble of all EURO-CORDEX RCMs (RCA4, CCLM, REMO, WRF) and (b-e) spatial downscaling signal (SDS) of extreme precipitation changes based on the 8-member ensemble of all EURO-CORDEX RCMs (RCA4, CCLM, REMO, WRF) over different European sub-regions for (b, d) 5- and (c, e) 15-year return periods and under (b, c) RCP4.5 and (d, e) RCP8.5. In panel a, the median of regionalization factors over all model grid cells across Europe is shown by black cross. In panels b-e, the scatters for each season from left to right are for north EU (-11-40° longitudes & 54.5-71° latitudes), west EU (-11-12° longitudes & 44-54.5° latitudes), east EU (12-40° longitudes & 44-54.5° latitudes) and south EU (-11-40° longitudes & 36-44° latitudes), respectively.

As the extreme precipitation signals are independent of spatial pooling (Figure 2.14), their scale dependency is further investigated before the spatial pooling at a regional scale (for four European regions). The research question here is which of spatial and time scales is more important for future changes in extreme precipitation. The results will identify the potential areas of improvement in climate modeling and provide a future outlook for climate change impact studies. Figure 2.18 shows the temporal (TDS) and spatial (SDS) downscaling signals for different European regions. The TDS (SDS) values

greater than one point to larger changes for 3-hourly extreme precipitation (RCMs) compared to the daily ones (GCMs). Larger signals of 3-hourly extreme precipitation in comparison to daily extremes (TDS >1) are generally projected for all regions. TDS is robust in all regions except north Europe where only summer TDS is robust (not shown). The largest TDS is seen seasonally in summer and regionally in south Europe when/where short-duration convective precipitation is the dominant type of precipitation. On sub-daily time scales, the highest precipitation intensities during the summer season are usually associated with convective showers (Lenderink and van Meijgaard, 2008), while the life cycle of individual storms is not resolved at daily precipitation statistics and the effects of more intense storms are potentially masked (Singleton and Toumi, 2013). Our results also show a larger TDS for RCP8.5 compared with RCP4.5, both peaking for summer extremes in south Europe at the rate of 1.67 and 1.25 for RCP8.5 an5d RCP4.5, respectively. This is because of a larger increase of sub-daily extreme precipitation with the emission level (from RCP4.5 to RCP8.5) than daily extremes, enlarging the difference between sub-daily and daily changes.

Although the importance of the model spatial resolution for the simulation of summer extreme precipitation has also been emphasized in previous studies (Tabari et al., 2016; Karmacharya et al., 2017; Gadian et al., 2018; Tabari and Willems, 2018), a clear pattern is not found in this study. Nevertheless, SDS is mostly less than one except for winter in north and west Europe (Figures 2.18 and 2.17b-e). Similar to TDS, south Europe shows the highest sensitivity to model spatial resolution, with a robust SDS in almost all cases (season, RCP and return period). A comparison between the magnitude and the direction of TDS and SDS reveals that the temporal resolution is of more significance than the spatial resolution for climate change impact analysis on extreme precipitation.

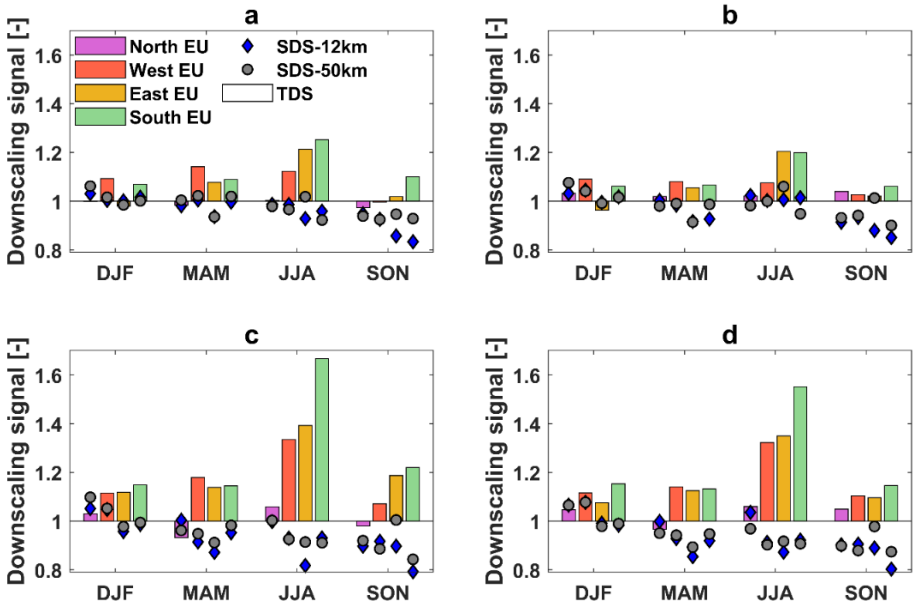


Figure 2.18: Comparison between the spatial downscaling signal (SDS) and the temporal downscaling signal (TDS) of extreme precipitation changes based on the 5-member ensemble of the RCA4 model over different European sub-regions for (a, c) 5- and (b, d) 15-year return periods and under (a, b) RCP4.5 and (c, d) RCP8.5 (North EU: -11-40° longitudes & 54.5-71° latitudes; West EU: -11-12° longitudes & 44-54.5° latitudes; East EU: 12-40° longitudes & 44-54.5° latitudes; South EU: -11-40° longitudes & 36-44° latitudes).

2.4 Conclusions

This research was performed at the European scale, addressing the projected changes in 3-hourly and daily extreme precipitation using the RCA4 model ensemble simulations along with testing the robustness of the changes for different return periods (5, 15, 25 and 50 years) and seasons. Moreover, the effectiveness of the spatial pooling in the reduction of noise was evaluated by considering the spatial dependency for extreme precipitation. The significance of the projected forced response was assessed by the S2N ratio and the sensitivity analysis of the regionalization to precipitation time scale and intensity, model spatial scale, season and RCP was performed by comparing the S2N values after and before the spatial pooling.

The results indicate an intensification of 3-hourly extreme precipitation over Europe for all seasons except summer for which an approximately north–south bipolar pattern is found. This summer pattern with an increasing extreme precipitation in northern Europe and a decreasing signal in southern Europe is more apparent for less extreme precipitation. The amount of extreme precipitation changes is highly influenced by season, return period and RCP. From a seasonal aspect, the percentage of the European area with significant S2N is less in summer compared to the other seasons, demonstrating that summer 3-hourly precipitation extremes are more uncertain. For the non-mitigation scenario RCP8.5, the regionalized winter 3-hourly extreme precipitation changes are statistically significant in approximately 72%, 65%, 59% and 48% of the European area for 5-, 15-, 25- and 50-year return periods respectively, whereas the percentage area goes down to less than 21% for summer extremes.

The internal variability plays an important role in the projections of 3-hourly extreme precipitation changes for most of Europe especially for the higher return periods and the summer season. However, this uncertainty weakens as one applies regionalization through the spatial pooling. The results emphasize that the spatial pooling is an effective method to obtain less noisy extreme precipitation. The S2N values for 3-hourly extreme precipitation changes increase after the spatial pooling by a factor in the range 1.4-1.7 for all seasons except summer when S2N values decrease by about a factor of 0.78. The efficacy of the spatial pooling on the robustness of extreme precipitation changes greatly appertains to season, precipitation time scale and intensity, while regionalization is less sensitive to greenhouse gas concentration and climate model spatial resolution. Whenever and wherever short-duration convective precipitation is dominant, the precipitation time scale is found to be more important, which is the case seasonally for summer and regionally for south Europe.

Albeit the use of larger multi-model ensemble is always recommended for climate change impact assessment, less attention has been paid to the role of internal variability and the robustness of the climate change signals. Our results reveal that even large climate change signals can be insignificant due to a larger

internal variability. This highlights the importance of assessing the robustness of extreme precipitation changes. The superiority of internal variability to anthropogenic changes should not be a barrier for decision making for adaptation strategy implementation, as the robustness of signals is strongly dependent on the model grid scale noise which can be effectively reduced by regionalization.

CHAPTER 3

Climate Change Impact on IDF Curves in Belgium

This chapter was published as:

Hosseinzadehtalaei, P., Tabari, H., Willems, P. (2017) Uncertainty assessment for climate change impact on intense precipitation: how many model runs do we need?. *International Journal of Climatology*, 37(S1), 1105–1117

Hosseinzadehtalaei, P., Tabari, H., & Willems, P. (2018) Precipitation intensity–duration–frequency curves for central Belgium with an ensemble of EURO-CORDEX simulations, and associated uncertainties. *Atmospheric Research*, 200, 1-12

Summary

An ensemble of 88 regional climate model (RCM) simulations at 0.11° and 0.44° spatial resolutions from the EURO-CORDEX project as well as an ensemble of 140 CMIP5 GCM runs including 15 GCMs, 3-10 GCM initial conditions and 4 representative concentration pathways (RCPs) are analyzed for central Belgium to investigate the projected impact of climate change on precipitation intensity–duration–frequency (IDF) relationships and extreme precipitation quantiles typically used in water engineering designs. For the RCM ensemble, the rate of uncertainty arising from the choice of RCM, driving GCM, and representative concentration pathway (RCP4.5 & RCP8.5) is quantified using a variance decomposition technique after reconstruction of missing data in GCM×RCM combinations. For the GCM ensemble, the uncertainties related to GCMs, GCM initial conditions and RCPs and their sensitivity to the selection of GCM runs are investigated. The RCM-based results reveal that making a temporal stationarity assumption for the climate system may lead to underestimation of precipitation quantiles up to 70% by the end of this century. This projected increase is generally larger for the 0.11° RCMs compared with the 0.44° RCMs. The relative changes in extreme precipitation do depend on return period and duration, indicating an amplification for larger return periods and for smaller durations. The variance decomposition approach generally identifies RCM as the most dominant component of uncertainty in changes of more extreme precipitation (return period of 10 years) for both 0.11° and 0.44° resolutions, followed by GCM and RCP scenario. The uncertainties associated with cross-contributions of RCMs, GCMs, and RCPs play a non-negligible role in the associated uncertainties of the changes. In the GCM based analysis, albeit the choice of GCM is the major contributor (up to 65% for some cases) to intense precipitation change uncertainty for all return periods (1 year, 10 years) and aggregation levels (1-, 5-, 10-, 15-, 30-day), uncertainties related to the GCM initial conditions and RCPs of up to 38% and 23% respectively are found in some cases. The sensitivity analysis reveals that the GCM, RCP and GCM initial condition uncertainties are greatly influenced by the set of climate model runs considered, especially for more extreme precipitation at finer time scales.

3.1 Introduction

More frequent and intense occurrence of extreme precipitation events by the end of the 21st century is expected under climate change conditions (Willems et al., 2012a; Sunyer et al., 2012; IPCC, 2013; Willems, 2013; Liew et al., 2014; Tabari et al., 2015; Pohl et al., 2017). This leads to an increase in the flood hazard with adverse impact on existing water infrastructure, resulting in human harm and economic losses. Urban water infrastructure (i.e., different components of storm water management systems such as sewer conduits, storm water management ponds, retention/detention basins) and flood control structures (e.g., dikes, dams) are typically designed based on the properties of extreme precipitation in the form of intensity-duration-frequency (IDF) curves (Peck et al., 2012; Hosseinzadehtalaei et al., 2017). The IDF curves quantify the frequency of occurrence of a storm with a specific intensity at different durations and its application for developing design standards has been common practice for many decades (e.g., Willems et al., 2012b). The infrastructure design is sensitive to potential changes in extreme precipitation characteristics under climate change, and non-stationary climate conditions will increase the probability of failure of the structures designed by applying the current IDF curves. Therefore, the current design standards based on IDF curves need to be revised and the expected changes in precipitation properties must be incorporated for the future infrastructure designs.

Global climate models (GCMs) have been considered as initial and proper tools for climate change projections (Randall et al., 2007; Liu et al., 2014; Chen et al., 2014; Alfieri et al., 2015; Panday et al., 2015). Recently, GCMs provided by the Coupled Model Intercomparison Project Phase 5 (CMIP5) have been widely applied in climate change analysis (Kharin et al., 2013; Yin et al., 2013; Rana et al., 2014; Liu et al., 2014; Tabari et al., 2015; Janssen et al., 2016; Hosseinzadehtalaei et al., 2016). The CMIP5 provides a set of coordinated climate model simulations for the Intergovernmental Panel on Climate Change (IPCC) 5th Assessment report (AR5). Compared to the earlier phase (CMIP3), CMIP5 simulations represent a larger number of more complex models with higher spatial resolution and an improvement in models' physics, leading to

incorporation of more progressed behavior of land use changes and better demonstration of the mean condition of atmospheric variables including surface temperature and precipitation (Hawkins and Sutton, 2009; Meehl and Bony, 2011; Taylor et al., 2012; Knutti and Sedláček, 2013; Sierra et al., 2015).

GCMs have, however, a coarse spatial resolution (mainly ranging between 100 and 500 km) at which capturing the detail of regional/local climate change is not competently possible (Endris et al., 2013; Tabari et al., 2016; Saeed et al., 2017). Hence, dynamically downscaled climate models to finer spatial scale (regional climate models: RCMs) have been developed to provide climate change information suitable for impact studies (Alfieri et al., 2015). For the European area, the PRUDENCE (Christensen et al., 2007; Jacob et al., 2007) and ENSEMBLES (Van der Linden and Mitchell, 2009) projects have provided RCM simulations nested in the CMIP3 GCMs on grid-sizes down to 0.44° and 0.22°, respectively. Recently, a high resolution European RCM ensemble within the World Climate Research Program Coordinate Regional Downscaling Experiment (EURO-CORDEX) has been established using the CMIP5 GCMs as driving models for RCMs with 0.44° and 0.11° spatial resolutions.

Projections of future climate conditions are subject to uncertainties with distinct sources due to different future emission/concentration scenarios, parameterization and structure of GCMs/RCMs, boundary and initial conditions (Min et al., 2007; Liepert and Previdi, 2012; Halmstad et al., 2012; Brekke and Barsugli, 2013; Strobach and Bel, 2017). The uncertainty is larger for the future projections of climate extremes (Ahmed et al., 2013; Horton et al., 2015; Ning et al., 2015, 2016), due to the difficulty in the modeling of extremes.

Quantification of the uncertainty is one of the main steps in identifying adaptation measures for water resources management in the face of climate change. Therefore, the relative magnitude of each of the uncertainty sources must be defined to achieve the minimal uncertainties to extreme precipitation and construction of future IDF curves.

The application of multi-model ensembles to quantify the projection uncertainty of climate change has recently increased in hydrological studies (Minville et al., 2008; Kingston et al., 2011; Chen et al., 2011; Hughes et al., 2011; Dessu and Melesse, 2013; Mandal et al., 2016). The larger the ensemble

size of independent climate models considered, the better the quantification of climate change uncertainty would be. Independent and most accurate climate models for each region can be selected using envelope and past-performance approaches (Cannon, 2015; Lutz et al., 2016; Mendlik and Gobiet, 2016). Nevertheless, maximizing the model diversity to cover the total uncertainty through a larger ensemble of representative climate models places a greater demand on computational resources (Ferro et al., 2012). Due to the expense of larger ensembles of simulations and resource constraints, a perennial question is how sensitive are the uncertainty results to the size of the climate model ensemble and the selected climate model runs. This research question is addressed in this study by performing a sensitivity analysis on how changes in ensemble size affect the magnitude of uncertainty for intense precipitation changes.

The impact of climate change on intense precipitation and IDF curves has been investigated before in several studies (e.g. Mailhot et al., 2007; Madsen et al., 2009; Willems et al., 2012; Yilmaz et al., 2014; Kim et al., 2015). Such impact analysis is complemented in this study with a thorough investigation of the uncertainties. This is done for IDF statistics and curves under projections of climate change scenarios provided by the CMIP5 GCMs and EURO-CORDEX RCMs for different return periods and durations, for central Belgium. The magnitude of the uncertainty in the future precipitation extremes and IDF statistics related to the choice of the GCMs, RCMs, RCPs and initial conditions is assessed.

3.2 Materials and methods

3.2.1 Model data

In this study, daily precipitation data from 15 GCMs are used, from 1961 to 1990 for the control period and from 2071 to 2100 for the scenario period. The GCMs having precipitation data for all RCPs at the time of analysis were selected. Table 3.1 presents the CMIP5 model simulations considered in this study. Four future greenhouse gas scenarios in the form of the standard

representative concentration pathways (RCPs) are used, including RCP2.6, RCP4.5, RCP6.0 and RCP8.5. These scenarios represent a range from low to high levels of greenhouse gas concentrations by the year 2100. For each GCM, just one run is selected which is the first initial condition. However, for considering the uncertainty in the GCM initial conditions 10 available runs of CSIRO-Mk3.6.0 GCM are also evaluated. In addition, three runs of CCSM4 and HadGEM2-ES GCMs are also used. The preliminary analysis showed that the first run of the MIROC5 model was an extreme outlier. Such deficiency of the model was reported in the literature (e.g., Sillmann et al., 2013a, 2013b). As this extreme outlier will overshadow the results and regarding the non-selective choice of the GCMs and their respective runs in this study, we used the second run of MIROC5 for further analysis. In total, 140 CMIP5 GCMs runs are analyzed.

Table 3.1: Summary of 15 climate models from CMIP5 used in this study.

Model	Spatial resolution (Lon × Lat)	Number of runs				
		His.	RCP2.6	RCP4.5	RCP6.0	RCP8.5
BCC-CSM1.1	~ 2.81°×2.79°	1	1	1	1	1
BCC-CSM1.1(m)	~ 2.81°×2.79°	1	1	1	1	1
CCSM4	1.25°×0.94°	3	3	3	3	3
CSIRO-Mk3.6.0	1.875°×1.875°	10	10	10	10	10
GFDL-CM3	2.5°×2°	1	1	1	1	1
GFDL-ESM2G	2°×2.02°	1	1	1	1	1
GFDL-ESM2M	2.5°×2°	1	1	1	1	1
HadGEM2-ES	1.875°×1.25°	3	3	3	3	3
IPSL-CM5A-LR	3.75°×1.895°	1	1	1	1	1
IPSL-CM5A-MR	2.5°×1.27°	1	1	1	1	1
MIROC-ESM	~ 2.8°×2.8°	1	1	1	1	1
MIROC-ESM-CHEM	~ 2.8°×2.8°	1	1	1	1	1
MIROC5	1.40°×1.40°	1	1	1	1	1
MRI-CGCM3	1.125°×1.121°	1	1	1	1	1
NorESM1-M	2.5°×1.9°	1	1	1	1	1

In addition to the CMIP5 GCMs, daily precipitation data from eight EURO-CORDEX RCMs are used. The models are RCA4, RACMO22E, HIRHAM5, CCLM4-8-17, WRF331F, REMO2009, ALADIN52 and RegCM4-3 whose data are publicly available through the Earth System Grid Federation server (https://esgf-data.dkrz.de/search/cordex-dkrz/). These high-resolution RCMs are forced by 10 CMIP5 GCMs. Daily precipitation from historical simulations from 1961 to 1990 and climate projections from 2071 to 2100 at 0.11° and 0.44° horizontal resolutions are obtained from the EURO-CORDEX database for the model gridcell covering central Belgium. Simulations from a matrix of 3×3 EURO-CORDEX model gridcells centered over Uccle station (main meteorological station of Belgium) are analyzed. A comparison between the extreme precipitation simulations from the central gridcell (closest grid to Uccle station) and its eight neighboring cells assure us that using the simulations from only the central gridcell can accurately simulate local climate information (examples are shown in Figure 3.1). Nearest neighbor method is used to get the data from the closest model gridcell (with dimensions 0.44° × 0.44° and 0.11° × 0.11°) to the Uccle station location.

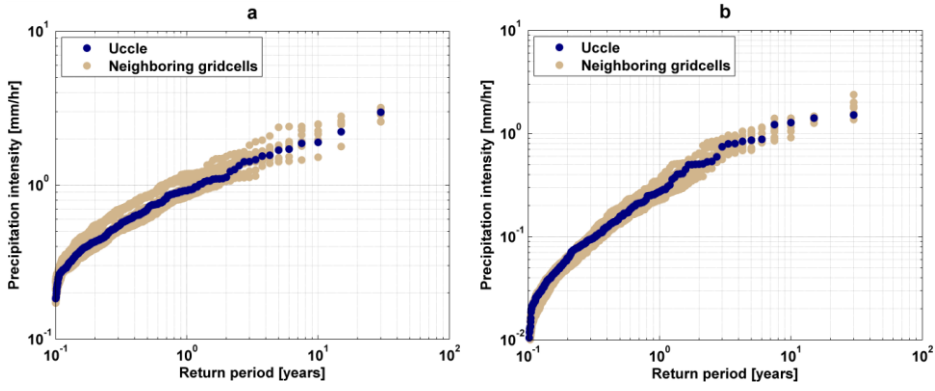


Figure 3.1: Comparison of precipitation simulations over a matrix of 3×3 EURO-CORDEX model gridcells in which the central grid is the closest to Uccle station, a: 0.11° simulations of RCA4 RCM nested in MPI-ESM-LR GCM, b: 0.44° simulations of REMO2009 RCM nested in MPI-ESM-LR GCM.

It should be noted that the control runs of the RCA4 RCM for 0.11° resolution and the WRF331F RCM for both 0.11° and 0.44° resolutions do not

have data for the 1960s, hence, the period 1971-2000 is used as their control period. This difference in the time period poses no limitation to the analysis as a 30-year RCM integration just represents one possible 30-year realization of the climate and not the actual sequence of weather events (Maraun et al., 2010). The changes reported in this chapter are for a 110-year period (from 1961-1990 to 2071-2100) for all the RCMs except for WRF331F and RCA4 RCMs for which the changes correspond to a period of 100 years (from 1971-2000 till 2071-2100). To make the changes obtained from WRF331F and RCA4 RCMs consistent with those from the other RCMs, the changes from these two models are modified by applying a factor 110/100, hence assuming a linear change in time.

For the future climate, the projections of the EURO-CORDEX RCMs are available mainly for the representative concentration pathways RCP4.5 and RCP8.5, which correspond respectively to mid and high concentration scenarios of greenhouse gases in the atmosphere. In total, 88 RCM simulations including 42 runs for 0.11° ensemble and 46 runs for 0.44° ensemble are analyzed in this study.

3.2.2 Observed data

To evaluate the model simulations for daily precipitation, the observations for the period 1961-1990 at Uccle (Brussels) station (4.4° E and 50.8° N) operated by the Royal Meteorological Institute of Belgium are used since this station has high quality, long rainfall records. One might argue that the characteristics of the precipitation distribution observed in Uccle may not be captured by the RCMs in this exact location. To address this issue, as there is no raingauge with high quality and long precipitation data in the vicinity, the RCM simulations over a larger domain of nine gridcells (3×3 matrix) are compared for possible different extreme precipitation pattern in the neighboring gridcells (Figure 3.1). The results show a consistent pattern over the larger domain ($1.32^o \times 1.32^o$ for the 0.44^o runs and $0.33^o \times 0.33^o$ for the 0.11^o runs). This is not performed for CMIP5 GCMs because of their course resolution only the grid box covering Uccle is considered.

Next to the Uccle station observations, gridded daily precipitation values from the E-OBS (v12.0, Haylock et al., 2008) for the period 1961-1990, dataset from the European Climate Assessment and Data (ECA&D: http://www.ecad.eu/download/ensembles/download.php), for 0.5º and 0.25º spatial resolutions are used. The E-OBS data for the closest gridcell to Uccle station are derived using the nearest neighbor method.

These gridded data are aggregated to larger pixels of 111 km and 445 km for comparison with the gridded CMIP5 GCM results at similar spatial resolutions.

3.2.3 Development of IDF curves for the current and future climate

To construct the IDF curves, statistical extreme value analysis is required. The most popular practice in extreme value analysis is to assume that extreme values belong to the same population and follow the same type of distribution. However, single-component distributions may not work well for the upper tail of the distribution when extreme precipitation arises from two different physical mechanisms: predominantly stratiform and convective storm types. Hence, a two-component distribution is needed to properly fit precipitation extremes resulting from both micro-scale thunderstorms (convective rain cells) and macro-scale frontal/cyclonic storms (Rulfová et al., 2016; Yan et al., 2017). For Belgium, IDF curves have been set up by Willems (2000), based on Peak-Over-Threshold (POT) extreme value statistics after calibration of a two-component exponential distribution. The distribution was calibrated by weighted regression in the exponential quantile plot to the POT extremes extracted from the full time series. For POT selection, wet days are first separated with a 0.1 mm threshold and then the values above the 98th percentile of wet days are used as the POT. The same procedure is used in this study to develop IDF curves for the simulations of the EURO-CORDEX RCMs for 1-month, 1-year and 10-year return periods. Although very low return periods are not important in design applications, the precipitation intensity of 1-month return period is analyzed to compare the climate change impact on more extreme precipitation with that on less extreme precipitation. Following Willems (2000, 2013), in this study, the return period T for independent precipitation extremes x obtained from the POT method is defined for the two-component exponential distribution as:

$$T = \frac{n}{t(p_a(1-G_a(x))+(1-p_a)(1-G_b(x)))} \quad (3.1)$$

in which $G_a(x)$ and $G_b(x)$ are two different exponential distribution functions for subpopulations *a* and *b* that are presumed to be associated with convective and frontal types of rain storms (Willems, 2000):

$$G_a(x) = 1 - \exp(-\frac{x-x_t}{\beta_a}) \quad (3.2)$$

$$G_b(x) = 1 - \exp(-\frac{x-x_t}{\beta_b}) \quad (3.3)$$

where n is the total length of the precipitation time series (30 years in our case), t is the observed order of the threshold level above which the distribution is considered, β is the distribution parameter, x_t is the optimal threshold and p_a represents the proportion of population a.

The IDF curves for the future climate are developed on the basis of a quantile perturbation downscaling approach (Willems, 2013) by applying change factors to the extreme precipitation statistics from station observations for each return period and duration as presented below:

$$IDF_F(D,T) = IDF_O(D,T) \times \frac{IDF_S(D,T)}{IDF_C(D,T)} \quad D=1, 5, 10, 15, 30 \text{ days}, \; T=1, 10 \text{ years} \quad (3.4)$$

where $IDF_S(D,T)$, $IDF_C(D,T)$, $IDF_O(D,T)$ and $IDF_F(D,T)$ are the extreme precipitation intensities of return period T and duration D for the scenario and control runs, the observations, and the perturbed observations representing the future climate conditions, respectively. The ratio $\frac{IDF_S(D,T)}{IDF_C(D,T)}$ is the climate change factor defined as the ratio between the precipitation intensity for the scenario period and the corresponding intensity in the control period for the same return period and aggregation level. In the quantile perturbation approach, given that the relative changes are applied to the observations based IDF curves, bias correction is intrinsically considered. In fact, this type of methods assumes that the bias under future climate conditions is identical to the bias in current climate conditions.

The IDF curves are developed in this study for a broad range of durations from 1 up to 30 days. The studied range of durations depends on the application. The concentration time (travel time of water from the most remote point in a watershed to the outlet) or response time to rainfall of the system under study, which can be a sewer system, river or catchment runoff, define the largest duration relevant for the application. The shorter durations of 1 or few days are representative for the concentration/recession time of the runoff flows in Belgian catchments. The longer durations up to 30 days are of relevance for water availability studies or soil saturation analysis. By considering the wide range of durations from 1 to 30 days, we moreover compare the difference in climate change impact on precipitation between small and large time scales.

3.2.4 Uncertainty analysis

The total ensemble uncertainty for climate change signals of extreme precipitation is split in the variance contributions using a variance decomposition approach. The contributions of the uncertainties in the GCMs, RCMs and RCPs to the overall uncertainty are investigated for each return period and duration for both RCM resolutions (0.11° and 0.44°). The total variance can be split into the above three contributors as well as the interactions among them using the following relationship:

$$Var\,(T) = Var\,(R) + Var\,(G) + Var\,(S) + Var\,(RG) + Var\,(RS) + Var\,(GS) + Var\,(RGS) \quad (3.5)$$

where $Var\,(T)$ is the total variance, $Var\,(R)$ is the variance associated with the ensemble of RCMs, similarly $Var\,(G)$ for the ensemble of GCMs, and $Var\,(S)$ for the RCPs and $Var\,(RG)$, $Var\,(RS)$, $Var\,(GS)$ and $Var\,(RGS)$ are the variance associated with the interactions between the three contributors. For instance, the full contribution of GCM uncertainty ($Var_f\,(G)$) to $Var\,(T)$ can be obtained by:

$$Var_f\,(G) = Var\,(G) + Var\,(RG) + Var\,(GS) + Var\,(RGS) \quad (3.6)$$

In a similar procedure, the full contributions of RCM and RCP uncertainties are computed. The method was described in detail in Déqué et al. (2007, 2012).

The variance decomposition would be a simple exercise when there are no missing data (gaps) in the RCM-GCM matrix (Tables 3.2 and 3.3). Tables 3.2 and 3.3 display which CMIP5 GCM is driving which EURO-CORDEX RCM. The missing RCM-GCM combinations make it an unbalanced matrix. For example, for 0.11° resolution (Table 3.2) three RCMs are forced by the HadGEM2-ES (r1i1p1) GCM, while only one RCM is driven by the EC-EARTH (r1i1p1) GCM. This leads to overweighting of the HadGEM2-ES (r1i1p1) GCM in comparison to the EC-EARTH (r1i1p1) GCM. A solution to avoid this biased ensemble estimation would be to reconstruct missing combinations by means of statistical techniques such as principal component analysis (PCA). Due to the existence of many missing combinations in our case, PCA method can produce strange artifacts. Déqué et al. (2007, 2012), therefore, developed an alternative method to estimate change factors for missing combinations. As a simple example to explain how the method works, let us consider a missing combination in the RCM-GCM matrix that is related to RCM *I* forced by GCM *II*. The change factor for this missing combination is estimated by assuming an additive contribution of GCM *II* and RCM *I*. It means the mean anomaly of the change factors derived from the GCM *II*-driven pairs from the overall mean of the change factors (considering all RCMs × GCMs) and the mean anomaly of the change factors derived from the RCM *I*-driven pairs from the overall mean are added to the overall mean to estimate the missing value. The method has been applied in several European studies to complete the set of simulations by the PRUDENCE and ENSEMBLES RCMs (Vidal and Wade, 2008; Sunyer et al., 2015). In our application, three instead of two uncertainty contributors (GCM, RCM, RCP) are considered. The small sample size of EURO-CORDEX RCMs is a limitation for the robustness of the uncertainty assessment.

To determine the GCM uncertainty, we calculate the scenario range in the extreme precipitation statistics for the different GCM runs after averaging these statistics over different RCPs and different runs of the CSIRO-Mk3.6.0 model. The scenario range is computed as the difference between the high and low

climate scenarios defined based on the 95% confidence interval limits. Similarly, to estimate RCP uncertainty we average different runs of the CSIRO-Mk3.6.0 model and different GCMs within each RCP and then calculate the scenario range between the four RCPs. For computing the uncertainty associated with the GCM initial conditions, the scenario range between the different runs of the CSIRO-Mk3.6.0 model is calculated after averaging over the different RCPs. The above-mentioned uncertainty analysis for each of the three components is repeated for different ensemble sizes of GCMs, RCPs and GCM initial conditions to analyze the sensitivity of the uncertainty rate to the ensemble size.

Table 3.2: The EURO-CORDEX 0.11° RCM × driving CMIP5 GCM matrix; labels Y and X indicate the availability of the corresponding RCM × GCM pair for the scenarios RCP 4.5 and 8.5, respectively.

RCM/Driving GCM	CNRM-CM5-r1i1p1	EC-EARTH-r1i1p1	EC-EARTH-r3i1p1	EC-EARTH-r12i1p1	MPI-ESM-LR-r1i1p1	IPSL-CM5A-MR-r1i1p1	HadGEM2-ES-r1i1p1
RCA4	XY			XY	XY	XY	XY
RACMO22E		XY					XY
HIRHAM5			XY				
CCLM4-8-17	XY			XY	XY		XY
WRF331F						XY	
REMO2009					XY		

Table 3.3: The EURO-CORDEX 0.44° RCM × driving CMIP5 GCM matrix; labels Y and X indicate the availability of the corresponding RCM × GCM pair for the scenarios RCP 4.5 and 8.5, respectively.

RCM/Driving GCM	CNRM-CM5-r1i1p1	EC-EARTH-r1i13p1	EC-EARTH-r3i1p1	EC-EARTH-r12i1p1	MPI-ESM-LR-r1i1p1	IPSL-CM5A-MR-r1i1p1	HadGEM2-ES_r1i1p1	CanESM2-r1i1p1	CSIRO-Mk3-6-0_r1i1p1_	MIROC5-r1i1p1	NorESM1-M-r1i1p1	GFDL-ESM2M-r1i1p1
RCA4	XY	X		XY	XY	XY	XY	XY	XY	XY	XY	XY
ALADIN52	Y											
RACMO22E		XY										
HIRHAM5			XY									
CCLM4-8-17					XY							
WRF331F						XY						
RegCM4-3							Y					

3.3 Results and discussion

3.3.1 Current climate IDF curves

3.3.1.1 GCM-based current IDF curves

The general validation of the CMIP5 GCM ensemble-based current IDF curves compared to those driven from the observations for different return periods (1 year and 10 years) and aggregation levels (1-, 5-, 10-, 15- and 30- day) is presented in Figure 3.2. As shown, all GCMs have a tendency to underestimate design precipitation for different return periods and aggregation levels compared with the station observations which are typically used for hydraulic design. This underestimation is more obvious for the smaller (i.e., daily) time scales. This bias is a well-known feature of GCMs, and may be at least partly explained by the spatial scale difference between point observations and gridded model results (Willems et al., 2012; Sunyer et al., 2013a; Rana et al., 2014). When the GCM-driven IDF curves are compared with those from the gridded observations, the systematic deviation reduces, which confirms that the underestimation in comparison with the point observations is due to the spatial scale difference. After comparison with the gridded observations, however, still overestimations and underestimations are detectable for individual model runs.

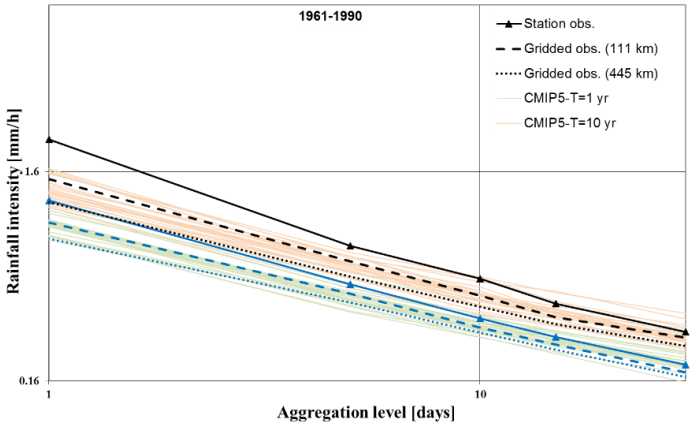


Figure 3.2: Validation of precipitation IDF curves derived from CMIP5 runs based on Uccle observations for the historical period (1961-1990) (observation lines for the 1- and 10-year return periods are shown in blue and black colors, respectively).

3.3.1.2 RCM-based current IDF curves

Figure 3.3 shows the IDF curves of the historical period for the EURO-CORDEX 0.11° and 0.44° RCMs for different durations and return periods. The performance evaluation of IDF curves is done by comparing the simulation results with the Uccle observations. We also compare the EURO-CORDEX results with the E-OBS gridded observations with similar grid size (E-OBS data for exactly the same grid size as that of the EURO-CORDEX RCMs are not available). Since gridded (spatially averaged) precipitation leads to lower values in comparison to station precipitation values (Chen and Knutson, 2008; Hofstra et al., 2009; Sunyer et al., 2013), the higher values of the current IDF curves derived from the EURO-CORDEX RCMs compared with the station observations should be clearly interpreted as "overestimation". Figure 3.3 shows that for the shorter durations the IDF curves for the Uccle station and E-OBS do not show a strong agreement especially for T=10 years for which the spread is the largest. Nonetheless, for intermediate and long durations, there is a strong agreement between the IDF curves from the two observation sources. For the spatial resolution of 0.11° using 14 RCM runs, it can be seen in Figure 3.3a that extreme precipitation intensity for 1-month and 1-year return periods is mostly overestimated compared to the Uccle station and E-OBS observations. For a 10-year return period with daily duration, the 0.11° RCMs overestimate the precipitation intensity with respect to the E-OBS observations and both overestimations and underestimations are observed in comparison with the Uccle station observations. The range of IDF curves from the ensemble of simulations at 0.11° resolution encompasses the IDF curve derived from the observations, both for the Uccle station measurements and E-OBS in the surrounding area. For the 0.44° RCMs (16 runs), the spread of the IDFs from the model ensemble is quite large, especially for the 10-year and 1-month return periods, which indicate a high level of uncertainty, but centered around the IDFs from the observations (Figure 3.3b). The strongest agreement (the least spread) for the model ensemble is for T=1 year.

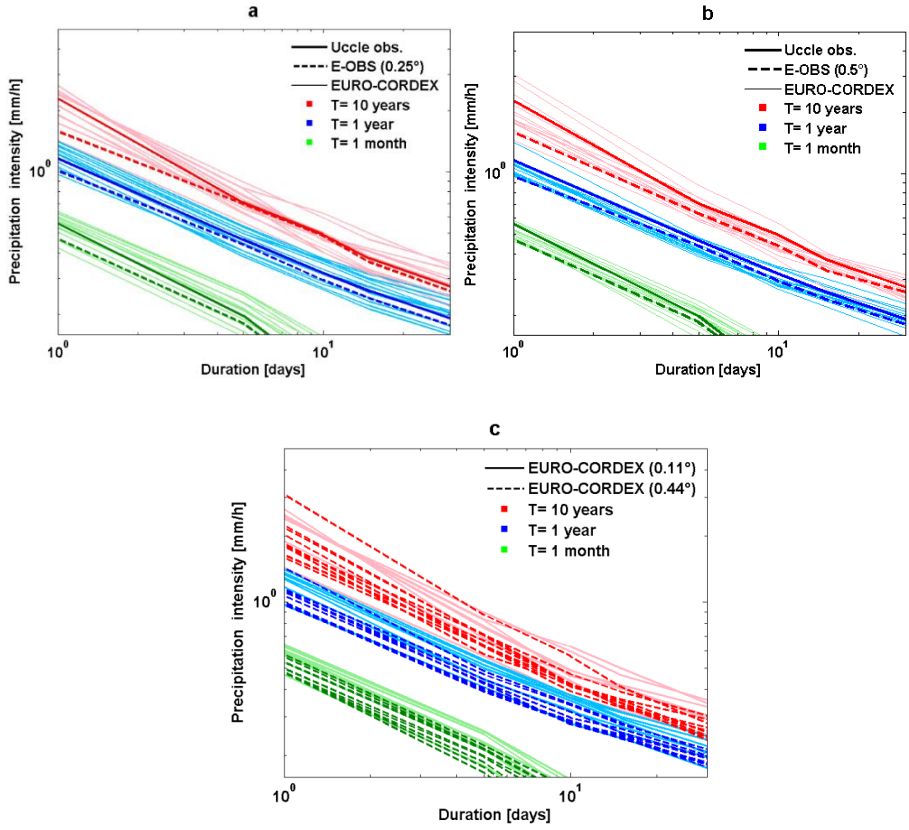


Figure 3.3: Validation of the current climate IDF curves for the 0.11° (a) and 0.44° (b) RCMs based on the Uccle station and E-OBS observations for 10-year, 1-year and 1-month return periods and (c) comparison between the 0.11° and 0.44° simulations with identical combination of GCMs and RCMs (both the vertical and horizontal axes are scaled logarithmically).

A comparison between 9 simulations at 0.11° and 0.44° resolutions with identical combination of GCMs and RCMs indicates that the precipitation intensity simulated by the 0.11° runs is mostly higher than that of the 0.44° runs (Figure 3.3c). Precipitation intensity simulated by the RCA4 (nested in CNRM-CM5, EC-EARTH, IPSL-CM5A-MR, MPI-ESM-LR and HadGEM2-ES) and HIRHAM5 (nested in EC-EARTH) RCMs of 0.11° resolution is higher than that of 0.44° resolution, while for two RCM runs (CCLM4-8-17 nested in MPI-ESM-LR and RACMO22E nested in EC-EARTH) an opposite pattern is seen: lower intensities for the 0.11° runs. The WRF331F RCM (nested in the IPSL-

CM5A-MR GCM) shows a mixed behavior. A comparison between the median of the EURO-CORDEX 0.44° and 0.11° simulations shows a larger difference between the IDF curves of these two datasets for more extreme precipitation (Table 3.4). The difference goes up to 30% for daily precipitation of 10-year return period. In general, more intense precipitation is simulated by the 0.11° simulations for all durations and return periods except for 15- and 30-day precipitation of 1-month return period.

It can be generally inferred from the model validation analysis that the IDF curves derived from the EURO-CORDEX simulations have a large spread around the IDFs from observations. This indicates a high level of uncertainty in these simulations which needs to be quantified.

Table 3.4: Precipitation intensity difference (%) between the median of EURO-CORDEX 0.44° and 0.11° simulations (0.44°-0.11°) for different return periods and durations

Duration/Return period	10 years	1 year	1 month
1 day	30.30	24.64	19.22
5 days	16.31	18.06	15.13
10 days	14.76	25.73	10.60
15 days	17.36	17.84	-7.20
30 days	17.30	14.06	-7.21

3.3.2 Future climate IDF curves

3.3.2.1. GCM-based future IDF curves

To construct future downscaled IDF curves based on the quantile perturbation downscaling method, change factors need to be calculated. These change factors are computed for design precipitation after consideration of intensity, duration and frequency aspects. Figure 3.4 shows the change factors for precipitation IDF statistics of different return periods and durations under different RCP scenarios. The results indicate an intensification of extreme precipitation for almost all durations and return periods. This intensification is more pronounced for more extreme precipitation and smaller time scales. As expected, the increment in extreme precipitation increases from RCP2.6 to RCP8.5. Generally, the intense

precipitation and IDF statistics will increase up to around 64% by the end of this century. This projected increase in extreme precipitation for Belgium based on the CMIP5 GCM results is higher than the increase obtained in earlier studies for the same location. Willems and Vrac (2011) projected an increase of up to about 30% using a set of 17 ensemble runs from the ECHAM5 GCM, whereas Willems (2013) obtained a maximum increase of 50% using a large ensemble of older generation (CMIP3) RCM and GCM runs. In Figure 3.4, the highest changes go up to about 64% for a return period of 10 years and the smallest duration (1 day) considered under the RCP8.5 scenario.

In the framework of the quantile perturbation downscaling method, the change factors were applied on the Uccle observations to obtain future IDF curves as shown in Figure 3.5. For all RCPs, the precipitation intensities for the future IDF curves are larger than those for the existing curves, with more intensification for the more extreme RCP scenario (i.e., RCP8.5). The inadequacy of the existing IDF curves, as a result of intense precipitation amplification especially for longer recurrence interval and higher temporal resolution, increases the water infrastructure failure risks for the future.

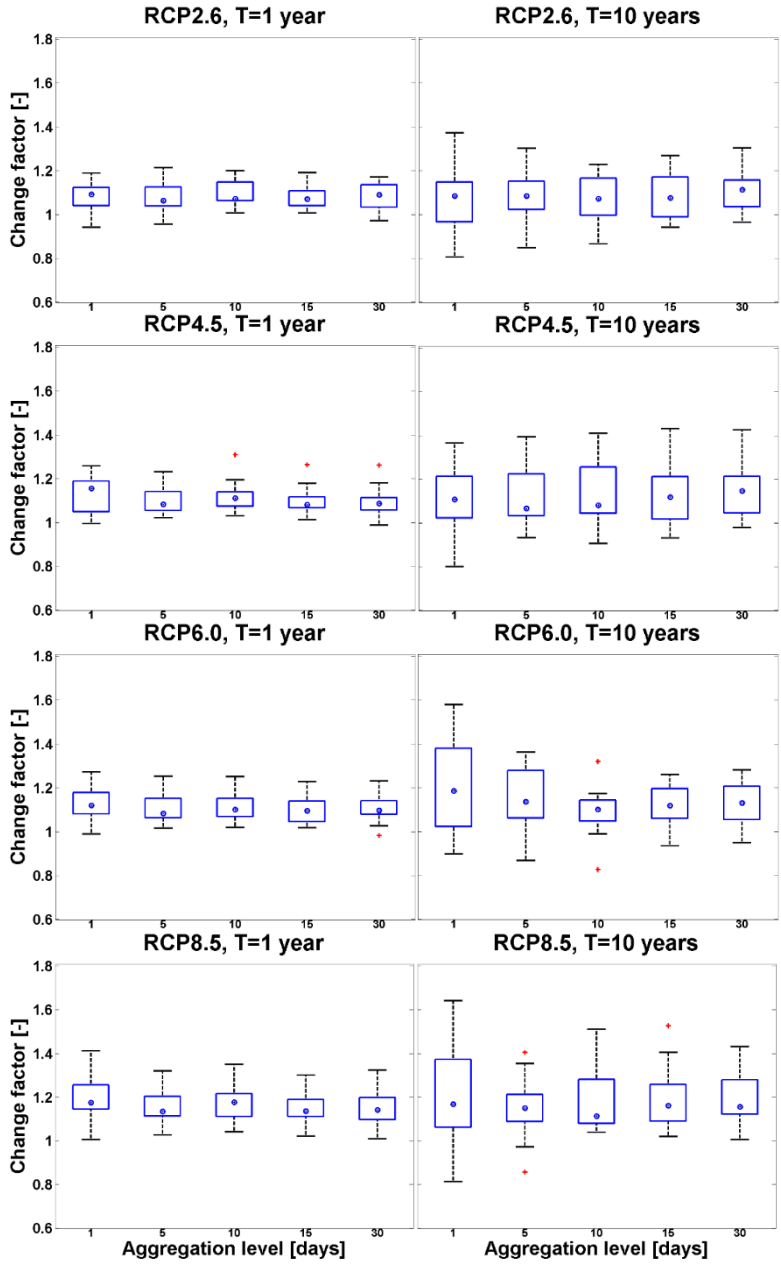


Figure 3.4: Change factors (from 1961-1990 to 2071-2100) for precipitation IDF statistics of different return periods and aggregation levels, and for different RCPs (top and bottom of the box show the 75th and 25th percentiles of change factors, respectively; top and bottom of the whiskers show the 5th and 95th percentiles, respectively; blue and red dots represent the median and outliers, respectively).

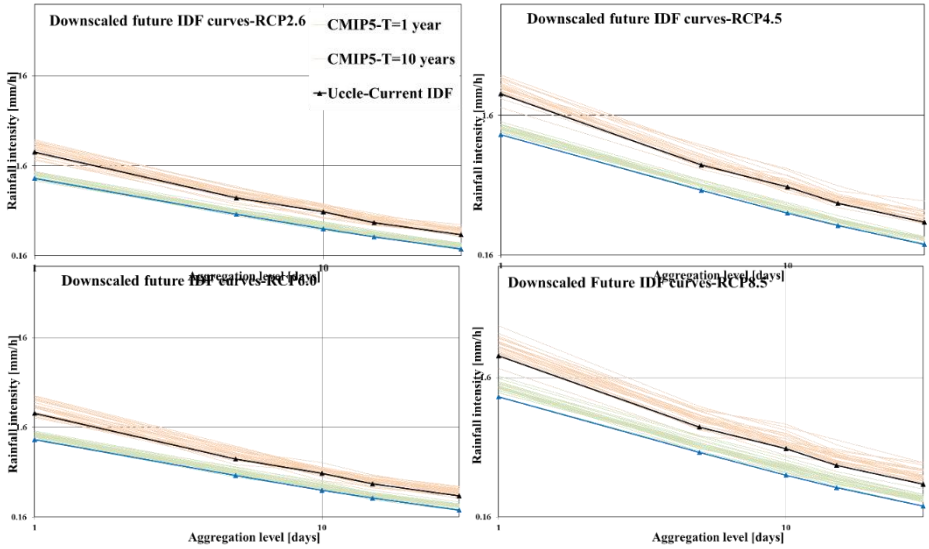


Figure 3.5: Future IDF curves (2071-2100) after quantile perturbation based on the CMIP5 GCMs for different RCPs versus the existing IDF curves (1961–1990) at Uccle station (observation lines for the 1- and 10-year return periods are shown in blue and black colors, respectively).

3.3.2.2. RCM based future IDF curves

Figure 3.6 shows the change factors (CFs) of extreme precipitation for the 0.11° and 0.44° RCMs. According to the boxplots, the future extreme precipitation quantiles will increase for most durations and return periods based on the median of the change factors. The decrease (CF < 1) is observed for less extreme precipitation (i.e., smaller return periods and larger durations). For the daily time scale, the 10-year precipitation intensity for RCP8.5 and RCP4.5 can increase up to about 70% (95th percentile of CF=1.66) and 50% (95th percentile of CF= 1.48) for the future, respectively (Figures 3.6a and b). Considering the RCP8.5 scenario (Figures 3.6b, d and f), the amount of increase in extreme precipitation is smaller for larger durations. However, such clear pattern is not detectable for RCP4.5, probably because the climate change signal on precipitation is less strong. Further, by increasing the return period, the changes in precipitation tend to intensify. Comparing the results for RCP4.5 and RCP8.5, as expected from

the literature (e.g., Toreti et al., 2013; Donat et al., 2016), RCP8.5 mostly indicates larger changes in precipitation intensity. Generally, the results show that the projected changes in extreme precipitation intensity do depend on return period, duration and the RCP scenario.

A comparison between the change factors of precipitation intensity for the 0.11° and 0.44° runs with identical combination of GCMs and RCMs is shown in Figure 3.7. Taking the 95th percentile of the change factors, the 0.11° RCMs project a larger future change compared with the 0.44° RCMs for both RCP4.5 and RCP8.5, while such pattern is not seen for the 1-year return period considering the median of the change factors. Also, the largest difference between change factor distributions for the ensemble of simulations is for the largest return period considered (T=10 years).

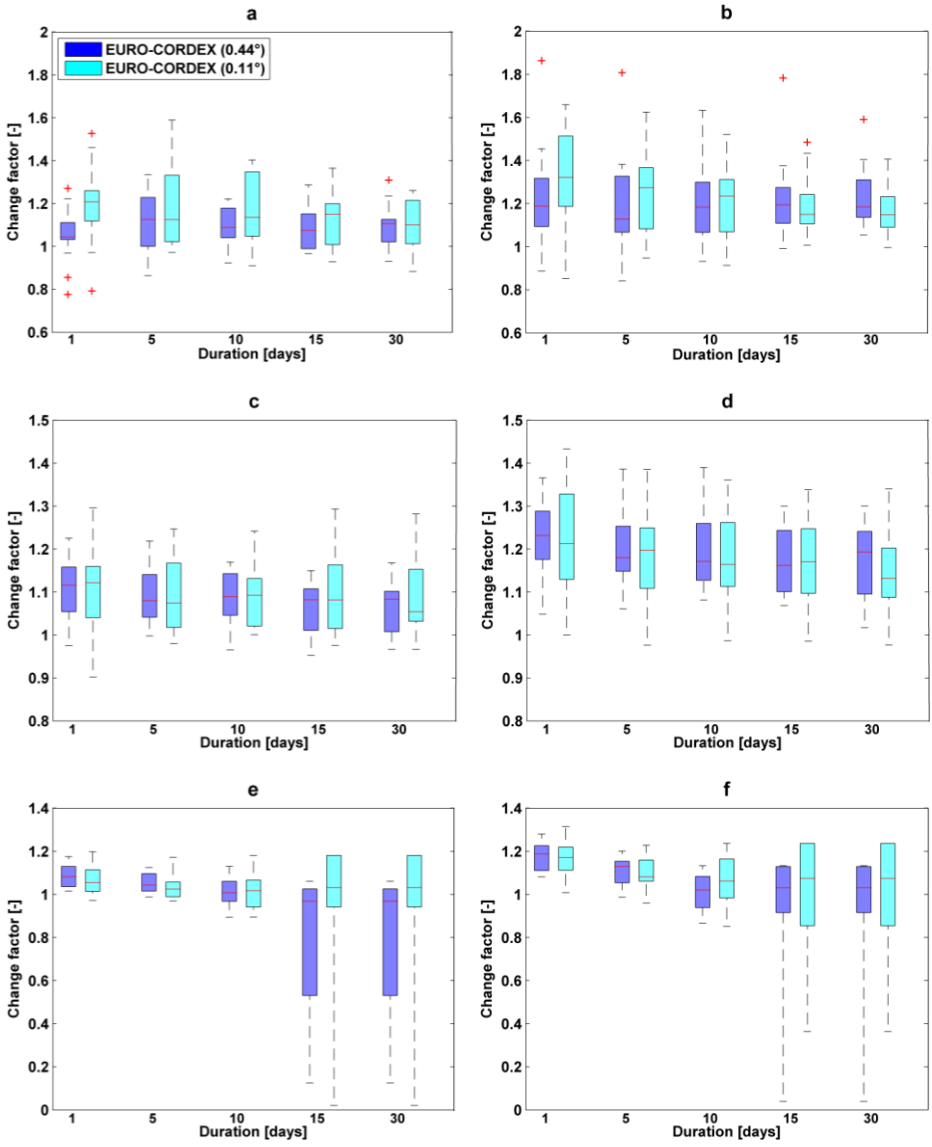


Figure 3.6: Change factors of the EURO-CORDEX RCMs for extreme precipitation for 10-year (a, b), 1-year (c, d) and 1-month (e, f) return periods and under RCP4.5 (a, c, e) and RCP8.5 (b, d, f) scenarios (Box defines interquartile range with its top and bottom corresponding to the 25th and 75th percentiles, respectively; horizontal red line inside the box represents the median (50th percentile); whiskers represent the 5th and 95th percentiles, respectively; outliers are depicted as red crosses).

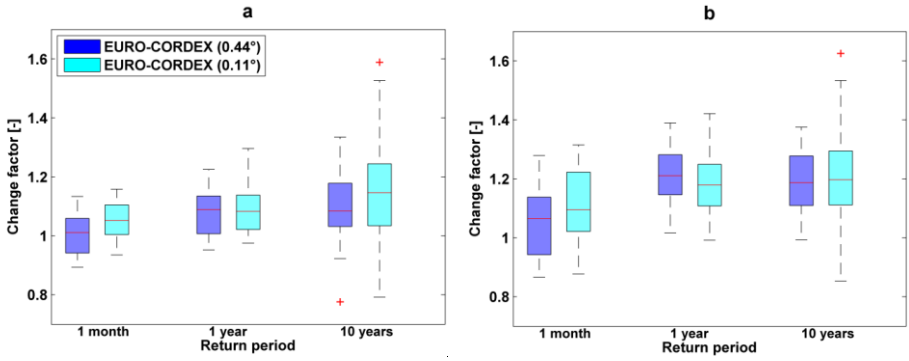


Figure 3.7: Comparison between change factors of the EURO-CORDEX simulations of 0.11° and 0.44° resolutions with identical combination of GCMs and RCMs for extreme precipitation under RCP4.5 (a) and RCP8.5 (b) scenarios, combining all durations (Box defines interquartile range with its top and bottom corresponding to the 25th and 75th percentiles, respectively; horizontal red line inside the box represents the median (50th percentile); whiskers represent the 5th and 95th percentiles, respectively; outliers are depicted as red crosses).

The projected IDF curves for the future based on all 0.11° and 0.44° RCMs are shown in Figures 3.8a and b, respectively. Both ensembles of RCMs show a general tendency to increase precipitation intensities for different return periods and durations, locating the future IDF curves higher than the observed ones from Uccle station for the present climate. This means that hydraulic structures designed based on the current climate IDF relationships may not be suitable for the future intensified precipitation extremes. When the future IDF curves derived from the 0.11° RCMs are compared with those from the 0.44° RCMs (Figures 3.8c and d), the 0.11° RCM projections for more extreme precipitation further emphasize the necessity to revise the existing IDF curves. Main question here is whether further increase of the climate model resolution would further increase the extreme precipitation changes; see also the debate by Willems et al. (2012a), Arnbjerg-Nielsen et al. (2013), Casanueva et al. (2016), Lind et al. (2016), Prein et al. (2016), Rummukainen (2016) and Tabari et al. (2016) on this.

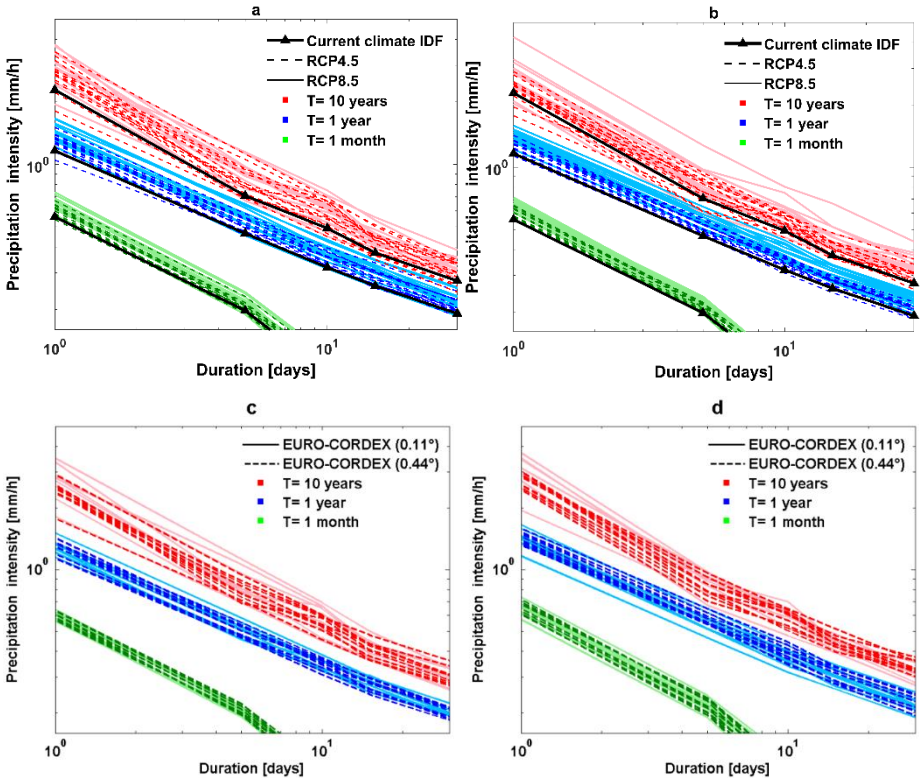


Figure 3.8: Projected IDF curves for all 0.11° (a) and 0.44° RCM (b) runs for 10-year, 1-year and 1-month return periods and (c, d) comparison between the 0.11° and 0.44° simulations with identical combination of GCMs and RCMs for RCP4.5 (c) and RCP8.5 (d) (both the vertical and horizontal axes are scaled logarithmically; current climate IDF curves based on the Uccle station observations are shown in black color in the sub-plots a and b).

3.3.3 Uncertainty analysis of projected changes in IDF statistics

3.3.3.1. GCM-based uncertainty analysis

The design precipitation changes over different RCPs, GCMs and GCM initial conditions are presented in Figure 3.9. In general, the changes in the future extreme precipitation projections increase from RCP2.6 to RCP8.5, which is trivial given the higher hypothesized increase in greenhouse gas concentrations in the more extreme scenarios. The uncertainty in the changes of extreme

precipitation due to different RCPs is generally large, ranging from 8% in RCP2.6 to 19-21% in RCP8.5. The difference is larger for more intense precipitation, as is shown for a return period of 10 years in comparison to the 1-year return period. Projected change difference over GCMs shows that the change amount varies substantially across the various GCMs. The related changes vary from 1.39% for the BCC-CSM1.1 GCM for the 10-year daily intensity to 44% for the GFDL-CM3 for the same return period and time scale. The NorESM1-M model is the only GCM which shows a negative change for the 10-year return period. Similar to GCMs and RCPs, the projected changes vary considerably over different CSIRO-MK3-6-0 GCM initial conditions, with run 7 for 10-year return period showing the lowest change of 1.8% and run 1 showing the highest change of 35% for the same return period (Figure 3.9). Generally, it is found from the results that the magnitude of changes in design precipitation at different return periods and durations is very sensitive to the choice of any of the three considered variates, GCMs, RCPs and GCM initial conditions.

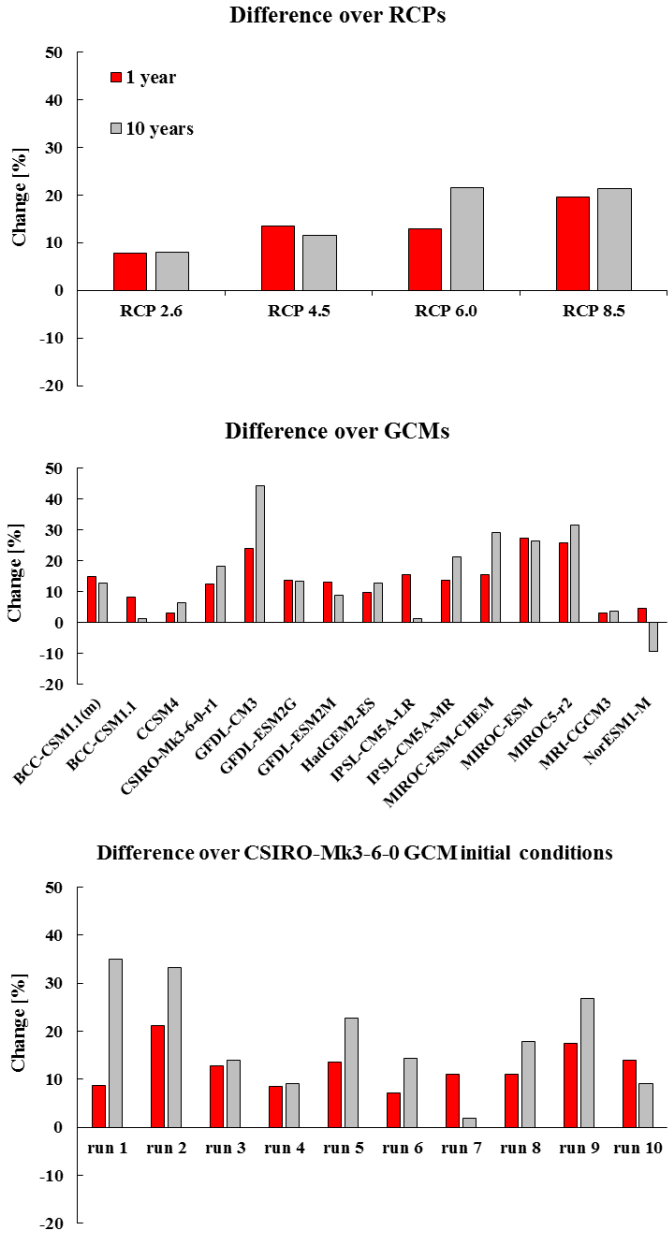


Figure 3.9: Changes (from 1961-1990 to 2071-2100) in daily design precipitation for different GCMs, RCPs and GCM initial conditions. In each of the subplots, one uncertainty source is varied and the changes for the other two uncertainty sources are averaged.

Percentage of total variation in change factors for design precipitation explained by GCM, RCP and GCM initial condition uncertainties for the selected return periods and durations is illustrated in Figure 3.10. As can be seen, GCM uncertainty is dominant throughout different durations and return periods: always larger than 49% and as high as 65%. This large GCM uncertainty is in agreement with the results reported in the literature (Minville et al., 2008; Hawkins and Sutton, 2011; Solaiman and Simonovic, 2011; Chen et al., 2011; Alam and Elshorbagy, 2015). Although GCM is the major contributor to the total uncertainty, GCM initial condition and RCP are also important. The relative contribution of the latter uncertainty sources depends on the return period and duration. The fractional contribution of each source is indeed subject to estimation uncertainties due to the limited sample size, as can be noticed by the non-monotonous changes in the contributions from low to higher return periods or from small to longer durations. General tendencies in the results show that the GCM initial condition uncertainty has a contribution percentage between 16% and 38%. The importance of GCM initial condition uncertainty has also been underlined by many climate change studies (Hawkins and Sutton, 2011; Deser et al., 2012, 2014; Peel et al., 2015). The RCP uncertainty ranges between 10% and 23%. This is surprisingly low, if one takes into account that the greenhouse gas concentrations are the forces driving the simulated climate changes, but consistent with the findings by other researchers (Hawkins and Sutton, 2011; Chen et al., 2011; Werner, 2011; Bürger et al., 2012). For all uncertainty sources, the absolute magnitude of uncertainty increases for increasing return period, from 1-year to 10-years. However, since the rate of the increase for the GCM and GCM initial condition uncertainties is higher than that for the RCP, the relative contribution of the RCP uncertainty decreases from 1-year to 10-year return period. To investigate whether the conclusions are sensitive to the method used for uncertainty definition, uncertainty was defined as the variance of change factors. When the results of the two uncertainty methods are compared, the results obtained from the scenario range method remain valid.

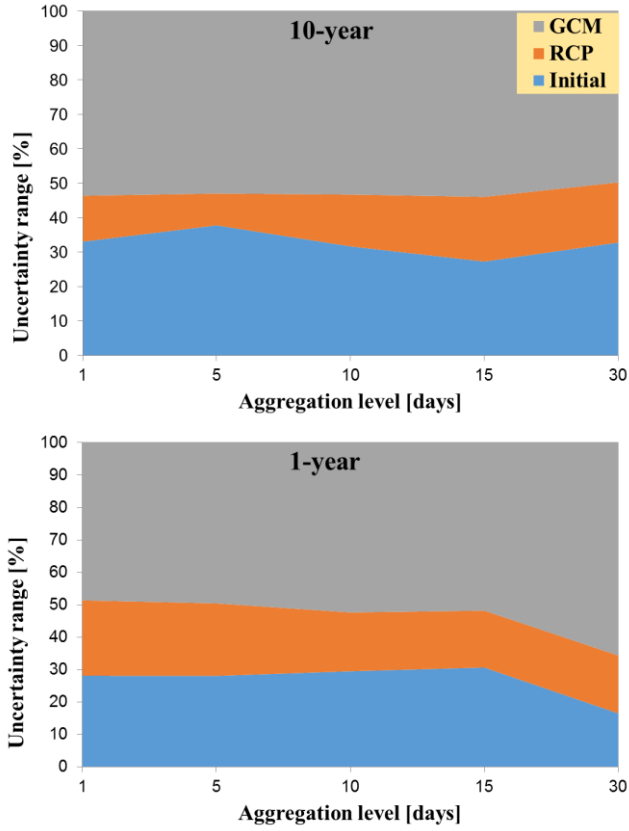


Figure 3.10: Percentage of total variation in change factors for design precipitation amounts explained by GCMs, RCP scenarios and GCM initial conditions uncertainties (uncertainty is defined as the scenario range of change factors).

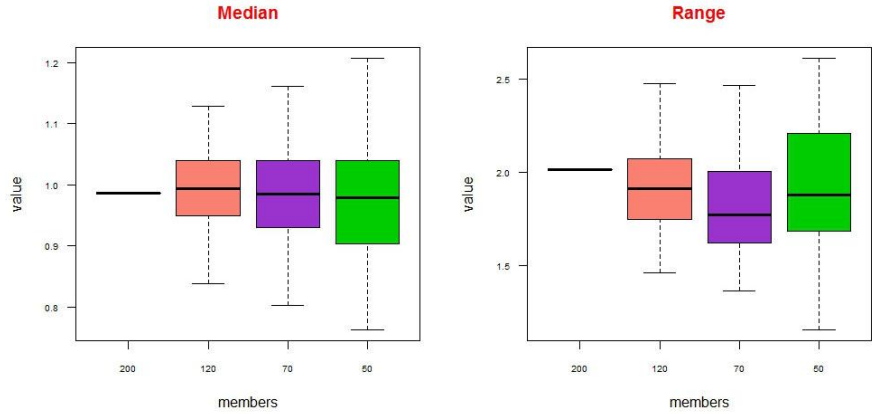


Figure 3.11: Comparison of median (left column) and range (right column) in the ensembles with different sample sizes (population consists of 200 randomly produced numbers with similar value range to precipitation change factors; smaller sample sizes are randomly selected from the population and this is repeated a large number of times; top and bottom of the box show the 75th and 25th percentiles of randomly generated values, respectively; top and bottom of the whiskers show the 5th and 95th percentiles, respectively; horizontal black line in the middle of the box represents the median).

Because the larger uncertainty of GCM compared with the GCM initial condition and RCP uncertainties may be due to its larger sample size (15 GCMs vs. 10 GCM initial conditions and 4 RCPs), the uncertainties of GCMs, GCM initial conditions and RCPs with the same sample size (i.e., 4 members) are compared (Figure 3.12). The results show that the GCM uncertainty is still the main source of uncertainty, albeit its magnitude decreased after decreasing its sample size. Sensitivity of the uncertainty magnitude to sample size is further investigated next.

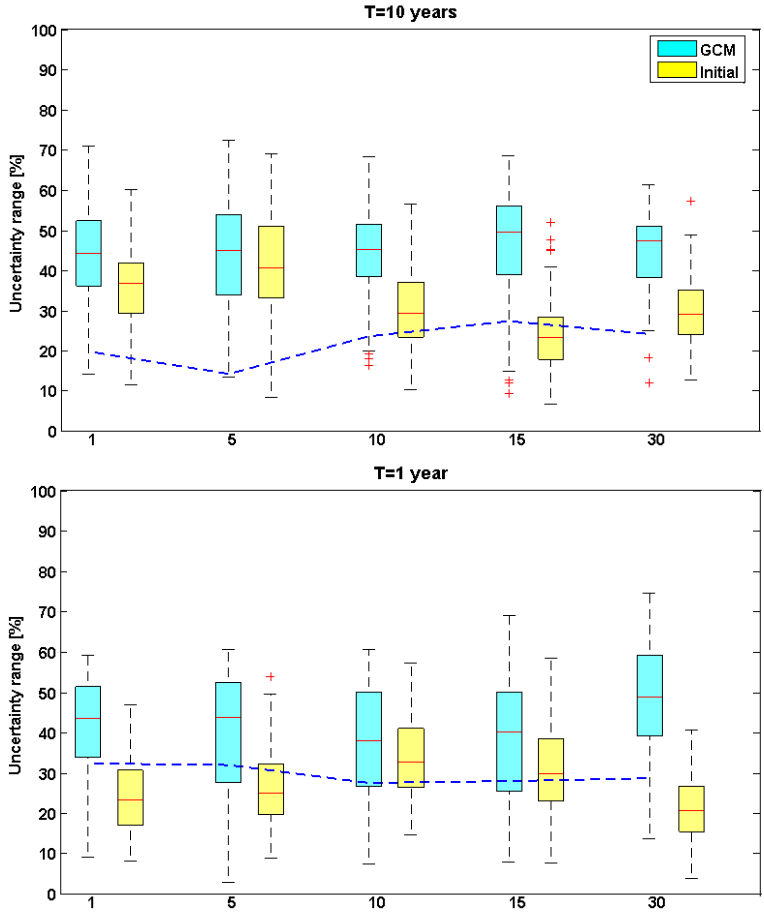


Figure 3.12: GCM and GCM initial condition uncertainties using the same sample size (4 members) as RCPs for design precipitation changes (4 GCMs or CSIRO-Mk3.6.0 runs are randomly selected from the 15 GCMs or the 10 CSIRO-Mk3.6.0 runs and this is repeated a large number of times; GCM and GCM initial condition uncertainties are shown in cyan and yellow boxes, respectively; RCP uncertainty is shown with blue dashed line; top and bottom of the box show the 75th and 25th percentiles of uncertainty range, respectively; top and bottom of the whiskers show the 5th and 95th percentiles, respectively; horizontal red line in the middle of the box and red cross represent the median and outliers, respectively).

For the GCM uncertainty, our ensemble consists of 15 GCMs and for each GCM, one control run and four scenario runs (the four RCPs) are considered, hence 75 runs in total. To investigate the influence of the number of GCM runs on the GCM uncertainty, smaller sample sizes (with random selection) with

varying number of GCM members between 14 and 4 are created. Afterwards, the GCM uncertainty from these new ensembles is compared with that from the original ensemble with 15 GCMs (Figure 3.13). The results show that the bigger the GCM ensemble size is, the larger uncertainty will be. However, median of change factors remains more or less same among the GCM ensembles with different sample sizes. It implies that in climate change studies the mean climate scenario (median of projected changes) can be constructed based on the results of few GCMs. However, one has to be careful in constructing the high and low climate scenarios and for analyzing uncertainty using few GCMs, as the results are expected to be different from those achieved from a larger ensemble of GCMs. This is due to the fact that at such ensemble size (population size=15), the upper and lower limits of the 95% confidence interval are equal to the maximum and minimum values (15×0.025 for the upper limit and 15×0.975 for the lower limit) which are very sensitive to sample size. However, for very large size of GCM ensemble (e.g., population=100 or 200) at which the upper and lower limits of the 95% confidence level are not equal to the maximum and minimum values, range of uncertainties (high climate scenario minus low climate scenario) remains more or less the same when changing the size of ensemble (see Figure 3.11). The analysis is also done for the GCM initial condition uncertainty and similar results are obtained: decreasing uncertainty with decreasing sample size and a constant median of changes for different sample sizes (Figure 3.14).

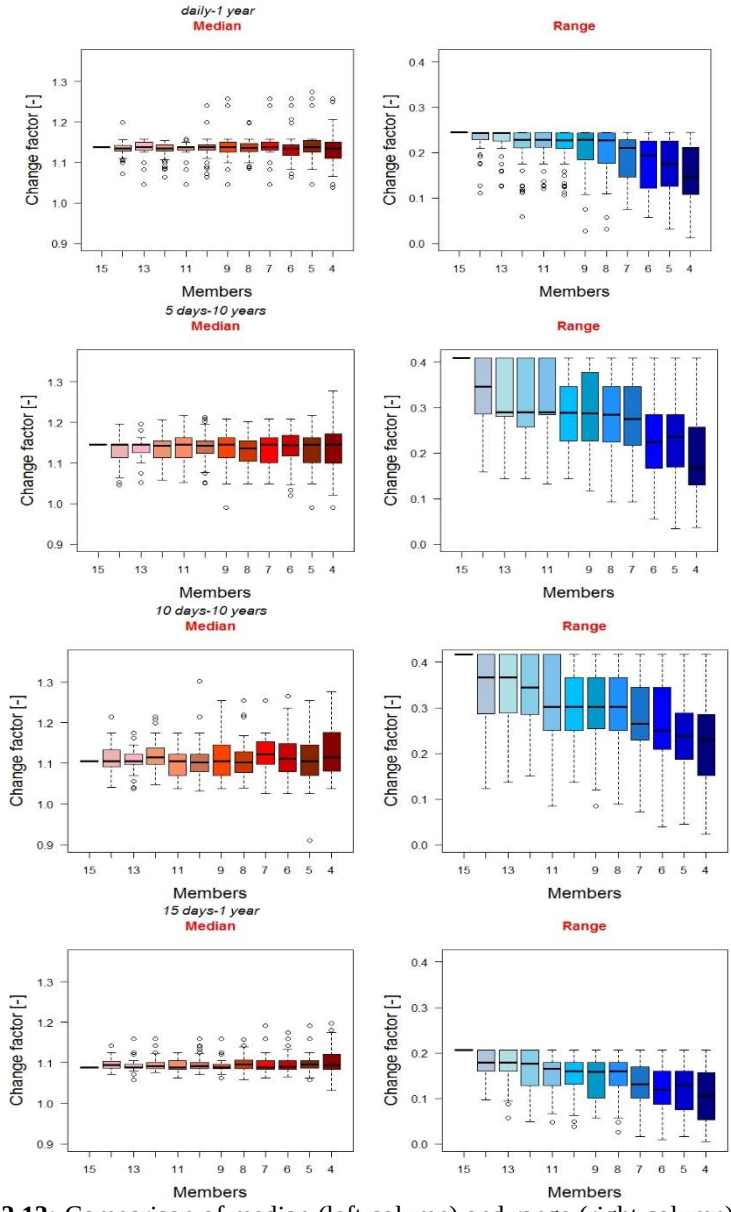


Figure 3.13: Comparison of median (left column) and range (right column) of change factors for different GCM ensemble sizes (smaller sample sizes are randomly selected from the 15 GCMs and this is repeated a large number of times; uncertainty range is computed as the difference between the high and low climate scenarios defined based on the 95% confidence intervals; top and bottom of the box show the 75th and 25th percentiles of change factors, respectively; top and bottom of the whiskers show the 5th and 95th percentiles, respectively; horizontal black line in the middle of the box and hollow black dot represent the median and outliers, respectively).

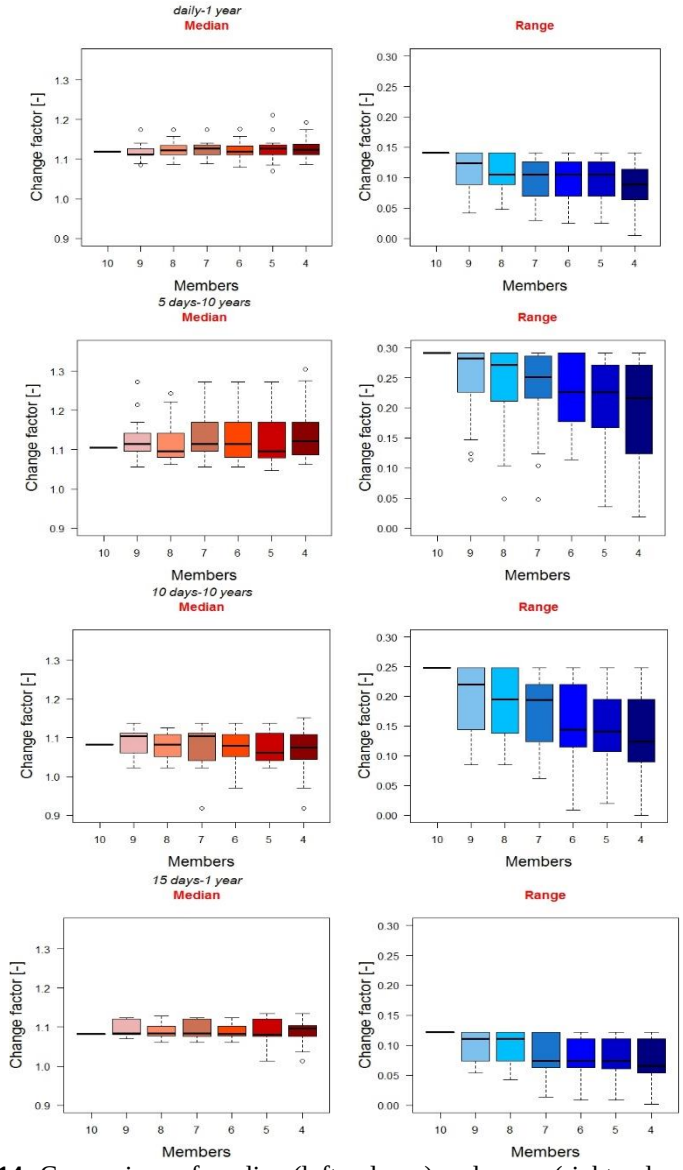


Figure 3.14: Comparison of median (left column) and range (right column) of change factors for GCM initial conditions with different number of runs (smaller sample sizes are randomly selected from the 10 GCM initial conditions and this is repeated a large number of times; Uncertainty range is computed as the difference between the high and low climate scenarios defined based on the 95% confidence intervals; top and bottom of the box show the 75th and 25th percentiles of change factors, respectively; top and bottom of the whiskers show the 5th and 95th percentiles, respectively; horizontal black line in the middle of the box and hollow black dot represent the median and outliers, respectively).

The sensitivity analysis of the RCP uncertainty results to the sample size is also performed. In the case of future concentration scenarios, this study made use of the precipitation simulations for all four RCP scenarios (RCP2.6, RCP4.5, RCP6.0, RCP8.5). However, all RCPs have not been mostly considered in hydrological impact studies of climate change (Booth et al., 2013; Mohammeda et al., 2015; Mandal et al., 2016; Monjo et al., 2016; Fatichi et al., 2016) and for simplifying and based on the research purpose, the climate model outputs for only one RCP (RCP8.5 representing the extreme future conditions or RCP4.5 representing the medium future conditions) or two RCPs (RCP4.5 & RCP8.5) have been used. From uncertainty analysis point of view, all RCPs are needed to cover the total ensemble uncertainty of climate change. Although considering RCP2.6 and RCP8.5 as the lower and upper limits of projected concentrations approximately covers this range (Hosseinzadehtalaei et al., 2016); however, considering only RCP4.5 and RCP8.5 might underestimate the total uncertainty. This issue is investigated in this study by comparing the RCP uncertainty derived from 2-RCP cases (RCP2.6 & RCP8.5, RCP4.5 & RCP8.5 and RCP6.0 & RCP8.5) with that from the 4-RCP case (RCP2.6, RCP4.5, RCP6.0, RCP8.5). The results indicate that the use of extreme scenarios (RCP2.6 & RCP8.5) covers the total uncertainty range in extreme precipitation change for almost all cases, while the use of RCP4.5 & RCP8.5 and RCP6.0 & RCP8.5 will underestimate the full uncertainty (Figure 3.15). Similar to the GCM uncertainty, the RCP uncertainty is more sensitive to the number of runs for more extreme events and smaller time scales.

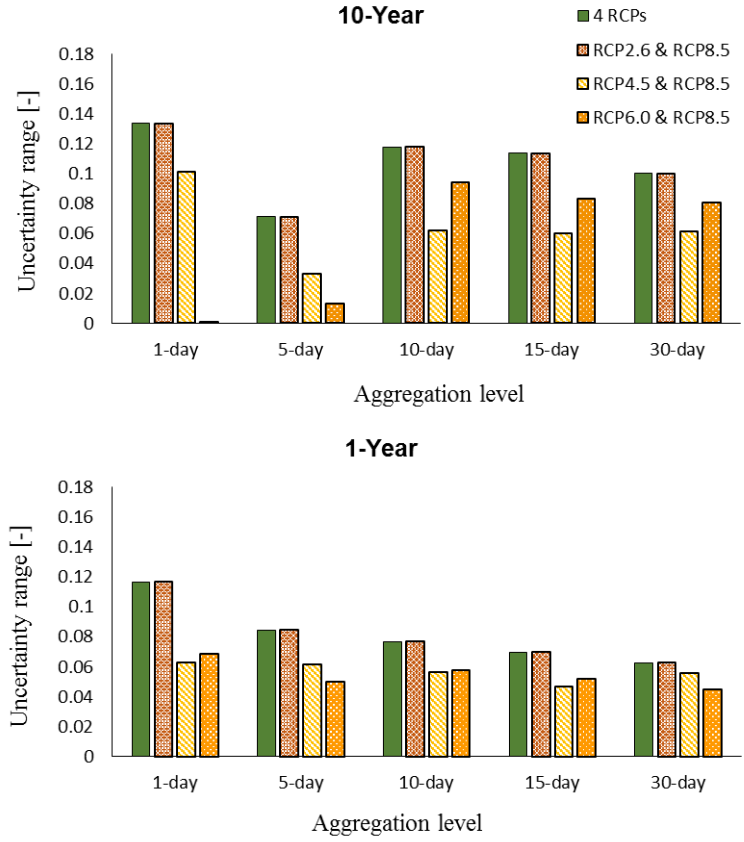


Figure 3.15: Comparison of uncertainty ranges considering four and two RCPs (uncertainty range is computed as the difference between the high and low climate scenarios defined based on the 95% confidence intervals).

To assess the uncertainty in the initial conditions, we used 50 runs of the CSIRO-Mk3.6.0 GCM (10 runs for the control period and 40 runs for the four RCPs). Such high numbers of GCM/RCM members are rarely available in climate model ensembles; the number of runs per GCM and RCP combination in the CMIP5 ensemble (as the largest ensemble available) is still of the order of 3 to 10. Due to this lack of available runs per GCM, a limited number of runs have been used for initial condition uncertainty in climate change impact assessments, e.g., five runs of a GCM in Chen et al. (2011) and five and three runs for two GCMs in Velázquez et al. (2013). Despite the high number of runs available for the CSIRO-Mk3.6.0 model, the fractional uncertainty related to the

GCM initial conditions in Figure 3.10 was related to that single GCM only. A critical question here is how much the uncertainty associated to the GCM initial conditions will change when choosing another GCM instead of the CSIRO-Mk3.6.0 model. To answer this research question, the initial condition uncertainty is reperformed using the simulations of the HadGEM2-ES, CCSM4 GCMs and CSIRO-Mk3.6.0 with 3 runs (i.e., different initial conditions) for each control and four RCPs periods (that makes the total runs of this GCM equal to 15). A comparison of uncertainty ranges for GCM initial conditions using the same number of runs (i.e., 3 runs) for the three GCMs is presented in Figure 3.16. For daily precipitation of 10-year return period, the CCSM4 model has the largest uncertainty range, while the CSIRO-Mk3.6.0 model shows the largest uncertainty for 5-daily precipitation of the same return period. Apart from more extreme precipitation at smaller time scales, the difference between the uncertainty range for different GCMs is negligible.

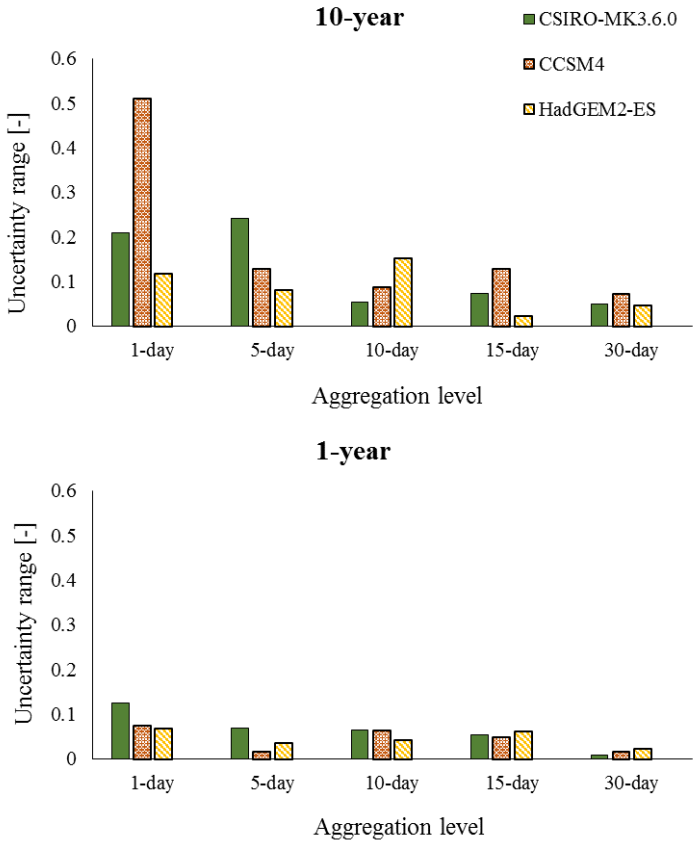


Figure 3.16: Comparison of uncertainty ranges for GCM initial conditions for different GCMs with the same number of runs (uncertainty range is computed as the difference between the high and low climate scenarios defined based on the 95% confidence intervals).

3.3.3.2. RCM-based uncertainty analysis

In the following, the uncertainty of RCMs, driving GCMs, RCPs and the interaction between them are presented. An unbiased uncertainty analysis is performed once a balanced matrix of RCM×GCM is created by filling the missing combinations.

Figure 3.17 shows the respective uncertainty of RCMs, GCMs and RCPs for different return periods (1-month, 1-year, 10-year) and durations (1-, 5-, 10-, 15- and 30-day) for the RCMs of 0.11° resolution. Based on the results, the uncertainty in the RCM results is in 53% of the cases larger than the other

uncertainty components. When comparing RCM and GCM uncertainties, the RCM uncertainty in 80% of the cases is larger than the GCM uncertainty. In the case of 10-day duration of 1- and 10-year return periods and 15-day duration of 1-year return period, GCMs produce larger uncertainty compared to RCMs. This is probably due to their coarse resolution, which induces a higher bias to the more extreme precipitation intensities. The RCP related uncertainty differs from 3.1% for a 10-day duration and a 10-year return period to 29.1% for a 1-day duration and a 1-month return period. In general, the choice of RCM is the dominant source of uncertainty for shorter durations of 1- and 5-day precipitation, while there is no clear pattern for larger durations.

In the case of the RCMs of 0.44° resolution (Figure 3.18), the largest uncertainty for 60% of the durations and return periods comes from the RCMs. For the rest of the cases (1- and 5-day durations of 1-month and 1-year return periods, 10-day duration of 1-month return period and 30-day duration of 1-year return period), the GCM source shows larger uncertainty. For 1-, 5- and 10-day durations, the amount of GCM uncertainty decreases with increasing return period. In the case of RCM uncertainty, the uncertainty increases with return period for 1- and 5-day durations. It's worthwhile to note that strong uncertainty in the RCP component hardly occurs for the 0.44° RCMs, similar to the 0.11° RCMs. This is partly due to the unavailability of precipitation data for RCP2.6 and RCP6.0 especially for the former RCP in the EURO-CORDEX RCM dataset, which leads to an underestimation of the RCP variance and the related uncertainty.

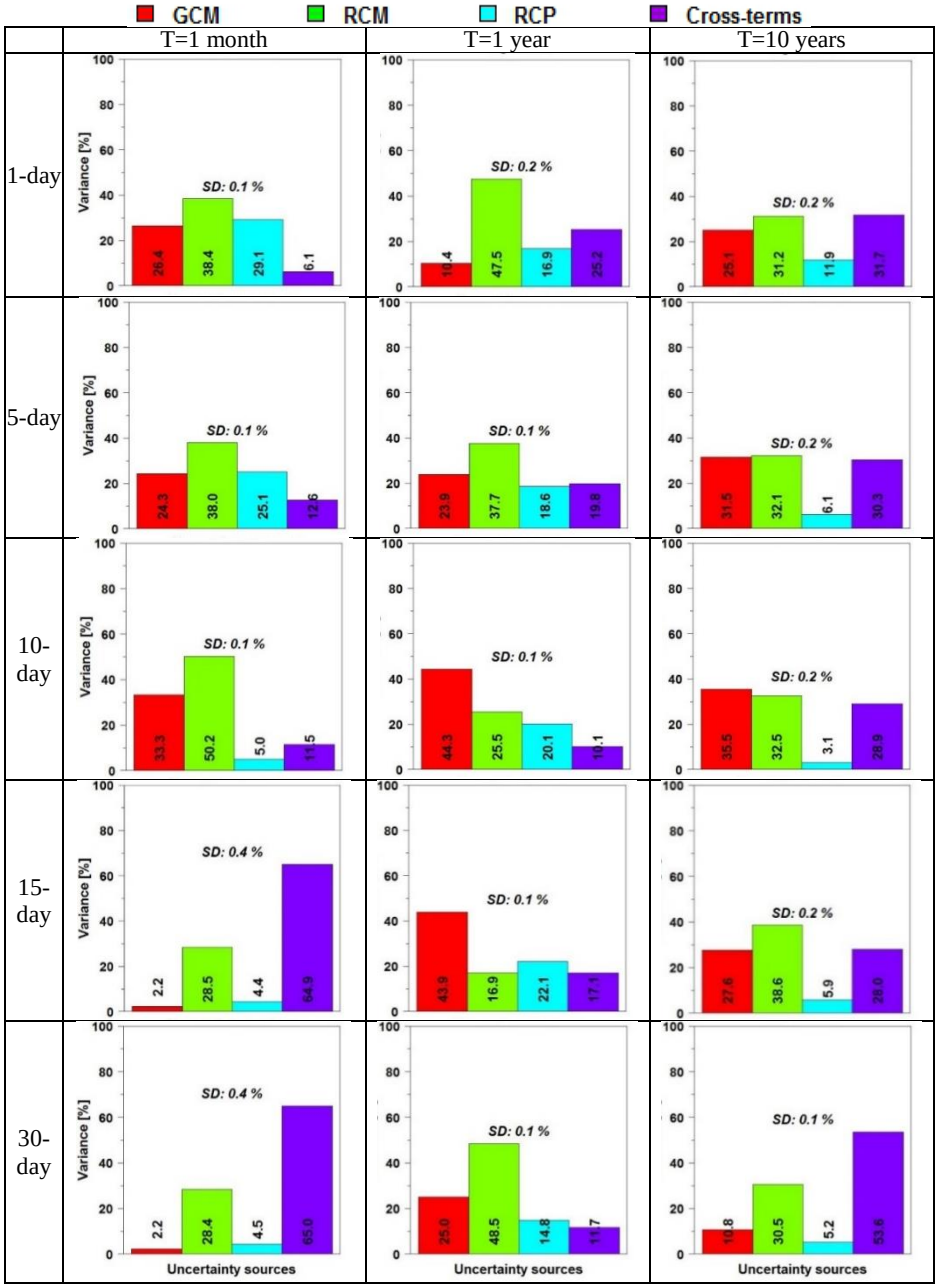


Figure 3.17: Variance decomposition results for the total uncertainty in the change factors computed using the EURO-CORDEX 0.11° RCMs for extreme precipitation after missing data construction in RCM×GCM combinations: percentage of total variance explained by GCMs, RCMs, RCPs and cross-terms components.

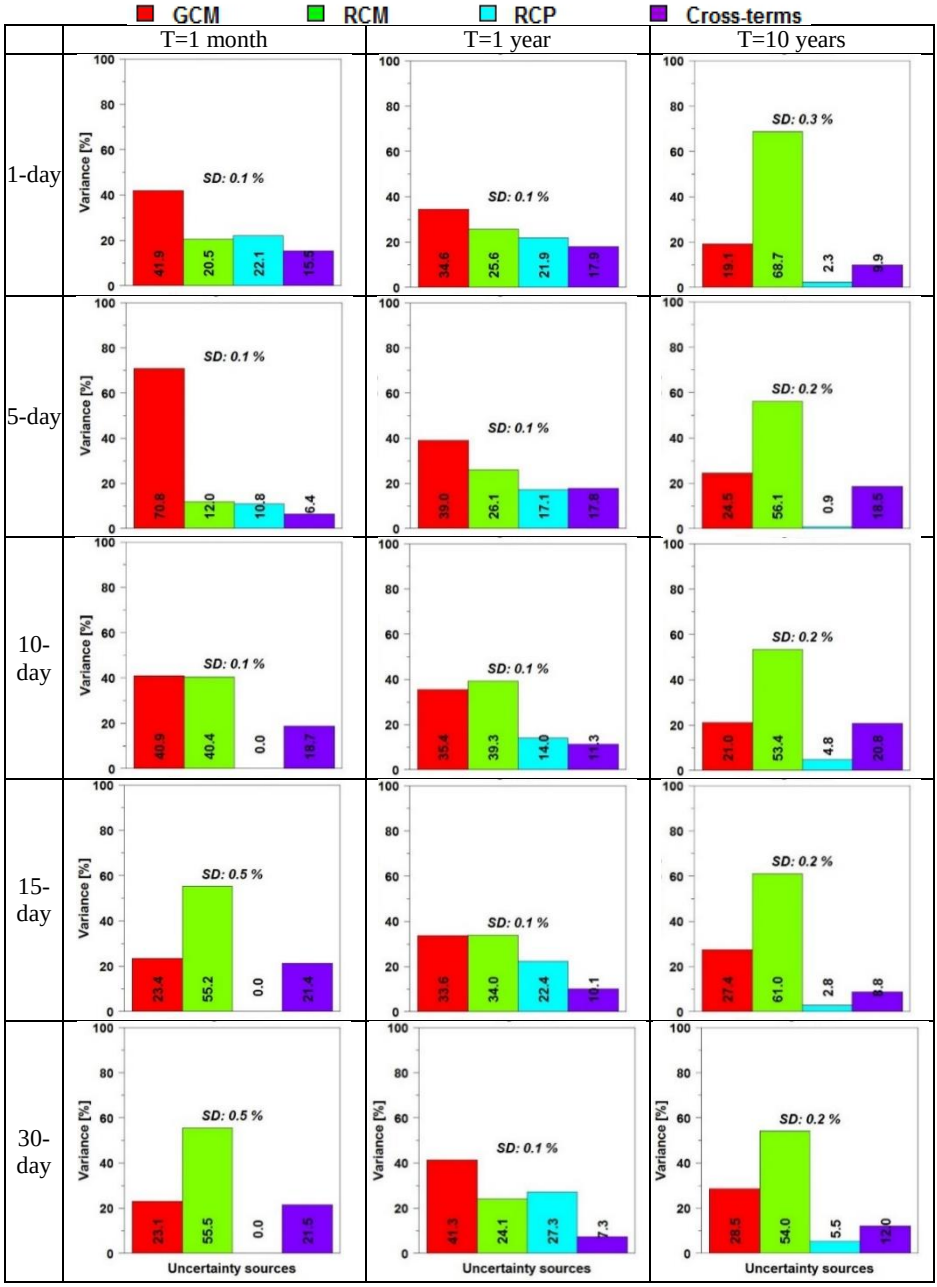


Figure 3.18: Variance decomposition results for the total uncertainty in the change factors computed using the EURO-CORDEX 0.44° RCMs for extreme precipitation after missing data construction in RCM×GCM combinations: percentage of total variance explained by GCMs, RCMs, RCPs and cross-terms components.

The overall results for both ensembles of RCMs indicate that RCMs play the main role in the uncertainty of the projected changes in more extreme precipitation for construction of IDF curves. For less extreme precipitation, the dominate source varies very much according to duration. The RCM uncertainty is because of different techniques used by the models to discretize the differential equations and to represent subgrid physical processes (Déqué et al., 2012).

For some cases, especially for the 0.11° RCMs, the uncertainty analysis indicates small contributions of RCMs, GCMs and RCPs and large cross-contribution. It can be ascribable by internal variability. According to Mearns et al. (2013), large values of cross term compared to other components, can be related to (i) large internal variability of the climate system or (ii) similar response of RCM-GCM combinations to the climate change. To investigate the reason for the large cross-contribution, uncertainty rates for two cases (daily precipitation with T=10 years and monthly precipitation with T=1 month) with high amount of cross uncertainty (HCU) are compared with those for two cases (daily precipitation with T=1 month and 10-daily precipitation with T=1 year) with low amount of cross uncertainty (LCU) (Figure 3.19). From a mathematical point of view, the value for the cross-contribution uncertainty is high when the values for the other three components are low. The analysis shows that the uncertainty rates of the GCM, RCM and RCP components in the HCU cases are not lower than those for the LCU cases. Hence, HCU is because of the large rate of the total uncertainty rather than the small rates of the other components, suggesting the large internal variability as the reason. Generally, the interactions between the uncertainty sources for the 0.11° RCMs account for about 6%–65% of the total ensemble uncertainty, which is larger than the contribution of the interaction term for the 0.44° RCMs ranging between 6% and 22%. This highlights the importance of considering the interactions among individual uncertainty sources especially for finer resolution RCMs: neglecting the interaction term would lead to overestimation of the uncertainty rates associated to individual sources.

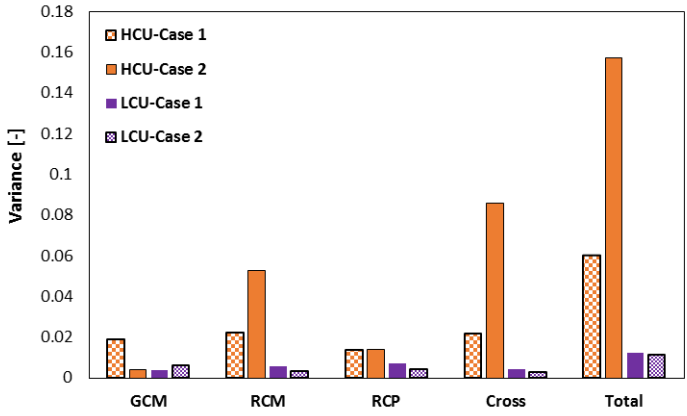


Figure 3.19: Comparison of total variance contributions between two cases with high and two cases with low amount of cross term (HCU: high amount of cross uncertainty; LCU: low amount of cross uncertainty).

As the results of the variance decomposition analysis may be influenced by the method used to fill the matrix (Sunyer et al., 2015), another method (linear equation system: LES) is also used to reconstruct the missing combinations in the RCM–GCM matrix. The LES method is based on solving the linear equation system of the ANOVA design matrix which differs from the iterative linear reconstruction method developed by Déqué et al., (2007). The uncertainty analysis (not shown) by the variance decomposition approach after reconstructing the missing combinations by the LES method shows very similar results to those obtained from the iterative linear reconstruction method.

Next to the uncertainty analysis of changes in extreme precipitation after reconstructing missing values in the RCM×GCM combinations, uncertainty analysis is also performed using original data (without reconstruction) to find out the bias involved with the uncertainty results in the latter analysis (Figures 3.20 and 3.21). The results of this analysis for both the 0.11° and 0.44° RCMs attributes the largest uncertainty to the GCMs. On average, the uncertainty rate of the GCM component for the 0.44° (0.11°) RCMs increases from 34% (24%) in the constructed missing value case to 48% (31%) in the unconstructed case. Generally, the results show that the biases in using an unbalanced RCM×GCM matrix can be quite large, leading to a misconclusion for uncertainty analysis.

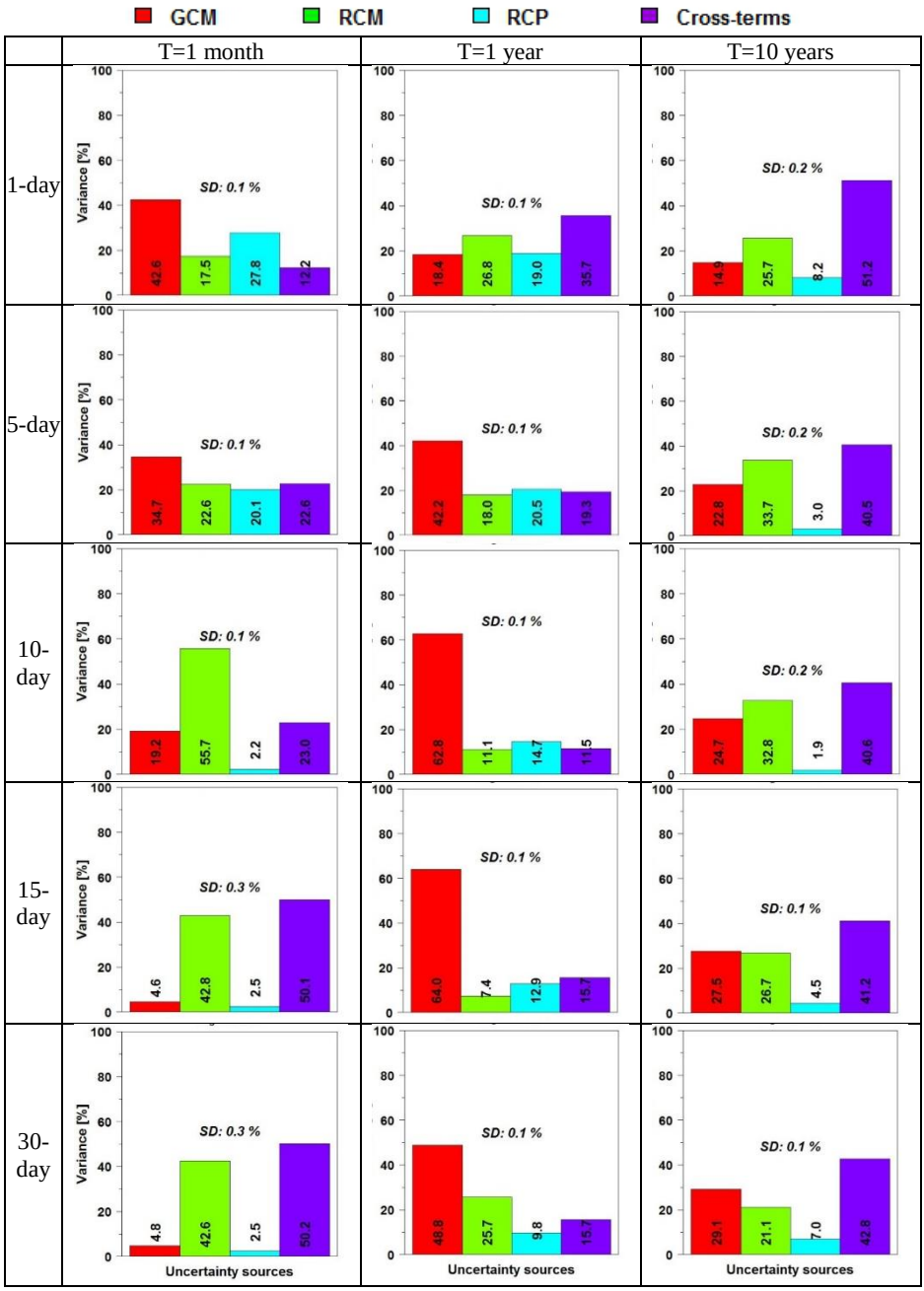


Figure 3.20: Variance decomposition results for the total uncertainty in the change factors computed using the EURO-CORDEX 0.11° RCMs for extreme precipitation without missing data construction in the RCM×GCM combinations: percentage of total variance explained by GCMs, RCMs, RCPs and cross-terms components.

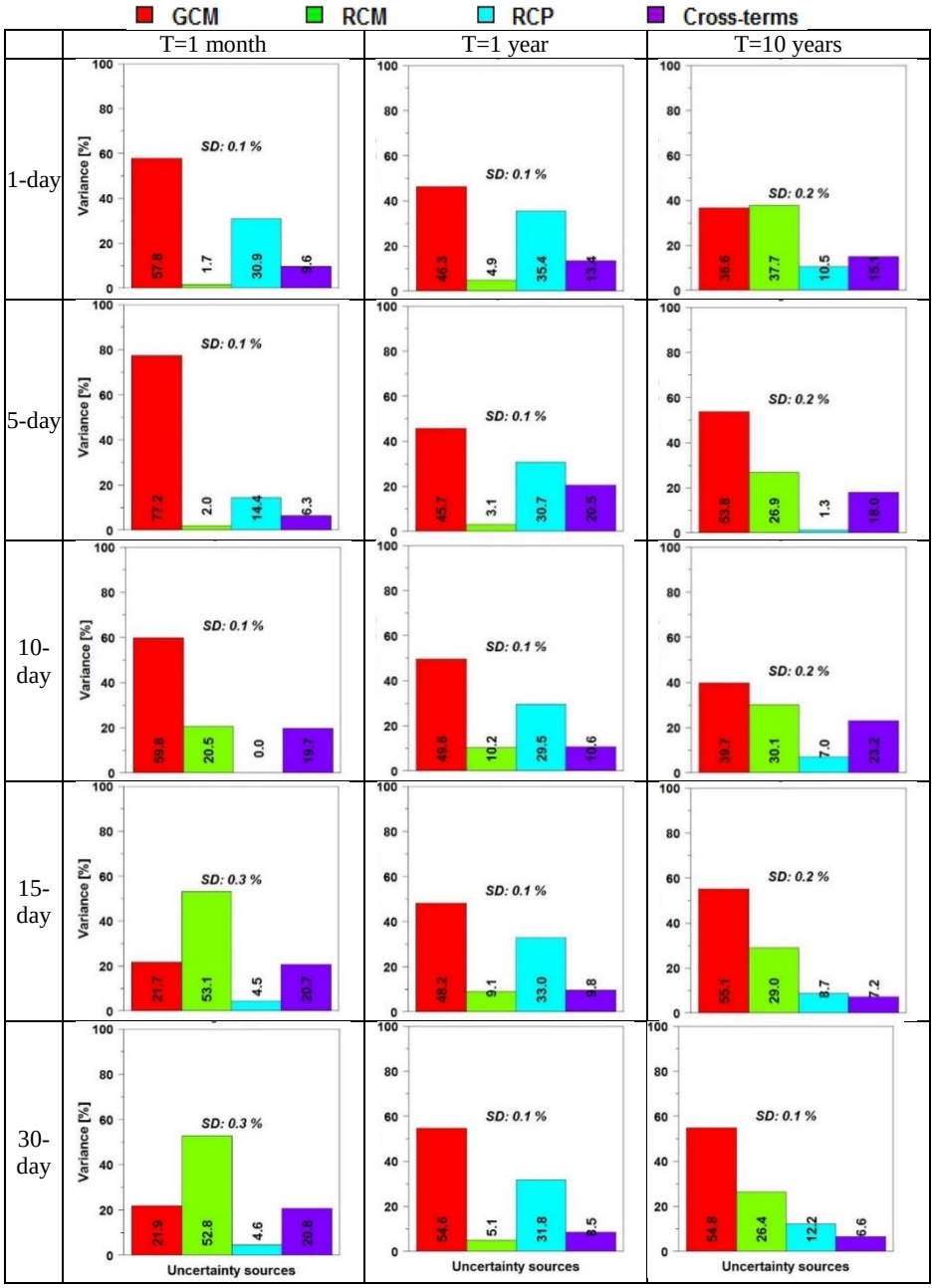


Figure 3.21: Variance decomposition results for the total uncertainty in the change factors computed using the EURO-CORDEX 0.44° RCMs for extreme precipitation without missing data construction in RCM×GCM combinations: percentage of total variance explained by GCMs, RCMs, RCPs and cross-terms components.

3.4 Conclusions

In the current study, future changes in intense precipitation and possible impact of climate change on the IDF curves for Belgium and associated uncertainties were quantified by using a large ensemble of projections gained from 15 CMIP5 GCMs under four representative concentration pathways (RCP2.6, RCP4.5, RCP6.0 and RCP8.5) and an ensemble of EURO-CORDEX with two resolutions of 0.11° and 0.44° for different return periods and durations.

The results indicate an amplification in the intensity of precipitation extremes for the end of the 21st century relative to the current climate. The amount of increase varies depending on the GCMs, RCPs and GCM initial conditions and can go up to around 64%.

A comparative assessment between the RCMs of 0.11° and 0.44° grid spacing along with an analysis of the associated uncertainties are performed for precipitation of 1-month, 1-year and 10-year return periods and durations ranging between 1 and 30 days. Based on the validation results, the 0.11° RCMs generally overestimate historical precipitation intensities compared to the Uccle station and E-OBS observations, while the simulations for the 0.44° RCMs lie mostly between the Uccle station and E-OBS observations, implying higher precipitation intensities by higher resolution runs. Similarly, the climate projection ensemble with RCMs at 0.11° resolution shows a larger increase in precipitation than with RCMs at 0.44° resolution for the end of the 21st century, at the region of interest in central Belgium. In the case of the daily duration, based on the 0.11° RCMs the 10-year precipitation intensity for RCP4.5 and RCP8.5 can increase up to around 50% and 70% respectively, whereas smaller increases are projected for the 0.44° RCMs: 25% and 50% for RCP4.5 and RCP8.5, respectively.

The uncertainty in the extreme precipitation changes is, however, large in all cases. The highest contribution to this uncertainty for more extreme precipitation is the RCM uncertainty. For the 0.11° ensemble, the choice of RCM roughly contributes between 17% and 50% to the total uncertainty, while the RCM contribution for the 0.44° ensemble peaks up to 69%. This means that one can give slightly higher trust to the higher changes obtained from the higher

resolution RCMs than from the coarser models. The uncertainty analysis also reveals a greater role of the boundary forcing (i.e., GCM) compared to the future greenhouse gas scenario (i.e., RCP). The uncertainties associated with cross-contributions of RCMs, GCMs and RCPs are also of the same order of magnitude or higher than the primary source of uncertainty, for the majority of cases considered.

The uncertainty analysis for the CMIP5 GCMs ensemble shows that the choice and set of GCMs is the largest source of uncertainty for all the return periods and aggregation levels considered. However, the other sources of uncertainties cannot be neglected and need to be taken into account as well, as for some cases fractional uncertainties of up to 38% and 23% are observed for GCM initial conditions and RCPs, respectively. This quantification of uncertainties in future IDF curves represents useful information for hydraulic and water engineering design and modeling, as well as impact and adaptation studies. It is also found from the sensitivity analysis that the uncertainties in the GCMs, RCPs and GCM initial conditions are sensitive to the size of climate model ensemble, particularly in the case of more intense precipitation at smaller temporal resolution.

Generally, there is no practical method to identify the optimal size of a climate model ensemble. Although some approaches based on climate model performance for the present-day climate and giving corresponding weight to them (e.g., reliability ensemble average (REA) method by Giorgi and Mearns, 2002) have been developed for optimizing climate model projections for the future, better skill of a climate model for present-day climate simulations does not guarantee the validity of its future projections (Tebaldi and Knutti, 2007). However, with regard to quantification of all aspects of uncertainty in future climate change in a probabilistic way, a large multi-model ensemble is needed. In addition, including more independent climate models boosts our confidence on climate change projections for the future, since combining the outputs of several individual models will lead to better ability and higher reliability of projections for the highly complex climate system. This is the case for the ensembles at which climate models are less homogeneous in the sense of the climate processes they include or neglect and in their structure.

The results of this study highlight the importance of ensemble size for the uncertainty analysis of climate change. The increase in the climate model ensemble size to cover the full uncertainty in climate change projections and the improvement of model accuracy (e.g., increasing model resolution) to present a more realistic simulation of the climate system are two competing demands for climate modeling centers. These are two important issues for climate change impact assessments and neither should be sacrificed for another and there must be a balance between them based on available computational resources.

In this study, the sensitivity of climate change uncertainty to the number of GCM runs was analyzed, assuming that the GCMs in the multi-model ensemble provide statistically independent information. However, some factors may affect the validity of this assumption since some GCMs are developed in the same climate modeling center or they are developed in different centers but may share some part of the code or use the same theoretical arguments for parameterizations (Sunyer et al., 2013b). The assumption of model independence hence needs further investigation.

CHAPTER 4

Climate Change Impact on IDF Curves in Europe

This chapter was published as:

Hosseinzadehtalaei, P., Tabari, H., Willems, P. (2020) Climate change impact on short-duration extreme precipitation and intensity–duration–frequency curves over Europe. *Journal of Hydrology*, 590, 125249

Summary

To build future climate-proof water systems and to reduce the failure risk of infrastructure, short-duration extreme precipitation design storms must be updated. However, a robust future projection of such storms on a continental scale has not been presented due to the scarcity of long, high quality sub-daily data both for observations and model simulations. To address this need, we develop current and future precipitation intensity-duration-frequency (IDF) curves for Europe for 0.5-, 1-, 3-, 6-, 12- and 24-hour durations and for different return periods ranging between 1 and 100 years derived from a Generalized Pareto Distribution (GPD). Future IDF curves are developed in the framework of the quantile perturbation downscaling method by applying climate change signals from the EURO-CORDEX RCMs on current IDF curves obtained from high-resolution remote sensing based products. Here we show that rarer sub-daily extreme precipitation events will intensify more than less rare events and that changes may depend on precipitation duration. The frequency of sub-daily extreme precipitation events of 50- and 100-year return periods will be tripled under the high-end RCP8.5 scenario. Such intensification will lead to a substantial uplift (16-27% depending on duration and return period) and steepening (17-25% depending on return period) of the IDF curves under future climate change, calling attention to the vulnerability of the existing water infrastructure systems.

4.1 Introduction

Flash floods caused by short, intense rainstorms are amongst Earth's most common, costliest and destructive weather-related hazards, leading to loss of life or property and destruction of infrastructure (Gaume et al., 2009; Papagiannaki et al., 2015; Willner et al., 2018). They are more likely to happen in urban areas with fast runoff processes and short response times because of a greater prevalence of impermeable surfaces (Mishra et al., 2012). They, in turn, lead to cross-sectoral cascading infrastructure system failures because of extensive interdependencies in urban areas, threatening human health and local

economies (Wilbanks and Fernandez, 2014; Penny et al., 2018). The design of flood control structures and urban water infrastructure is typically based on the statistical properties of extreme precipitation in the form of intensity-duration-frequency (IDF) curves, which quantify the frequency of occurrence of a given precipitation intensity over a range of time scales or temporal durations (Hosseinzadehtalaei et al., 2017, 2018; Yan et al., 2018; Boukhelifa et al., 2018). The IDF curves also have important implications for other infrastructure vulnerable to heavy precipitation such as land-based transportation systems (e.g., streets and railways) (Kermanshah et al., 2017), electricity and telecommunication networks and those related to river floods and landslides (Nissen, and Ulbrich, 2017).

The IDF relationships and design criteria are usually developed for a single and specific location based on historical precipitation data. Raingauge data provide the most liquid accurate precipitation (rain) estimates and thereby the most accurate design criteria in rainfall-dominated areas and seasons. Nevertheless, raingauge measurements are affected by systematic errors such as underestimations due to wind-induced undercatch, which is much larger when precipitation turns into snow (Grossi et al., 2017), and to heating-related losses in tipping-bucket gauges for snowfall measurements (Savina et al., 2012). The availability of long, high quality gauge records is also restricted in some regions (Lumbroso et al., 2011; Vu et al., 2018; Libertino et al., 2019). Further, the spatial pattern of precipitation cannot be captured using a sparse gauging network (Courty et al., 2019). The scarcity of long-term precipitation records of high temporal resolution is another restriction for engineering practice and infrastructure design e.g., for flash flood events which are of a short duration of several minutes to a few hours (Berne et al., 2004). In fact, daily precipitation cannot capture the life cycle of single storms and masks the effect of more intense precipitation at sub-daily time scales (Singleton and Toumi, 2013).

Thanks to high spatial and temporal resolution remote sensing based precipitation products, we are now able to estimate the design storms in ungauged regions and to capture intergauge gradients, and to analyze the large-scale (regional, continental and global) spatial structure of extreme precipitation to explore different orographic and climatic drivers of such events (Sun et al.,

2018; Nguyen et al. 2019; Marra and Nikolopoulos, 2019). Caution should, however, be exercised when comparing raingauge and gridded data based IDF curves because of the scale mismatch between point gauge observations and grid-average estimates (Maraun, 2013; Tabari et al., 2016). Recent generations of remotely sensed datasets have been developed by merging satellite estimates with gauge and reanalysis data to provide global precipitation estimates that have uniform reliability both spatially and temporally (Beck et al., 2017, 2019). Accordingly, satellite based precipitation has more recently been utilized in a handful number of studies to develop IDF curves, but with a focus on current climate conditions, small regions and/or daily precipitation (Gado et al., 2017; Marra et al., 2017; Ombadi et al., 2018).

The lack of sub-daily precipitation is also an issue for future assessments of extreme precipitation as climate model data are very limited at sub-daily scales (Olsson et al., 2015). Hence, future changes in sub-daily extreme precipitation especially on larger spatial scales are less quantified. This is particularly important as the changes in sub-daily extreme precipitation under anthropogenic forcing can be greater than those in daily extremes (Hanel and Buishand, 2010; Molnar et al., 2015; Tabari et al., 2016; Miao et al., 2016; Hosseinzadehtalaei et al., 2019).

The expected and already experienced increase in the intensity and frequency of extreme precipitation under climate change (Wang et al., 2017, Tabari and Willems, 2018), as the most notable change among hydrological variables (Hegerl et al., 2015), calls for updating the current IDF curves under the different climate scenarios to plan and build more resilient, climate-proof systems (Wang et al., 2014; Sandink et al., 2016, So et al., 2017). They more specifically can be applied to quantify flood and overflow frequencies of urban drainage systems and storage facilities, and to design adaptation strategies. Although the urgency of integrating climate change impacts into infrastructure design through updating IDF curves has been recognized by local authorities and decision makers (Simonovic et al., 2017), practical development of the future IDF curves is complicated because of the aforementioned limitations.

In view of these limitations, in this study, 30 minutes 8 km precipitation outputs from the National Oceanic and Atmospheric Administration (NOAA)

Climate Prediction Center morphing (CMORPH) technique (Xie et al., 2017) and 3-hourly 12 km precipitation outputs from the Multi-Source Weighted-Ensemble Precipitation (MSWEP; 20) are used in conjunction with 3-hourly 12 km precipitation simulations from the EURO-CORDEX climate models to estimate current and future climate IDF curves for Europe. Precipitation intensities for different return periods ranging between 1 and 100 years are calculated by fitting a Generalized Pareto Distribution (GPD) to the partial duration series for different storm durations ranging between 0.5 and 24 hours. A Bayesian inference based Differential Evolution Markov Chain (DE-MC) approach is used for estimation of the GPD distribution parameters and associated uncertainties. The future IDF curves are derived by applying climate change signals on the current climate IDF curves in the framework of the quantile perturbation downscaling method.

4.2 Materials and Methods

The overall methodological framework adopted in this study contains three main parts: data preprocessing, extreme value analysis and IDF curve development (Figure 4.1).

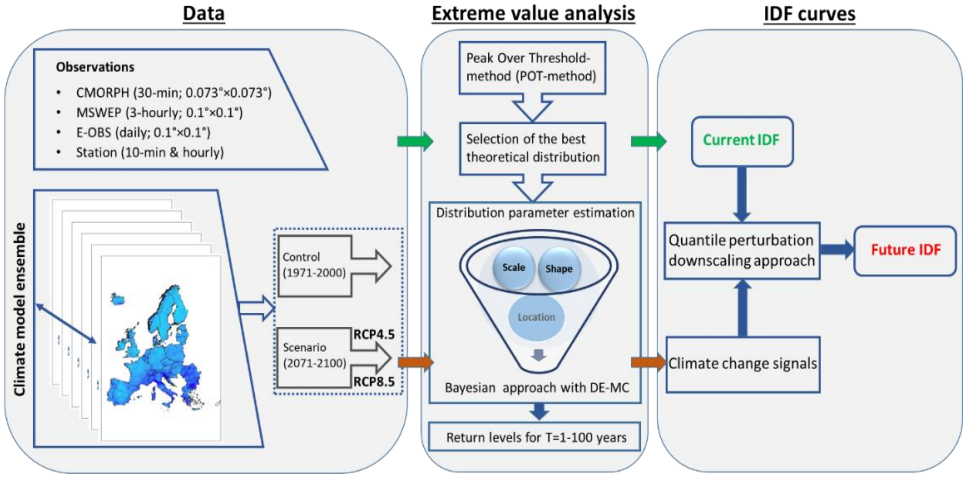


Figure 4.1: Methodological framework of the study (DE-MC: Differential Evolution Markov Chain; T: Return period).

4.2.1 Data

4.2.1.1 Observation datasets

Two high resolution datasets are used to develop current climate IDF curves and base the presentation of future curves after applying climate change impacts. The selected datasets are CMORPH and MSWEP. These datasets were selected based on their spatial resolution, temporal scale, quality (bias-corrected) and length. The CMORPH precipitation products with the highest spatial and temporal resolutions among satellite datasets (Wang et al., 2019) have been shown by numerous studies to have a comparable accuracy with ground station observations (Zeweldi and Gebremichael, 2009). The CMORPH dataset has been derived from low orbiter passive satellite microwave (PMW) observations which are propagated by motion vectors derived from geostationary satellite infrared data (Joyce et al., 2004). It has a quasi-global precipitation coverage (60° S - 60° N) from 1 January 1998 onwards with a high temporal resolution of 30 minutes and spatial resolution of 0.073°×0.073° (or 8 km at the equator). We make use of the newly product of this dataset for the period 1998-2017 (CMORPHv1.0., 2015), which is bias corrected based on daily precipitation at almost 30,000 gauges around the world (Xie et al., 2017). The new CMORPH product showed much improved estimates of precipitation compared to the original version concerning spurious trends and biases (Gehne et al., 2016). MSWEP dataset also has a high accuracy, with their best overall performance among 26 precipitation datasets evaluated against gauge data (Beck et al., 2019). It is a fully global precipitation dataset obtained from merging precipitation data from different sources of gauge, satellite and reanalysis (Beck et al., 2017). We use version 2.1 of this dataset with a 3-hourly temporal resolution and 0.1° (~12 km) spatial resolution for the period 1979-2016.

In addition to the CMORPH and MSWEP datasets, daily precipitation data from the E-OBS v20.0e dataset with 0.1° (~12 km) spatial resolution for the period from 1950-01-01 to 2019-07-31 are used to quantify the bias in estimation of high quantiles with short records. The unique, high-quality 10-min precipitation data recorded with the same instrument for the period 1901-2000 at Uccle near Brussels and hourly precipitation data for the period 1951-2020 at

De Bilt, De Kooy, Eelde, Flushing and Volkel stations in The Netherlands are used to scrutinize the bias in the estimation of the high quantiles with short records, to evaluate the performance of the quantile perturbation downscaling method and to assess the calibration of the extreme value distributions.

4.2.1.2 Climate model simulations

For developing future IDF curves, climate change signals are calculated using the Coordinated Downscaling Experiment over Europe (EURO-CORDEX; Jacob et al., 2014). Climate simulations of the EURO-CORDEX regional climate models (RCMs) have been produced by a dynamically downscaling of the global climate model (GCM) simulations from the fifth phase of the Coupled Model Intercomparison Project (CMIP5; Taylor et al., 2012). The downscaled EURO-CORDEX climate simulations have spatial resolutions of 0.44° (50 km) and 0.11° (12.5 km) and temporal resolutions of daily and 3-hourly. It is expected that the higher resolution of the RCMs improves the representation of meso-scale processes associated with the formation of extreme precipitation as well as orographic features. As higher resolution precipitation is more relevant for urban hydrology climate impact studies, we use the finest resolutions of the EURO-CORDEX RCMs: 3-hourly temporal resolution and 0.11° spatial resolution. These high resolution simulations for the EURO-CORDEX domain are only available for the RCA4 RCM developed at the Swedish Meteorological and Hydrological Institute (SMHI; Strandberg et al., 2014). The model has downscaled five CMIP5 GCMs: CNRM-CM5, EC-EARTH, IPSL-CM5A-MR, HadGEM2-ES and MPI-ESM-LR. The period 1971-2000 is considered as the reference period, and climate change signals are evaluated for medium (2041-2070) and far (2071–2100) future periods with respect to the reference period under two Representative Concentration Pathways (RCPs; Moss et al., 2010) of RCP4.5 and RCP8.5. RCP8.5 corresponds to a pathway with the highest emission level or business-as-usual scenario in which radiative forcing reaches 8.5 W/m2 at the end of the century (Riahi et al., 2011), while RCP4.5 is a stabilization scenario that stabilizes radiative forcing at 4.5 W/m2 (Thomson et al., 2011).

4.2.2 Extreme value analysis

Two main sampling methods for extreme value analysis are annual maxima and peak-over-threshold (POT) (also called partial duration series). The POT method provides a larger extreme precipitation data sample for a more accurate estimation of distribution parameters (Yilmaz et al., 2017; Marra and Nikolopoulos, 2019). The POT analysis also allows for a more rational selection of extreme events instead of considering only one event per year in the annual maxima method (Lang et al., 1999) as the second or even higher order extremes in some years can be larger than the annual extremes in other years (Pasarić and Cindrić, 2019). The threshold method also works quite well when the tails of distributions are asymmetric (McNeil and Frey, 2000). Despite the aforementioned advantages of the POT method, most of the previous studies have applied the annual maxima method (Pombo and de Oliveira, 2015; Ombadi et al., 2018; Faridzad et al., 2018). The results are hereafter shown using the POT framework. However, to characterize the extreme value distribution uncertainty, precipitation extremes are also analyzed using the annual maxima method based on the GEV.

For the POT selection, the extreme value threshold and inter-event time are the main criteria (Willems, 2009). The threshold for extreme precipitation values is chosen high enough equal to the 98th percentile of all days to include only extreme values more relevant for pluvial flooding and to ensure reliable tail asymptotics underlying the distribution approximation and whereby reducing the related bias (Scarrott and MacDonald, 2012). The percentile of all daily precipitation values rather than wet days is chosen to avoid the effects of varying number of wet days in Europe on the percentile level (Fisher and Knutti, 2015). Higher thresholds reduce the sample size of extremes, thus increasing the variance of the parameter estimates (Scarrott and MacDonald, 2012). The inter-event time defines dependency of subsequent extreme events (i.e., serial correlation in the time series) which results from the duration of mesoscale rainstorm events (Willems et al., 2007). To ensure that the extremes are taken from independent events, the maximum sub-daily precipitation per day is considered.

To find the best distribution to POT series, we fit 16 distributions (Birnbaum-Saunders, Exponential, Extreme Value, Gamma, Generalized Extreme Value, Generalized Pareto, Inverse Gaussian, Logistic, Log-logistic, Log-normal, Nakagami, Normal, Rayleigh, Rician, t location-scale and Weibull) to over three million POT series examined in this study. The distribution with the lowest Bayesian information criterion (BIC) is chosen as the best fitted distribution. The results indicate that the POT series in all the datasets (CMORPH, MSWEP and EURO-CORDEX) can be approximated most accurately with a Generalized Pareto Distribution (GPD) (Figure 4.2a). This is in agreement with previous studies (Katz et al., 2002; Renard et al., 2006; Lazoglou et al., 2019). The percentage of the POT series with GPD as the best fitting distribution ranges between 94.7 for the RCM simulations under RCP8.5 to 99.9 for the historical RCM simulations. Figure 4.2b shows that the spatial distribution of the BIC of the best fitted model has a south-north bipolar pattern with a better fit for the southern Europe. Based on these results, we use the GPD for the POT series.

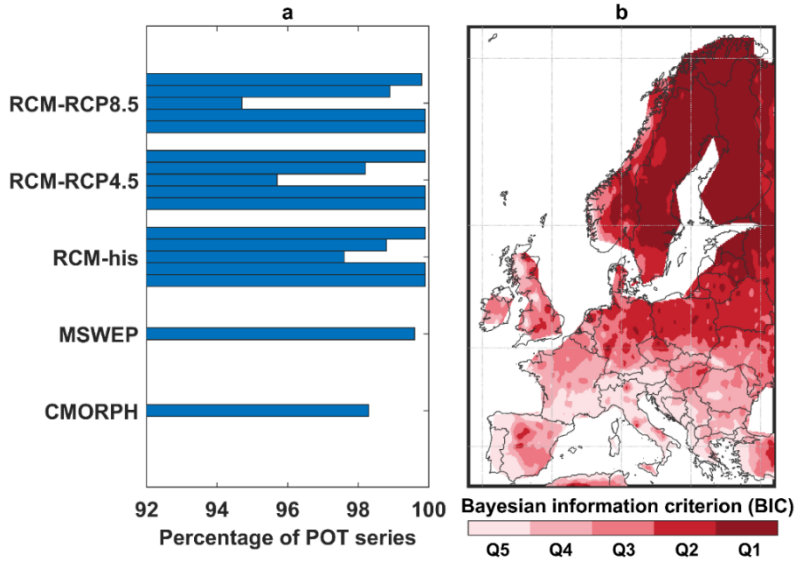


Figure 4.2: (a) Percentage of the POT series of different datasets with GPD as the best fitting distribution and (b) the spatial distribution of Bayesian information criterion (BIC) of the best fitted model. In panel a, clustered bar plots represent the results for five RCM runs. In panel b, the BIC values are normalized over the location parameters of the corresponding grid cells and Q1, Q2, Q3, Q4 and Q5 denote the first, second, third, fourth and fifth quintiles of the BIC values, respectively.

The standard cumulative distribution function of the GPD is defined by:

$$f_{(\zeta,\mu,\sigma)}(x)=\begin{cases}1-\left(1+\dfrac{\zeta(x-\mu)}{\sigma}\right)^{\frac{-1}{\zeta}} & for \quad \zeta\neq 0\\ 1-\exp\left(-\dfrac{x-\mu}{\sigma}\right) & for \quad \zeta=0\end{cases} \tag{4.1}$$

The GPD distribution is characterized by three parameters including location (μ), scale (σ) and shape (ζ) of the distribution, describing the center of distribution, the deviation around the mean and the tail behavior of the distribution, respectively (Embrechts et al., 1997). According to the shape parameter, three extreme distributions are defined as Pareto, Exponential and Beta corresponding to ζ>0, ζ=0 and ζ <0, respectively. The return level x_p (i.e., the value that is expected to be exceeded once every T years on average) associated with the return period 1/p for the chosen threshold u is given by:

$$x_p=\begin{cases}u+\left[\dfrac{\sigma}{\zeta}\left(\dfrac{1}{p}\zeta_u\right)-1\right] & for \quad \zeta\neq 0\\ u+\sigma\log\left(\dfrac{1}{p}\zeta_u\right) & for \quad \zeta=0\end{cases} \tag{4.2}$$

The parameters of the selected distribution are estimated classically by various parametric (e.g., Probability Weighted Moment, Maximum Likelihood and Two-Step and Three-Step estimators) and semi-parametric (e.g., Moment, Hill and Pickands estimators) methods (AghaKouchak, and Nasrollahi, 2010). However, these classical methods do not take into account the uncertainty associated with the point estimate of parameters (Rupa et al., 2015). Bayesian method has the capability to reasonably address the uncertainties in the estimation of parameters (Mélèse et al., 2018). Another advantage of the Bayesian method is its feasibility in non-regular likelihood cases (e.g., short tail of the parent population from which the data is drawn) (Rupa et al., 2015). Let us consider $X=\{x_1,x_2,\ldots,x_n\}$ as the set of n POT values extracted from the precipitation time series and as the parameter of a given distribution. Following

the Bayes theorem, the posterior distributions are estimated based on knowledge of the prior distribution and the observation vector as (Renard et al., 2006):

$$p\left(\theta|X\right) \propto \prod_{i=1}^{n} p\left(\theta\right).p\left(x_i|\theta\right) \tag{4.3}$$

In our case, θ is a vector containing the GPD distribution parameters:

$$p\left(\mu,\sigma,\zeta|X\right) \propto \prod_{i=1}^{n} p\left(\mu\right).p(\sigma).p(\zeta).p\left(x_i|\mu,\sigma,\zeta\right) \tag{4.4}$$

The default priors (prior knowledge of analysts about parameters) are non-informative normal distributions for the location and scale parameters, and a normal distribution with a standard deviation of 0.3 for the shape parameter as suggested in Renard et al. (2006) and Cheng et al. (2014). The Differential Evolution Markov Chain (DE-MC) with a Metropolis–Hastings sampler (Haario et al., 1999, 2001) is then applied to sample a large number of realizations (in our case, 5000 iterations including 2000 burn-in iterations) from the GPD parameters' posterior distributions. In fact, the DE is used for a global optimization over the parameter space with the Markov Chain Monte Carlo (MCMC) approach, by proposing candidate values for the posterior distribution (Ter Braak, 2006; Vrugt et al., 2009). The DE-MC with a higher convergence speed is faster than the conventional MCMC (Ter Braak, 2006). To assess convergence of the sampling approach, we use the $\hat{R}$ criterion (Gelman and Shirley, 2011) with the upper limit of 1.1 (Cheng et al., 2014, Ragno et al., 2018). Merging Bayesian inference with DE-MC allows the derivation of the confidence interval and uncertainty bounds of estimated extreme precipitation intensities for IDF curves based on the sampled parameters. To assess the influence of the distribution parameter estimation method, the parameters are also estimated using the maximum likelihood method.

4.2.3 Development of IDF curves

We analyze sub-daily precipitation data for a whole year from the observations and the control and scenario simulations of the RCMs to obtain the POT time series for individual native grid cells of each dataset in the European domain. We then aggregate 0.5-hr precipitation for each grid cell into accumulations of non-overlapping 1-, 3-, 6-, 12-, and 24-hr periods, and the GPD is fitted to the

POT precipitation values for the selected storm durations. The duration of precipitation events for the MSWEP dataset and the RCMs simulations is constrained to the range of 3-24 hours as their finest time resolution is 3-hourly. Different precipitation intensities are estimated for different return periods (T) from 1 to 100 years, while the results for the selected T of 2, 10, 50 and 100 years and the respected durations for each dataset are used for plotting the IDF curves. In addition to the BIC statistical measure, the goodness-of-fit of the GPD model and the current climate IDF curves are visually assessed by comparing the probability distribution function of the observed and theoretical GPD based POT values. We consider GPD simulations reliable when the envelope (90% confidence interval) of the DE-MC simulations encompasses all of the empirical return levels, with a closer median of the simulated ensemble to the empirical values as a better goodness-of-fit.

Once the GPD is fitted to the observed and modeled extreme precipitation, future IDF curves are developed using the quantile perturbation downscaling method (Willems, 2013). Numerous hydrological impact studies of climate change have found this method superior to simpler methods that correct the bias only in mean or mean and variance of precipitation series (Gudmundsson et al., 2012; Teutschbein and Seibert, 2012; Chen et al., 2013). Applying the corrections per quantile (in our case, return periods ranging between 1 and 100 years) maintains distinct bias of climate models for different quantiles. The quantile perturbation method necessitates regridding the observations and RCM grid sizes to a common rectangular grid. The regridding is performed using the bilinear interpolation method. Afterwards, quantile-specific bias correction factors are calculated for each duration and individual grid cell over Europe. By assuming that the systematic bias of climate models to be corrected is temporally stationary, the bias correction factors derived from historical simulations for each grid cell are applied on future simulations of the same cell (Cannon et al., 2015). The assumption ensures that the changes in quantiles are unaffected by the bias correction. This process is performed for each climate model run and RCP separately, thus preserving the sensitivity of the models to external forcings and allowing a climate model uncertainty quantification. The bias-corrected quantiles in the future simulations are used to develop future IDF curves. Due

to the unavailability of 0.5- and 1-hr precipitation results in the EURO-CORDEX simulations, 3-hourly RCM simulations are bias corrected based on 0.5- and 1-hr CMORPH quantiles to derive future quantiles for the respected durations. In this way, the bias correction factors involve both the systematic bias of the climate model results and the temporal disaggregation ratio. The latter can also be seen as temporal statistical downscaling. The temporal disaggregation ratio for 30-min (hourly) duration is obtained at each model grid over Europe by comparing 3-hourly and 30-min (hourly) precipitation quantiles from gridded observations for the same return period.

To validate the downscaling results, the 3-hourly historical EURO-CORDEX simulations for the period 1971-2000 are downscaled based on hourly observations at some stations with long-term records for the same period using the quantile perturbation method. Afterwards, the bias correction factors are applied on the RCP8.5 simulations for the same quantiles and at respected station's location for the period 2006-2019.

In the investigation of the future changes in the form of IDF curves, the changes in the intensity of extreme precipitation are translated into the changes in the ordinate of the curves (either upward or downward shift). For the changes in the slope of IDF curves, the ratios of the slope of extreme precipitation with durations between the current and future climates for individual grid cells are calculated for different return periods between 1 and 100 years.

We also assess the uncertainty in projected extreme precipitation changes for different durations and return periods. The changes in extreme precipitation are computed as the ratio of the values for the future period 2041-2070 or 2071–2100 over those for the historical period 1971-2000. The total uncertainty includes the uncertainties associated with the choice of climate models (five EURO-CORDEX RCM members), emission scenarios (RCP4.5 & RCP8.5), extreme value distributions (GPD & GEV) and distribution parameter estimation methods (DE-MC & maximum likelihood). To quantify the uncertainty propagated due to emission scenarios (hereafter scenario uncertainty), we estimate the variability across RCPs, here characterized by the standard deviation, after taking the median of the changes derived from different climate model runs, extreme value distributions and distribution parameter

estimation methods. A similar procedure is adopted to quantify the uncertainties related to climate model runs (hereafter model uncertainty), extreme value distributions (hereafter distribution uncertainty) and distribution parameter estimation methods (hereafter parameter uncertainty). The fractional uncertainty is finally calculated as a ratio of the uncertainty of each source to the total uncertainty which is the sum of the variations due to all the four uncertainty sources.

4.2.4 High quantile estimation bias from short records

The larger the extrapolation beyond the record length, the less reliable is the return level. A common rule of thumb in conventional at-site quantile estimates is to restrict extrapolation to return periods of up to twice the record length (Kidson and Richards, 2005). However, for making an estimate of a 100-year event, we extrapolate quantiles larger than twice as long as the record length. In order to quantify the bias in estimation of high quantiles from short records (i.e., extrapolated quantiles) using the GPD, the estimated quantiles from short and long records are compared for individual grid cells. To this end, an extrapolation ratio is first defined as the ratio of return periods (T) to the record length (L). Because the CMORPH dataset has the shortest record among the considered datasets in this study, a 20-year length is used as the denominator of the extrapolation ratio for all datasets. The bias in high quantiles is then calculated by dividing the quantiles estimated from the full time series for specific return periods over those from a 20-year sub-series for the same return periods. For each dataset, the upper limit of return periods is equal to the length of the full time series to avoid extrapolation bias in the long record which is used as the benchmark. For example for the E-OBS data, the quantiles estimated from the full E-OBS data with a 70-year length (1950-2019) for the return periods between 20 and 70 years are divided over those from a sub-series of the E-OBS data with a 20-year length (2000-2019) for the same return periods. Afterwards, the bias is plotted against the extrapolation ratios which range between 1 and 3.5 for the E-OBS dataset (T/L when L=20 and T=20, 21, 22,…, 70) (see Figure 4.18a). Similar analyses are performed using 3-hourly MSWEP and 30-min Uccle raingauge data. In the former, the bias is obtained by comparing the

quantiles between 38 (1979-2016) and 20 (1997-2016) year data and in the latter between 100 (1908-2007) and 20 (1988-2007) year data. The extrapolation ratios range between 1 and 1.9 for MSWEP dataset (L=20 and T=20, 21, 22,…, 38) and between 1 and 5 for Uccle raingauge data (L=20 and T=20, 21, 22,…, 100). We also analyze the bias in terms of the shape parameter of the GPD, by comparing the parameter value between short and long records.

4.3 Results and discussion

4.3.1 Changes in the probability distribution of short-duration extreme precipitation

The distribution parameters for different storm durations derived from CMORPH and MSWEP datasets are shown in Figure 4.3. The location parameters (representing the mean of the distribution) from CMORPH are larger than the ones from MSWEP, and the difference gets smaller with increasing rainstorm durations (Figure 4.3a). A larger location parameter from CMORPH means higher extreme value estimates from this dataset. Spatially, the location parameter has larger variations over Europe for longer duration intensities, that are more pronounced in MSWEP (Table 4.1). This is because the spatial patterns in the longer duration intensities become more visible due to the lower uncertainties (less random scatter spatially) compared to the shorter duration intensities. The climate change impact assessment using the high-resolution EURO-CORDEX RCM projections indicates that the location parameter will increase all over Europe (> 97% of the area) by a continental average change of 10% and 17% for RCP4.5 and RCP8.5, respectively (Figures 4.4 and 4.5). The projected changes go up to 32% and 48% in some areas for RCP4.5 and RCP8.5, respectively. Furthermore, the changes in the location parameter are roughly independent of the duration (Figure 4.3b).

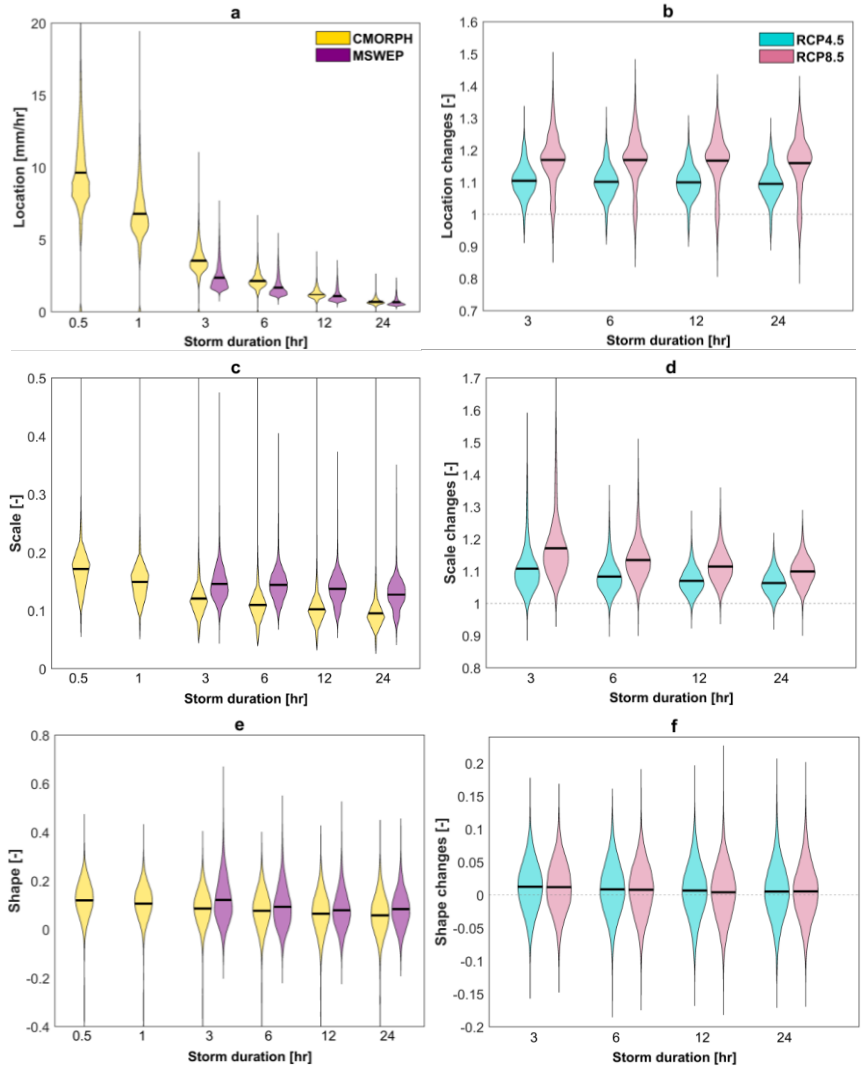


Figure 4.3: Violin plots comparing the median, the spread, and the density of (a, c, e) the GPD parameters around corresponding durations derived from the CMORPH and MSWEP datasets and (b, d, f) the changes in the GPD parameters for 3-hourly extreme precipitation between RCP4.5 and RCP8.5 for different durations using the median of the EURO-CORDEX RCM simulations (a, b: location; c, d: scale; e, f: shape). The median is shown by the thick horizontal line on the violin plots and the maximum and minimum values are represented as the top and bottom of the plots, respectively. Note that the wider the violin plot, the higher the density. The scale parameters for the current climate are normalized over the corresponding location parameters. Note that the absolute changes are calculated for the shape parameter owing to the existence of negative shape parameter values.

Table 4.1: Spatial coefficient of variation (CV) of the GPD parameters over Europe for observed extreme precipitation events of different durations derived from the CMORPH and MSWEP datasets.

Distribution parameter	Dataset	Storm duration (hr)					
		0.5	1	3	6	12	24
Location	CMORPH	0.28	0.27	0.27	0.28	0.29	0.30
	MSWEP	-	-	0.35	0.35	0.37	0.38
Scale	CMORPH	0.16	0.13	0.11	0.10	0.10	0.10
	MSWEP	-	-	0.34	0.24	0.20	0.18
Shape	CMORPH	0.77	0.82	1.02	1.20	1.46	1.61
	MSWEP	-	-	0.77	0.93	0.99	0.91

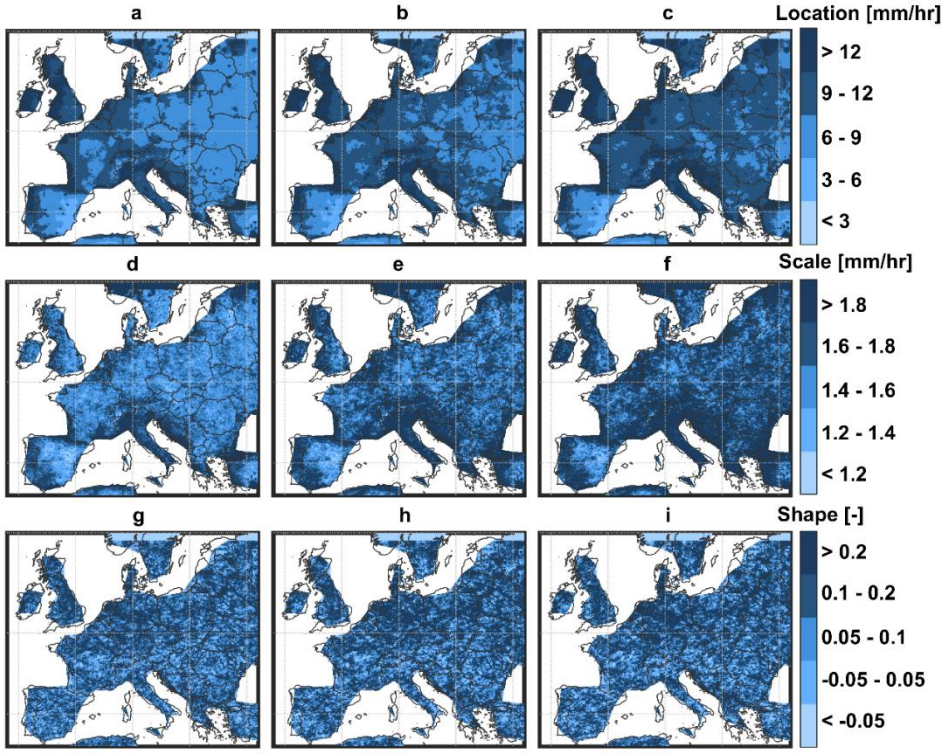


Figure 4.4: Spatial distribution of the GPD parameters (location: a, b, c; scale: d, e, f; shape: g, h, i) for (a, d, g) historical (1998-2017) and (b, c, e, f, h, i) future (2071-2100) extreme precipitation events of 30-min duration under (b, e, h) RCP4.5 and (c, f, i) RCP8.5 over Europe derived from the CMORPH dataset. The future parameter values are obtained by applying climate change signals on historical parameter values in the framework of the quantile perturbation downscaling method. The climate change signals are computed for the period 2071–2100 with respect to the reference 1971-2000.

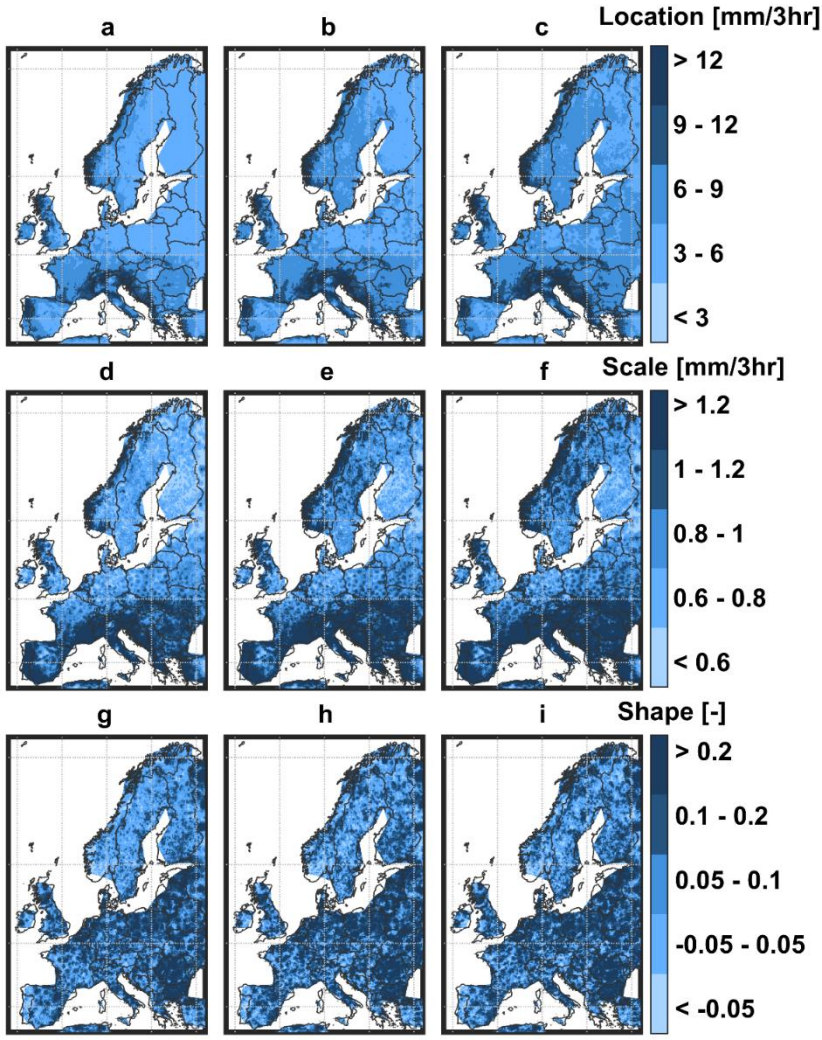


Figure 4.5: Spatial distribution of the GPD parameters (location: a, b, c; scale: d, e, f; shape: g, h, i) for (a, d, g) historical (1979-2016) and (b, c, e, f, h, i) future (2071-2100) extreme precipitation events of 3-hr duration under (b, e, h) RCP4.5 and (c, f, i) RCP8.5 over Europe derived from the MSWEP dataset. The future parameter values are obtained by applying climate change signals on historical parameter values in the framework of the quantile perturbation downscaling method. The climate change signals are computed for the period 2071–2100 with respect to the reference 1971-2000.

In contrast to the location parameter, the scale parameter (representing the dispersion of the distribution) is smaller in CMORPH compared to MSWEP (Figure 4.3c), with the spatial median values ranging between 0.12 and 0.09 for

3-hr to 24-hr durations for the former and around 0.14 for the latter. The scale parameter decreases with storm duration in both datasets, particularly in CMORPH from 0.17 to 0.09 (Figure 4.3c). Similarly, its spatial variation also decreases with duration (Table 4.1). The spatial variation patterns of the location and scale parameters over Europe show some similarities (Figures 4.4 and 4.5), pointing to a larger variability for higher extreme values over Europe. The scale parameter is expected to increase under climate change in 98% of the European area at a higher rate compared to the location parameter, accounting for continental averaged increases of 11% and 17% for RCP4.5 and RCP8.5, respectively (Figures 4.4 and 4.5). The signals of relative increase in the scale parameter reach 57% and 79% in some locations for RCP4.5 and RCP8.5, respectively. The projected increase in the scale parameter means that climate change will widen the distribution of extreme precipitation, indicating an amplified variability of extreme precipitation in the warmer world. An increase in mean daily precipitation variability has been shown before for a majority of global land area in response to warming (Pendergrass et al., 2017; Kharin et al., 2018; He and Li, 2019). The larger spread of the distribution is caused by the larger magnitudes of change in extreme precipitation for higher intensities/return periods (see the results in the next section). The future changes in the scale parameter slightly decrease with increasing storm duration, accounting for 13% (9%) and 5% (3%) differences in the spatial 90th and 50th percentiles of changes between 3-hourly and daily intensities for RCP8.5 (RCP4.5) (Figure 4.3d).

The median shape parameter over Europe for all storm durations and for both datasets is positive with values ranging between 0.06 and 0.13 for different durations, suggesting a heavy tailed distribution for extreme precipitation over Europe (Figure 4.3e). The positive shape parameter is observed over 94% of the European area for 0.5-hr extreme precipitation, and is within the range of 78-92% for multi-hourly extreme precipitation (Figures 4.4 and 4.5). Similar to the location parameter, but with a much lesser extent, the shape parameter in both datasets decreases when moving from short to long durations (Figure 4.3e), implying that the tail of the distribution becomes less heavy for longer duration intensities. A positive shape parameter was also previously reported for daily

gauge extreme precipitation based on the generalized extreme value (GEV) distribution (Koutsoyiannis, 2004; Ragulina and Reitan, 2017), with a global average of 0.093 (Papalexiou and Koutsoyiannis, 2013). The median shape parameters from the continental analysis for CMORPH are 0.13, 0.11, 0.09, 0.08, 0.07 and 0.06 for 0.5-, 1-, 3-, 6-, 12-, 24-hr storm durations, respectively. The MSWEP shape parameters tend to be larger for the corresponding durations (Figure 4.3e). Comparing the spatial variation of the shape parameter between the two datasets shows higher values for CMORPH (Figures 4.4 and 4.5). The spatial variation of the shape parameter is the highest among the GPD parameters for all durations and both datasets (Table 4.1). Projections from the EURO-CORDEX RCM show an increase in the shape parameter, but not as widespread as that in the location and scale parameters (Figure 4.3f). The increase is indeed projected for 61-63% of the continental area (Figures 4.4 and 4.5), making the tail of the distribution heavier for short-duration extreme precipitation in the future. Similar to the location parameter, the changes in the shape parameter are shown to be independent of the storm duration (Figure 4.3f).

4.3.2 Changes in the intensity and frequency of short-duration extreme precipitation

The climate change projections show that 3-hr extreme precipitation will increase for all return periods under both RCP4.5 and RCP8.5 (Figure 4.6a,b). The longer the return period and the shorter the duration, the larger is the change (Figure 4.6a,b). The dependency of the changes on the return period is more pronounced compared to the duration. In agreement with previous studies (Kharin et al., 2018; Cannon and Innocenti, 2019), the results suggest that rarer extreme precipitation events will intensify more than less rare events and that changes may depend on event duration. A greater intensification of rarer extremes is attributed to the increase in the dispersion of the GPD distribution shown in Figure 4.3d. The median of the expected changes over Europe for RCP8.5 (RCP4.5) ranges between 20% (12%) and 27% (20%) depending on the return period. In some areas, the intensity of 100-year short-duration

precipitation will be about doubled at the end of the 21st century, with increases of 95% and 122% for RCP4.5 and RCP8.5, respectively (Figure 4.7 and 4.8)

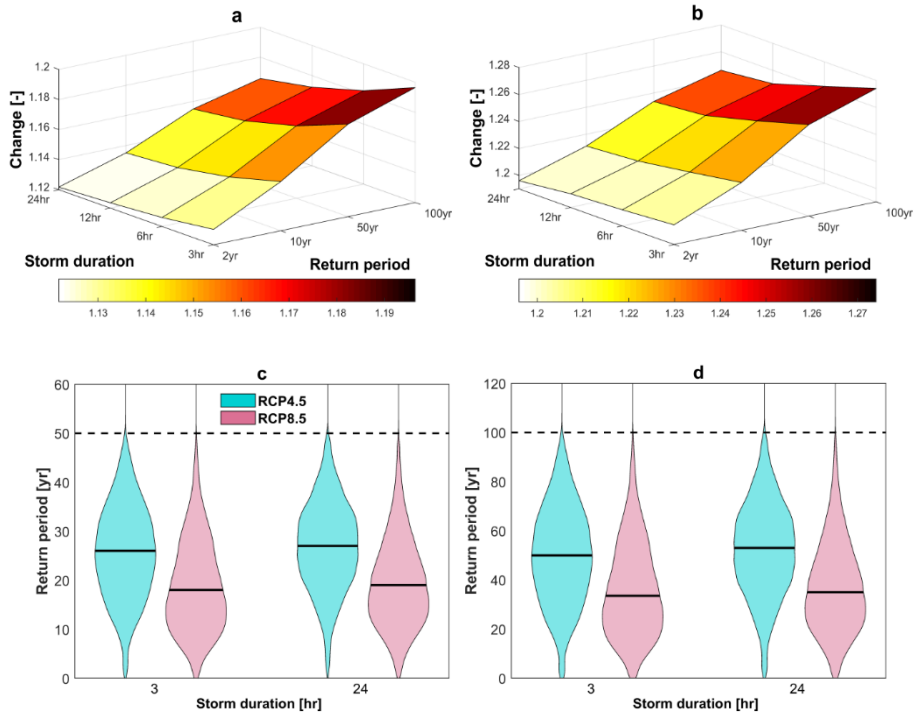


Figure 4.6: (a, b) Spatial median of the extreme precipitation changes derived from the median of the EURO-CORDEX RCM simulations as a function of storm durations and return periods for (a) RCP4.5 and (b) RCP8.5, and (c, d) violin plots showing the median, the spread, and the density of return periods under future climatic conditions of extreme daily and 3-hourly precipitation events historically associated with return periods of (c) 50 and (d) 100 years for individual grid cells. The median is shown by the thick horizontal line on the violin plots and the maximum and minimum values are represented as the top and bottom of the plots, respectively. Note that the wider the violin plot, the higher the density. The changes are computed for the period 2071–2100 with respect to the reference 1971-2000.

The expected values of 3- and 24-hr extreme precipitation intensities of 50- and 100-year return periods are shown in Figure 4.6c,d. The frequency of such events medianed over the continent will be roughly doubled in the future under RCP4.5 and tripled under RCP8.5. In fact, 3-hr (daily) extreme events expected to occur every 50 years would occur every 25 (27) and 18 (19) years for RCP4.5 and RCP8.5, respectively. Similarly, 3-hr (daily) 100-year precipitation would

occur more frequently every 50 (53) and 33 (35) years in the future under RCP4.5 and RCP8.5, respectively. The overall conclusion is that short-duration extreme precipitation will be intensified at a greater rate compared to long-duration storms, thus supporting the results of the previous studies regarding a super Clausius–Clapeyron (CC) scaling of sub-daily extreme precipitation with warming (e.g., Mishra et al., 2012).

The spatial distribution of the changes shows that the 3-hourly extreme precipitation increases over almost the entire domain, while the increase is generally larger for the eastern half (longitudes > ≃5°) (Figure 4.7 and 4.8). The changes in daily extreme precipitation follow a similar spatial pattern, but with a smaller magnitude which turns into a decreasing signal for 2-year extremes over the southern part of Europe.

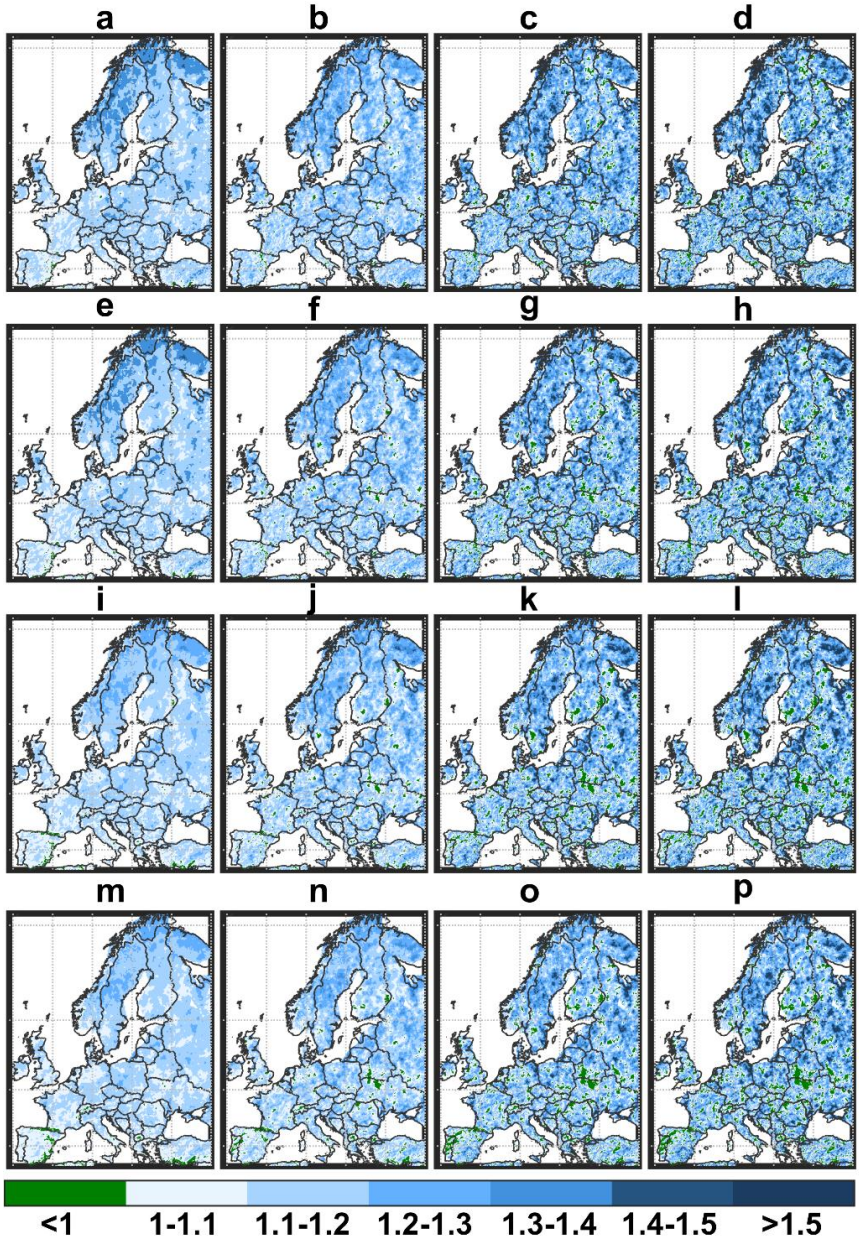


Figure 4.7: Spatial distribution of the changes in extreme precipitation of (a, b, c, d) 3-, (e, f, g, h) 6-, (i, j, k, l) 12- and (m, n, o, p) 24-hr durations and (a, e, i, m) 2-, (b, f, j, n) 10-, (c, g, k, o) 50- and (d, h, l, p) 100-year return periods derived from the ensemble median of the EURO-CORDEX RCM runs under RCP4.5. The climate change signals are computed based on GPD with its parameters estimated by the DE-MC method for the period 2071–2100 with respect to the reference 1971-2000.

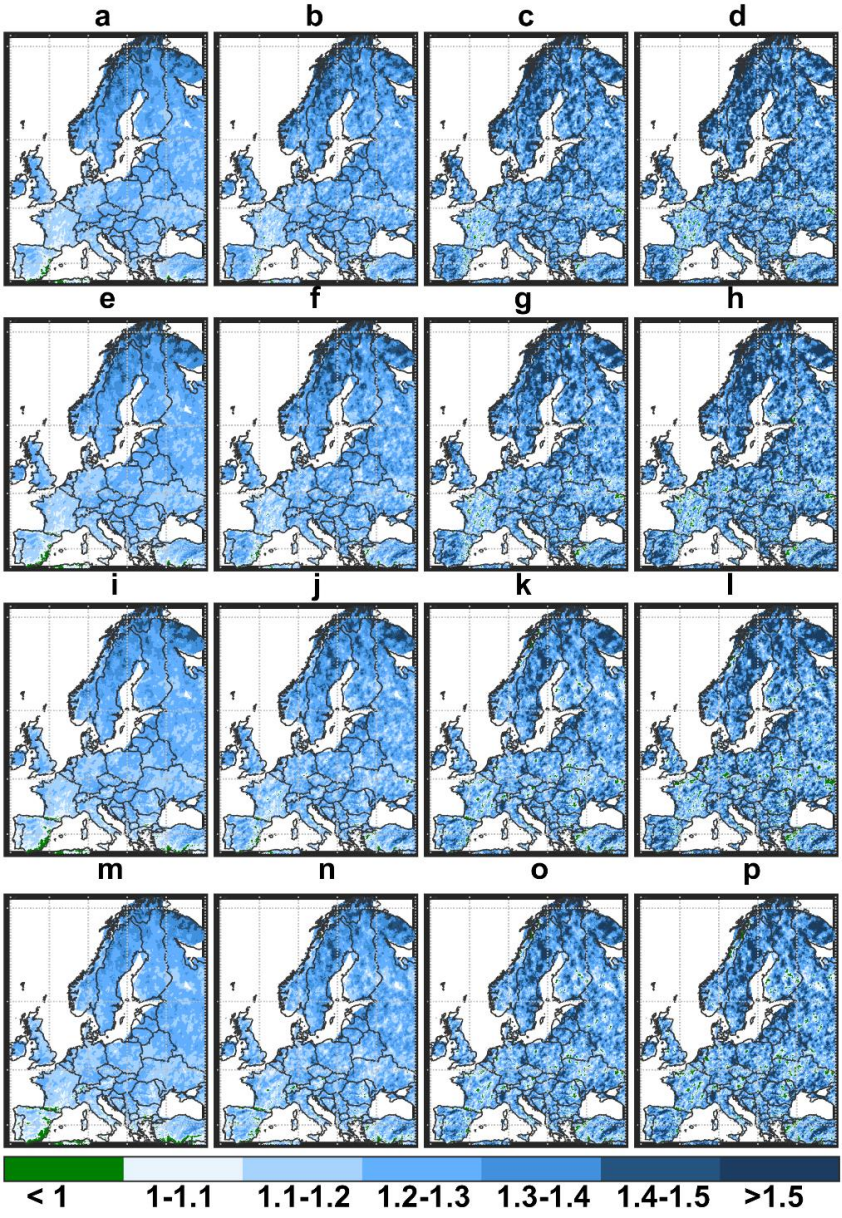


Figure 4.8: As Figure 4.7 but for RCP8.5.

The extreme precipitation changes for the medium future period (2041-2070) are also increasing for all return periods and durations (Figure 4.9). As expected, the amount of changes is smaller for the medium future period compared to the

far future (2071-2100) period; however, the spatial distribution of the changes is similar (not shown). The change difference between the two future horizons is larger for RCP8.5 in comparison to RCP4.5 (Figure 4.9). For RCP4.5, the changes for the far future period are about 37-65% larger than those for the medium future period, depending on duration and return period, while it increases to 54-74% for RCP8.5. The model uncertainty also increases with lead time, being larger for the far future period (Figure 4.9).

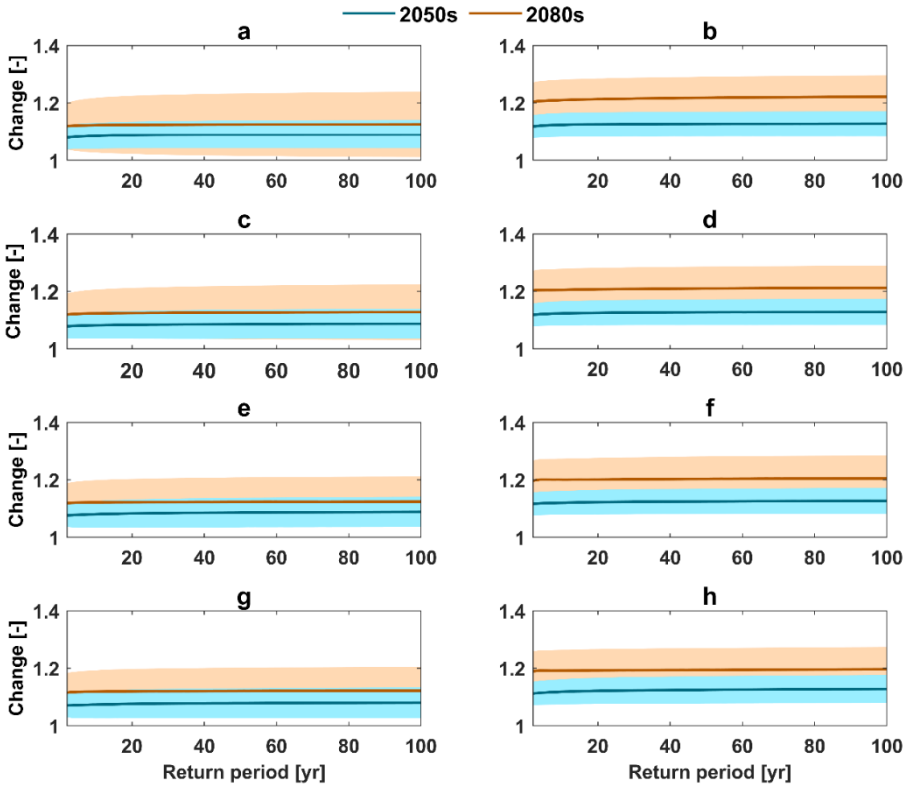


Figure 4.9: Comparison of the spatial median of the extreme precipitation changes between medium (2050s) and far (2080s) future periods as a function of return periods for (a, b) 3-, (c, d) 6-, (e, f) 12- and (g, h) 24-hr storm durations under (a, c, e, g) RCP4.5 and (b, d, f, h) RCP8.5. Lines and uncertainty bands represent ensemble median and ± 2 EURO-CORDEX RCM ensemble standard deviation, respectively. The climate change signals are computed based on GPD with its parameters estimated by the maximum likelihood method for the period 2041–2070 or 2071–2100 with respect to the reference 1971-2000.

The sensitivity of the climate change signals to the method for extreme value analysis (annual maxima vs. POT) and the related extreme value distribution selected (GEV vs. GPD) is also investigated; see the signals computed based on the GEV in Figure 4.10. The results show a good consistency between the extreme precipitation changes derived from GEV and GPD, although the changes by GEV are slightly larger for RCP8.5 (Figure 4.10).

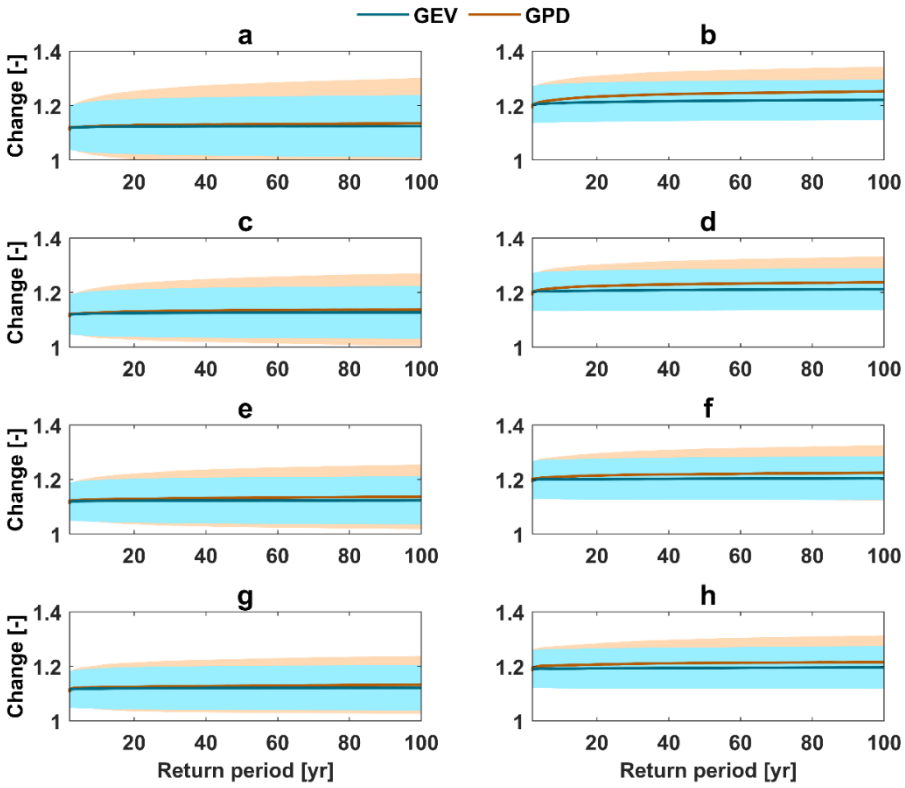


Figure 4.10: Comparison of the spatial median of the GPD and GEV derived extreme precipitation changes as a function of return periods for (a, b) 3-, (c, d) 6-, (e, f) 12- and (g, h) 24-hr storm durations under (a, c, e, g) RCP4.5 and (b, d, f, h) RCP8.5. Lines and uncertainty bands represent ensemble median and ± 2 EURO-CORDEX RCM ensemble standard deviation, respectively. The climate change signals are computed for the period 2071–2100 with respect to the reference 1971-2000. The parameters are estimated by the maximum likelihood method.

4.3.3 Towards building future climate-proof infrastructure

To reduce the failure risk of infrastructure and design a reliable and durable construction, they should be resilient to future climate change. To build such a future climate-proof infrastructure, the design storms estimated from the IDF curves should be revised to adapt the infrastructure to a changing climate through implementing adaptation actions. As the failure of different types of infrastructure occurs at different precipitation thresholds and even for each type there is no universal critical value over Europe (Nissen, and Ulbrich, 2017), the expected changes in common return periods for infrastructure design (i.e., rainstorms of 2-, 10-, 50- and 100-year return periods) are analyzed.

Future extreme precipitation values are obtained by applying climate change signals on historical extreme precipitation in the framework of the quantile perturbation downscaling method. Our results indicate that the quantile perturbation method performs well in correcting the bias in future quantiles from model simulations (Figure 4.11). The future short-duration precipitation maps for different return periods are presented in Figures 4.12 and 4.13, from which the failure risk of different infrastructure types with different thresholds for all areas within Europe can be obtained (e.g., between 10- and 20-year return periods for urban drainage systems (Willems et al., 2012) or 10-year return period for the International Union for Railways (UIC, 2008). For example, the spatial 95th and 50th percentiles of 0.5-hr 100-year precipitation depth over the continent under present-day climate conditions are ≃99 and ≃66 mm/hr that will increase to ≃127 and ≃82 mm/hr by the end of the century for RCP8.5 scenario (Figure 4.12).

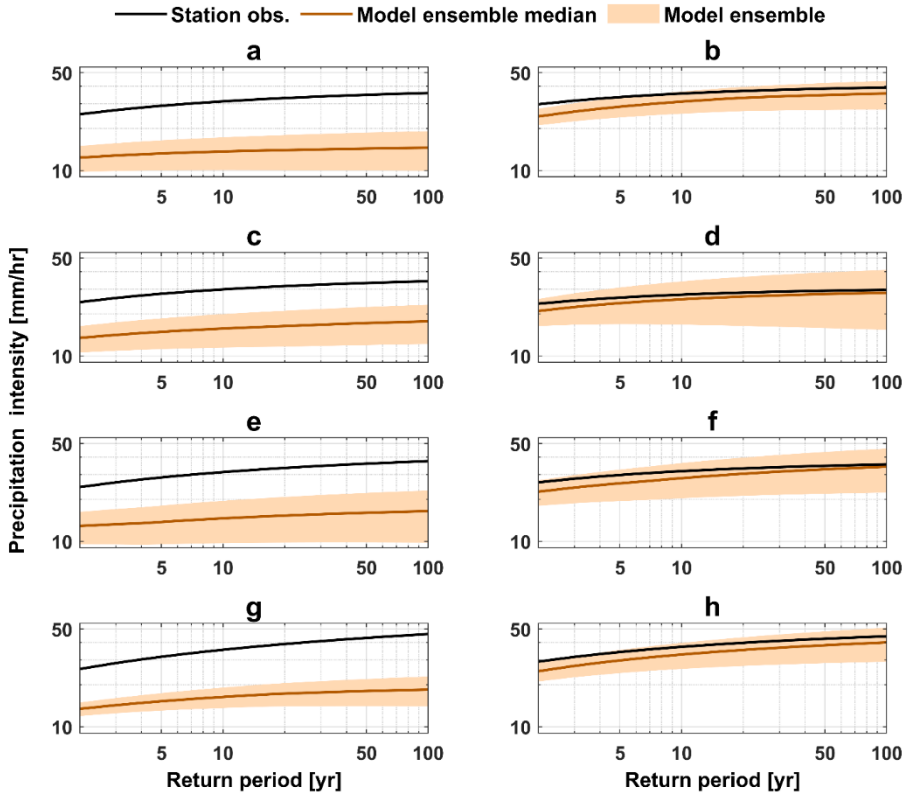


Figure 4.11: Precipitation quantiles of the EURO-CORDEX RCM runs (a, c, e, g) before and (b, d, f, h) after bias correction using the quantile perturbation method based on hourly precipitation observations at (a, b) De Bilt, (c, d) Eelde, (e, f) Flushing and (g, h) Volkel stations in The Netherlands. The quantiles are computed based on GPD with its parameters estimated by the maximum likelihood method.

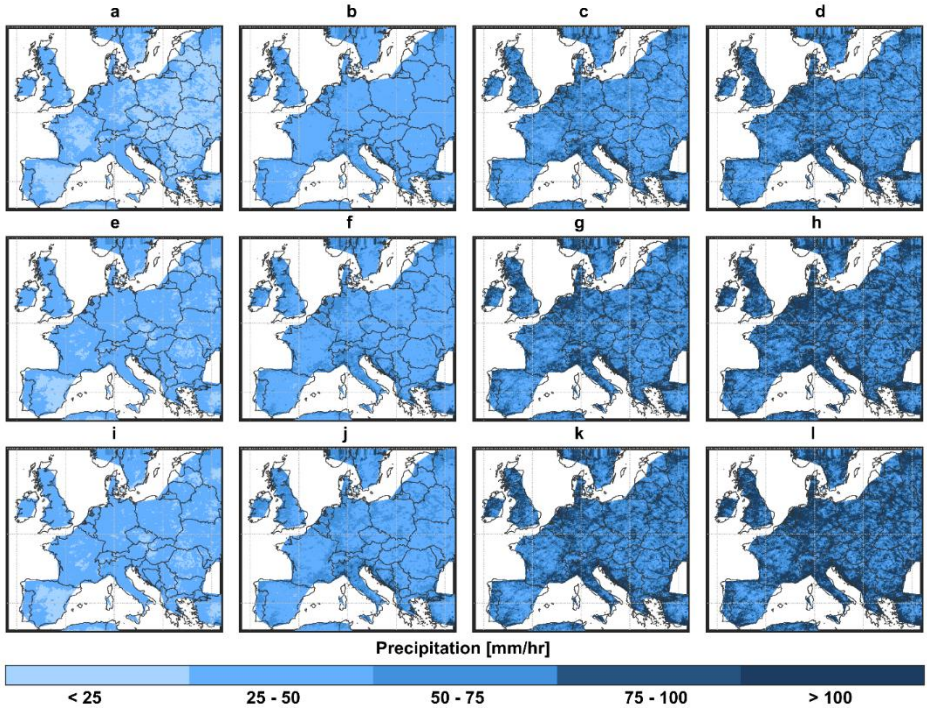


Figure 4.12: Spatial distribution of (a-d) historical (1998-2017) and (e-l) future (2071-2100) extreme precipitation events of 30-min duration for the return periods of (a, e, i) 2, (b, f, j) 10, (c, g, k) 50 and (d, h, l) 100 years under (e, f, g, h) RCP4.5 and (i, j, k, l) RCP8.5 over Europe based on the CMORPH dataset. The future extreme precipitation values are obtained by applying climate change signals on historical extreme precipitation in the framework of the quantile perturbation downscaling method. The climate change signals are computed based on GPD with its parameters estimated by the DE-MC method for the period 2071–2100 with respect to the reference 1971-2000.

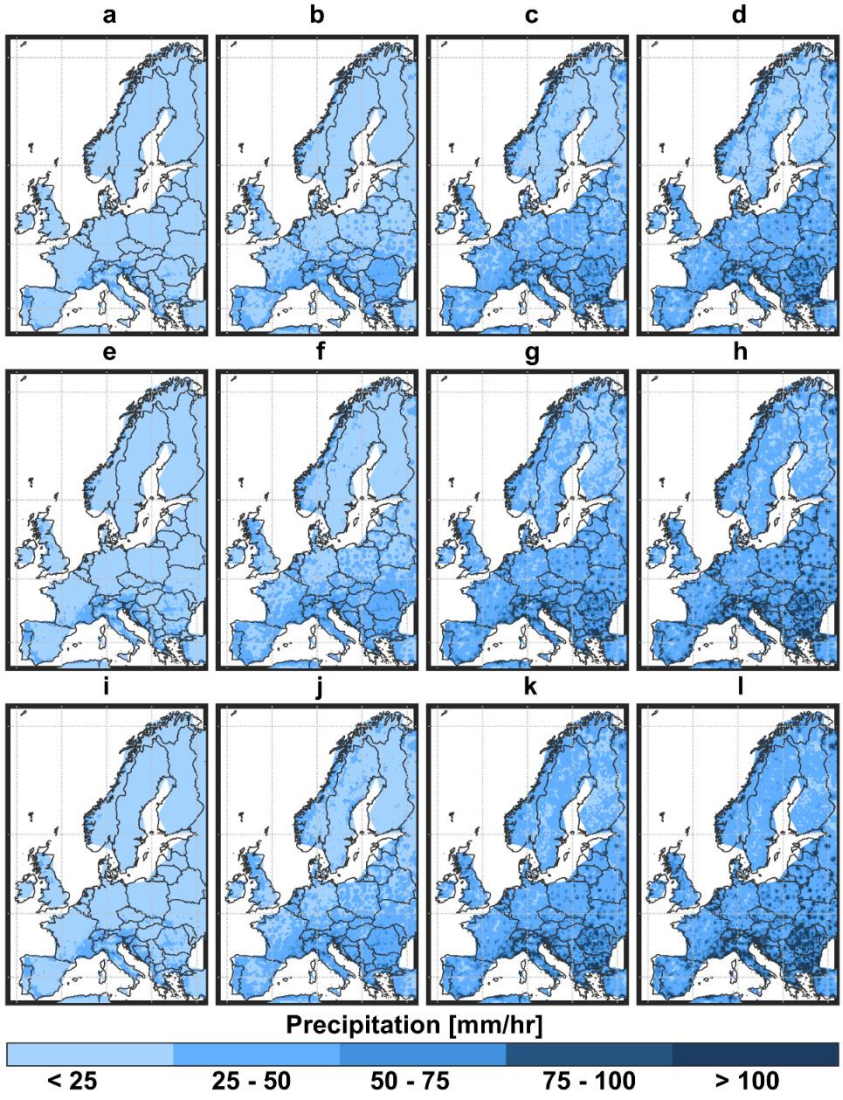


Figure 4.13: Spatial distribution of (a-d) historical (1979-2016) and (e-l) future (2071-2100) extreme precipitation events of 3-hr duration for the return periods of (a, e, i) 2, (b, f, j) 10, (c, g, k) 50 and (d, h, l) 100 years under (e, f, g, h) RCP4.5 and (i, j, k, l) RCP8.5 over Europe based on the MSWEP dataset. The future extreme precipitation values are obtained by applying climate change signals on historical extreme precipitation in the framework of the quantile perturbation downscaling method. The climate change signals are computed based on GPD with its parameters estimated by the DE-MC method for the period 2071–2100 with respect to the reference 1971-2000.

The expected increase in the frequency and intensity of short-duration precipitation compromises the resilience of infrastructure designed and constructed based on the current climate IDF curves. Figure 4.14 illustrates the current and future downscaled IDF curves for 2- and 100-year storms for some European cities under RCP8.5 along with distribution parameter and climate change uncertainties. The best fitting distribution in all cities is the GPD whose probability distribution function has a good match with that of the empirical distribution (Figure 4.15 and 4.16). The future IDF curves in the six selected locations are developed by applying climate change signals on the current IDF curves (Figure 4.14). A comparison between the current and future IDF curves reveals an upward shift and a steepening of the curves in the future in all the locations.

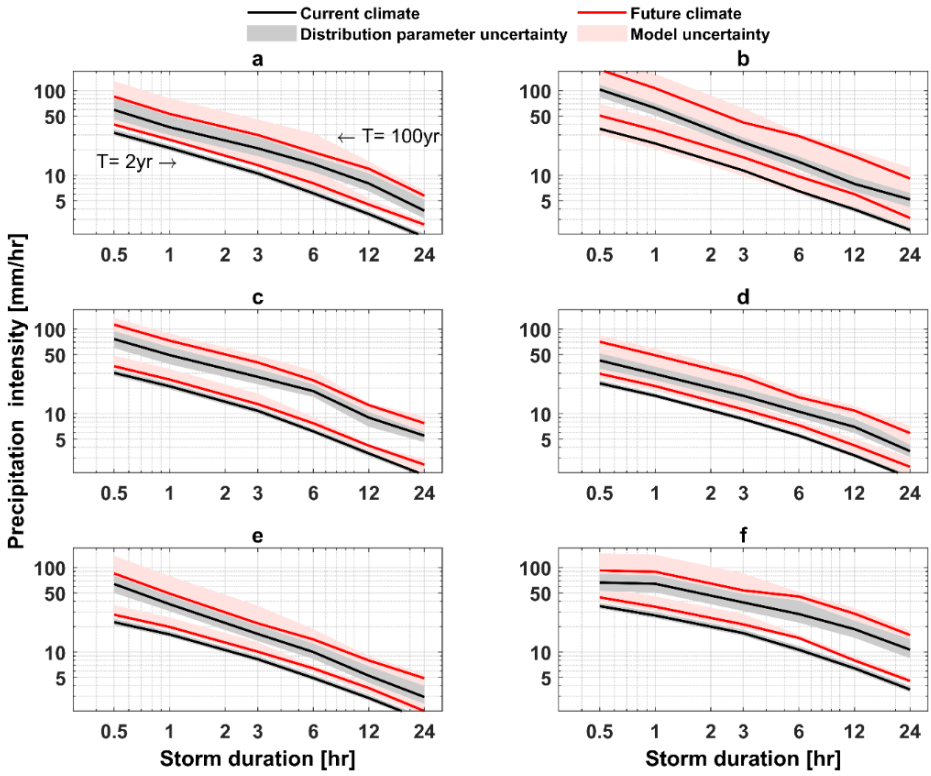


Figure 4.14: Comparison between current CMORPH and future climate scenario IDF curves at some European locations for RCP8.5, along with the model uncertainty bound, indicating different projections of the EURO-CORDEX ensemble members, and distribution parameter uncertainty bound, indicating different estimations of the DE-MC method (a: Brussels (BL), b: De Kooy (NL), c: Eelde (NL), d: Kiev (UA), e: Prague (CZ), f: Barcelona (ES)). The uncertainty bounds are based on the 90% confidence intervals.

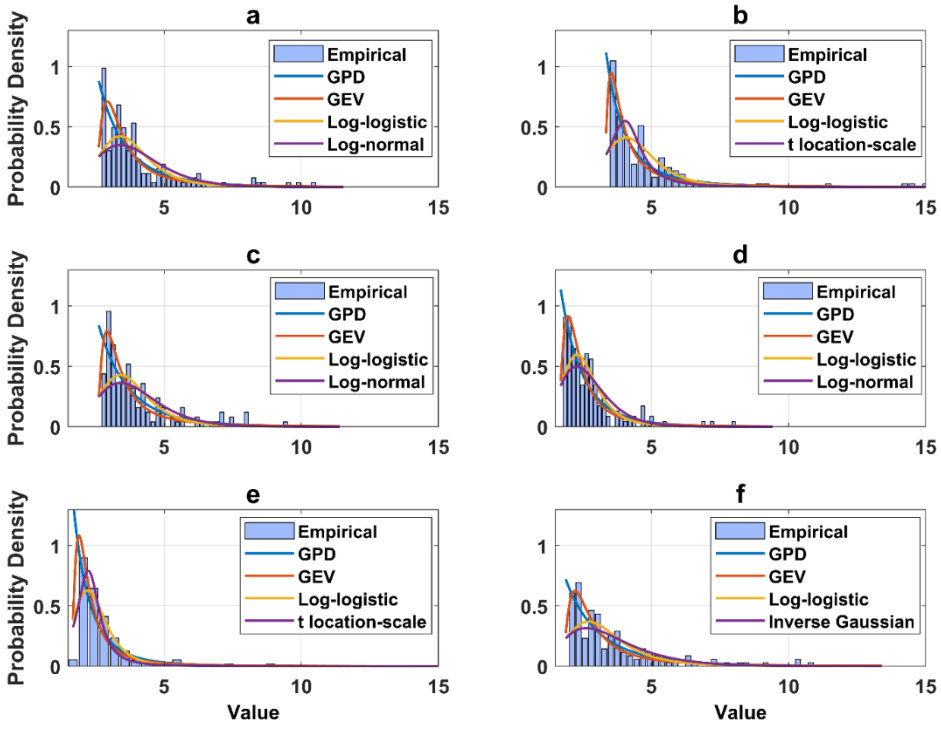


Figure 4.15: Probability distribution function (PDF) of the top four theoretical distributions among the 16 considered distributions and of the empirical distribution based on the CMORPH dataset at some European locations (a: Brussels (BL), b: De Kooy (NL), c: Eelde (NL), d: Kiev (UA), e: Prague (CZ), f: Barcelona (ES)).

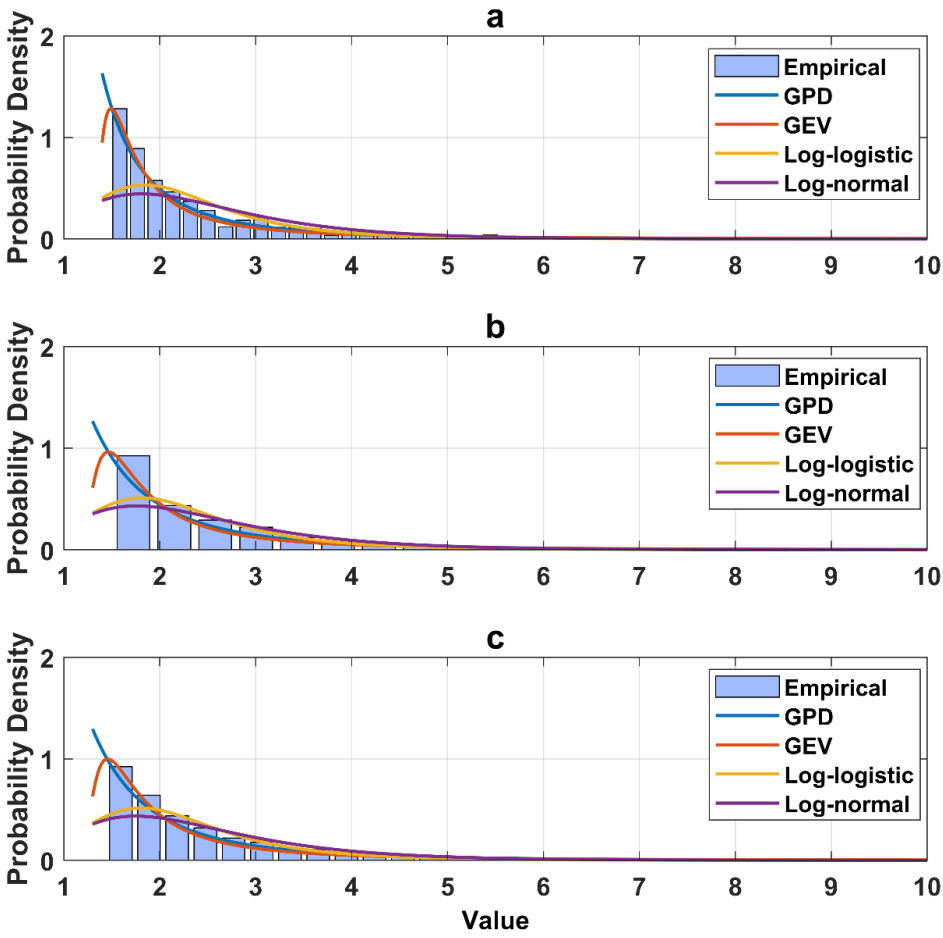


Figure 4.16: Probability distribution function (PDF) of the top four theoretical distributions among the 16 considered distributions and of the empirical distribution based on 10-min precipitation observations at (a) Uccle station for a 100-year period (1901-2000) and hourly precipitation observations at (b) De Kooy and (c) Eelde stations for a 70-year period (1951-2020).

The overall uplift and steepening are also found for IDF relationships at the continental scale, which are larger for RCP8.5 compared to RCP4.5 (Figure 4.17). The magnitudes of the changes in the ordinate and slope of IDF curves are comparable, with larger ordinate changes in 3- and 6-hourly extreme precipitation and smaller ordinate changes for 12- and 24-hourly extremes. The uplift is due to the intensification of extreme precipitation under climate change (Figure 4.6a,b). The steepening of IDF curves is attributed to the larger increase

of shorter duration extremes (Figure 4.6a,b). The steepening of IDF curves grows with return periods, from 17% (10%) for 1-year extreme precipitation to 25% (16%) for 100-year events under RCP8.5 (RCP4.5). The upward shift in IDF curves ranges between 16% (9%) and 27% (18%) under RCP8.5 (RCP4.5), increasing gradually with return period and decreasing with duration (Figure 4.17). The upward shift and steepening of future IDF curves were also observed over North America (Cannon and Innocenti, 2019). The plots also show that the current climate intensity uncertainty is larger for longer return periods (e.g., because of larger sampling errors; Cheng et al., 2015) and even in some cases, the lower bound of the future climate intensity falls within the observation confidence interval bounds related to the uncertainty of the GPD parameter estimation by the DE-MC approach.

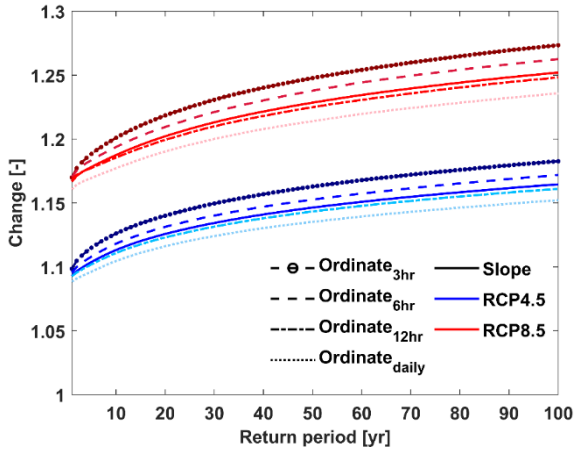


Figure 4.17: Spatial median of the changes in the form of IDF curves (slope and ordinate) derived from the ensemble median of the EURO-CORDEX RCMs. Changes in the ordinate of IDF curves are shown for different precipitation durations. The relative changes are computed based on GPD with its parameters estimated by the DE-MC method for the period 2071-2100 with respect to the reference 1971-2000.

In order to quantify the uncertainty of the quantile estimates from short records, we compared high quantiles between the full time series of the E-OBS (70-year data) and MSWEP (38-year data) over the entire European domain as well as Uccle raingauge (100-year data) with those from a sub-sample with a 20-year length (equal to the length of the CMORPH time series as the shortest

series examined) (Figure 4.18). The results show that short records in all datasets underestimate extreme precipitation and the amount of the underestimation increases with the extrapolation ratio (Figure 4.18a). The bias increment with the extrapolation ratio is more evident for the century-long 0.5-hr raingauge data. For the MSWEP data, the bias in high quantile estimations by short records is slightly larger for a shorter duration. The underestimation of daily quantiles by short records is less than 6%, while it may go up to 18% for sub-daily quantiles. The results are in contrast to the findings of Marra et al. (2017) for a small study area in the eastern Mediterranean. They found an overestimation of the IDF values with short records which decreases with the time aggregation of precipitation. The results also reveal that the underestimation of extreme precipitation quantiles from short records mainly stems from the underestimation of the GPD shape parameter (Figure 4.18b). Care should, however, be taken in generalizing the underestimation of the GPD shape parameter by short records to other regions and time periods. From a multi-decadal climate oscillation perspective, the location of the 20-year period in an oscillation high or an oscillation low period may change the results.

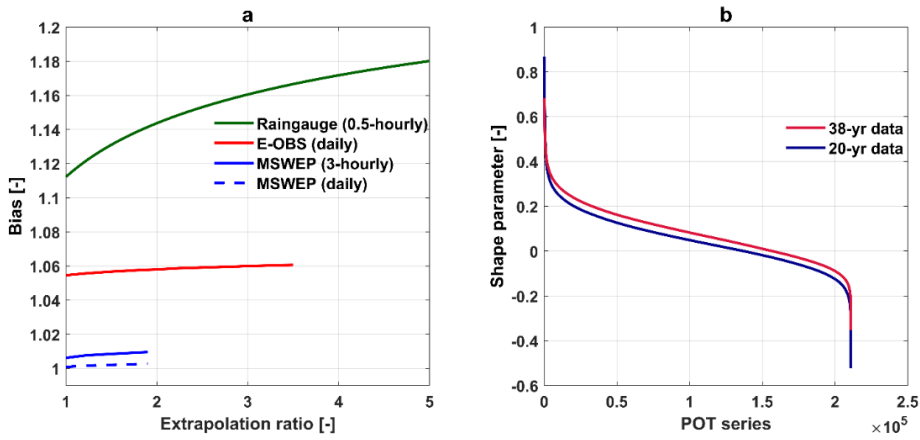


Figure 4.18: Bias in GPD-based quantile estimations using short records. (a) Ratio of the quantiles derived from short records to those from long records versus extrapolation ratio; (b) Comparison of the shape parameter estimated by the DE-MC method from 3-hourly MSWEP precipitation data of 20 (1997-2016) and 38 (1979-2016) year lengths at all European grid cells. In panel a, for the gridded observations, the continental median of the ratios over all European grid cells is shown and century-long 10-min raingauge data (1901-2000) are from Uccle station in central Belgium.

Quantifying the climate change uncertainty over the entire Europe reveal a clear dependency of the total uncertainty on the return period: the longer the return period, the larger the uncertainty (not shown). A larger uncertainty in the projected changes of more extreme precipitation has also been reported in a recent study by Tabari et al. (2019). The increase of uncertainty with the extreme precipitation rarity is found for all four uncertainty components. The total uncertainty as well as the uncertainty of individual components also depends on the duration: the shorter the duration, the larger the uncertainty. The dependency of the uncertainty to duration is more pronounced in the model and scenario uncertainties than in the distribution and parameter uncertainties. The total uncertainty in projected extreme precipitation changes decomposed into its main sources is shown in Figure 4.19. Due to different gradients of the absolute uncertainties of the components with return period, the relative contribution of model and scenario uncertainties is decreasing with return period, while that of distribution and parameter uncertainties is increasing with return period. Models and scenarios with comparable uncertainty magnitudes ranging between 36% and 46% provide the largest uncertainties. Parameter and distribution uncertainties have the lowest contributions to the total uncertainty in extreme precipitation changes, respectively. The parameter and distribution contributions are within the range of 8-15% and 5-12%, respectively.

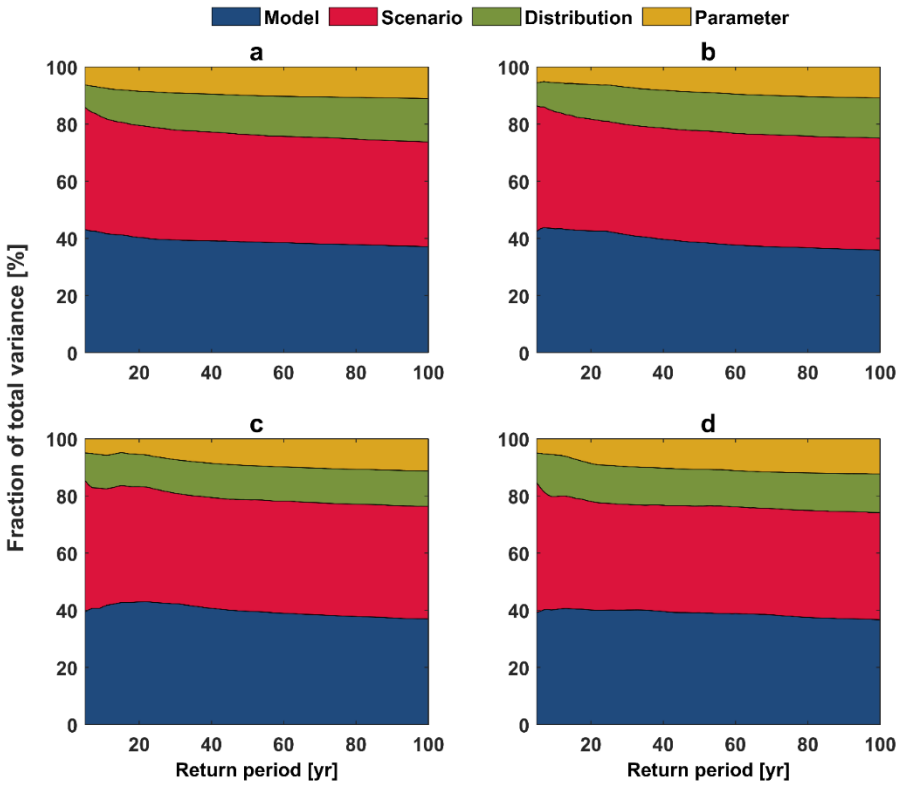


Figure 4.19: Fraction of the total uncertainty in the projected extreme precipitation changes for (a) 3-, (b) 6-, (c) 12-, and (d) 24-hr durations as a function of return periods explained by the uncertainties of climate models (Model), emission scenarios (Scenario), extreme value distributions (Distribution) and distribution parameter estimation methods (Parameter). The relative changes are computed for the period 2071–2100 with respect to the reference 1971-2000.

4.4 Conclusions

This study investigated the impact of climate change on short-duration extreme precipitation over Europe using the EURO-CORDEX RCMs for medium and far future periods. The IDF curves were accordingly revised considering storm durations ranging between 30 minutes and 24 hours and return periods ranging between 1 and 100 years. The results reveal that under climate change, future IDF curves will be uplifted and steepened, with a larger degree under RCP8.5 compared to RCP4.5. The continental median of the uplift is between 16% and 27% depending on the duration and return period, whereas the steepening is

between 17% and 25% depending on the return period. The upward shift in IDF curves is caused by the intensification of extreme precipitation under climate change. A larger increase of shorter duration extreme precipitation under climate change leads to steeper future IDF curves and the expected steepening is larger for higher return periods. The upward shift and steepening of future IDF curves were also observed over North America (Cannon and Innocenti, 2019). The expected changes in IDF curves call into question the resilience of the existing infrastructure systems under more frequent and intense rainstorms in the future. This is of particular importance in urban areas where the failure risk can be cascaded owing to extensive interconnections between different infrastructure systems. Hence, in order to create resilient societies, the breakdown risk of infrastructure systems designed based on historical rainstorms and dependent subsystems in urban areas must be reduced by proper adaptation strategies. To avoid lock-in inflexible strategies and decrease the risk of decision failure regarding the evolving nature of risks over time, capacity building, win-win or low-regret, synergy options or iterative adaptation pathways must be undertaken.

The longer the return period and the shorter the duration of rainstorm is, the larger the change will be. The dependency of the changes on the return period is more pronounced compared to the duration. In addition to the intensity of extreme precipitation, the frequency of sub-daily extreme precipitation is projected to increase. The frequency of 50-year and 100-year extreme precipitation events will be doubled under RCP4.5 and tripled under RCP8.5. The expected changes in precipitation characteristics namely intensity, duration and frequency (IDF curves) must be incorporated for the future design of urban water systems as well as in adaptation planning.

This study also investigated the uncertainty in future projections of extreme precipitation and IDF curves across different durations and return periods which has not been quantified at such scales in previous studies. The results showed that the future projections of IDF curves are subject to a large uncertainty. The uncertainty increases with rainstorm extremity and decreases with duration. The large uncertainty in the future projections calls for a flexible and iterative adaptation approach, based on a framework for decision making under

uncertainty, adaptation pathways and so-called ‘adaptive management’. This kind of adaptations can be iteratively updated by taking the advantages of new information and feedbacks and the lessons learned from the success and failure of actions.

CHAPTER 5

Climate Change Impact on European Pluvial Flood Risk

This chapter was published as:

Hosseinzadehtalaei, P., Tabari, H., Willems, P. (2020) Satellite-based data driven quantification of pluvial floods over Europe under future climatic and socioeconomic changes. *Science of the Total Environment*, 721, 137688

Summary

Flooding is one of the major threats jeopardizing lives and properties of the people, and its risk is expected to increase remarkably under changing climatic and socioeconomic conditions. Yet, future flood risk has not been well studied due primarily to a limited availability of detailed and consistent data on future vulnerability components and the computationally expensive continental flood modeling. Here we perform a top-down data driven flood risk assessment for 20-, 30-, 50- and 100-year return periods over Europe at the continental, regional and national levels for the late 21st century. To account for the impact of changes in both climatic and socioeconomic conditions on floods, the Shared Socioeconomic Pathways (SSPs) are merged with Representative Concentration Pathways (RCPs), integrating hazard and several social, economic and agricultural exposure-vulnerability proxy indicators. The results show a ubiquitous drastic increase up to 87% in future flood risks of different return periods over Europe, with eastern and southern regions experiencing the highest risk increase. A fossil-fuel based development in the future would lead to 14-15% higher flood risk compared to a sustainable development, which goes up to 23% in north Europe. The amplified future flood risk is predominantly driven by climate change, although with a large uncertainty, rather than socioeconomic drivers.

5.1 Introduction

Flood is one of the major climate-related disasters which causes thousands of fatalities and billions of euros in damages each year (Hirabayashi et al., 2013; Khajehei et al., 2020). Over Europe, flood damages during 1998–2009 are estimated to be around EUR 5 billion per year with yearly affected population of 250,000 (EEA, 2010). The economic losses from Europe's floods are on the rise, driven by the growing exposure of people and economic assets due to the illusion of safety (levee effect) as well as the changing climate (Kundzewicz et al., 2014; Tabari et al., 2019; Kron et al., 2019). As a result, strategic flood risk assessments, such as the supranational flood risk reduction policy in Europe

under the Floods Directive released in 2007 (EU, 2007), have received a great deal of attention in recent years. Deliberate disaster risk reduction (DRR) efforts and effective adaptation strategies aim at diminishing flood risks by reducing the magnitude of its components (UNISDR, 2013; Alfieri et al., 2016), being hazard, exposure and vulnerability (Kron, 2005). Implementing an appropriate adaptation strategy for future flood risks is tremendously challenging as all the three determinants of risk are subject to change over time and space under socioeconomic development and climate change (Alfieri et al., 2015a; Jongman et al., 2015).

Despite the importance of flood risk assessments, large-scale future flood risk studies are limited. To the best of the authors' knowledge, the risk of continental/global pluvial flooding has not also been addressed. Such paucity of future flood risk analyses can primarily be attributed to the intensive computational time of the continental flood modeling as well as data limitation for detailed hydrodynamic simulations (Falter et al., 2016; Schumann et al., 2013; Sampson et al., 2015) and for future vulnerability components. Data driven approaches based on satellite imagery and remote-sensing techniques constitute a resource- and cost-efficient alternative for the large-scale flood modeling (Lugeri et al., 2010; Karlsson and Arnberg, 2011; Kaspersen et al., 2017). Specifically, satellite imagery provides high spatial and temporal resolution climate and geographical data for large-scale flood simulations.

Future river and coastal flood hazards have been investigated by several researchers (e.g., Arnell and Lloyd-Hughes, 2014; Dankers et al., 2014; Giuntoli et al., 2015; Alfieri et al., 2015b; Roudier et al., 2016; Alfieri et al., 2017), broadly pointing to weak and sometimes opposite direction of changes in flood hazard in Europe. Recent studies on future floods have been based on global (GCM) or regional climate model (RCM) projections under new climate scenarios of the Representative Concentration Pathways (RCPs; Moss, et al., 2010). The RCP scenarios are not, however, associated with future socioeconomic developments in contrast to the SRES scenarios (IPCC, 2000). To address the influence of the future socioeconomic changes, Shared Socioeconomic Pathways (SSPs) have been developed by assuming no climate change and related impacts and adopted policies during the twenty-first century

(O'Neill et al., 2014). Some river and coastal flood risk assessments have combined the RCP and SSP scenarios to characterize the impacts of both climatic and socioeconomic changes (e.g., Jongman et al., 2015; Winsemius et al., 2016; Dottori et al., 2018).

In addition to the scarcity of future flood risk analyses, the majority of the existing studies have taken into account only (current or future) population exposure and economic vulnerability in terms of gross domestic product (GDP) (Hirabayashi et al., 2013; Hinkel et al., 2014; Jongman et al., 2015; Willner et al., 2018; Kinoshita et al., 2018; Fang et al., 2019; Liao et al., 2019; Vafeidis et al., 2019). Some studies have included urbanization and agricultural value in river and coastal flood risk assessments (Jongman et al., 2012; Winsemius et al., 2013, 2016; Dottori et al., 2018; Vousdoukas et al., 2018), while others assumed that these elements do not change through the 21st century (Arnell and Gosling, 2016) or focused on current risks (Ward et al., 2013). The previous flood risk studies have, moreover, overlooked the possible influence of the changes in social vulnerabilities concerning people's knowledge/awareness and capacity for innovation and technological strength to mitigate and adapt to flood hazard. The available literature also falls short in quantifying the total uncertainty in future flood risk assessments and decomposing it into socioeconomic and climatic related uncertainties, while quantitative uncertainty description in risk analyses is indispensable for informed policy decisions and actions (Webster et al., 2003).

In light of the aforementioned knowledge gaps in the risk analysis of future floods, the overarching goal of this chapter is to assess future pluvial flood risks in Europe at the continental, regional and national (per country) levels by taking into account the impacts of future socioeconomic developments and climate change. This chapter therefore does not aim to quantify the flood hazard and risk in a detailed and costly/time-consuming way, as is done in case-specific hydrological studies, but to obtain an order of magnitude assessment at pan-EU scale. Pluvial flood hazard is quantified using a satellite-based data driven method, making use of CMORPH (Climate Prediction Center Morphing method) hourly precipitation, impervious surface data and digital elevation model (DEM). Future flood hazard is projected by applying sub-daily climate

change signals from the EURO-CORDEX RCM simulations on the hazard of the current climate in the framework of the quantile perturbation downscaling method. A combined exposure-vulnerability index is used, integrating social, economic and agricultural exposure-vulnerability proxy indicators. The pluvial flood risk analysis is performed for two RCP-SSP combined scenarios, namely 'Sustainability' (SSP1 & RCP4.5) and 'Fossil-fuel based development' (SSP5 & RCP8.5). The contribution of the changes in climatic and socioeconomic conditions to flood risk changes is disentangled and the associated uncertainties are decomposed into several sources.

5.2 Materials and methods

5.2.1 Data

5.2.1.1 Precipitation observations

Precipitation products with the highest spatial and temporal resolutions among satellite datasets (Wang et al., 2019) were obtained from the CMORPH (Climate Prediction Center Morphing method) dataset. The CMORPH data have shown a comparable accuracy with ground station observations (Zeweldi and Gebremichael, 2009). The dataset has been derived from low orbiter passive satellite microwave (PMW) observations which are propagated by motion vectors derived from geostationary satellite infrared data (Joyce et al., 2004). It has a quasi-global precipitation coverage (60° S - 60° N) from 1 January 1998 onwards with a high temporal resolution of 30 minutes and spatial resolution of 0.073°×0.073° (or 8 km at the equator). We made use of the newly product of this dataset (CMORPHv1.0., 2015) which is bias corrected based on daily precipitation at almost 30,000 gauges around the world (Xie et al., 2017). The new CMORPH product showed much improved estimates of precipitation compared to the original version concerning spurious trends and biases (Gehne et al., 2016).

5.2.1.2 Climate model simulations

To derive climate change signals, the Coordinated Downscaling Experiment over Europe (EURO-CORDEX; Jacob et al., 2014) simulations were used. Among the EURO-CORDEX regional climate models (RCMs), the RCA4 RCM developed at the Swedish Meteorological and Hydrological Institute (SMHI; Strandberg et al., 2014) provides the finest scale precipitation (3-hourly precipitation at 0.11° model grid size). The RCA4 RCM has downscaled five GCMs from the fifth phase of the Coupled Model Intercomparison Project (CMIP5; Taylor et al., 2012): CNRM-CM5, EC-EARTH, IPSL-CM5A-MR, HadGEM2-ES and MPI-ESM-LR. The periods 1971-2000 and 2071–2100 were considered as current and future climates, respectively. The future climates were projected under representative concentration pathways (RCPs) RCP4.5 and RCP8.5, which correspond to stabilized and high-end scenarios with radiative forcings of 4.5 and 8.5 W/m2 at the end of the century, respectively.

5.2.1.3 Exposure and vulnerability data

National level data for total population, the proportion of urban population, age-specific population, education level of age-specific population and GDP for a decadal resolution from 2010 to 2100 were retrieved from the global SSPs (O'Neill et al., 2015). The International Institute for Applied Systems Analysis (IIASA) developed all of the indicators except the proportion of urban population which was developed by the National Center for Atmospheric Research (NCAR). The total population was divided by the land area of each country to compute population density. The gridded land use data were acquired from AIM-SSP/RCP Gridded Emissions and Land-use dataset (Fujimori et al., 2018) which is available for different combinations of five SSPs (SSP1, SSP2, SSP3, SSP4 and SSP5) and six mitigation levels specified by radiative forcing (RF) targets (1.9, 2.6, 3.4, 4.5, 6.0 and baseline). We made use of the cropland proportion at each grid cell for the combinations SSP1&RF4.5 and SSP5&RF6.0 as RF8.5 is not available to be coupled with SSP5. It was then averaged for each European country.

5.2.1.4 Spatial data for flood estimation

This study used the following spatial data for flood quantification:

- Digital Elevation Model (DEM): Digital Elevation Model over Europe (EU-DEM) from the European Environment Agency (EEA, 2013) developed in the GMES RDA project with a 25 m resolution was applied, which is a hybrid product of SRTM and ASTER GDEM data. We later derived slope from the EU-DEM.
- Soil texture classes: Data from the United States Department of Agriculture (USDA) on soil texture classes at 500 m grid cell resolution for Europe were obtained from the European Soil Data Centre (ESDAC) (Ballabio et al., 2016).
- Impervious surface (IS): Imperviousness high resolution layer for the 2015 reference year with a 20 m resolution from Copernicus Land Monitoring Service Pan-European Component governed by the European Environment Agency was used. The degree of imperviousness, ranging between 0 and 100%, is produced by a combination of interactive rule-based classification and automatic processing of multi-source high resolution satellite imagery (Langanke et al., 2016).

5.2.2 Quantification of flood hazard

Flood hazard for current and future climate conditions was initially quantified for observations and separately for each RCM run at the grid cell level and then aggregated to the national (for 29 European countries), regional (for 4 European regions) and continental levels. To this end, the following empirical formula (Kaspersen et al., 2017), which considers both urban and non-urban floods, was used:

$$R_{T,g} = \left(P_{T,g} - f_g\right)\left(1 - IS_g\right) + \left(P_{T,g} - P_{S,g}\right)IS_g \quad (5.1)$$

where at each grid cell g, $R_{T,g}$ is the net runoff of the return period T, $P_{T,g}$ is the precipitation of the return period T, f_g is the potential infiltration rate, IS_g is the impervious surface fraction (dimensionless) and $P_{S,g}$ is the design precipitation used for sewer systems. The first part of the formula is the simplified version of

the Horton's infiltration model (Horton, 1933), in which the initial infiltration capacity is assumed to be negligible. The potential infiltration rate at grid cells (Figure 5.1a) was estimated based on the dominant soil texture and the average slope of each grid cell following the USDA procedure (Table 5.1) and the slope was computed from the EU-DEM (Figure 5.1b). Due to different grid sizes of the EU-DEM and soil texture layers, they were regridded to the same grid size using the bilinear interpolation method. The second part of the formula estimates urban flooding in which hourly precipitation with T=10 years was assumed to be used for sewer system design. This return period may vary from region to region, e.g. for some countries lower at 2 years, for other countries higher at 20 years. Results therefore may spatially vary more than what this chapter reports. The precipitation corresponding to the threshold of flooding was determined per grid cell. Note that the first part of the formula is applied for rural areas where $IS_g = 0$ and the second part to totally urbanized areas where $IS_g = 1$.

$P_{T,g}$ for the return periods of 10, 20, 30, 50 and 100 years was estimated using the generalized Pareto distribution (GPD).

$$x_p = \begin{cases} u + \left[\frac{\sigma}{\xi}\left(\frac{1}{p}\xi_u\right) - 1\right] & for\ \xi \neq 0 \\ u + \sigma \log(\frac{1}{p}\xi_u) & for\ \xi = 0 \end{cases} \quad (5.2)$$

where x_p is the return level (i.e., the value that is expected to be exceeded once every T years on average) associated with the return period 1/p for the chosen threshold u, and σ and ξ are the scale and shape parameters of the distribution expressing the deviation around the mean and the tail behavior of the distribution, respectively. The GPD parameters were estimated at individual grid cells using the Differential Evolution Markov Chain (DE-MC) which it is feasible in non-regular likelihood cases (e.g., in the case of short tail of the parent population) (Rupa et al., 2015) and provides the uncertainties in parameter estimation (Mélèse et al., 2018). To assess the convergence of the sampling approach, we used the $\hat{R}$ criterion (Gelman and Shirley, 2011) with the upper limit of 1.1 (Cheng et al., 2014, Ragno et al., 2018). Also, the maximum sub-daily precipitation per day was considered to select almost independent extreme precipitation events, following an interevent time criterion

of 12 hours proposed by Ntegeka and Willems (2008) to fulfil the independence of precipitation events.

To quantify flooding at the grid cell level in the current climate, CMORPH hourly precipitation was used. Future floods were projected by applying climate change signals from the EURO-CORDEX RCM simulations on the CMORPH hourly precipitation in the framework of the quantile perturbation downscaling method (Willems, 2013). In both cases, the precipitation threshold for the return period of 10 years (assumed sewer system design return period) was taken from CMORPH hourly precipitation.

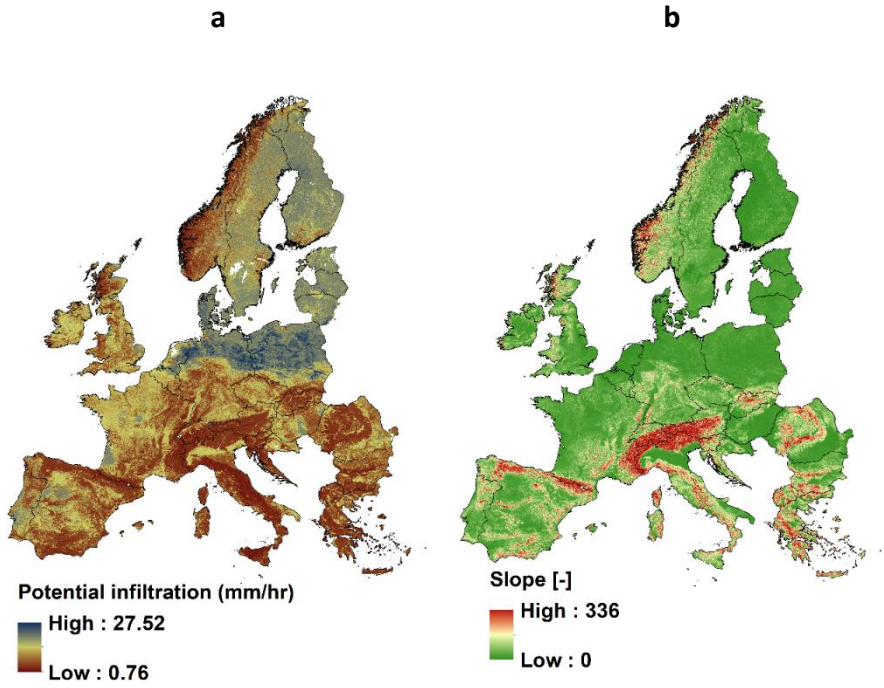


Figure 5.1: (a) Potential infiltration over Europe calculated based on (b) slope along with the soil type classes presented in Table 5.1.

Table 5.1: Modified USDA (USDA, 2016) potential soil infiltration rates (mm/hr) based on soil texture and slope.

Soil class	Soil texture	Slope (%)				
		0-4	5-8	8-12	12-16	> 16
1	Clay	3.30	2.54	2.03	1.27	0.76
2	Silty Clay	4.83	3.81	2.79	2.03	1.27
3	Silty Clay Loam	5.59	4.45	3.30	2.29	1.40
4	Sandy Clay	7.87	6.35	4.83	3.05	2.03
5	Sandy Clay loam	7.11	5.72	4.32	2.79	1.78
6	Clay Loam	6.35	5.08	3.81	2.54	1.52
7	Slit	11.18	8.89	6.60	4.57	2.79
8	Slit Loam	12.70	10.16	7.62	5.08	3.30
9	Loam	13.72	10.92	8.38	5.59	3.56
10	Sand	27.52	22.01	16.51	11.01	6.94
11	Loamy Sand	22.35	17.78	13.46	8.89	5.59
12	Sandy Loam	19.05	15.24	11.43	7.62	4.83

5.2.3 Quantification of exposure and vulnerability

To compute the socioeconomic dimension of flood risk, a combined exposure-vulnerability index (EVI) was used, combining economic (*Econi*), social (*Soci*) and agricultural (*Agri*) components at each geographic location (i; continent, region and country). The components were characterized by a set of proxy indicators, each demonstrating a quantitative or qualitative aspect of vulnerability to floods. Since no well-established platform to select the proxy indicators for assessing flood vulnerability exists, we based our indicator selection on their close association with the flood vulnerability and the public availability of the required data. Following the previous large-scale flood risk studies (e.g., Ward et al., 2013; Arnell and Gosling, 2016), population density (representing the population exposure), the proportion of urban population (representing the degree of urbanization), GDP (representing the mitigation ability of individuals and governments) and the proportion of croplands (representing agricultural damages) proxy indicators were selected. In addition, population's age and education level were considered as two other proxy indicators for the social component: the former associated to the adaptation ability and the latter to the awareness and knowledge of flood hazard prevention. The relevance of all six proxy indicators to flood risk is presented in Table 5.2. As most of the proxy indicators are available at the country level, EVI and risk

assessments were performed at the national, regional and continental levels (Table 5.3). Assuming a uniform population over each country may, however, lead to an underestimation of the flood risk in urban areas due to their higher population density compared to rural areas.

Table 5.2: Determinants of combined exposure-vulnerability index and their relevance to flood risk.

Component	Proxy indicators	Relevance to flood risk
Social	Population density	Population density is an indicator of population exposure to floods.
	Urban population (% of total population)	Urban population was considered as a proxy of the degree of urbanization which is closely associated with urban flooding.
	Age dependency ratio (ratio of population typically not in the labor force aged below 15 and above 64 to those typically in the labor force aged between 15 and 64)	Children and elderly people have lower adaptation ability and higher mortality rates when a flood happens. So, a higher ADR increases the pressure on health care and on emergency services during hazards.
	Education level (% of people aged 24–64 with tertiary education)	A higher literacy rate is linked to higher awareness and better knowledge of flood hazard prevention, while a lower literacy rate implies a lower capacity for innovation and technological strength to mitigate and adapt to flood hazard (Lutz et al., 2014; Vescovi et al. 2005).
Economic	GDP per capita	Economic or income levels indicate the financial ability of individuals and governments to mitigate flood hazards and to reduce disaster risk. Higher GDP is associated with better-prepared infrastructure and better risk management strategies for quick responses and recovery in the time of flood hazards and better communication of both direct and long-term risks, while poorer countries have low levels of capacity to respond to flood hazards because of their limitation for choosing a living place and weaker preparedness (Jongman et al., 2015).
Agricultural	% of croplands	Higher proportion of croplands is directly associated with higher agricultural damages and interrupted food supplies when a flood occurs (Kundzewicz et al., 2019).

Table 5.3: European regions and corresponding countries considered in this study.

Region	Country	Country code
North Europe	Denmark	DNK
	Estonia	EST
	Finland	FIN
	Ireland	IRL
	Lithuania	LTU
	Latvia	LVA
	Norway	NOR
	Sweden	SWE
	United Kingdom	GBR
South Europe	Greece	GRC
	Spain	ESP
	Croatia	HRV
	Italy	ITA
	Macedonia	MKD
	Portugal	PRT
	Slovenia	SVN
West Europe	Austria	AUT
	Belgium	BEL
	Switzerland	CHE
	Germany	DEU
	France	FRA
	Luxembourg	LUX
	Netherlands	NLD
East Europe	Bulgaria	BGR
	Czech Republic	CZE
	Hungary	HUN
	Poland	POL
	Romania	ROU
	Slovakia	SVK

As there is no universal weighting scheme for the determinants of the exposure and vulnerability (Naumann et al., 2014), three weighting schemes were adopted to examine the sensitivity of the EVI values to weighting: equal weights (EW), proportional weights (PW) and random weights (RW). In the EW scheme, after taking a mean over proxy indicators of the social component, equal weights (W= 0.33) were assigned to the economic, social and agricultural components. In the PW scheme, the components were weighted according to the number of the proxy indicators in each component: W = 0.17 for the economic and agricultural components with one proxy indicator and W = 0.66 for the social component with four proxy indicators. In the RW scheme, after averaging over the proxy indicators of the social component, random weights

were generated for each component and then the weights were normalized to make their sum equal to 1. Following the Monte Carlo procedure, this process was repeated 100 times and the medians of the runs were taken as the final weighs of the risk components. The mathematical expressions of the weighting schemes are as follows:

$$EVI_i = f(Soc_i, Econ_i, Agr_i)$$
$$= \begin{cases} 0.33\,Soc_i + 0.33Econ_i + 0.33Agr_i = \dfrac{\left[\dfrac{Pop_i + UrPop_i + Edu_i + ADR_i}{4}\right] + GDP_i + Crop_i}{3} & for\ \ EW \\ 0.66\,Soc_i + 0.17Econ_i + 0.17Agr_i = \dfrac{Pop_i + UrPop_i + Edu_i + ADR_i + GDP_i + Crop_i}{6} & for\ \ PW \\ W_S.Soc_i + W_E.Econ_i + W_A.Agr_i = W_S.\left[\dfrac{Pop_i + UrPop_i + Edu_i + ADR_i}{4}\right] + W_E.GDP_i + W_A.Crop_i & for\ \ RW \end{cases} \quad (5.3)$$

where at each geographic domain i, Pop_i is the total population density, $UrPop_i$ is the proportion of urban population, Edu_i is the proportion of 25- to 64-year-olds with higher education, ADR_i is the age dependency ratio [ratio of population typically not in the labor force (age <15 and age ≥ 65) to those typically in the labor force (15≥ age <65)], GDP_i is the gross domestic product per capita, $Crop_i$ is the average proportion of croplands over all grid cells of each geographic domain (continent, region and country) and WS, WE and WA are the final random weights (i.e., median of the Monte Carlo runs) for social, economic and agricultural components, respectively. EVI is computed under baseline socioeconomic conditions (2010) and under two SSP scenarios for the future. In order to be consistent to the future period of the RCP scenarios (2071-2100), the decadal values of the proxy indicators for 2080 and 2090 were linearly interpolated to derive EVI for 2085 (middle year of the 2071-2100 period).

As the proxy indicators have different units, they were spatially and temporally normalized using a linear min-max rescaling between 0.05 (lowest vulnerability) and 0.95 (highest vulnerability). Two normalization schemes were adopted in this study: a spatial normalization for EVI proxy indicators considering direct and indirect relationships with EVI and an overall normalization for the display purpose of hazard, vulnerability and risk.

a. Spatial normalization

$$Z_c = \begin{cases} 0.05 + (0.9 \times \frac{X_c - X_{min}}{X_{max} - X_{min}}) & for\ direct\ relationship \\ 1 - [0.05 + (0.9 \times \frac{X_c - X_{min}}{X_{max} - X_{min}})] & for\ indirect\ relationship \end{cases} \quad (5.4)$$

where Z_c and X_c are respectively the normalized and original indicator values for a given country *c* and X_{min} and X_{max} are respectively the minimum and maximum values across all countries. The spatial normalization of EVI proxy indicators was done separately for current and future socioeconomic conditions.

b. Overall normalization

$$Z(c,s,t) = 0.05 + (0.9 \times \frac{X(c,s,t) - X_{Min}}{X_{Max} - X_{Min}}) \quad (5.5)$$

where $Z(c,s,t)$ and $X(c,s,t)$ are respectively the normalized and original component values for a given country *c*, scenario *s* (radiative forcing, socioeconomic and combined scenarios) and time period *t* (current and future periods) and X_{Min} and X_{Max} are respectively the overall minimum and maximum values across all countries, scenarios and time periods. Flood risk maps after the overall normalization were classified into five classes according to their numerical values from very low to very high, each of which corresponding to a quintile of the 0.05-0.95 range.

5.2.4. Quantification of flood risk

We defined flood risk as being the multiplicative combination of the normalized hazard and combined exposure-vulnerability index (UNDRO, 1991). As the future development of socioeconomic driving forces and the future climate changes are not known, the use of a range of combined scenarios rather than a single most plausible storyline is recommended in impact assessments (Kundzewicz et al., 2018). To cover the range of the uncertainty in the climatic and socioeconomic changes, we selected the lower and upper bounds of the plausible combinations of the RCP and SSP scenarios, although the total uncertainty could have been even larger if the simulations for RCP2.6 were available. Following O'Neill et al. (2016) and Rogelj et al. (2018), RCP4.5

was coupled with a global sustainable development (SSP1) and RCP8.5 with the socioeconomic developments driven by mitigation challenges (SSP5). SSP1 and SSP5 both envision a world with a relatively high income growth, rapid urbanization and higher investments in health and education. While this relatively optimistic trend for future economic and social developments is obtained by an increasing shift towards sustainable practices in SSP1, it is achievable by an energy-intensive, fossil fuel-based economy in SSP5 (Jones and O'Neill, 2016).

The risk of future 20-, 30-, 50- and 100-year floods was assessed for the two combined scenarios of 'Sustainability' (RCP4.5 & SSP1) and 'Fossil-fuel based development' (RCP8.5 & SSP5), while current flood risk was based on observations. The future risk was derived by applying the expected changes in risk on the current flood risk, where change being the multiplicative combination of the changes in hazard and EVI:

$$Risk_{future} = Risk_{current} \times \left[\frac{Hazard_{future}}{Hazard_{current}} \times \frac{EVI_{future}}{EVI_{current}}\right] \quad (5.6)$$

where $\frac{Hazard_{future}}{Hazard_{current}}$ and $\frac{EVI_{future}}{EVI_{current}}$ show the expected changes at the end of this century in the hazard and EVI, respectively. The expression in the brackets, the ratio of the flood risk in the future period to that in the current period, denotes changes in flood risk. The changes in flood risk were also disentangled in the changes in hazard and exposure-vulnerability which provide useful information to prioritize adaptation actions. The decomposition of the flood risk changes was carried out for each country and for the two combined scenarios. Furthermore, we estimated the extent to which the projected risk can be avoided by shifting future climatic and socioeconomic from the Fossil-fuel based development scenario to the Sustainability scenario. The avoided flood risk was quantified by the difference in the future flood risk changes between the two scenarios.

The use of five climate models, two combined future scenarios, three weighting schemes and four return periods makes the size of the flood risk ensemble equal to 120 for each geographical unit (country, region and continent), enabling an uncertainty quantification. For each return period, the total uncertainty in flood risk changes was decomposed into the uncertainties

pertaining to climate models, combined future scenarios and weighting schemes of EVI. While the climate model uncertainty corresponds to flood hazard changes and the weighting scheme uncertainty to the formulation of EVI, the uncertainty of combined future scenarios corresponds to both hazard and EVI changes. To characterize the climate model uncertainty, the coefficient of variation (CV) of the risk changes across climate models was calculated after taking the median of the changes across difference scenarios and weighting schemes. In a similar way, the uncertainties in combined future scenarios and weighting schemes of EVI were quantified. We finally calculated the relative contribution of each uncertainty source to the total uncertainty, while the total uncertainty is the sum of the variation due to climate models, combined future scenarios and weighting schemes of EVI.

5.3 Results and discussion

The projected changes in Europe's floods of 20-, 30-, 50- and 100-year return periods at different spatial scales for RCP4.5 and RCP8.5 are illustrated in Figure 5.2. The results show that flood magnitude in Europe will increase under climate change. It agrees with the general expectation of future increases in flood frequency and severity as a consequence of increases in extreme precipitation under warmer climates (Hosseinzadehtalaei et al., 2019) dictated by the Clausius–Clapeyron (CC) relation (Berg et al., 2013; Barbero et al., 2017; Lenderink et al., 2017). The increase in flood hazard in Europe broadly corroborates the findings of Alfieri et al. (2015) and Roudier et al. (2016) and contradicts those of Rojas et al. (2012), Hirabayashi et al. (2013), Dankers et al. (2014) and Giuntoli et al. (2015). The differences in flood hazard projections in the previous studies can be attributed, among others, to the differences in the type and number of climate models, greenhouse gas scenarios, historical and future periods and extreme value analysis techniques. Discussion of the possible causes of the discrepancies in flood hazard projections over Europe can be found in Kundzewicz et al. (2017).

The results show that the flood magnitude for all return periods at the end of this century is - on average for Europe - 6-7% greater under RCP8.5 than

RCP4.5 (Figure 5.2a). The longer the return period of floods, the larger the expected changes. The median changes vary from 53% (43%) for 20-year floods to 72% (62%) for 100-year floods under RCP8.5 (RCP4.5). As the climate change signals get stronger by return periods, the discrepancy among countries and regions gets smaller (Figure 5.2b).

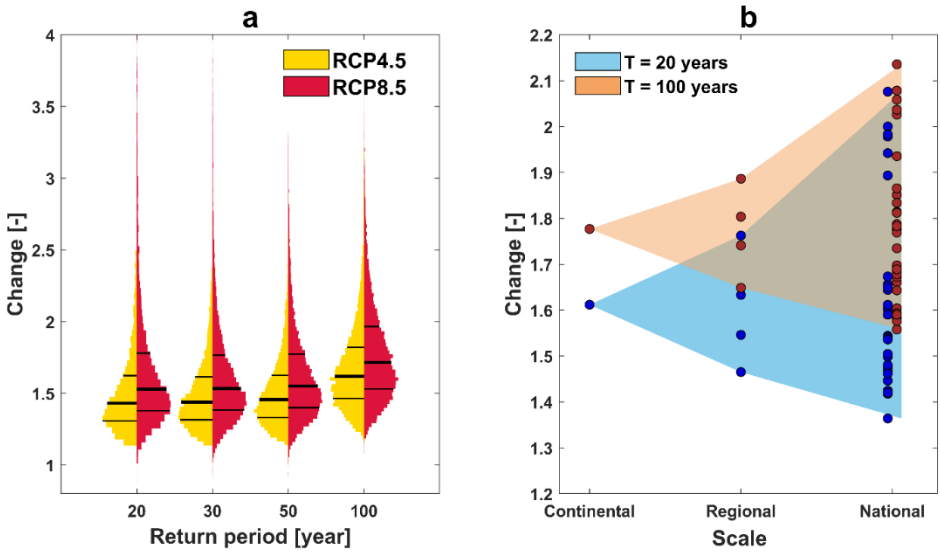


Figure 5.2: a) Comparison of changes in Europe's floods of 20-, 30-, 50- and 100-year return periods between RCP4.5 and RCP8.5 at the grid level and b) changes in Europe's floods of 20- and 100-year return periods under RCP8.5 at the continental, regional and national scales. The changes are computed for the period 2071–2100 with respect to the reference 1971-2000 and the results for the median of the EURO-CORDEX RCM simulations are shown. Note that the wider the violin plot, the higher the density. Horizontal lines in violin plots show 25th, 50th and 75th percentiles of the changes in all grid cells over Europe. See Table 5.3 for countries considered in each European region.

For the country-level analysis, an overall normalization over all the 12 cases (see Figure 5.3) was performed to better visualize the changes among different time periods (current & future), return periods (20, 30, 50 and 100 years) and RCP scenarios (4.5 & 8.5). The results emphasize the magnitude increase for the floods of all return periods in all countries under both RCP4.5 and RCP8.5 (for each return period, from the first row to the last row in Figure 5.3). The

increasing gradient of flood hazards from 20-year floods in the current climate to 100-year floods in the future climate under RCP8.5 is obvious in the hazard maps (from the first row & the first column [1, 1] to the last row & the last column [4, 4] in the maps matrix in Figure 5.3). Changes in the flood hazard for the future are not homogeneously distributed across European countries, with the changes for 100-year floods under RCP8.5 ranging from 56% in Switzerland to 114% in Sweden.

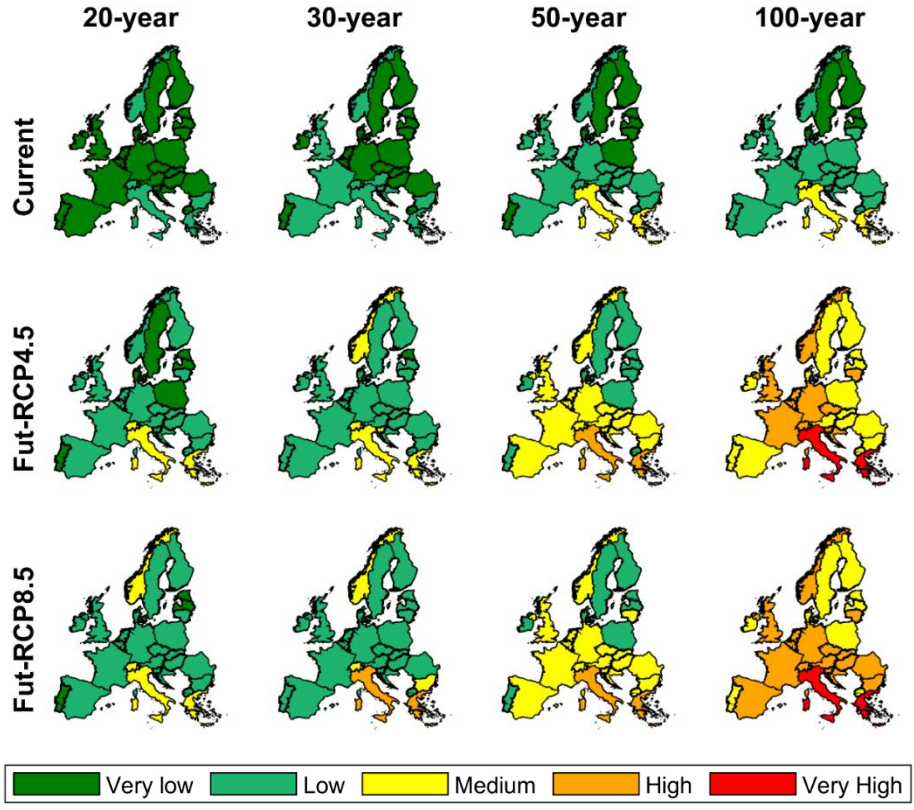


Figure 5.3: Flood hazard of 20-, 30-, 50- and 100-year return periods in Europe for current climate conditions (1971-2000) and for the 2071-2100 period under RCP4.5, and RCP8.5. The index was normalized over all countries, return periods, scenarios and time periods (i.e., normalization over all the 12 cases) and then classified into five classes from very low to very high, each of which corresponding to a quintile of the 0.05-0.95 range.

At a regional level, flood hazard will increase in the future at least by 46% for all return periods and scenarios (Figure 5.4). In all cases, north Europe indicates the highest footprint of climate change on flooding (61-89% increase), whereas for south Europe the footprint is lower (39-65% increase). Continental results reveal a flood hazard increase of 60-78% for the end of this century for different return periods and scenarios (Figures 5.2b and 5.4).

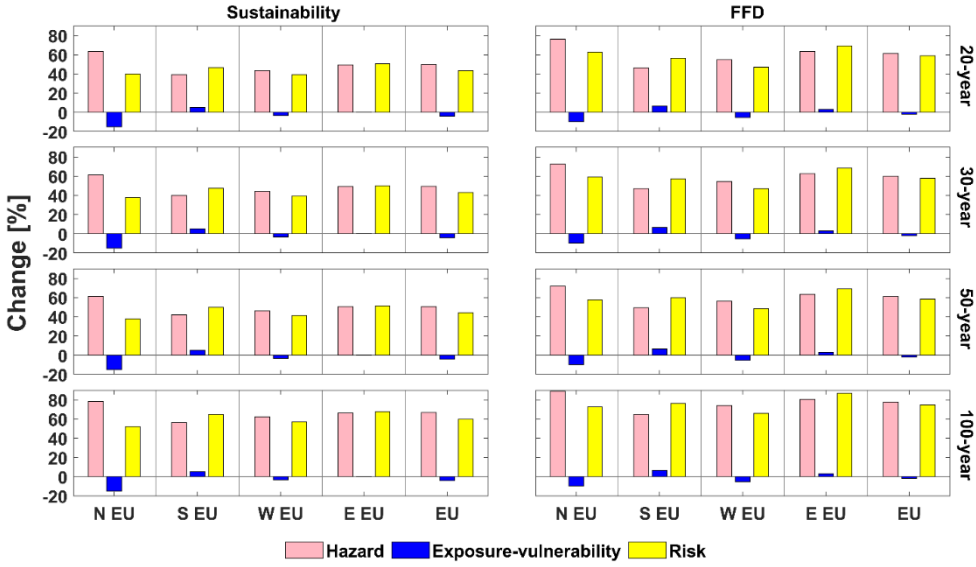


Figure 5.4: Decomposition of projected changes in 20-, 30-, 50- and 100-year flood risks at the regional and continental levels into exposure-vulnerability and hazard components under Sustainability and Fossil-fuel based development (FFD) scenarios. N EU: North Europe; S EU: South Europe; W EU: West Europe; E EU: East Europe; EU: Europe. See Table 5.3 for countries considered for each region. The EVI and risk results are based on an equal weight (EW) scheme.

Combining exposure and vulnerability in the form of the combined exposure-vulnerability index (EVI) reveals different trends among future socioeconomic scenarios. While future European EVI will be smaller than in 2010 under both Sustainability and Fossil-fuel based development scenarios, the decrease is a bit larger for the Sustainability scenario (Figure 5.4). Looking at the regional scale, a north-south bipolar pattern of EVI changes is observed for both socioeconomic scenarios where EVI is expected to decrease in north Europe and to increase in the south. This bipolar pattern is due to opposite

expected changes in total population and cropland area in north and south Europe. Similar to north Europe, the western European region shows a decreasing signal for both scenarios, while the eastern region shows a mixed behavior under different scenarios: steady state under the Sustainability scenario and increase under the Fossil-fuel based development scenario.

Several studies have used equal weights (EW) scheme to compute vulnerability (Collins et al. 2009; Dong et al. 2014). To examine the influence of the weighting scheme of EVI proxy indicators on the results, the results of EW scheme were compared with those from proportional weights (PW) and random weights (RW) schemes. The comparison shows higher EVI values computed with EW scheme compared to those computed with PW and RW schemes (Figure 5.5a). Similar results were reported for drought vulnerability index for Africa (Naumann et al., 2014) and at a global scale (Carrao et al., 2016). EVI values with a PW scheme are also smaller than those with a RW scheme. EVI values computed based on a PW scheme have a larger decreasing gradient from baseline socioeconomic conditions to the Fossil-fuel based development, making its difference with the other two schemes larger for future conditions.

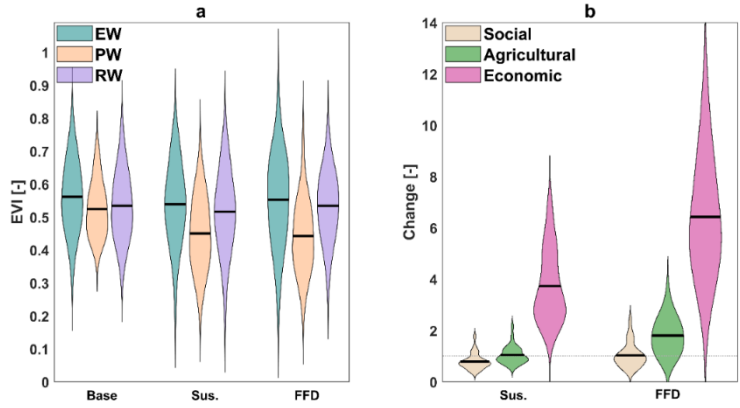


Figure 5.5: a) Comparison of combined exposure-vulnerability index (EVI) with equal weights (EW), proportional weights (PW) and random weights (RW) schemes for baseline socioeconomic conditions and for the year 2085 under Sustainability (Sus.) and Fossil-fuel based development (FFD) scenarios and b) country level projected changes in social, agricultural and economic vulnerabilities under Sus. and FFD scenarios. Note that the wider the violin plot, the higher the density. Horizontal line in violin plots show 50th percentile of EVI over European countries. In panel b, the changes are computed for the year 2085 with respect to the baseline year 2010.

Based on the results of EW and RW schemes, Romania and Hungary are the most vulnerable European countries to floods in the current socioeconomic conditions (Figure 5.6). Changing the weighting scheme to a PW scheme, in which the economic vulnerability component has a lower weight compared to EW and RW schemes, makes Belgium, the Netherlands and Denmark the most vulnerable European countries. The underlying drivers of the vulnerability for these two groups of countries differ. While economic and agricultural vulnerabilities (i.e., low GDP and high percentage of croplands) are the main driving forces for the eastern countries, social vulnerability (i.e., high population density, high proportion of urban population and high age-dependency ratio) are more responsible for the western countries. Under different future socioeconomic scenarios, the spatial distribution of the vulnerability varies. The eastern and southern countries (e.g., Macedonia, Hungary, Romania and Portugal) will be more vulnerable to floods, while less vulnerability of northern and western countries is expected under the future scenarios.

Generally, future changes in European EVI can be mainly attributed to the economic vulnerability element, more than the social and agricultural elements (Figure 5.5b). As the economic vulnerability element has a strong increasing trend for the future, it leads to an EVI decrease because of an indirect relationship between them. The contribution of the agricultural vulnerability under the Fossil-fuel based development scenario is noticeable, resulting in an increase in EVI values.

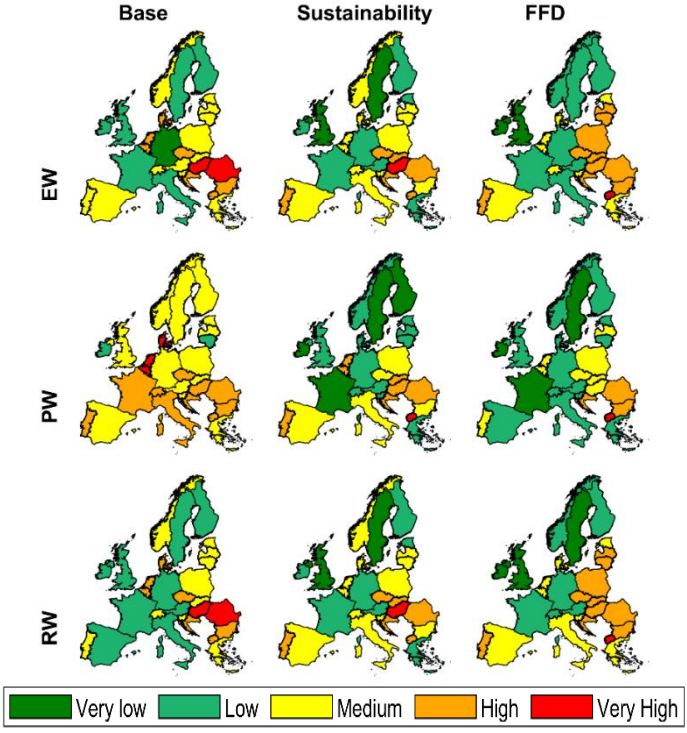


Figure 5.6: Combined exposure-vulnerability index (EVI) with equal weights (EW), proportional weights (PW) and random weights (RW) schemes in Europe for baseline socioeconomic conditions (2010) and for the year 2085 under Sustainability and Fossil-fuel based development (FFD) scenarios. The index was normalized spatially (over all countries) and temporally (over all scenarios and time periods) for each weighting scheme separately (i.e., normalization over the three cases in each row) and then classified into five classes from very low to very high, each of which corresponding to a quintile of the 0.05-0.95 range.

Being a product of hazard and EVI, flood risk is projected to increase over Europe for different return periods and future scenarios. Following the pattern of flood hazard, the changes in flood risk increase with the return period (Figure 5.4). The projected increases in the future flood risk for different return periods under the Fossil-fuel based development and Sustainability scenarios are within the ranges of 59-75% and 44-60%, respectively. For most of the cases, the higher than the Europe-wide average risk change is projected for east and south Europe (Figure 5.4). Despite the projected large changes in flood hazards in north and west Europe, the flood risk change in these regions is lower than the

Europe-wide average risk, thanks to their projected decreasing vulnerability. The flood risk change over Europe for different return periods is 14-15% higher under the Fossil-fuel based development scenario compared to the Sustainability scenario. Switching the future socioeconomic scenario to a fossil-fuel based one has the greatest effect on north Europe by 20-23% flood risk increase for different return periods.

At the country level, the largest risk increases under the Sustainability scenario are seen in Germany, Poland, Slovakia, Latvia and Portugal (Figure 5.7). As for the Fossil-fuel based development scenario, the countries located in south and east Europe (Greece, Italy, Bulgaria, Macedonia, Romania) as well as Luxembourg will face the most substantial increases in flood risk.

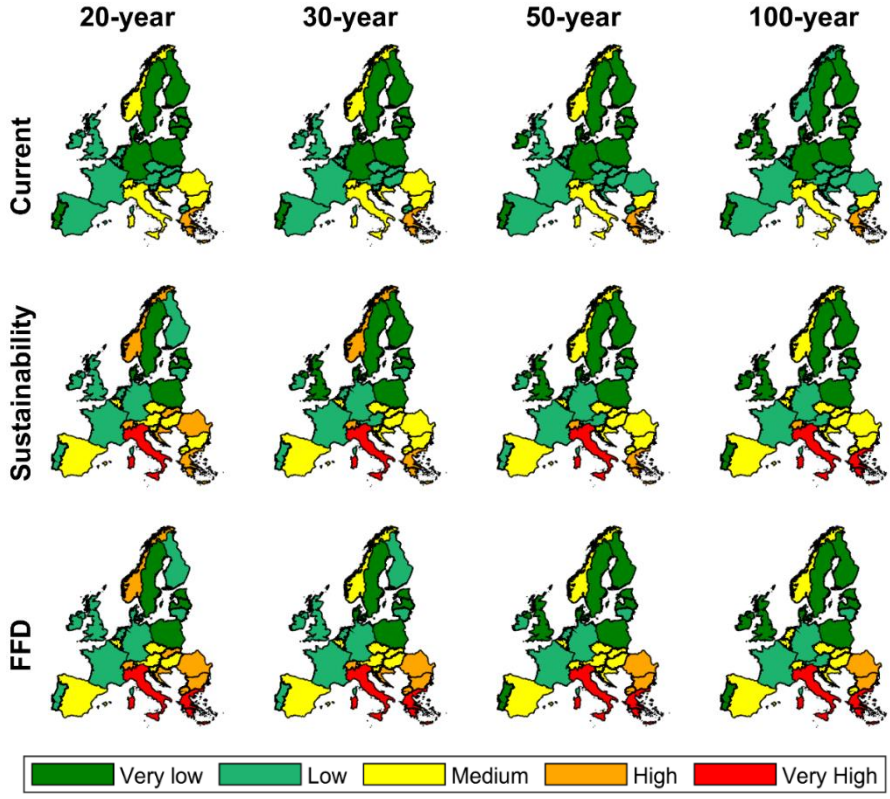


Figure 5.7: Risk of floods with return periods of 20, 30, 50 and 100 years in Europe for current climate conditions and for the 2071-2100 period under Sustainability and Fossil-fuel based development (FFD) scenarios. The index was normalized over all countries, return periods, scenarios and time periods (i.e., normalization over all the 12 cases) and then classified into five classes from very low to very high, each of which corresponding to a quintile of the 0.05-0.95 range.

The increases in flood risk in the countries with the highest risks were driven by an increase in both hazard and vulnerability, especially for the Fossil-fuel based development scenario (Figures 5.8 and 5.9). In almost all the European countries, the changes in flood hazard are far larger than the exposure-vulnerability changes.

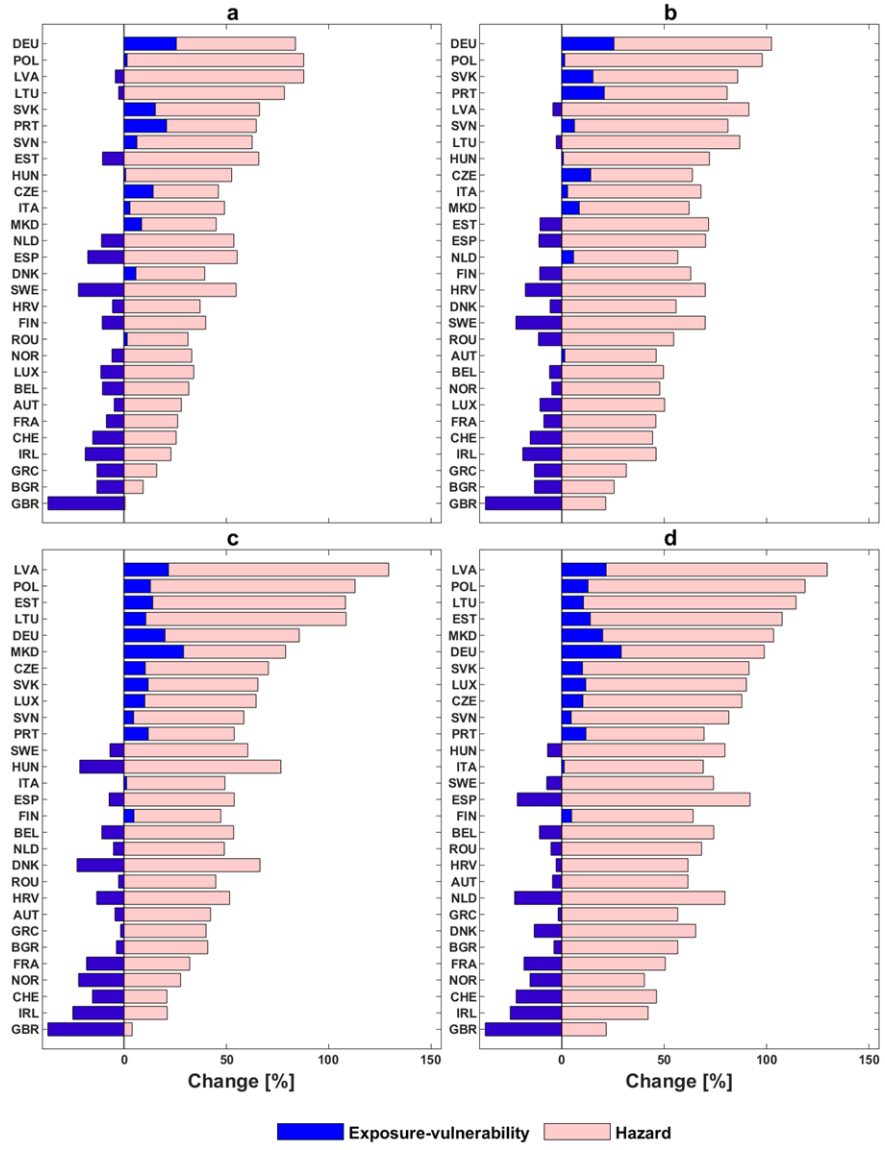


Figure 5.8: Decomposition of country-level projected changes in (a, c) 20- and (b, d) 100-year flood risks into exposure-vulnerability and hazard components under (a, b) Sustainability and (c, d) Fossil-fuel based development scenarios. In each case, countries are sorted in a descending order of flood risk changes. See Table 5.3 for countries code. See Figure 5.9 for 30- and 50-year flood risks.

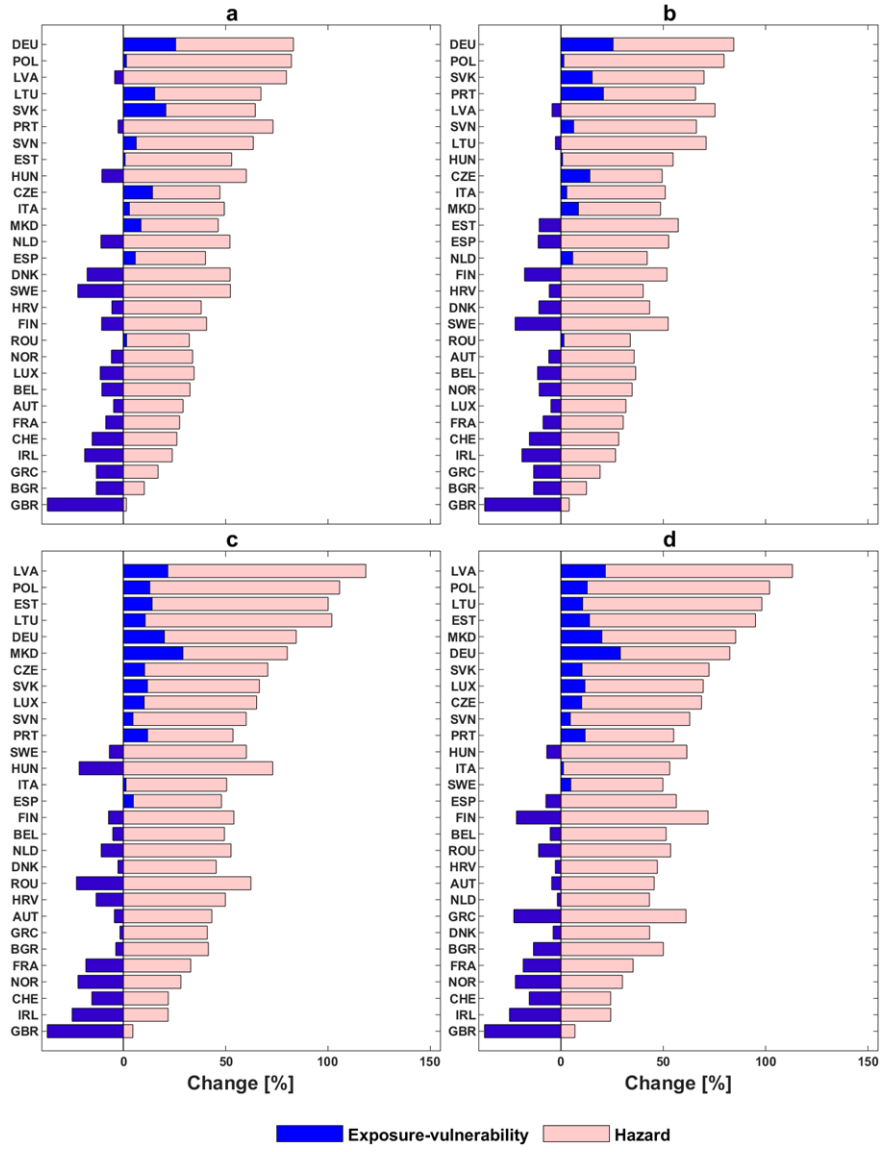


Figure 5.9: Decomposition of country-level projected changes in (a, c) 30- and (b, d) 50-year flood risks into exposure-vulnerability and hazard components under (a, b) Sustainability and (c, d) Fossil-fuel based development scenarios. In each case, countries are sorted in descending order of flood risk changes. See Table 5.3 for countries code.

The opposite directions of the changes in hazard and exposure-vulnerability in north and west Europe diminish the resulting increasing signals for risk (Figure 5.4). A more important role of climate change than socioeconomic

developments was also found for future coastal flooding over Europe (Vousdoukas et al., 2018). However, at the global scale, an opposite pattern was reported for future river flood risk (Winsemius et al., 2016).

The total uncertainty in the projected flood risk changes was decomposed into the uncertainties associated with climate models, combined future scenarios and weighting schemes of EVI. For all return periods, the climate model uncertainty is the dominant uncertainty source for flood risk changes over Europe, while the combined scenario source has the smallest contribution (Figure 5.10). The uncertainty associated with the choice of climate models has been found to be the main contributor to future hydrological projections uncertainty for the end of the twenty-first century (e.g., Hawkins and Sutton, 2011; Hosseinzadehtalaei et al., 2017; Tabari and Willems, 2018)..

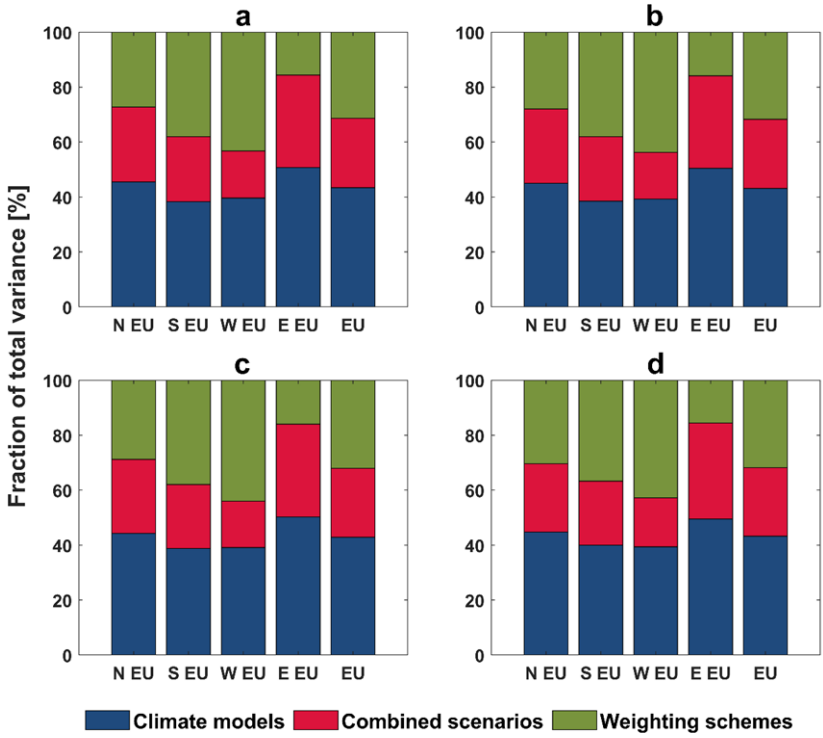


Figure 5.10: Fraction of the total variance of projected risk changes of floods with return periods of (a) 20, (b) 30, (c) 50 and (d) 100 years at the continental and regional scales explained by the uncertainties of climate models, combined future scenarios and weighting schemes of EVI. N EU: North Europe; S EU: South Europe; W EU: West Europe; E EU: East Europe; EU: Europe. See Table 5.3 for countries considered in each region.

5.4 Conclusions

We showed in this chapter that flood risks of different return periods over Europe increase up to 87% under future climatic and socioeconomic changes, with a higher increase for larger return periods. The projected increase varies with space, and the highest risk increase is found in eastern and southern regions. The results aggregated at the continental level indicated that shifting from the Fossil-fuel based development scenario (SSP5 combined with RCP8.5) to the Sustainability scenario (SSP1 combined with RCP4.5) would reduce flood risk by 14-15%. The shift in socioeconomic and climatic pathways is more influential in north Europe, with a risk reduction potential of 20-23%.

We also revealed which components of exposure-vulnerability modulate future flood risk in different countries the most under different socioeconomic development scenarios (Figure 5.11). The analysis identified exposure-vulnerability hotspots of each country and tracked changes in country performance under different future socioeconomic storylines. For each socioeconomic condition in current and future periods, the countries were ranked in a descending order in terms of each proxy indicator (e.g., from the highest to the lowest population density). Due to the indirect relationship of GDP and education level with vulnerability, the country rankings for GDP and education level were done in an ascending order. The country rankings for different indicators were compared and the vulnerability hotspot of each country was the proxy indicator for which the country had the highest rank. Although we found that all the European countries will be richer by an average two- to six-fold GDP increase depending on scenarios, the attention must be paid particularly to social and agricultural vulnerabilities. The results suggest that future flood risks over Europe can be reduced primarily by limiting emissions to reach a lower level of radiative forcing and thereby reducing the flood hazard. Urban population density should also be controlled which is increasing in all the 29 countries under both Sustainability and Fossil-fuel based development scenarios. The diminution of the future flood risk over Europe is also achievable by reducing the added value of agriculture to the GDP (cropland area in 90% of the countries increases under the Fossil-fuel based development scenario) and

raising public awareness and knowledge of flood hazards through deliberate DRR efforts and effective adaptation strategies. The within-country and -region DRR can also be implemented by limiting the adverse expected changes in the exposure-vulnerability proxy indicators. The results in Figure 5.11 show that the weakest exposure-vulnerability indicator for most of the European countries (83%) remain the same under both future socioeconomic storylines (Figure 5.11). The analysis is, however, only valid to identify the weakness of each European country relative to the other countries and proxy indicators considered in this study. The results should be viewed in a comparative context. For example, GDP is the weakest indicator for Estonia, Lithuania and Slovenia. It does not imply that the GDP of these countries is low in an absolute term, but it is considered weak relative to the other European countries and the other five indicators. Note that GDP of these countries is projected to be at least doubled in the future. It is worthwhile to mention that by changing the competitors, i.e., the composition of the proxy indicators and countries (e.g., putting the European countries in a global context) or socioeconomic scenarios, the exposure-vulnerability hotspot of each country may change. Similarly, the most vulnerable European countries to pluvial flooding may also change by including additional dimensions of vulnerability.

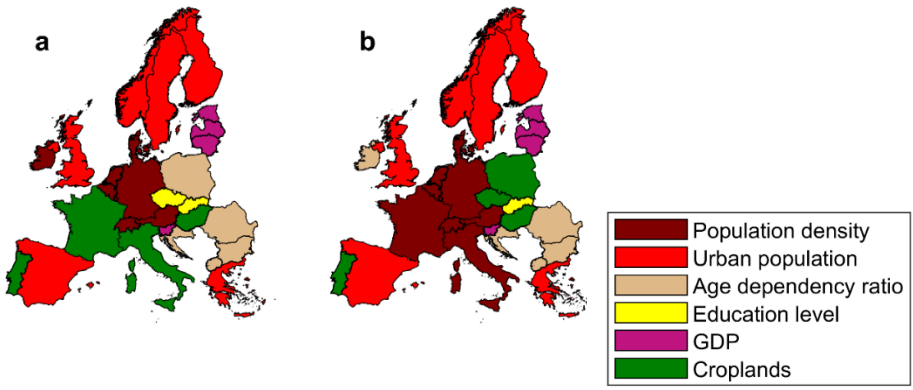


Figure 5.11: Exposure-vulnerability hotspots for European countries under (a) Sustainability and (b) Fossil-fuel based development scenarios. These hotspots should be taken into account for a disaster risk reduction (DRR) for future flood risks in Europe.

The results also showed that Europe's flood hazards of different return periods will increase in the future. Apart from the DRR efforts to reduce exposure and vulnerability to floods, there is also an urgent need to establish or reinforce preparedness plans by applying flood protection measures (Kundzewicz et al., 2019) and updating design criteria (Hosseinzadehtalaei et al., 2018) to reduce inundation humanitarian and financial losses. Willner et al. (2018) highlighted the need for the increase in flood protection in order to maintain the historic high-end flood risk in the next decades. Nevertheless, as hard adaptation strategies have their own cons such as increasing exposure (Kates et al., 2006) and vulnerability (Ludy and Kondolf, 2012), creating social injustice (Di Baldassarre et al., 2014), adversely affecting biodiversity and ecological functions (Auerswald et al., 2019), a combined grey-green-soft strategy that makes use of the benefits of all three strategies is more favorable. In this regard, in order to decrease the risk of decision failure regarding the evolving nature of flood risks over time, capacity building, win-win or low-regret, synergy options or iterative adaptation pathways must be undertaken.

CHAPTER 6

Synthesis and Outlook

6.1 Introduction

In this research, the continental changes in the frequency and magnitude of daily and sub-daily extreme precipitation under climate change were first quantified. In the next phase of this research, the applicability of integrating satellite remote sensing with regional climate model simulations to develop future intensity-duration-frequency curves as a pan European case study was demonstrated. Finally, a comprehensive analysis of future European pluvial flood risk assessment according to obtained changes in design precipitation in the previous phases, considering impact of climate change and socioeconomic development was presented. Furthermore, the identification and quantification of uncertainties in climate change projections were addressed throughout entire research study. Overall, the findings of this PhD study might arguably build essential information for decision-makers to plan climate change adaptation actions at European level.

This chapter includes an overview of the key findings of this research, followed by a description of associate limitations and caveats as well as future challenges, prospects and recommendations.

6.2 Key research findings

The answer of the research questions defined in this thesis as presented in chapter 1 is provided below.

RQ1| How will climate change affect extreme precipitation?

The results of the pan-European study presented in chapter 2 revealed an amplification of sub-daily extreme precipitation for all seasons except summer all over the continent for both RCP4.5 and RCP8.5 with more pronounced changes for RCP8.5. For summer, a north-south bipolar pattern with increasing extreme precipitation in northern Europe and a decreasing signal in southern Europe was identified.

Changes in extreme precipitation were found to be more influenced by season and return period with larger uncertainty in summer and higher return

periods in which internal variability plays a major role. It was indicated that the uncertainty can be reduced by applying regionalization through spatial pooling. As a result, spatial pooling was found to be an effective way to get less noisy extreme precipitation. The performance of spatial pooling to obtain more robust extreme precipitation changes greatly was shown to be dependent on season, precipitation time scale and intensity whereas it was less sensitive to greenhouse gas concentration and climate model spatial resolution. It was also found that precipitation time scale is an important factor in regionalization whenever and wherever short-duration convective precipitation is dominant, which is the case seasonally for summer and regionally for south Europe.

Although the signals get larger when precipitation gets more extreme from a return period of 5 to 50 years, their robustness has an opposite pattern. This is attributed to the larger internal variability of more extreme events and/or of a high spatial heterogeneity in physical processes resulting in extreme precipitation intensification.

To detect the effect of spatial resolution of climate models on climate change signals, daily EURO-CORDEX simulations with two spatial resolution of 0.44° and 0.11° were compered. This comparative analysis showed larger changes in design precipitation intensities by the finer resolution models.

The influence of the temporal resolution of climate model simulations for extreme precipitation was also evaluated by using daily and sub-daily EURO-CORDEX RCMs. Generally, larger climate change signals of 3-hourly extreme precipitation in comparison to daily extremes were projected for all regions over Europe. South Europe was found to have the highest sensitivity to both spatial and temporal resolutions of climate model simulations for the projections of extreme precipitation.

At the pan-European scale, the changes in sub-daily extreme precipitation was larger for higher return periods and shorter durations. Also, it was concluded that projection changes in extreme precipitation were more depended to return periods than precipitation durations. Spatially, extreme precipitation changes were generally larger for longitudes larger than 5°, pointing to the eastern half of Europe.

Lastly, this research highlighted that the temporal resolution was of more significance than the spatial resolution for climate change impact analysis on extreme precipitation. Results moreover indicated that one has to be careful in assuming spatial and temporal scale independency of climate change signals in the climate change impact studies. In agreement with other researches (Seneviratne et al., 2012; Pinto, 2015), it was also concluded that a higher resolution of regional climate models, EURO-CORDEX RCMs in this case, better represent extremes than the course spatial resolution CMIP5 GCMs.

RQ2| How will climate change affect IDF curves?

This research question was addressed in chapters 3 and 4. As a pilot study, future IDF curves were firstly developed for Belgium by using large ensembles of CMIP5 GCMs and EURO-CORDEX RCMs. The results of the both ensembles indicated that extreme precipitation will be amplified by the end of this century and this amplification varies depending on GCMs, RCPs and GCM initial conditions.

Building upon the findings for the case study in Belgium, the methodology was extended for Europe and future IDF curves were developed considering durations ranging from 30 minutes to 24 hours and return periods ranging between 1 and 100 years. The continental-scale IDF curves were developed based on high spatial and temporal resolution remote sensing based precipitation products and sub-daily precipitation simulations from the EURO-CORDEX RCMs. The results revealed that under climate change, future IDF curves will be uplifted and steepened, with a larger degree under RCP8.5 compared to RCP4.5. The upward shift in IDF curves is caused by the intensification of extreme precipitation under climate change. A larger increase of shorter duration extreme precipitation under climate change leads to steepen future IDF curves and the expected steepening is larger for higher return periods. Statistically, future IDF curves are uplifted as a result of an increase in the location parameter which is representing the mean of extreme precipitation distribution. The steepening of IDF curves arises from an increase in the scale parameter representing the dispersion of extreme precipitation distribution.

According to the findings of this research, both location and scale parameters of the extreme precipitation distribution will increase all over Europe under climate change.

The longer the return period and the shorter the duration of rainstorm is, the larger the change will be. The dependency of the changes on the return period is more pronounced compared to the duration. In addition to the intensity of extreme precipitation, the frequency of sub-daily extreme precipitation is projected to increase. The frequency of 50-year and 100-year extreme precipitation events will be doubled under RCP4.5 and tripled under RCP8.5. The expected changes in precipitation characteristics namely intensity, duration and frequency (IDF curves) must be incorporated for the future hydraulic and hydrology design and modeling as well as adaptation planning.

RQ3| How will climate and socio-economic changes affect pluvial flooding?

Pluvial flood and associated risks under climatic and socio-economic changes were quantified in chapter 5. To this end, pluvial flooding was determined using a satellite-based data driven approach as an alternative to the computationally expensive continental flood simulations. A country-level analysis of flood hazard showed that the expected changes in 100-year floods under RCP8.5 is not homogenously distributed across Europe, ranging from 56% in Switzerland to 114% in Sweden. Regionally, under changing climate, flood hazard increases at least by 46% for all return periods and scenarios with the highest change in north Europe and the lowest one in the south. Continentally, flood hazard will also increase for different return periods and scenarios by the end of this century. The expected changes in flood are generally larger for longer return periods.

Consequently, flood risk as a product of hazard and exposure-vulnerability, is projected to increase across Europe for different return periods and scenarios. It was demonstrated that flood risk of different return periods over Europe increases up to 87%. Spatially, the eastern and southern parts of Europe (Greece, Italy, Bulgaria, Macedonia, Romania) will face with the highest risk of pluvial floods. Although flood hazard changes are projected to increase in north and west of Europe, their projected changes in flood risk are lower than other

regions, owing to decrease in their projected vulnerability. Following the pattern of flood hazard changes, flood risk gets larger for longer return periods.

The increases in flood risk in the European countries with the highest risks were driven by an increase in both hazard and vulnerability, especially for the Fossil-fuel based development scenario (SSP5 combined with RCP8.5). In almost all the countries, the changes in flood hazard are far larger than the exposure-vulnerability changes.

From socio-economic and climate pathways point of view, flood risks can be reduced by shifting from a fossil-fuel based future to a more sustainable future (SSP1 scenario combined with RCP4.5). The avoided impact resulting from this shift is largest in northern Europe.

Among the vulnerability elements, a larger change is projected for economic vulnerability. As all European countries will be richer in the future and given the indirect relationship between flood risk and GDP, priority should be given to reduce social and agricultural vulnerabilities in order to diminish future flood risk. It should also be accompanied with a global effort to limit the radiative forcing to reduce the increasing flood hazard.

RQ4| How large is the uncertainty in extreme precipitation and flood projections and what are the main uncertainty contributors?

Since uncertainty assessment in climate change projections is essential for any application as well as to avoid over-optimistic results, special attention was paid to this matter throughout this thesis. The uncertainty was therefore quantified in the future projections of different variables including extreme precipitation, IDF curves and flood risk.

Initially, the uncertainty in the projections of extreme precipitation in Belgium as a pilot case study was evaluated by using a large ensemble of CMIP5 GCMs. To this end, the uncertainties related to GCMs, GCM initial conditions, RCPs and their sensitivity to the selection of different sub-ensembles of GCMs were assessed. In this case, the uncertainty analysis showed that the largest source of uncertainty is GCMs for all return periods and durations. Although, the other source of uncertainty namely GCMs initial condition and RCPs need

to be taken into account and cannot be neglected. It was also concluded that the uncertainty is more sensitive to the ensemble size for more extreme events and smaller time scales. For the same study area, by taking an ensemble of the EURO-CORDEX RCMs, the uncertainty associated with the choice of the RCMs was found to be larger than the other uncertainty components in the projection of more extreme precipitation.

Similar to the pilot case study, the uncertainty in the projections of extreme precipitation and IDF curves at the European scale was found to be larger for longer return periods. The uncertainty is, with lesser extent, is dependent on duration, being larger for shorter durations. These uncertainties need to be taken into consideration for design of infrastructure and adaptation planning.

The uncertainty in the projections of European pluvial flood risk was also assessed, by considering both climatic and socioeconomic elements. The total uncertainty in the future pluvial flood risk projections was decomposed into climate model, combined future scenario and weighing scheme of exposure vulnerability components. It was found that the choice of climate models is the dominant source of uncertainty for flood risk analysis over Europe, whereas the contribution of combined scenario is smallest.

The total uncertainty in flood risk projections and its main contributors vary over space. The relative contribution of the climate model uncertainty is largest in east Europe, while it is smallest in south Europe. In east Europe, the largest magnitude of the scenario uncertainty was obtained, while the weighting scheme exhibited the largest contribution in west Europe.

6.3 Caveats and future works

Several challenges and limitations are associated with the current study which need to be taken into consideration for the interpretation of the results. In the following section, key points that need to be considered in the future works are outlined as this thesis highlights several key factors and challenges that need to be investigated in the future work.

The results of this thesis broadly point to an increase in the intensity and frequency of extreme precipitation and pluvial flooding over Europe. There

might be differences in the results of the current research with previous studies. The driver of these differences can be, among others, type and number of climate models, greenhouse gas scenarios, historical and future periods and extreme value analysis technique. Therefore, the comparison of obtained results in some aspects are not straight forward. Hence, it is highlighted to unify the definition of extreme indices and analysis of extreme value analysis for the purpose of fair comparison. In this regard, in future work extreme precipitation can be defined based on the Expert Team on Climate Change Detection and Indices (ETCCDI) and the sensitivity of spatial pooling to these indices be tested. Likewise, the results of flood risk vary with data and methodology applied, including methodology applied to obtain flood hazard and infiltration, as well as the threshold of the design storms for drainage systems.

To quantify pluvial flooding, sub-daily extreme precipitation is required whereas both sub-daily climate models and observations are limited at continental scales. In the current research, available sub-daily ensemble of climate model at the time of analysis was used, while future work can be continued by applying higher temporal resolution of climate models upon availability. This study made use of 3-hourly precipitation simulations from 12-km RCMs for the climate change impact assessment. Nevertheless, summer sub-hourly precipitation extremes are usually produced by convective storms that cannot be well modelled by RCMs because of their coarse spatial and temporal resolutions. The convection-permitting climate models (CPMs; models with a spatial resolution < 4 km) are therefore required to more realistically represent local and short duration storm dynamics and reliably project future changes relevant for urban hydrology over Europe. The fine-scale simulations from such models are, however, still rare and limited to few modeling centers due to their high computational expenses. Future research directions within this area should focus on developing continental-scale fine-scale climate simulations. By applying an ensemble of such climate models, the climate change signals obtained in this study and applied in a statistical downscaling framework may be tested and compared with a dynamic downscaling approach. In addition, an ensemble of CPMs also provides more robust information for developing adaptation strategies. In the case of limited

resources, it could be worthwhile to examine whether going to higher temporal and spatial resolutions of CPMs or having a larger ensemble. Large ensembles of CPMs are, however, not available yet.

Another important issue is unavailability or inadequacy of observed sub-daily precipitation data to detect historical changes which is necessary for a better understanding of future changes and for statistical downscaling/bias correction of climate model data. Therefore, providing a comprehensive sub-daily precipitation dataset is crucial. In this research, future IDF curves were developed by applying remote sensing data and validated base on some stations in Belgium and the Netherlands with sub-daily precipitation of good quality and quantity. However, the validation at these sites may not valid for the continent with diverse climate conditions. Unfortunately, long-enough sub-daily ground rainfall data are not available for the validation of satellite estimates. Although sub-daily raingauge records have been recently collected (Lewis et al., 2019), the data are not publicly available. Upon the availability of such datasets, the rainfall estimations from the CMORPH and MSWEP can be validated for the entire Europe and the simulations of climate models be bias-corrected. Additionally, remote sensing dataset used in this study was available for 20 years at the time of analysis, possibly more precious changes in extreme precipitation with higher confidence can be obtained by applying longer dataset in the case of emerging in the future.

The results were drawn using combinations of multiple GCMs with one RCM. It is therefore recommended to repeat the analysis with new CMIP6 models or include more RCMs in the case of availability to validate the current results as the present results are model dependent and is not clear how general the obtained results are. The results of spatial pooling to obtain robustness of changes in extreme precipitation in this thesis are based on the five-member ensemble of the RCA4 RCM. Further research using a multi-model ensemble is needed to explore whether the results are sensitive to climate models. A multi-model multi-member convection-permitting model experiments, which are able to explicitly represent local convective events, are required to assess the effectiveness of the spatial pooling for local convective precipitation storms.

One of the future research work that can be built upon the investigations carried out in this thesis is to examine the effect of different temporal and spatial downscaling methods on the results and a comparison with the outputs of the quantile perturbation method applied in this study. In this way, the uncertainty associated to downscaling and bias correction methods can be quantified.

The uncertainties in the future projections of extreme precipitation, IDF curves and flood risk were quantified. For all the variables, the uncertainty associated with the choice of climate models was found to be the dominant source, although with spatially and temporally varying contributions. The large discrepancy across climate models needs further attention from climate modeling centers. The discrepancy is due to the fact that the models use different techniques to discretize the equations and to represent sub-grid effects. By reducing the horizontal grid spacing in climate models, surface characteristics (e.g., orography and coastlines) are better represented and the equations of motion are more accurately solved. It can thereby help to improve the representation of the interaction of the atmospheric flow with the surface, the large-scale atmospheric circulation and cloud processes and convection (the last ones when using a grid spacing finer than 4 km) (Prein et al., 2016). It is particularly important for extreme precipitation where there is a mismatch between the actual size of meteorological systems producing the extreme events and the temporal and spatial scales of the outputs provided by climate models (Mailhot and Duchesne, 2010). Future model development and improvement efforts should therefore focus on the improvements of climate models to better represent unresolved and poorly understood processes relevant for extreme precipitation especially moist convection are necessary to reduce climate model uncertainty (Tabari et al., 2019).

The simulations performed in this study for the development of IDF curves are computationally expensive because of the size of the study domain and the use of the DE-MC method for sampling the GPD parameters. This is indeed the first large-scale study which considers uncertainty in distribution parameter estimation; a large number of realizations (in our case, 5000 iterations including 2000 burn-in iterations) were sampled using the DE-MC method from the GPD parameters' posterior distributions at each model grid over Europe. The

development of IDF curves at a catchment scale would substantially decrease the simulation time. For reasons of comparison, the distribution parameters were also estimated using the classical maximum likelihood method. The point estimation of distribution parameters by these classical methods is much less computationally demanding, but this is at the expense of disregarding the uncertainties in the estimation of the parameters. Furthermore, The IDF curves were developed in this study by assuming that precipitation is primarily in the form of rainfall whose extreme events are more intense than snowmelt events. This assumption may not, however, be valid in snow-dominated regions where an extreme precipitation event can be mainly snowfall, which is not immediately available for rainfall-runoff processes, or where snowmelt or rain-on-snow rates exceed extreme rainfall. The rainfall-based IDF curves in these regions may lead to design-storm overestimation and infrastructure overdesign in the former case and design-storm underestimation and infrastructure underdesign in the latter (Yan et al., 2018). Future research may address snow processes in the development of IDF curves in the snow-dominated regions in Europe.

The methodology applied in this research to estimate flood risk is based on a satellite-based data driven approach. Although data-driven approaches have the advantages of simplicity without the requirement to deal with the mathematics behind the simulators, a substantially shorter run time which is essential for applications such as decision support and a high performance in the case of data limitation, their results need to be validated against detailed hydrodynamic simulations. It is therefore recommended to use an advanced hydrological model including drainage system components for the purpose of comparison to the results of current thesis.

In this thesis, for the aim of flood risk assessment, 10-year return period was considered as the threshold over which pluvial floods may happen, while urban drainage systems in different parts of Europe in practice are designed for various return periods ranging from 2 and 20 years, depending on the specific system properties. It would be interesting to further examine this matter in the analysis of flood risk for the future works.

Another venue for further work might be considering compound flood events including pluvial, fluvial and coastal floods as most of these hazards occur at

the same time particularly in the coastal or fluvial regions. Therefore, analyzing joint flood hazards considering multi-dimensional hazard impact would be useful for climate change adaptation.

For the flood risk analysis, a combined exposure-vulnerability index was developed at national, regional and continental scales, integrating six social, economic and agricultural proxy indicators. Inclusion of more proxy indicators relevant to flooding and at smaller spatial scales (e.g., at pixel or municipality levels) would provide useful information for more detailed flood risk analysis.

Bibliography

Aalbers, E.E., Lenderink, G., van Meijgaard, E., van den Hurk, B.J. (2017) Local-scale changes in mean and heavy precipitation in Western Europe, climate change or internal variability? *Climate Dynamics*, DOI: 10.1007/s00382-017-3901-9.

Agard, J., et al., (2014), Annex II: Glossary, in Climate Change 2014: Impacts, Adaptation, and Vulnerability. Part A: Global and Sectoral Aspects. Contribution ofWorking Group II to the Fifth Assessment Report of the Intergovernmental Panel on Climate Change , pp. 1757–1776 , Cambridge Univ. Press, Cambridge, U. K.

AghaKouchak, A., Nasrollahi, N. (2010) Semi-parametric and parametric inference of extreme value models for rainfall data. *Water Resources Management*, 24(6), 1229–1249.

Ahmadalipour, A., Moradkhani, H., Castelletti, A., Magliocca, N. (2019) Future drought risk in Africa: Integrating vulnerability, climate change, and population growth. *Science of the Total Environment*, 662, 672-686.

Ahmed, K.F., Wang, G., Silander, J., Wilson, A.M., Allen, J.M., Horton, R., Anyah, R. (2013) Statistical downscaling and bias correction of climate model outputs for climate change impact assessment in the U.S. northeast. *Global and Planetary Change*, 100: 320–332.

Ahmed, S., Tsanis, I. (2016) Climate Change Impact on Design Storm and Performance of Urban Storm-Water Management System- A Case Study on West Central Mountain Drainage Area in Canada. *Hydrology: Current Research*, 7,229.

Alam, M.S., Elshorbagy, A. (2015) Quantification of the climate change-induced variations in Intensity–Duration–Frequency curves in the Canadian Prairies. *Journal of Hydrology*, 527:990–1005.

Alfieri, L., Burek, P., Feyen, L., Forzieri, G. (2015) Global warming increases the frequency of river floods in Europe. *Hydrology and Earth System Sciences*, 19:2247–2260.

Alfieri, L., et al., (2017) Global projections of river flood risk in a warmer world. *Earth's Future*, 5(2), 171-182.

Alfieri, L., Feyen, L., Di Baldassarre, G. (2016) Increasing flood risk under climate change: a pan-European assessment of the benefits of four adaptation strategies. *Climatic Change*, 136, 507–521.

Alfieri, L., Feyen, L., Dottori, F., & Bianchi, A. (2015). Ensemble flood risk assessment in Europe under high end climate scenarios. *Global Environmental Change*, 35, 199-212.

Arnbjerg-Nielsen, K. (2012) Quantification of climate change effects on extreme precipitation used for high resolution hydrologic design. *Urban water*, J 9(2):57-65.

Arnbjerg-Nielsen, K., Willems, P., Olsson, J., Beecham, S., Pathirana, A., Gregersen, I.B., Madsen, H., Nguyen, V.T.V. (2013) Impacts of climate change on rainfall extremes and urban drainage systems: a review. *Water Science & Technology*, 68(1):16-28.

Arnell, N.W., Gosling, S.N. (2016) The impacts of climate change on river flood risk at the global scale. *Climatic Change*, 134(3), 387-401.

Arnell, N.W., Lloyd-Hughes, B. (2014) The global-scale impacts of climate change on water resources and flooding under new climate and socio-economic scenarios. *Climatic Change*, 122, 127–140.

Auerswald, K., Moyle, P., Seibert, S. P., Geist, J. (2019) HESS Opinions: Socio-economic and ecological trade-offs of flood management–benefits of a transdisciplinary approach. *Hydrology and Earth System Sciences*, 23, 1035–1044.

Ballabio, C., Panagos, P., Monatanarella, L. (2016) Mapping topsoil physical properties at European scale using the LUCAS database. Geoderma, 261, 110-123.

Ban, N., Schmidli, J., Schär. C (2015) Heavy precipitation in a changing climate: Does short-term summer precipitation increase faster? *Geophysical Research Letters*, 42 1165-1172.

Barbero, R., Fowler, H.J., Lenderink, G., Blenkinsop, S. (2017) Is the intensification of precipitation extremes with global warming better detected at hourly than daily resolutions?. *Geophysical Research Letters*, 44(2), 974-983.

Bardet, L., Duluc, C.M., Rebour, V., L'Her, J. (2011) Regional frequency analysis of extreme storm surges along the French coast. *Natural Hazards and Earth System Sciences*, 11 1627–1639.

Barra, M. (2016) Comparing the costs of grey and green infrastructure in the Paris region. 7th Global Forum on Urban Resilience & Adaptations, 6-8 July 2016, Bonn, Germany.

Beck, H. E., Pan, M., Roy, T., Weedon, G. P., Pappenberger, F., Van Dijk, A. I., ... & Wood, E. F. (2019). Daily evaluation of 26 precipitation datasets

using Stage-IV gauge-radar data for the CONUS. *Hydrology & Earth System Sciences*, 23(1).

Beck, H. E., Van Dijk, A. I., Levizzani, V., Schellekens, J., Gonzalez Miralles, D., Martens, B. and De Roo, A. (2017) MSWEP: 3-hourly 0.25 global gridded precipitation (1979-2015) by merging gauge, satellite, and reanalysis data. *Hydrology and Earth System Sciences*, 21(1), 589–615.

Berg, P., Moseley, C., Haerter, J.O. (2013) Strong increase in convective precipitation in response to higher temperatures. *Nature Geoscience*, 6(3), 181–185.

Berggren, K., Svensson, G., Viklander, M. (2008) Urban drainage and climate change: a problematic approach. Luleå University of Technology, Newsletter, 1.

Berne, A., Delrieu, G., Creutin, J. D. and Obled, C. (2004) Temporal and spatial resolution of rainfall measurements required for urban hydrology. *Journal of Hydrology*, 299(3–4), 166–179.

Blaikie, P., Cannon, T., Davis, I., & Wisner, B. (2004) At Risk: Natural Hazards, People's Vulnerability, and Disasters, 2nd edition. Routledge, London, UK.

Blenkinsop, S., Lewis, E., Chan, S.C., Fowler, H.J. (2017) Quality-control of an hourly rainfall dataset and climatology of extremes for the UK. *International Journal of Climatology*, 37(2):722-740.

Booth, B.B.B., Bernie, D., McNeall, D., Hawkins, E., Caesar, J., Boulton, C., Friedlingstein, P., Sexton, D.M.H. (2013) Scenario and modelling uncertainty in global mean temperature change derived from emission-driven global climate models. *Earth System Dynamics*, 4(1):95-108.

Booth, B.B.B., Dunstone, N.J, Halloran, P.R., Andrews, T. Bellouin, N. (2012) Aerosols implicated as a prime driver of twentieth-century north Atlantic climate variability. *Nature*, 484 228–232.

Boteler, B., Abhold, K., Tröltzsch, J., Penha-Lopes, G., Fonseca, A.L., Campos, I., ... Zandervoort, M. (2015) Experiences in bottom-up adaptation approaches in Europe and elsewhere: Deliverable D4.2, European Community's Seventh Framework Programme.

Boukhelifa, M., Meddi, M., and Gaume, E. (2018) Integrated Bayesian Estimation of Intensity-Duration-Frequency Curves: Consolidation and Extensive Testing of a Method. *Water Resources Research*, 54(10), 7459-7477.

Brekke, L., Barsugli, J. (2013) Uncertainties in projections of future changes in extremes. In:AghaKouchak A, Easterling D, Hsu K, Schubert S, Sorooshian S (eds) Extremes in a changing climate: detection, analysis and uncertainty. Springer, Dordrecht. p 309−346.

Bürger, G., Sobie, S.R., Cannon, A.J., Werner, A.T., Murdock, T.Q. (2012). Downscaling Extremes: An Intercomparison of Multiple Methods for Future Climate. *Journal of Climate*, 26:3429-3449.

Cannon, A. J, Innocenti, S. (2019) Projected intensification of sub-daily and daily rainfall extremes in convection-permitting climate model simulations over North America: implications for future intensity–duration–frequency curves. *Natural Hazards and Earth System Sciences*, 19(2), 421–440.

Cannon, A. J., Sobie, S. R., Murdock, T. Q. (2015) Bias correction of GCM precipitation by quantile mapping: How well do methods preserve changes in quantiles and extremes?. *Journal of Climate*, 28(17), 6938-6959.

Cannon, A.J. (2015). Selecting GCM scenarios that span the range of changes in a multimodel ensemble: application to CMIP5 climate extremes indices. *Journal of Climate*, 28(3): 1260-1267.

Cardona, O. D., Van Aalst, M. K., Birkmann, J., Fordham, M., Mc Gregor, G., Rosa, P., ... & Keim, M. (2012). Determinants of risk: exposure and vulnerability. In Managing the Risks of Extreme Events and Disasters to Advance Climate Change Adaptation: Special Report of the Intergovernmental Panel on Climate Change (pp. 65-108). Cambridge University Press.

Carrao, H., Naumann, G., Barbosa, P. (2016) Mapping global patterns of drought risk: An empirical framework based on sub-national estimates of hazard, exposure and vulnerability. *Global Environmental Change*, 39, 108-124.

Casanueva, A., Kotlarski, S., Herrera, S., Fernández, J., Gutiérrez, J. M., Boberg, F., ... & Keuler, K. (2016) Daily precipitation statistics in a EURO-CORDEX RCM ensemble: added value of raw and bias-corrected high-resolution simulations. *Climate dynamics*, 47(3-4), 719-737.

Chandra, R., Saha, U., Mujumdar, P.P. (2015) Model and parameter uncertainty in IDF relationships under climate change. *Advances in Water Resources*, 79:127-139.

Chen, C. T., & Knutson, T. (2008). On the verification and comparison of extreme rainfall indices from climate models. *Journal of Climate*, 21(7), 1605-1621.

Chen, H., Sun, J., Chen, X. (2014). Projection and uncertainty analysis of global precipitation-related extremes using CMIP5 models. *International Journal of Climatology*, 34: 2730–2748.

Chen, J., Brissette, F. P., Chaumont, D., Braun, M. (2013) Finding appropriate bias correction methods in downscaling precipitation for hydrologic impact studies over North America. *Water Resources Research*, 49, 4187–4205.

Chen, J., Brissette, F. P., Poulin, A., & Leconte, R. (2011) Overall uncertainty study of the hydrological impacts of climate change for a Canadian watershed. *Water Resources Research*, 47(12).

Cheng, L., AghaKouchak, A., Gilleland, E., Katz, R. W. (2014) Non-stationary extreme value analysis in a changing climate. *Climatic Change*, 127(2), 353–369.

Cheng, L., Phillips, T. J., AghaKouchak, A. (2015) Non-stationary return levels of CMIP5 multi-model temperature extremes. *Climate Dynamics*, 44(11-12), 2947–2963.

Chini, C.M., Canning, J.F., Schreiber, K.L., Peschel, J.M., Stillwell, A.S. (2017) The Green Experiment: Cities, Green Stormwater Infrastructure, and Sustainability. *Sustainability*, 9(1):105, doi: 10.3390/su9010105.

Christensen, J.H., Carter, T.R., Rummukainen, M., Amanatidis, G. (2007) Evaluating the performance and utility of regional climate models: the prudence project Climatic Change. 81 1–6.

CMORPHv1.0. (2015) NOAA CPC Morphing Technique ("CMORPH"), version 1.0, CRT. NOAA Center for Weather and Climate Prediction, Climate Prediction Center.

Collins, M., Booth, B.B.B., Bhaskaran, B., Harris, G.R., Murphy, J.M., Sexton, D.M.H., Webb, M.J. (2011) Climate model errors, feedbacks and forcings: a comparison of perturbed physics and multi-26 model ensembles. *Climate Dynamics*, 36 1737–1766 27.

Collins, T.W., Grineski, S.E., de Lourdes Romo Aguilar, M. (2009) Vulnerability to environmental hazards in the Ciudad Juárez (Mexico)–El Paso (USA) metropolis: a model for spatial risk assessment in transnational context. *Applied Geography*, 29, 448–461.

Coulthard, T.J., Ramirez, J., Fowler, H.J., Glenis, V. (2012) Using the UKCP09 probabilistic scenarios to model the amplified impact of climate change on drainage basin sediment yield. *Hydrology and Earth System Sciences*, 16(11):4401–4416.

Courty, L., Wilby, R. L., Hillier, J., Slater, L. J. (2019) Intensity-Duration-Frequency curves of precipitation at the global scale (accessed via https://eartharxiv.org/w56b8/download).

Daigneault, A., Brown, P., Gawith, D. (2016) Dredging versus hedging: Comparing hard infrastructure to ecosystem-based adaptation to flooding. *Ecological Economics*, 122:25-35.

Dale, M., Luck, B., Fowler, H.J., Blenkinsop, S., Gill, E., Bennett, J., ... Chan, S. (2015) New climate change rainfall estimates for sustainable drainage. Proceedings of the Institution of Civil Engineers. *Engineering Sustainability*, doi:10.1680/jensu.15.00030.

Dankers, R., et al. (2014) First look at changes in flood hazard in the Inter-Sectoral Impact Model Intercomparison Project ensemble. PNAS 111 (9), 3257-3261.

De Moel, H., Jongman, B., Kreibich, H., Merz, B., Penning-Rowsell, E., & Ward, P. J. (2015). Flood risk assessments at different spatial scales. *Mitigation and Adaptation Strategies for Global Change*, 20(6), 865-890.

De Paola, F., Giugni, M., Topa, M.E., Bucchignani, E. (2014) Intensity-Duration-Frequency (IDF) rainfall curves, for data series and climate projection in African cities. *SpringerPlus*, 3(1):1.

Déqué, M., Rowell, D.P., Lüthi, D., Giorgi, F., Christensen, J.H., Rockel, B., van den Hurk, B.J.J.M. (2007) An intercomparison of regional climate simulations for Europe: assessing uncertainties in model projections. *Climatic Change*, 81(1), 53-70.

Déqué, M., Somot, S., Sanchez-Gomez, E., Goodess, C.M., Jacob, D., Lenderink, G., Christensen, O.B. (2012) The spread amongst ENSEMBLES regional scenarios: regional climate models, driving general circulation models and interannual variability. *Climate Dynamics*, 38(5), 951-964.

Derkzen, M.L., van Teeffelen, A.J., Verburg, P.H. (2017) Green infrastructure for urban climate adaptation: How do residents' views on climate impacts and green infrastructure shape adaptation preferences? *Landscape and Urban Planning*, 157:106-130.

Deser, C., Phillips, A., Bourdette, V., Teng, H. (2012) Uncertainty in climate change projections: the role of internal variability. *Climate Dynamics*, 38:527–546.

Deser, C., Phillips, A.S., Alexander, M.A., Smoliak, B.V. (2014) Projecting North American climate over the next 50 years: Uncertainty due to internal variability. *Journal of Climate*, 27:2271–2296.

Desramaut, N. (2008) Estimation of intensity duration frequency curves for current and future climates (Doctoral dissertation, McGill University Montreal, Quebec, Canada).

Dessu, S.B., Melesse, A.M. (2013) Impact and uncertainties of climate change on the hydrology of the Mara River basin, Kenya/Tanzania. *Hydrological Processes*, 27(20): 2973-2986.

Di Baldassarre, G., Kemerink, J.S., Kooy, M., Brandimarte, L. (2014) Floods and societies: the spatial distribution of water-related disaster risk and its dynamics. Wiley Interdisciplinary Reviews: *Water*, 1, 133–139.

Döll, P., Romero-Lankao, P. (2017). How to embrace uncertainty in participatory climate change risk management—A roadmap. *Earth's Future*, 5(1), 18-36.

Donat, M.G., Lowry, A.L., Alexander, L.V., O'Gorman, P.A., Maher, N. (2016) More extreme precipitation in the world's dry and wet regions *Nature Climate Change*, 6 508–513.

Dong, W., Liu, Z., Zhang, L., Tang, Q., Liao, H., Li, X. (2014) Assessing heat health risk for sustainability in Beijing's urban heat island. *Sustainability*, 6, 7334–7357.

Dosio, A., Fischer, E.M. (2018) Will half a degree make a difference? Robust projections of indices of mean and extreme climate in Europe under 1.5 C, 2 C, and 3 C global warming. *Geophysical Research Letters*. 45 935-944

Dottori, F., et al. (2018) Increased human and economic losses from river flooding with anthropogenic warming. *Nature Climate Change*, 8(9), 781.

EEA, (2010) Mapping the impacts of natural hazards and technological accidents in Europe – An overview of the last decade, European Environment Agency Technical report 13/2010, Copenhagen, Denmark, 144 pp.

EEA, (2013) Digital Elevation Model over Europe (EU-DEM), European Energy Agency, available at: http://www.eea.europa.eu/data-and-maps/data/eu-dem (last access: 5 February 2019).

Embrechts, P., Klüppelberg, C., Mikosch, T. (1997) Modelling extremal events for insurance and finance, vol 33. Springer, Berlin.

Endris, H.S., Omondi. P., Jain, S., Lennard, C., Hewitson, B., Chang'a, L., Awange, J.L., Dosio. A., Ketiem, P., Nikulin, G., Panitz, H.J., Büchner, M., Stordal, F., Tazalika, L. (2013) Assessment of the performance of CORDEX regional climate models in simulating east African rainfall. *Journal of Climate*, 26(21), 8453–8475.

EU, (2007) Directive 2007/60/EC of the European Parliament and of the Council of 23 October 2007 on the assessment and management of flood risks. Off. J. Eur. Union L288, 27–34.

European Environment Agency (EEA) (2012) Urban Adaptation to Climate Change in Europe: Challenges and opportunities for cities together with supportive national and European policies (No. 2/2012). Publications Office of the European Union, Luxembourg.

European Environment Agency (EEA) (2013) Adaptation in Europe — Addressing risks and opportunities from climate change in the context of socio-economic developments, EEA Report No 3/2013, European Environment Agency, Copenhagen, Denmark.

European Environment Agency (EEA) (2016) Flood risks and environmental vulnerability exploring the synergies between floodplain restoration, water policies and thematic policies. Technical report No 1/2016. ISBN 978-92-9213-716-8.

Falter, D., Dung, N. V., Vorogushyn, S., Schröter, K., Hundecha, Y., Kreibich, H., Apel, H., Theisselmann, F., Merz, B. (2016) Continuous, large-scale simulation model for flood risk assessments: proof-of-concept. *Journal of Flood Risk Management*, 9, 3–21.

Fang, J., et al. (2019) Coastal flood risks in China through the 21st century – An application of DIVA. *Science of The Total Environment*, doi: 10.1016/j.scitotenv.2019.135311.

Faridzad, M., Yang, T., Hsu, K., Sorooshian, S., Xiao, C. (2018) Rainfall frequency analysis for ungauged regions using remotely sensed precipitation information. *Journal of Hydrology*, 563, 123–142.

Fatichi, S., Ivanov, V.Y., Paschalis, A., Peleg, N., Molnar, P., Rimkus, S., Kim, J., Burlando, P., Caporali E. (2016) Uncertainty partition challenges the predictability of vital details of climate change. *Earth's Future*, 4(5): 240–251.

Ferro, C.A., Jupp, T.E., Lambert, F.H., Huntingford, C., Cox, P.M. (2012) Model complexity versus ensemble size: allocating resources for climate prediction. *Philosophical Transactions of the Royal Society A: Mathematical, Physical and Engineering Sciences*, 370(1962):1087-1099.

Feser, F., Rockel, B., von Storch, H., Winterfeldt, J., Zahn, M. (2011) Regional climate models add value to global model data: a review and selected examples. *Bulletin of the American Meteorological Society*, 92 1181–1192.

Fischer, E. M., Knutti, R. (2015) Anthropogenic contribution to global occurrence of heavy-precipitation and high-temperature extremes. *Nature Climate Change*, 5(6), 560–564.

Fischer, E.M., Beyerle, U., Knutti, R. (2013) Robust spatially aggregated projections of climate extremes. *Nature Climate Change*, 3 1033-1038.

Fischer, E.M., Sedláček, J., Hawkins, E., Knutti, R. (2014) Models agree on forced response pattern of precipitation and temperature extremes. *Geophysical Research Letters*, 41 8554-8562.

Fletcher, T.D., Shuster, W., Hunt, W. F., Ashley, R., Butler, D., Arthur, S., ... Mikkelsen, P.S. (2015) SUDS, LID, BMPs, WSUD and more–The evolution and application of terminology surrounding urban drainage. *Urban Water*, 12(7):525-542.

Fowler, H., Ekström, M., Blenkinsop, S., Smith, A. (2007) Estimating change in extreme European precipitation using a multi model ensemble. *Journal of Geophysical Research: Atmospheres*, 112 D1804.

Frei C, Schöll R, Schmidli J, Fukutome S, Vidale PL. (2006) Future change of precipitation extremes in Europe: an intercomparison of scenarios from regional climate models. *Journal of Geophysical Research: Atmospheres* 111, D06105.

Frei, C., Schöll, R., Fukutome, S., Schmidli, J., Vidale, P.L. (2006) Future change of precipitation extremes in Europe: intercomparison of scenarios from regional climate models. *Journal of Geophysical Research: Atmospheres*, 111 D06105.

Friedlingstein, P. et al., (2006) Climate-carbon cycle feedback analysis: Results from the C4MIP model intercomparison. *Journal of Climate*, 19 3337–3353.

Fujimori, S., Hasegawa, T., Ito, A., Takahashi, K., Masui, T. (2018) Gridded emissions and land-use data for 2005–2100 under diverse socioeconomic and climate mitigation scenarios. *Scientific Data*, 5, 180210.

Gadian, A.M., Blyth, A.M., Bruyere, C.L., Burton, R.R., Done, J.M., Groves, J. et al.,. (2018) A case study of possible future summer convective precipitation over the UK and Europe from a regional climate projection. *International Journal of Climatology*, 38 2314–2324.

Gado, T. A., Hsu, K., Sorooshian, S. (2017) Rainfall frequency analysis for ungauged sites using satellite precipitation products. *Journal of Hydrology*, 554, 646–655.

Gaume, E., Bain, V., Bernardara, P., Newinger, O., Barbuc, M., Bateman, A., ... & Daliakopoulos, I. (2009). A compilation of data on European flash floods. *Journal of Hydrology*, 367(1-2), 70-78.

Gehne, M., Hamill, T. M., Kiladis, G. N., Trenberth, K.E. (2016) Comparison of global precipitation estimates across a range of temporal and spatial scales. *Journal of Climate,* 29(21), 7773–7795.

Gelman, A., Shirley, K. (2011) Inference from simulations and monitoring convergence. Handbook of Markov Chain Monte Carlo: 163–174.

Giorgi, F., Hewitson, B., Christensen, J., Hulme, M., Von Storch, H., Whetton, P., Jones, R., Mearns, L. et al., (2001) Regional Climate Information—Evaluation and Projections Geological and Atmospheric Sciences Publications. 110. https://lib.dr.iastate.edu/ge_at_pubs/110.

Giorgi, F., Torma, C., Coppola, E., Ban, N., Schär, C., Somot, S. (2016) Enhanced summer convective rainfall at Alpine high elevations in response to climate warming. *Nature Geoscience*, 9 584–589.

Giuntoli, I., et al. (2015) Future hydrological extremes: the uncertainty from multiple global climate and global hydrological models. *Earth System Dynamics*, 6 (1), 267-285.

Goudenhoofdt, E., Delobbe, L., Willems, P. (2017) Regional frequency analysis of extreme rainfall in Belgium based on radar estimates. *Hydrology and Earth System Sciences*, 21 5385-5399.

Gudmundsson, J., Bremnes, J., Haugen, J. E., Engen-Skaugen, T. (2012) Technical note: Downscaling RCM precipitation to the station scale using statistical transformations—A comparison of methods. *Hydrology and Earth System Sciences*, 16, 3383–3390.

Haario, H., Saksman, E., Tamminen, J. (1999) Adaptive proposal distribution for random walk Metropolis algorithm. *Computational Statistics*, 14(3), 375– 395.

Haario, H., Saksman, E., Tamminen, J. (2001) An adaptive Metropolis algorithm. Bernoulli 7, 223– 242.

Haerter, J.O., Berg, P., Hagemenn, S. (2010) Heavy rain intensity distributions on varying time scales and at different temperatures. *Journal of Geophysical Research*, 115, D17102, doi:10.1029/2009JD013384.

Hallegatte, S., Dumas, P. (2008) Adaptation to climate change: soft vs. hard adaptation. OECD Expert workshop on Economic aspects of adaptation to Climate Change.

Halmstad, A., Najafi, M. R., Moradkhani, H. (2012) Analysis of precipitation extremes with the assessment of regional climate models over the Willamette River Basin-U.S. *Hydrological Processes*, 27, 2579–2590.

Hanel, M., Buishand, T. A. (2010) On the value of hourly precipitation extremes in regional climate model simulations. *Journal of Hydrology*, 393, 265–273.

Hanel, M., Buishand, T.A., Ferro, C.A. (2009) A nonstationary index flood model for precipitation extremes in transient regional climate model simulations. *Journal of Geophysical Research: Atmospheres*, 114 D15107.

Hassanzadeh E, Hassanzadeh A, Elshorbagy A. (2014) Quantile-based downscaling of precipitation using genetic programming: application to IDF curves in Saskatoon. *Journal of Hydrologic Engineering*, 19(5), 943-955.

Hawkins, E., Sutton, R. (2009) The potential to narrow uncertainty in regional climate predictions. *Bulletin of the American Meteorological Society*, 90:1095–1107.

Hawkins, E., Sutton, R. (2011) The potential to narrow uncertainty in projections of regional precipitation change. *Climate Dynamics*, 37(1-2):407-418.

Haylock, M.R., Hofstra, N., Klein Tank, A.M.G., Klok, E.J., Jones, P.D., New, M. (2008) A European daily high-resolution gridded dataset of surface temperature and precipitation. *Journal of Geophysical Research*, (Atmospheres). 113, D20119.

He, C., Li, T. (2019) Does global warming amplify interannual climate variability?. *Climate Dynamics*, 52, 2667–2684.

Hegerl, G. C., Black, E., Allan, R. P., Ingram, W. J., Polson, D., Trenberth, K. E., ... & Dai, A. (2019). Challenges in quantifying changes in the global water cycle. *Bulletin of the American Meteorological Society*, 100(10).

Hinkel, J., et al. (2014) Coastal flood damage and adaptation costs under 21st century sea-level rise. Proceedings of the National Academy of Sciences, 111(9), 3292-3297.

Hirabayashi, Y., et al. (2013) Global flood risk under climate change. Nature *Climate Change*, 3(9), 816.

Hofstra, N., Haylock, M., New, M., Jones, P.D. (2009) Testing EOBS European high-resolution gridded data set of daily precipitation and surface temperature. *Journal of Geophysical Research*, 144, D21101.

Horton, R.E. (1933) The Rôle of infiltration in the hydrologic cycle, EOS T. Am. Geophys. Un., 14, 446–460.

Horton, R.M., Coffel, E.D., Winter, J.M., Bader, D.A. (2015) Projected changes in extreme temperature events based on the NARCCAP model suite. *Geophysical Research Letters*, 42: 7722–7731.

Hosking, J.R.M., Wallis, J.R. (1988) The effect of intersite dependence on regional flood frequency analysis. *Water Resources Research*, 24 588–600.

Hosseinzadehtalaei, P., Tabari, H., & Willems, P. (2017) Quantification of uncertainty in reference evapotranspiration climate change signals in Belgium. *Hydrology Research*, 48(5), 1391-1401.

Hosseinzadehtalaei, P., Tabari, H., Willems, P. (2017) Uncertainty assessment for climate change impact on intense precipitation: how many model runs do we need?. *International Journal of Climatology*, 37(S1), 1105–1117.

Hosseinzadehtalaei, P., Tabari, H., Willems, P. (2018) Precipitation intensity–duration–frequency curves for central Belgium with an ensemble of EURO-CORDEX simulations, and associated uncertainties. *Atmospheric Research*, 200 1-12.

Hosseinzadehtalaei, P., Tabari, H., Willems, P. (2019) Regionalization of anthropogenically forced changes in 3 hourly extreme precipitation over Europe. *Environmental Research Letters*, 14(12), 124031.

Hughes, D.A., Kingston, D.G., Todd, M.C. (2011) Uncertainty in water resources availability in the Okavango River basin as a result of climate change. *Hydrology and Earth System Sciences*, 15: 931-941.

IPCC (2012) Managing the risks of extreme events and disasters to advance climate change adaption: special report of the Intergovernmental Panel on Climate Change, Cambridge University Press, New York, NY.

IPCC, (2000) Special report on emissions scenarios. Cambridge University Press, Cambridge.

IPCC, (2014) Climate Change 2014: Synthesis Report. Contribution of Working Groups I, II and III to the Fifth Assessment Report of the Intergovernmental Panel on Climate Change [Core Writing Team, R.K. Pachauri and L.A. Meyer (eds.)]. IPCC, Geneva, Switzerland, 151 pp.

IPCC: Summary for Policymakers. Climate Change (2013)The Physical Science Basis, Contribution of Working Group I to the Fifth Assessment Report of the Intergovernmental Panel on Climate Change, In: Stocker TF, Qin D,

Plattner GK, Tignor M, Allen S, KBoschung J, Nauels A, Xia Y, Bex V, Midgley PM. (Eds.).

Jacob, D., Barring, L., Christensen, O.B., Christensen, J.H., Castro, M.D., Déqué, M., Giorgi, F., Hagemann, S., Hirschi, M., Jones, R., Kjellström, E., Lenderink, G., Rockel, B., Sanchez, E., Schär, C., Seneviratne, S.I., Somot, S., Ulden, A.V., Hurk, B.V.D. (2007) An intercomparison of regional climate models for Europe: model performance in present-day climate. *Climatic Change*, 81, 31–52.

Jacob, D., Petersen, J., Eggert, B., Alias, A., Christensen, O. B., Bouwer, L. M., ... & Georgopoulou, E. (2014). EURO-CORDEX: new high-resolution climate change projections for European impact research. *Regional environmental change*, 14(2), 563-578.

Janssen, E., Sriver, R.L., Wuebbles, D.J., Kunkel, K.E. (2016) Seasonal and regional variations in extreme precipitation event frequency using CMIP5. *Geophysical Research Letters*, 43(10), 5385-5393..

Jones, B., O'Neill, B.C. (2016) Spatially explicit global population scenarios consistent with the Shared Socioeconomic Pathways. *Environmental Research Letters*, 11(8), 084003.

Jongman, B., Ward, P.J., Aerts, J.C.J.H. (2012) Global exposure to river and coastal flooding: Long term trends and changes. *Global Environmental Change*, 22(4):823–835.

Jongman, B., Winsemius, H.C., Aerts, J.C., de Perez, E.C., van Aalst, M.K., Kron, W., Ward, P.J. (2015) Declining vulnerability to river floods and the global benefits of adaptation. *Proceedings of the National Academy of Sciences*, 112(18), E2271-E2280.

Joyce, R.J., Janowiak, J.E., Arkin, P.A., Xie, P. (2004) CMORPH: A Method that Produces Global Precipitation Estimates from Passive Microwave and Infrared Data at High Spatial and Temporal Resolution. *Journal of Hydrometeorology*, 5, 487–503.

Jung, I. W., Change, H., Moradkhani, H. (2011) Quantifying uncertainty in urban flooding analysis considering hydro-climatic projection and urban development effects. *Hydrology and Earth System Sciences*,15:617–633.

Karlsson, J.M., Arnberg, W. (2011) Quality analysis of SRTM and HYDRO1K: A case study of flood inundation in Mozambique. *International Journal of Remote Sensing*, 32, 267–285.

Karmacharya, J., New, M., Jones, R., Levine, R. (2017) Added value of a high-resolution regional climate model in simulation of intraseasonal variability of the South Asian summer monsoon. *International Journal of Climatology*, 37 1100-1116.

Kaspersen, P.S., Ravn, N.H., Arnbjerg-Nielsen, K., Madsen, H., Drews, M. (2017) Comparison of the impacts of urban development and climate change

on exposing European cities to pluvial flooding. *Hydrology and Earth System Sciences*, 21(8), 4131-4147.

Kates, R.W., Colten, C.E., Laska, S., Leatherman, S.P. (2006) Reconstruction of New Orleans after Hurricane Katrina: A research perspective. *Proceedings of the National Academy of Sciences of the United States of America*, 103, 14653–14660.

Katz, R. W., Parlange, M. B., Naveau, P. (2002) Statistics of extremes in hydrology. *Advances in Water Resources*, 25, 1287–1304.

Kay, J.E., Deser, C., Phillips, A., Mai, A., Hannay, C., Strand, G. et al.,. (2015) The Community Earth System Model (CESM) large ensemble project: A community resource for studying climate change in the presence of internal climate variability. *Bulletin of the American Meteorological Society*, 96 1333-1349.

Keers, J. F., Westcott, P. (1977) A computer-based model for design rainfall in the United Kingdom. Met. Office Scientific Paper No. 36. HMSO, London.

Kendon EJ, Roberts NM, Fowler HJ, Roberts MJ, Chan SC, Senior CA. (2014) Heavier summer downpours with climate change revealed by weather forecast resolution model. *Nature Climate Change*, 4, 570–576.

Kendon, E.J., Ban, N., Roberts, N.M., Fowler, H.J., Roberts, M.J., Chan, S.C. et al.,. (2017) Do convection-permitting regional climate models improve projections of future precipitation change? *Bulletin of the American Meteorological Society*, Soc. 98 79-93.

Kendon, E.J., Blenkinsop, S., Fowler, H.J. (2018) When will we detect changes in short-duration precipitation extremes?. *Journal of Climate*, 31 2945-2964.

Kendon, E.J., Rowell, D.P., Jones, R.G. (2010) Mechanisms and reliability of future projected changes in daily precipitation. *Climate Dynamics*, 35 489-509.

Kendon, E.J., Rowell, D.P., Jones, R.G., Buonomo, E. (2008) Robustness of future changes in local precipitation extremes. *Journal of Climate*, 21 4280-4297.

Kermanshah, A., Derrible, S., Berkelhammer, M. (2017) Using climate models to estimate urban vulnerability to flash floods. *Journal of Applied Meteorology and Climatology*, 56(9), 2637–2650.

Khajehei, S., Ahmadalipour, A., Shao, W., Moradkhani H. (2020) A place-based assessment of flash flood hazard and vulnerability in the Contiguous United States, *Scientific Reports*, 10, 448.

Kharin, V. V., Flato, G. M., Zhang, X., Gillett, N. P., Zwiers, F., Anderson, K. J. (2018) Risks from climate extremes change differently from 1.5° C to 2.0° C depending on rarity. *Earth's Future*, 6, 704–715.

Kharin, V., Zwiers, F., Zhang, X., Wehner, M. (2013) Changes in temperature and precipitation extremes in the CMIP5 ensemble. *Climatic Change*, 119:345–357.

Kianfar, B., Fatichi, S., Paschalis, A., Maurer, M., Molnar, P. (2016) Climate change and uncertainty in high-resolution rainfall extremes. *Hydrology and Earth System Sciences*, doi:10.5194/hess-2016-536, in review.

Kim, B.S., Jeung, S.J., Lee, D.S., Han, W.S. (2015) Nonstationary intensity-duration-frequency curves for drainge infrastructure coping with climate change. In EGU General Assembly Conference Abstracts. 17, p. 8349.

Kingston, D.G., Thompson, J.R., Kite, G. (2011) Uncertainty in climate change projections of discharge for the Mekong River Basin. *Hydrology and Earth System Sciences*, 15:1459-1471.

Kinoshita, Y., Tanoue, M., Watanabe, S., Hirabayashi, Y. (2018) Quantifying the effect of autonomous adaptation to global river flood projections: application to future flood risk assessments. *Environmental Research Letters*, 13(1), 014006.

Kjellström, E., Nikulin, G., Strandberg, G., Christensen, O.B., Jacob, D., Keuler, K. et al.,. (2017) European climate change at global mean temperature increases of 1.5 and 2 °C above pre-industrial conditions as simulated by the EURO-CORDEX regional climate models. *Earth System Dynamics*, 9 459-478.

Knutti, R. et al (2008) A review of uncertainties in global temperature projections over the twenty-first century. *Journal of Climate*, 21 2651–2663.

Knutti, R., Hegerl, G. (2008) The equilibrium sensitivity of earth's temperature to radiation changes. *Nature Geoscience*, 1 735–743.

Knutti, R., Sedláček, J. (2013) Robustness and uncertainties in the new CMIP5 climate model projections. *Nature Climate Change*, 3(4) 369–373.

Koutsoyiannis, D. (2004) Statistics of extremes and estimation of extreme rainfall: II. Empirical investigation of long rainfall records. *Hydrological Sciences Journal*, 49(4), 591–610.

Kron, W. (2005) Flood Risk = Hazard • Values • Vulnerability. *Water International*, 30, 58–68.

Kron, W., et al. (2019) Reduction of flood risk in Europe - Reflections from a reinsurance perspective. *Journal of Hydrology*, 576, 197-209.

Kröner, N. (2016) Identifying and quantifying large-scale drivers of European climate change. Dissertation ETH Zurich https://doi.org/10.3929/ethz-a-010793497.

Kröner, N., Kotlarski, S., Fischer, E., Lüthi, D., Zubler, E., Schär, C. (2017) Separating climate change signals into thermodynamic, lapse-rate and circulation effects: theory and application to the European summer climate *Climate Dynamics*, 48 3425-3440.

Kundzewicz, Z.W., et al. (2014) Flood risk and climate change: global and regional perspectives. *Hydrological Sciences Journal*, 59 (1), 1-28.

Kundzewicz, Z.W., et al. (2017) Differences in flood hazard projections in Europe—their causes and consequences for decision making. *Hydrological Sciences Journal*, 62 (1), 1-14.

Kundzewicz, Z.W., et al. (2018) Uncertainty in climate change impacts on water resources. *Environmental Science & Policy*, 79, 1-8.

Kundzewicz, Z.W., Su, B., Wang, Y., Wang, G., Wang, G., Huang, J., Jiang, T. (2019) Flood risk in a range of spatial perspectives–from global to local scales. *Natural Hazards and Earth System Sciences*, 19(7), 1319-1328.

Kundzewicz, Z.W., Ulbrich, U., Brucher, T., Graczyk, D., KruGer, A., Leckebusch, G.C., Menzel, L., Pinskwar, I., Radziejewski, M., Szwed, M. (2005) Summer floods in Central Europe–climate change track? *Natural Hazards*, 36:165–189.

Lang, M., Ouarda, T. B. M. J., Bobee, B. (1999) Towards operational guidelines for over-threshold modeling. *Journal of Hydrology*, 225, 103–117.

Langanke T., Moran A., Dulleck B., Schleicher C. (2016) Copernicus land monitoring service — high resolution layer water and wetness: product specifications document Technical Report, European Environment Agency.

Larsen, A.N., Gregersen, I.B., Christensen, O.B., Linde, J.J., Mikkelsen, P.S. (2009) Potential future increase in extreme one-hour precipitation events over Europe due to climate change. *Water Science & Technology*, 60:2205–2216.

Lazoglou, G., Anagnostopoulou, C., Tolika, K. and Kolyva-Machera, F. (2019) A review of statistical methods to analyze extreme precipitation and temperature events in the Mediterranean region. *Theoretical and Applied Climatology*, 136, 99–117.

Lee T, Park T. (2017) Nonparametric temporal downscaling with event-based population generating algorithm for RCM daily precipitation to hourly: model development and performance evaluation. *Journal of Hydrology*, 547, 498-516.

Lee, T.C.K., Zwiers, F.W., Zhang, X., Tsao, M. (2006) Evidence of decadal climate prediction skill resulting from changes in anthropogenic forcing. *Journal of Climate*, 19 5305–5318 13.

Lehner, F. et al. (2020) Partitioning climate projection uncertainty with multiple large ensembles and CMIP5/6. *Earth System Dynamics*, 11(2), 491-508.

Lehtonen, I., Ruosteenoja, K., Jylhä, K. (2014) Projected changes in European extreme precipitation indices on the basis of global and regional climate model ensembles. *International Journal of Climatology*, 34, 1208-1222.

Lenderink, G., Barbero, R., Loriaux, J.M., Fowler, H.J. (2017) Super-Clausius–Clapeyron scaling of extreme hourly convective precipitation and its relation

to large-scale atmospheric conditions. *Journal of Climate*, 30(15), 6037-6052.

Lenderink, G., Fowler, H.J. (2017) Hydroclimate: Understanding rainfall extremes. *Nature Climate Change*, 7 391-393.

Lenderink, G., Mok, H.Y., Lee, T.C., Van Oldenborgh, G.J. (2011) Scaling and trends of hourly precipitation extremes in two different climate zones—Hong Kong and the Netherlands. *Hydrology and Earth System Sciences*, 15:3033–3041.

Lenderink, G., van Meijgaard, E. (2008) Increase in hourly precipitation extremes beyond expectations from temperature changes. *Nature Geoscience*, 1 511–514.

Lewis, E., et al. (2019) GSDR: A Global sub-daily rainfall dataset. *Journal of Climate*, 32(15), 4715-4729.

Li, C., Zwiers, F., Zhang, X., Li, G. (2019) How Much Information Is Required to Well Constrain Local Estimates of Future Precipitation Extremes? *Earth's Future*, 7 11-24.

Liao, X., Xu, W., Zhang, J., Li, Y., Tian, Y. (2019) Global exposure to rainstorms and the contribution rates of climate change and population change. *Science of The Total Environment*, 663, 644-653.

Libertino, A., Ganora, D., Claps, P. (2019) Evidence for increasing rainfall extremes remains elusive at large spatial scales: The case of Italy. *Geophysical Research Letters*, 46(13), 7437-7446.

Liepert, B.G., Previdi, M. (2012) Inter-model variability and biases of the global water cycle in CMIP3 coupled climate models. *Environmental Research Letters*, **7**: 014006.

Liew, S.C., Srivatsan, V.R., Liong, S.H. (2014) Development of Intensity-Duration-Frequency curves at ungauged sites: risk management under changing climate. *Geoscience Letters*, 1(1), 8.

Lind, P., Lindstedt, D., Kjellström, E., Jones, C. (2016) Spatial and temporal characteristics of summer precipitation over central Europe in a suite of high-resolution climate models. *Journal of Climate*, 29(10), 3501-3518.

Liu, Z., Mehran, A., Phillips, T.J., AghaKouchak, A. (2014) Seasonal and regional biases in CMIP5 precipitation simulations. *Climate Research*, 60(1):35-50.

Loftus, A.C., Anton, B., Philip, R. (2011) Adapting urban water systems to climate change: a handbook for decision makers at the local level. Adapting urban water systems to climate change: a handbook for decision makers at the local level.

Loriaux, J.M., Lenderink, G., De Roode, S.R., Siebesma, P. (2013) Understanding convective extreme precipitation scaling using observations

and an entraining plume model. *Journal of the Atmospheric Sciences*,70:3641–3655.

Ludy, J., Kondolf, G.M. (2012) Flood risk perception in lands "protected" by 100-year levees. *Natural Hazards*, 61, 829–842.

Lugeri, N., Kundzewicz, Z.W., Genovese, E., Hochrainer, S., Radziejewski, M. (2010). River flood risk and adaptation in Europe – assessment of the present status. *Mitigation and Adaptation Strategies for Global Change*, 15, 621–639.

Lumbroso, D., Boyce, S., Bast, H., Walmsley, N. (2011) The challenges of developing rainfall intensity-duration-frequency curves and national food hazard maps for the Caribbean. *Journal of Flood Risk Management*, 4(1), 42–52.

Lutz, A.F., ter Maat, H.W., Biemans, H., Shrestha, A.B., Wester, P., Immerzeel, W.W. (2016) Selecting representative climate models for climate change impact studies: an advanced envelope-based selection approach. *International Journal of Climatology*, 36: 3988–4005.

Lutz, W., Muttarak, R., Striessnig, E. (2014) Universal education is key to enhanced climate adaptation. *Science*, 346(6213), 1061–1062.

Madsen, H., Arnbjerg-Nielsen, K., Mikkelsen, P.S. (2009) Update of regional intensity-duration-frequency curves in Denmark: Tendency towards increased storm intensities. *Atmospheric Research*, 92 (3):343-349.

Madsen, H., Gregersen, I.B., Rosbjerg, D., Arnbjerg-Nielsen, K. (2017) Regional frequency analysis of short duration rainfall extremes using gridded daily rainfall data as co-variate. *Water Science & Technology*, 75 1971-1981.

Madsen, H., Lawrence, D., Lang, M., Martinkova, M., Kjeldsen, T. (2014) Review of trend analysis and climate change projections of extreme precipitation and floods in Europe. *Journal of Hydrology*, 519:3634–3650.

Mailhot, A., Duchesne, S. (2010) Design criteria of urban drainage infrastructures under climate change. *Journal of water resources planning and management*, 136(2):201-208.

Mailhot, A., Duchesne, S., Caya, D., Talbot, G. (2007) Assessment of future change in intensity-duration-frequency (IDF) curves for Southern Quebec using the Canadian Regional Climate Model (CRCM). *Journal of Hydrology*, 347:197-210.

Mandal, S., Breach, P.A., Simonovic, S.P. (2016) Uncertainty in Precipitation Projection under Changing Climate Conditions: A Regional Case Study. *American Journal of Climate Change*, 5(01): 116.

Maraun, D. (2013) Bias correction, quantile mapping, and downscaling: Revisiting the inflation issue. *Journal of Climate*, 26(6), 2137-2143.

Maraun, D. (2013) When will trends in European mean and heavy daily precipitation emerge? *Environmental Research Letters*, 8 014004.

Maraun, D., Wetterhall, F., Ireson, A. M., Chandler, R. E., Kendon, E. J., Widmann, M., ... & Venema, V. K. C. (2010). Precipitation downscaling under climate change: Recent developments to bridge the gap between dynamical models and the end user. *Reviews of Geophysics*, 48(3).

Marra, F. and Nikolopoulos, E. I., (2019) Anagnostou, E. N., Bardossy, A. and Morin, E. Precipitation frequency analysis from remotely sensed datasets: a focused review. *Journal of Hydrology*, doi: 10.1016/j.jhydrol.2019.04.081.

Marra, F., Morin, E., Peleg, N., Mei, Y., Anagnostou, E. N. (2017) Intensity–duration–frequency curves from remote sensing rainfall estimates: Comparing satellite and weather radar over the eastern Mediterranean. *Hydrology and Earth System Sciences*, 21(5), 2389–2404.

Martel, J.L., Mailhot, A., Brissette, F., Caya, D. (2018) Role of natural climate variability in the detection of anthropogenic climate change signal for mean and extreme precipitation at local and regional scales. *Journal of Climate*, 31 4241-4263.

Martin, J., Heinrich, T., Pirc-Velkavrh, A., Jarosinska, D., Csagoly, P., Hoogeveen, Y., et al., (2010) The European environment. State and outlook 2010. Copenhagen: European Environment Agency.

McNeil, A. J., Frey, R. (2000) Estimation of tail-related risk measures for heteroscedastic financial time series: an extreme value approach. *Journal of Empirical Finance*, 7(3-4), 271–300.

Mearns, L.O., Sain, S., Leung, L.R., Bukovsky, M.S., McGinnis, S., Biner, S., Caya, D., Arritt, R.W., Gutowski, W., Takle, E., Snyder, M., Jones, R.G., Nunes, A.M.B., Tucker, S., Herzmann, D., McDaniel, L., Sloan, L. (2013) Climate change projections of the North American Regional Climate Change Assessment Program (NARCCAP). *Climatic Change*, 120(4), 965-975.

Meehl, G., Bony, S. (2011) Introduction to CMIP5. *CLIVAR Exchanges*, **16**: 4−5.

Mélèse, V., Blanchet, J., Molinié, G. (2018) Uncertainty estimation of Intensity–Duration–Frequency relationships: A regional analysis. *Journal of Hydrology*, 558, 579-591.

Mendlik, T., Gobiet, A. (2016) Selecting climate simulations for impact studies based on multivariate patterns of climate change. *Climatic Change*, 135: 381–393.

Mendoza PA, et al. (2016) Effects of different regional climate model resolution and forcing scales on projected hydrologic changes. *Journal of Hydrology*, 541, 1003-1019.

Miao, C., Sun, Q., Borthwick, A. G. L., Duan, Q. (2016) Linkage between hourly precipitation events and atmospheric temperature changes over china during the warm season. *Scientific Reports*, 6, 22543.

Min, S.K., Simonis, D., Hense, A. (2007) Probabilistic climate change predictions applying Bayesian model averaging. *Philosophical Transactions of the Royal Society A: Mathematical, Physical and Engineering Sciences*,. 365: 2103−2116.

Minville, M., Brissette, F., Leconte, R. (2008) Uncertainty of the impact of climate change on the hydrology of a nordic watershed. *Journal of Hydrology,* 358:70–83.

Mirhosseini, G., Srivastava, P., Stefanova, L. (2013) The impact of climate change on rainfall Intensity–Duration–Frequency (IDF) curves in Alabama. *Regional Environmental Change*, 13(1):25-33.

Mishra, V., Wallace, J. M., Lettenmaier, D. P. (2012). Relationship between hourly extreme precipitation and local air temperature in the United States. *Geophysical Research Letters*, 39, L16403.

Mohammeda, I.N., Arne Bomblies, A., Wemplea, B.C. (2015) The use of CMIP5 data to simulate climate change impacts on flow regime within the Lake Champlain Basin. *Journal of Hydrology: Regional Studies*, 3:160–186.

Molnar, P., Fatichi, S., Gaál, L., Szolgay, J., Burlando, P. (2015) Storm type effects on super Clausius–Clapeyron scaling of intense rainstorm properties with air temperature. *Hydrology and Earth System Sciences*, 19(4):1753–1766.

Monjo, R., Gaitán, E., Pórtoles, J., Ribalaygua, J., Torres, L. (2016) Changes in extreme precipitation over Spain using statistical downscaling of CMIP5 projections. *International Journal of Climatology*, 36: 757–769.

Morlot, J. C. (2003). OECD Workshop on the Benefits of Climate Policy. Improving Information for Policy Makers. OECD Workshop held 12-13 December 2002. Summary Report.

Moss, R. H., Edmonds, J. A., Hibbard, K. A., Manning, M. R., Rose, S. K., Van Vuuren, D. P., ... & Meehl, G. A. (2010). The next generation of scenarios for climate change research and assessment. *Nature*, 463(7282), 747-756.

Murphy, J.M., Sexton, D.M.H., Barnett, D.N., Jones, G.S., Webb, M.J., Collins, M., Stainforth, D.A. (2004) Quantification of modelling uncertainties in a large ensemble of climate change simulations. *Nature*, 430 768–772.

Nakicenovic, N., et al., (2000) IPCC Special Report on Emission Scenarios, Cambridge

Naumann, G., Barbosa, P., Garrote, L., Iglesias, A., Vogt, J. (2014) Exploring drought vulnerability in Africa: an indicator based analysis to be used in early warning systems. *Hydrology and Earth System Sciences*, 18(5), 1591-1604.

Nguyen, P., Shearer, E. J., Tran, H., Ombadi, M., Hayatbini, N., Palacios, T., ... & Kuligowski, B. (2019). The CHRS Data Portal, an easily accessible public repository for PERSIANN global satellite precipitation data. *Scientific data*, 6(1), 1-10.

Ning, L., Bradley, R.S. (2016) NAO and PNA influences on winter temperature and precipitation over the eastern United States in CMIP5 GCMs. *Climate Dynamics*, 46: 1257-1276.

Ning, L., Riddle, E.E., Bradley, R.S. (2015) Projected changes in climate extremes over the northeastern United States. *Journal of Climate*, 28: 3289-3310.

Nissen, K. M., Ulbrich, U. (2017) Increasing frequencies and changing characteristics of heavy precipitation events threatening infrastructure in Europe under climate change. *Natural Hazards and Earth System Sciences*, 17(7), 1177–1190.

Ntegeka, V., Willems, P. (2008) Trends and multidecadal oscillations in rainfall extremes, based on a more than 100-year time series of 10 min rainfall intensities at Uccle, Belgium. *Water Resources Research*, 44(7), doi:10.1029/2007WR006471.

Ntelekos, A.A., Oppenheimer, M., Smith, J.A., Miller, A.J. (2010) Urbanization, climate change and flood policy in the United States. *Climatic Change*, 103(3–4):597–616.

O'Neill, B.C., Kriegler, E., Ebi, K.L., Kemp-Benedict, E., Riahi, K., Rothman, D.S., van Ruijven B.J., van Vuuren D.P., Birkmann, J., Kok, K., Levy, M., Solecki, W. (2015) The roads ahead: Narratives for shared socioeconomic pathways describing world futures in the 21st century. *Global Environmental Change*, 42, 169-180.

O'Neill, B.C., Kriegler, E., Riahi, K., Ebi, K.L., Hallegatte, S., Carter, T.R., Mathur, R., van Vuuren, D.P. (2014) A new scenario framework for climate change research: the concept of shared socioeconomic pathways. *Climatic Change*, 122:387–400.

Olsson J, Berg P, Kawamura A. (2015) Impact of RCM spatial resolution on the reproduction of local, subdaily precipitation. *Journal of Hydrometeorology*, 16, 534–547.

Olsson, J., Berg, P., Kawamura, A. (2015) Impact of RCM Spatial Resolution on the Reproduction of Local, Subdaily Precipitation. *Journal of Hydrometeorology*, 16(2), 534-547.

Olsson, J., Berggren, K., Olofsson, M., Viklander, M. (2009) Applying climate model precipitation scenarios for urban hydrological assessment: a case study in Kalmar City, Sweden. *Atmospheric Research*, 92 (3):364–375.

Ombadi, M., Nguyen, P., Sorooshian, S., Hsu, K. L. (2018) Developing Intensity-Duration-Frequency (IDF) Curves From Satellite-Based Precipitation: Methodology and Evaluation. *Water Resources Research*, 54(10), 7752–7766.

Pall, P., Allen, M.R., Stone, D.A. (2007) Testing the Clausius-Clapeyron constraint on changes in extreme precipitation under CO2 warming. *Climate Dynamics*, 28 351–363.

Panday, P.K., Thibeault, J., Frey, K. E. (2015) Changing temperature and precipitation extremes in the Hindu Kush-Himalayan region: an analysis of CMIP3 and CMIP5 simulations and projections. *International Journal of Climatology*, 35: 3058–3077

Papagiannaki, K., Lagouvardos, K., Kotroni, V., Bezes, A. (2015) Flash flood occurrence and relation to the rainfall hazard in a highly urbanized area. *Natural Hazards and Earth System Sciences*, 15(8), 1859–1871.

Papalexiou, S. M., Koutsoyiannis, D. (2013) Battle of extreme value distributions: A global survey on extreme daily rainfall. *Water Resources Research*, 49(1), 187–201.

Pasarić, Z., Cindrić, K. (2019) Generalised Pareto distribution: impact of rounding on parameter estimation. *Theoretical and Applied Climatology*, 136, 417–427.

Peck, A., Prodanovic, P., Simonovic, S.P. (2012) Rainfall intensity duration frequency curves under climate change: City of London, Ontario, Canada. *Canadian Water Resources Journal*, 37(3):177-189.

Peel, M.C., Srikanthan, R., McMahon, T.A., Karoly, D.J. (2015) Approximating uncertainty of annual runoff and reservoir yield using stochastic replicates of global climate model data. *Hydrology and Earth System Sciences*, 19(4):1615-1639.

Pendergrass, A. G., Knutti, R., Lehner, F., Deser, C., Sanderson, B. M. (2017) Precipitation variability increases in a warmer climate. *Scientific Reports*, 7(1), 17966.

Pendergrass, A.G., Hartmann, D.L. (2014) Changes in the distribution of rain frequency and intensity in response to global warming. *Journal of Climate*, 27 8372–8383.

Penny, D., Zachreson, C., Fletcher, R., Lau, D., Lizier, J. T., Fischer, N., ... & Prokopenko, M. (2018). The demise of Angkor: Systemic vulnerability of urban infrastructure to climatic variations. *Science advances*, 4(10), eaau4029.

Pfahl, S., O'Gorman, P.A., Fischer, E.M. (2017) Understanding the regional pattern of projected future changes in extreme precipitation. *Nature Climate Change*,7 423–427.

Pinto, I. S. (2015). Future changes in extreme rainfall events and circulation patterns over southern Africa (Doctoral dissertation, University of Cape Town).

Pohl, B., Macron, C., & Monerie, P. A. (2017). Fewer rainy days and more extreme rainfall by the end of the century in Southern Africa. *Scientific reports*, 7(1), 1-7.

Pombo, S., de Oliveira, R. P. (2015) Evaluation of extreme precipitation estimates from TRMM in Angola. *Journal of Hydrology*, 523, 663–679.

Prein AF, Gobiet A, Suklitsch M, Truhetz H, Awan NK, Keuler K, Georgievski G. (2013) Added value of convection permitting seasonal simulations. *Climate Dynamics*, 41, 2655-2677.

Prein, A.F., Gobiet, A. (2017) Impacts of uncertainties in European gridded precipitation observations on regional climate analysis. *International Journal of Climatology*, 37 305-327.

Prein, A.F., Gobiet, A., Truhetz, H., Keuler, K., Goergen, K., Teichmann, C., Fox Maule, C., van Meijgaard, E., Déqué, M., Nikulin, G., Vautard, R., Vautard, A., Kjellström, E., Jacob, D. (2016) Precipitation in the EURO-CORDEX 0.11º and 0.44º simulations: high resolution, high benefits? *Climate Dynamics*, 46: 383-412.

Prein, A.F., Rasmussen, R.M., Ikeda, K., Liu, C., Clark, M.P., Holland, G.J. (2017) The future intensification of hourly precipitation extremes. *Nature Climate Change*, 7 48-52.

Ragno, E., AghaKouchak, A., Love, C. A., Cheng, L., Vahedifard, F., Lima, C. H. (2018) Quantifying Changes in Future Intensity-Duration-Frequency Curves Using Multimodel Ensemble Simulations. *Water Resources Research*, 54(3), 1751–1764.

Ragulina, G., Reitan, T. (2017) Generalized extreme value shape parameter and its nature for extreme precipitation using long time series and the Bayesian approach. *Hydrological Sciences Journal*, 62(6), 863–879.

Räisänen, J., Joelsson, R. (2001) Changes in average and extreme precipitation in two regional climate model experiments. *Tellus A: Dynamic Meteorology and Oceanography*, 53 547-566.

Rajczak, J., Pall, P., Schär, C. (2013) Projections of extreme precipitation events in regional climate simulations for Europe and the Alpine region. *Journal of Geophysical Research: Atmospheres*, 118 3610-3626.

Rajczak, J., Schär, C. (2017) Projections of future precipitation extremes over Europe: A multimodel assessment of climate simulations. *Journal of Geophysical Research: Atmospheres*, 122 10773-10800.

Rana, A., Foster, K., Bosshard, T., Olsson, J., Bengtsson, L. (2014) Impact of climate change on rainfall over Mumbai using Distribution-based Scaling of Global Climate Model projections. *Journal of Hydrology: Regional Studies*, 1: 107-128.

Randall, D.A., RA Wood, R.A., Bony, S., Colman, R., Fichefet, T., Fyfe, J., Kattsov, V., Pitman, A., Shukla, J., Srinivasan, J., Stouffer, R.J., Sumi, A.,

Taylor, K.E. (2007) Climate Models and Their Evaluation. In: Climate Change 2007: The Physical Science Basis. Contribution of Working Group I to the Fourth Assessment Report of the Intergovernmental Panel on Climate Change [Solomon, S., D. Qin, M. Manning, Z. Chen, M. Marquis, K.B. Averyt, M.Tignor and H.L. Miller (eds.)]. Cambridge University Press, Cambridge, United Kingdom and New York, NY, USA.

Refsgaard, J. C., Arnbjerg-Nielsen, K., Drews, M., Halsnæs, K., Jeppesen, E., Madsen, H., ... & Christensen, J. H. (2013). The role of uncertainty in climate change adaptation strategies—A Danish water management example. *Mitigation and Adaptation Strategies for Global Change*, 18(3), 337-359.

Renard, B., Lang, M., Bois, P. (2006) Statistical analysis of extreme events in a non-stationary context via a Bayesian framework: case study with peak-over-threshold data. Stochastic *Environmental Research and Risk Assessment*, 21(2), 97–112.

Riahi, K., Rao, S., Krey, V., Cho, C., Chirkov, V., Fischer, G., ... & Rafaj, P. (2011). RCP 8.5—A scenario of comparatively high greenhouse gas emissions. *Climatic change*, 109(1-2), 33.

Rojas, R., et al. (2012) Assessment of future flood hazard in Europe using a large ensemble of bias-corrected regional climate simulations. *Journal of Geophysical Research-Atmospheres*, 117, D17109.

Roudier, P., et al. (2016) Projections of future floods and hydrological droughts in Europe under a +2°C global warming. *Climatic Change*, 135 (2), 341-355.

Rulfová, Z., Buishand, A., Roth, M., & Kyselý, J. (2016) A two-component generalized extreme value distribution for precipitation frequency analysis. *Journal of hydrology*, 534, 659-668.

Rummukainen, M. (2016) Added value in regional climate modeling. *Wiley Interdisciplinary Reviews: Climate Change*, 7(1), 145-159.

Rupa, C., Saha, U., Mujumdar, P.P. (2015) Model and parameter uncertainty in IDF relationships under climate change. *Advances in Water Resources*, 79, 127– 139.

Ryo, M., Valeriano, O.C.S., Kanae, S., Ngoc, T.D. (2014) Temporal downscaling of daily gauged precipitation by application of a satellite product for flood simulation in a poorly gauged basin and its evaluation with multiple regression analysis. *Journal of Hydrometeorology*, 15:563–580.

Saeed, S., Brisson, E., Demuzere, M., Tabari, H., Willems, P., Van Lipzig, N. (2017) Multidecadal convection permitting climate simulations over Belgium: Sensitivity of future precipitation extremes. *Atmospheric Science Letters*, 18(1), 29-36..

Sampson, C.C., Smith, A.M., Bates, P.D., Neal, J.C., Alfieri, L., Freer, J.E. (2015). A high-resolution global flood hazard model. *Water Resources Research*, 51(9), 7358-7381.

Sandink, D., Simonovic, S. P., Schardong, A., Srivastav, R. (2016) A decision support system for updating and incorporating climate change impacts into rainfall intensity-duration-frequency curves: Review of the stakeholder involvement process. *Environmental Modelling & Software*, 84, 193–209.

Scarrott, C., MacDonald, A. (2012) A review of extreme value threshold estimation and uncertainty quantification. *REVSTAT-Statistical Journal*, 10(1), 33–60.

Schumann, G.J.-P., Neal, J.C., Voisin, N., Andreadis, K.M., Pappenberger, F., Phanthuwongpakdee, N., Hall, A.C., and Bates, P.D. (2013) A first large-scale flood inundation forecasting model. *Water Resources Research*, 49, 6248–6257.

Scoccimarro, E., Gualdi, S., Bellucci, A., Zampieri, M., Navarra, A. (2013) Heavy precipitation events in a warmer climate: Results from CMIP5 models *Journal of Climate*, 26 7902-7911.

Scoccimarro, E., Villarini, G., Vichi, M., Zampieri, M., Fogli, P.G., Bellucci, A., Gualdi, S. (2015) Projected changes in intense precipitation over Europe at the daily and subdaily time scales. *Journal of Climate*, 28 6193-6203.

Semadeni-Davies, A., Hernebring, C., Svensson, G., Gustafsson, L.G. (2008) The impacts of climate change and urbanization on drainage in Helsingborg, Sweden: Combined sewer system. *Journal of Hydrology*, 350(1):100-113.

Seneviratne, S. I., Nicholls, N., Easterling, D., Goodess, C., Kanae, S., Kossin, J., Luo, Y., Marengo, J., McInnes, K., Rahimi, M., et al. (2012). Changes in climate extremes and their impacts on the natural physical environment. Managing the risks of extreme events and disasters to advance climate change adaptation, pages 109–230.

Sharkey, P., Winter, H.C. (2017) A Bayesian spatial hierarchical model for extreme precipitation in Great Britain. *Environmetrics*, 30(1), e2529.

Shepherd, T.G. (2014) Atmospheric circulation as a source of uncertainty in climate change projections. *Nature Geoscience*, 7(10) 703–708.

Shrestha, A., Babel, M.S., Weesakul, S., Vojinovic, Z. (2017) Developing Intensity–Duration–Frequency (IDF) Curves under Climate Change Uncertainty: The Case of Bangkok, Thailand. *Water*, 9(2):145.

Sieck, K., Jacob, D. (2016) Influence of the boundary forcing on the internal variability of a regional climate model. *American Journal of Climate Change*, 5 373-382.

Sierra, J.P., Arias, P.A., Vieira, S.C. (2015) Precipitation over northern South America and its seasonal variability as simulated by the CMIP5 models. *Advances in Meteorology, 2015.* ,doi:10.1155/2015/634720.

Sillmann, J., Kharin, V.V., Zhang, X., Zwiers, F.W., Bronaugh, D. (2013a) Climate extremes indices in the CMIP5 multimodel ensemble: Part 1. Model

evaluation in the present climate. J*ournal of Geophysical Research: Atmospheres*, 118(4), 1716-1733.

Sillmann, J., Kharin, V.V., Zwiers, F.W., Zhang, X., Bronaugh, D. (2013b) Climate extremes indices in the CMIP5 multimodel ensemble: Part 2. Future climate projections. *Journal of Geophysical Research: Atmospheres,* 118(6), 2473-2493.

Simonovic, S. P., Schardong, A., Sandink, D. (2017) Mapping extreme rainfall statistics for Canada under climate change using updated intensity-duration-frequency curves. *Journal of water resources planning and management*, 143(3), 04016078.

Singleton, A., Toumi, R. (2013) Super-Clausius–Clapeyron scaling of rainfall in a model squall line. *Quarterly Journal of the Royal Meteorological Society*, 139(671), 334–339.

So, B. J., Kim, J. Y., Kwon, H. H., Lima, C. H. (2017) Stochastic extreme downscaling model for an assessment of changes in rainfall intensity-duration-frequency curves over South Korea using multiple regional climate models. *Journal of Hydrology*, 553, 321–337.

Soares, P.M., Cardoso, R.M. (2018) A simple method to assess the added value using high-resolution climate distributions: application to the EURO-CORDEX daily precipitation. *International Journal of Climatology*, 38 1484-1498.

Solaiman, T.A., Simonovic, S.P. (2011) Development of probability based intensity-duration-frequency curves under climate change, *Water Resources Research. Report*, No. 072, Facility for Intelligent Decision Support, Department of Civil and Environmental Engineering, London, Ontario, Canada.

Strandberg, G. et al. (2014) CORDEX scenarios for Europe from the Rossby Centre regional climate model RCA4 Rep. Meteorol. Climatol. 116 (www.smhi.se/polopoly_fs/1.90273!/Menu/general/extGroup/attachmentColHold/mainCol1/file/RMK_116.pdf).

Strobach, E., Bel, G. (2017) The Contribution of Internal and Model Variabilities to the Uncertainty in CMIP5 Decadal Climate Predictions. *Climate Dynamics*,49(9-10), 3221-3235.

Sun, Q., Miao, C., Duan, Q., Ashouri, H., Sorooshian, S., Hsu, K. L. (2018) A review of global precipitation data sets: Data sources, estimation, and intercomparisons. *Reviews of Geophysics*, 56(1), 79–107.

Sunyer, M.A., Hundecha, Y., Lawrence, D., Madsen, H., Willems, P., Martinkova, M., Loukas, A. (2015) Inter-comparison of statistical downscaling methods for projection of extreme precipitation in Europe. *Hydrology and Earth System Sciences*, 19(4), 1827-1847.

Sunyer, M.A., Madsen, H., Ang, P.H. (2012) A comparison of different regional climate models and statistical downscaling methods for extreme rainfall estimation under climate change. *Atmospheric Research*, 103, 119-128.

Sunyer, M.A., Madsen, H., Rosbjerg, D., Arnbjerg-Nielsen, K. (2013b) Regional interdependency of precipitation indices across Denmark in two ensembles of high-resolution RCMs. *Journal of Climate*. 26(20), 7912-7928.

Sunyer, M.A., Sørup, H.J.D., Christensen, O.B., Madsen, H., Rosbjerg, D., Mikkelsen, P.S., Arnbjerg-Nielsen, K. (2013a) On the importance of observational data properties when assessing regional climate model performance of extreme precipitation. *Hydrology and Earth System Sciences*, 17(11): 4323-4337.

Tabari, H., De Troch, R., Giot, O., Hamdi, R., Termonia, P., Saeed, S., Brisson, E., Van Lipzig, N., Willems, P. (2016) Local impact analysis of climate change on precipitation extremes: are high-resolution climate models needed for realistic simulations?. *Hydrology and Earth System Sciences*, 20(9), 3843-3857.

Tabari, H., Hosseinzadehtalaei, P., AghaKouchak, A., Willems, P. (2019) Latitudinal heterogeneity and hotspots of uncertainty in projected extreme precipitation. *Environmental Research Letters*, 14(12), 124032.

Tabari, H., Taye, M.T., Willems, P. (2015) Water availability change in central Belgium for the late 21st century. *Global and Planetary Change*, 131: 115–123.

Tabari, H., Willems, P. (2018) More prolonged droughts by the end of the century in the Middle East. *Environmental Research Letters*, 13(10), 104005.

Tabari, H., Willems, P. (2018) Seasonally varying footprint of climate change on precipitation in the Middle East. *Scientific Reports*, 8 4435.

Taylor, K. E., Stouffer, R. J., Meehl, G. A. (2012) An overview of CMIP5 and the experiment design. *Bulletin of the American Meteorological Society*, 93(4): 485–498.

Ter Braak, C. J. (2006) A Markov Chain Monte Carlo version of the genetic algorithm Differential Evolution: easy Bayesian computing for real parameter spaces. *Statistics and Computing*, 16, 239–249.

Teutschbein, C., Seibert, J. (2012) Bias correction of regional climate model simulations for hydrological climate-change impact studies: Review and evaluation of different methods. *Journal of Hydrology*, 456–457, 12–29.

Thieken, A.H., Cammerer, H., Dobler, C., Lammel, J., Schöberl, F. (2016) Estimating changes in flood risks and benefits of non-structural adaptation strategies-a case study from Tyrol, Austria. *Mitigation and Adaptation Strategies for Global Change*, 21(3):343-376.

Thomson, A. M., Calvin, K. V., Smith, S. J., Kyle, G. P., Volke, A., Patel, P., ... & Edmonds, J. A. (2011). RCP4. 5: a pathway for stabilization of radiative forcing by 2100. *Climatic change*, 109(1-2), 77.

Thorndahl, S., Einfalt, T., Willems, P., Nielsen, J.E., ten Veldhuis, M-C., Arnbjerg-Nielsen, K., ... Molnar, P. (2017) Weather radar rainfall data in urban hydrology. *Hydrology and Earth System Sciences*, 21(3):1359- 1380.

Toreti, A., Naveau, P., Zampieri, M., Schindler, A., Scoccimarro, E., Xoplaki, E., Dijkstra, H. A., Gualdi, S., Luterbacher, J. (2013) Projections of global changes in precipitation extremes from Coupled Model Intercomparison Project Phase 5 models. *Geophysical Research Letters*, 40(18), 4887-4892

Trenberth, K., Dai, A., Rasmussen, R., Parsons, D. (2003) The changing character of precipitation. *Bulletin of the American Meteorological Society*, 84(9):1205–1217.

UIC (2008) Earthworks and Track Bed for Railway Lines, Union Internationales des Chemins der Fer, 3 Edn., Paris, France.

UNDRO, (1991) Mitigating natural disasters : phenomena, effects and options : a manual for policy makers and planners. United Nations, New York.

UNISDR, (2013) Global Assessment Report on Disaster Risk Reduction 2013. From Share Risk to Shared Value: The Business case for Disaster Risk Reduction (UNISDR, Geneva).

USDA, (2016) Soil Infiltration Rates, United States Department of Agriculture, available at: http://qcode.us/codes/sacramentocounty/view.php?topic=14-14_10-14_10_110.

Vafeidis, A.T., et al. (2019) Water-level attenuation in global-scale assessments of exposure to coastal flooding: a sensitivity analysis. *Natural Hazards and Earth System Sciences*, 19(5), 973-984.

Van der Linden, P., Mitchell, J.F.B., (eds.) (2009) ENSEMBLES: Climate Change and its Impacts: Summary of research and results from the ENSEMBLES project. Tech. Rep., Met Office Hadley Centre, FitzRoy Road, Exeter EX1 3PB, UK. 160pp.

Vautard, R., Gobiet, A., Sobolowski, S., Kjellström, E., Stegehuis, A., Watkiss, P. et al.,. (2014) The European climate under a 2 C global warming. *Environmental Research Letters*, 9 034006.

Velázquez, J.A., Schmid, J., Ricard, S., Muerth, M.J., Gauvin St-Denis. B., Minville, M., Chaumont, D., Caya, D., Ludwig, R., Turcotte, R. (2013) An ensemble approach to assess hydrological models' contribution to uncertainties in the analysis of climate change impact on water resources. *Hydrology and Earth System Sciences,* 17: 565–578.

Vescovi, L., Rebetez, M., Rong, F. (2005) Assessing public health risk due to extremely high temperature events: climate and social parameters. *Climate Research*, 30, 71–78.

Vidal, J.P., Wade, S.D. (2008) Multimodel projections of catchment-scale precipitation regime. *Journal of Hydrology*, 353(1-2), 143-158.

Voskamp, I.M., Van de Ven F.H.M. (2015) Planning support system for climate adaptation: Composing effective sets of blue-green measures to reduce urban vulnerability to extreme weather events. *Building and Environment, Special Issue: Climate adaptation in cities*, 83:159–167.

Vousdoukas, M.I., Mentaschi, L., Voukouvalas, E., Bianchi, A., Dottori, F., Feyen, L. (2018) Climatic and socioeconomic controls of future coastal flood risk in Europe. *Nature Climate Change*, 8(9), 776-780.

Vrugt, J. A., Ter Braak, C. J. F., Diks, C. G. H., Robinson, B. A., Hyman, J. M., & Higdon, D. (2009). Accelerating Markov chain Monte Carlo simulation by differential evolution with self-adaptive randomized subspace sampling. *International Journal of Nonlinear Sciences and Numerical Simulation*, 10(3), 273-290.

Vu, M. T., Raghavan, S. V., Liu, J., Liong, S. Y. (2018) Constructing short-duration IDF curves using coupled dynamical–statistical approach to assess climate change impacts. *International Journal of Climatology*, 38(6), 2662–2671.

Wang, F., Yang, H., Wang, Z., Zhang, Z., Li, Z. (2019) Drought evaluation with CMORPH satellite precipitation data in the Yellow River basin by using gridded standardized precipitation evapotranspiration index. *Remote Sensing*, 11(5), 485, doi: 10.3390/rs11050485.

Wang, G., Wang, D., Trenberth, K. E., Erfanian, A., Yu, M., Bosilovich, M. G., Parr, D. T. (2017) The peak structure and future changes of the relationships between extreme precipitation and temperature. *Nature Climate Change*, 7(4), 268–275.

Wang, X., Huang, G., and Liu, J. (2014) Projected increases in intensity and frequency of rainfall extremes through a regional climate modeling approach. *Journal of Geophysical Research: Atmospheres*. 119(23), 13-271.

Ward, P.J., et al. (2013). Assessing flood risk at the global scale: Model setup, results, and sensitivity. *Environmental Research Letters*, 8(4), 044019.

Watt, E., Marsalek, J. (2013). Critical review of the evolution of the design storm event concept. *Canadian Journal of Civil Engineering*, 40(2), 105-113.

Webster, M., et al., 2003. Uncertainty analysis of climate change and policy response. *Climatic Change*, 61(3), 295-320.

Weiss, J., Bernardar,a P., Benoit, M. (2014) Modeling intersite dependence for regional frequency analysis of extreme marine events. *Water Resources Research*, 50 5926-5940.

Werner, A.T. (2011) BCSD Downscaled Transient Climate Projections for Eight Select GCMs over British Columbia, Canada. *Hydrologic Modelling Project Final Report (Part I)*, 63.

Westra, S., Fowler, H.J., Evans, J.P., Alexander, L.V., Berg, P., Johnson, F., ... & Roberts, N.M. (2014) Future changes to the intensity and frequency of short-duration extreme rainfall. *Reviews of Geophysics*, 52(3):522-555.

Wilbanks, T., Fernandez, S. (2014) Climate Change and Infrastructure, Urban Systems, and Vulnerabilities: Technical Report for the U.S. Department of Energy in Support of the National Climate Assessment. Island Press, Washington, DC.

Wilby RL, Wigley TML. (2000) Precipitation predictors for downscaling: observed and general circulation model relationships. *International Journal of Climatology*, 20(6), 641-661.

Willems, P. (2000) Compound intensity/duration/frequency-relationships of extreme precipitation for two seasons and two storm types. *Journal of Hydrology*. 233: 189–205.

Willems, P. (2009) A time series tool to support the multi-criteria performance evaluation of rainfall-runoff models. *Environmental Modelling & Software*, 24, 311–321.

Willems, P. (2013) Revision of urban drainage design rules after assessment of climate change impacts on precipitation extremes at Uccle, Belgium. *Journal of Hydrology*, 496, 166–177.

Willems, P., Arnbjerg-Nielsen, K., Olsson, J., Nguyen, V.T.V. (2012a) Climate change impact assessment on urban rainfall extremes and urban drainage: methods and shortcomings. *Atmospheric Research*, 103: 106-118.

Willems, P., Guillou, A., Beirlant, J. (2007) Bias correction in hydrologic GPD based extreme value analysis by means of a slowly varying function. *Journal of Hydrology*, 338, 221–236.

Willems, P., Olsson, J., Arnbjerg-Nielsen, K., Beecham, S., Pathirana, A., Gregersen, I.B., Madsen, H., Nguyen, V.T.V. (2012b) Impacts of Climate Change on Rainfall Extremes and Urban Drainage. IWA Publishing, London, UK.

Willems, P., Vrac, M. (2011) Statistical precipitation downscaling for small-scale hydrological impact investigations of climate change. *Journal of Hydrology*, 402: 193–205.

Willner, S. N., Levermann, A., Zhao, F., Frieler, K. (2018) Adaptation required to preserve future high-end river flood risk at present levels. *Science Advances*, 4(1), eaao1914.

Winsemius, H.C. et al. (2016) Global drivers of future river flood risk. Nature *Climate Change*, 6, 381-385.

Winsemius, H.C., Van Beek, L.P.H., Jongman, B., Ward, P.J., Bouwman, A. (2013) A framework for global river flood risk assessments. *Hydrology and Earth System Sciences*, 17, 1871–1892.

Wu, C.H., Huang, G.R., Yu, H.J. (2015) Prediction of extreme floods based on CMIP5 climate models: a case study in the Beijiang River basin, South China. *Hydrology and Earth System Sciences*, 19: 1385-1399.

Xie, P., Joyce, R., Wu, S., Yoo, S. H., Yarosh, Y., Sun, F., Lin, R. (2017) Reprocessed, bias-corrected CMORPH global high-resolution precipitation estimates from 1998. *Journal of Hydrometeorology*, 18(6), 1617–1641.

Yan, H., Sun, N., Wigmosta, M., Skaggs, R., Hou, Z., Leung, R. (2018) Next-generation intensity-duration-frequency curves for hydrologic design in snow-dominated environments. *Water Resources Research*, 54(2), 1093-1108.

Yan, L., Xiong, L., Liu, D., Hu, T., & Xu, C. Y. (2017) Frequency analysis of nonstationary annual maximum flood series using the time-varying two-component mixture distributions. *Hydrological Processes*. 31(1), 69-89.

Yilmaz, A. G., Imteaz, M. A. and Perera, B. J. C. (2017) Investigation of non-stationarity of extreme rainfalls and spatial variability of rainfall intensity–frequency–duration relationships: a case study of Victoria, Australia. *International Journal of Climatology*, 37(1), 430–442.

Yilmaz, A.G., Hossain, I., Perera, B.J.C. (2014) Effect of climate change and variability on extreme rainfall intensity–frequency–duration relationships: a case study of Melbourne. *Hydrology and Earth System Sciences*, 18, 4065-4076.

Yin, L., Fu, R., Shevliakova, E., Dickinson, R. E. (2013). How well can CMIP5 simulate precipitation and its controlling processes over tropical South America?. *Climate Dynamics*, 41(11-12), 3127-3143.

Zeweldi, D.A., Gebremichael, M. (2009) Evaluation of CMORPH precipitation products at fine space–time scales. *Journal of Hydrometeorology*, 10, 300–307.

Curriculum Vitae



Name: Parisa Hosseinzadehtalaei

Nationality: Iranian

E-mail: parisa.hosseinzadehtalaei@kuleuven.be; parisa.talaee@gmail.com

EDUCATION

PhD *2016-2020*	**Engineering Science - Civil Engineering, KU Leuven, Belgium** Thesis topic "*Impact of climate change on precipitation extremes and pluvial flooding in Europe*"
M.Sc. *2009-2011*	**Water Engineering, Irrigation and Drainage Engineering, Bu-Ali Sina University, Iran** Thesis: "*Rating curve modeling of rock-fill dams by artificial neural network*"
B.Sc. *2004-2008*	**Water Engineering, Bu-Ali Sina University, Iran** Project: "*A review of climate change impact on water resources in Iran*"
High School Diploma *2000-2004*	**Mathematics & Physics, Parvine Etesami School, Iran**

PhD-related Award, Publications and Activities

Award

- Granted for Water Travel Award 2019 for the work "Future Changes in European Pluvial Flooding under Climatic and Non-Climatic Factors".

Articles in internationally reviewed journals used as chapter

1) **Hosseinzadehtalaei, P**., Tabari, H., Willems, P. (2020) Future amplification of short-duration extreme precipitation over Europe. *Journal of Hydrology*, 590, 125249 (**Journal IF: 4.5**).

2) **Hosseinzadehtalaei, P**., Tabari, H., Willems, P. (2020) Satellite-based data driven quantification of pluvial floods over Europe under future climatic and socioeconomic changes. *Science of the Total Environment*, 721, 137688 (**Journal IF: 6.6**).

3) **Hosseinzadehtalaei, P**., Tabari, H., Willems, P. (2019) Regionalization of anthropogenically forced changes in 3 hourly extreme precipitation over Europe. *Environmental Research Letters*, 14(12), 124031 (**Journal IF: 6.1**).

4) **Hosseinzadehtalaei, P.**, Tabari, H., Willems, P. (2018) Precipitation intensity–duration–frequency curves for central Belgium with an ensemble of EURO-CORDEX simulations, and associated uncertainties. *Atmospheric Research*, 200:1–12 (**Journal IF: 4.7**).

5) **Hosseinzadehtalaei, P.**, Tabari, H., Willems, P. (2017) Uncertainty assessment for climate change impact on intense precipitation: how

many model runs do we need?. *International Journal of Climatology*, 37(S1), 1105–1117 (**Journal IF: 3.9**).

Other internationally reviewed journal articles

1) A market scoping methodology for climate change adaptation solutions in Europe. *Journal of Hydrology: Regional Studies*, (under review).

2) Tabari, H., **Hosseinzadehtalaei, P**., AghaKouchak, A., Willems, P. (2019) Latitudinal heterogeneity and hotspots of uncertainty in projected extreme precipitation. *Environmental Research Letters*, 14(12), 124032.

3) Wouters, H., Ridder, K.D., Poelmans, L., Willems, P., Brouwers, J., **Hosseinzadehtalaei, P**., Tabari, H., Broucke, S.V., Van Lipzig, N., Demuzere, M. (2017) Heat-stress increase under climate change twice as large in cities as in rural areas: a study for a densely populated mid-latitude maritime region. *Geophysical Research Letters*, 44, 8997–9007.

4) Termonia, P., De Cruz, L., De Troch, R., Caluwaerts, S., Giot, O., Hamdi, R., Vannitsem, S., Willems, P., Tabari, H., Van Uytven, E., **Hosseinzadehtalaei, P.**, Van Lipzig, N., van Ypersele, J.-P., Marbaix, P., Villanueva-Birriel, C., Fettweis, X., De Ridder, K., Gobin, A., Lauwaet, D., Stavrakou, T., Bauwens, M., Muller, J.-F., Luyten, P., Pottiaux, E., Van Schaeybroeck, B. (2018) The CORDEX.be initiative as a foundation for climate services in Belgium. *Climate Services*, 11, 49-61.

5) **Hosseinzadehtalaei, P**., Tabari, H., Willems, P. (2017) Quantification of uncertainty in reference evapotranspiration climate change signals in Belgium. *Hydrology Research*, 48(5), 1931–1401.

Research projects

1) **Hosseinzadehtalaei, P**. & Willems, P. (2018-2019) Development of a climate change web atlas for the Flanders' climate effects, 2017-2018, for Flemish Environment Agency (VMM), i.c.w. Stichting Wageningen Research (Alterra)

2) Termonia, P., Van Schaeybroeck, B., De Cruz, L., De Troch, R., Giot, O., Hamdi, R., Vannitsem, S., Willems, P., Tabari, H., Van Uytven, E., **Hosseinzadehtalaei, P**., Van Lipzig, N., Wouters, H., Vanden Broucke, S., van Ypersele, J-P., Marbaix, Ph., Villanueva-Birriel, C., Fettweis, X., Wyard, C., Scholzen, C., Doutreloup, S., De Ridder, K., Gobin, A., Lauwaet, D., Stavrakou, T., Bauwens, M., Müller, J-F., Luyten, P., Ponsar, S., Van den Eynde, D. & Pottiaux, E. (2017) CORDEX.be - Combining regional downscaling expertise in Belgium: CORDEX and beyond. Final report, Belgian Science Policy (Belspo), Brussels, 75 p.

3) Willems, P., Paprotny, D., **Hosseinzadehtalaei, P**., Tabari, H. (2017) Pan-European climate change indicators and loading conditions. Deliverable 6.1 Annex, EU-H2020 project BRIGAID (grant agreement no. 700699), April 2017, 91 p.

4) Bea, M. López-Gunn, E., Tröltzsch, J., McDonald, H., Anzaldúa, G., Willems, P., **Hosseinzadehtalaei, P.**, Tabari, H., Paprotny, D., Vassilopoulos, A., Xepapadeas, P., Hartman, M. (2017) Market scoping report. Deliverable 6.1, EU-H2020 project BRIGAID (grant agreement no. 700699), April 2017, 101 p.

Conference Proceedings

1) **Hosseinzadehtalaei, P**., Tabari, H., Willems, P. (2019) Updating precipitation intensity-duration-frequency (IDF) curves for Europe considering climate change impact. EGU General Assembly 2019, 7–12 April 2019, Vienna, Austria.

2) **Hosseinzadehtalaei, P**., Tabari, H., Willems, P. (2017) Climate change impacts on urban rainfall extremes: influence of time and space scales. 14th International Conference on Urban Drainage, Prague, Czech Republic, 10-15 September 2017.

3) Wouters, H., De Ridder, K., Poelmans, L., Willems, P., Brouwers, J., **Hosseinzadehtalaei, P**., Tabari H., Vanden Broucke, S., Van Lipzig, N., Demuzere, M. (2017) Heat-stress increase under climate change twice as large in cities as in rural areas. Geophysical Research Abstracts: vol. 19. EGU General Assembly. Vienna, Austria, 23-28 April 2017, Abstract No. EGU2017-9047.

4) Tabari, H., **Hosseinzadehtalaei, P**., Willems, P., Saeed, S., Brisson, E., Van Lipzig, N. (2016) How will be future rainfall IDF curves in the context of climate change?. Proceedings of the 4th IAHR Europe Congress, Liege, Belgium, 27-29 July 2016.

5) Wouter, H., Van Lipzig, N., Vanden Broucke, S., Poelmans, L., Tabari, H., **Hosseinzadeh Talaee, P**., Brouwers, J., Demuzere, M., Lauwaet, D., Maiheu, B., De Ridder, K. (2016) The impact of green-house gas emissions, climate downscaling and land-use change on Belgian urban heat stress scenarios. Geophysical Research Abstracts, Vienna, 17-22 April 2016.

Other scientific activates

Summer school:

- Summer School on "Natural Hazards in the Anthropocene", Centre of Natural Hazards & Disaster Science (CNDS), Sweden, 20-24 August 2018.

- 16th International Swiss Climate School on "High-Resolution Climate: Observations, Models and Projections", Switzerland, September 3-8, 2017.

- Supervision of 2 master student theses.

- Oral presentation at EGU 2019 entitled "Updating precipitation intensity-duration-frequency (IDF) curves for Europe considering climate change impact".